Improvement of Critical Current Density in $YBa_2Cu_3O_{7-\delta}$ Films with Nano-Inclusions

UNIVERSITY OF BIRMINGHAM

by

MOHD MUSTAFA AWANG KECHIK

A thesis submitted to the University of Birmingham
for the degree

DOCTOR OF PHILOSOPHY

School of Metallurgy and Materials
College of Engineering and Physical Sciences
University of Birmingham
November 2010

ABSTRACT

A high critical current density J_c is crucial for the application of HTS $YBa_2Cu_3O_{7-\delta}$ (YBCO) in the fabrication of energy efficient power devices and wires. We have prepared and studied YBCO films with nanoinclusions for increasing the current-carrying capability. All films were prepared by pulsed laser deposition (PLD) on single crystal $SrTiO_3$ (STO) substrates at optimised condition parameters. We found that the substrate temperature T_s of 780° C, laser energy E ~ 218 mJ/pulses, distance between target and substrate D_t of about 55 mm, annealing oxygen pressure O_{ap} 450 Torr and cooling rate C_t 8°/min were the optimum conditions for making good films with T_c = 91 K. We have used a method for introducing artificial pinning centers which has been shown to be successful in the nanotechnology of pinning centres: distributing a secondary phase, YBCO with 1% $Gd_2Ba_4CuWO_y$ (2411W) nano-inclusions, YBCO with 2% wt $BaZrO_3$ (BZO) and YBCO with 4% wt BZO nano-crystalline particles in the film. The superconducting properties were determined by AC susceptibility, magnetisation loops and transport measurements using a Quantum Design Magnetic property measurement system (MPMS) and a Physical properties measurement system (PPMS). Scanning and transmission electron microscopy (SEM) and (TEM), Atomic force microscopy (AFM) and X-ray were also used to characterise the micro-structure of the films. Both 2411W and BZO nano-inclusions led to increased J_c in applied fields and self-field. Scaling of the flux pinning force based on the Dew-Hughes model has been used in this work for investigating the flux pinning mechanism.

To my late father and mother,
my wife, fitrah, faheem & faikhah

ACKNOWLEDGMENTS

First of all, I would like to express my deepest sincere appreciation to my supervisors, Professor J.S. Abell, Dr. I.A. Crisan and Dr. P. Mikheenko for their valuable advices, suggestions, guidance, patience and constructive critics through the completion of my thesis work. Without their constant encouragement and support, this work would not have been possible and accomplished.

I would like to thanks Professor D.A. Cardwell (Material Group, University of Cambridge), Dr. N.H. Babu (Brunel University), and Dr. Petriina Paturi (University of Turku, Finland) for supplied me with targets with nano-phase inclusions.

A very special thank to Mr. Andy Bradshaw who has been supporting me all this time with his technical expertise. It is always a great feeling to have a knowledgeable and helpful person like you. Special appreciation to Dr. A Sarkar, Mr. VS Dang for helping me out and keeping me well informed. It had been a pleasure working with all of you. My sincerest thanks are extended to all my friends in our group. Thanks for your constant support and contributions.

A scholarship from the Higher Education Ministry of Malaysia (MOHE) and financial support from University of Putra Malaysia (UPM) are gratefully acknowledged. Thanks also to School of Metallurgy and Materials for some financial assistance.

Finally, a very special note of appreciation to my supportive and understanding family members (Rohani, Fitrah, Faheem and Faikhah), thanks for supporting me with all your love during the days of intensive work.

LIST OF PUBLICATIONS

M. M. Awang Kechik, P. Mikheenko, N. Hari Babu, D. A. Cardwell, J.S. Abell & A. Crisan. Improvement of critical current density in YBa_2Cu_3Ox films deposited from a melt-grown target. *Condensed Matter Material Physics* **2008**, Royal Holloway.

M. M. Awang Kechik, P. Mikheenko, N. Hari Babu, D. A. Cardwell, P. Paturi, H. Huhtinen, J.S. Abell and A. Crisan. Artificial pinning centres in superconducting films induced by secondary phase nano-inclusions. European Summer School on Superconductivity, Grenoble, France **2009**.

M.M. Awang Kechik, P. Mikheenko, A. Sarkar, V. S. Dang, N. Hari Babu, D. A. Cardwell, J. S. Abell and A. Crisan. Increased pinning force in $YBa_2Cu_3O_{7-\delta}$ thin films by $Gd_2Ba_4CuWO_y$ nano inclusions. 9th European Conference on Applied Superconductivity **2009**, Dresden, Germany.

M. M. Awang Kechik, P. Mikheenko, N. Hari Babu, D. A. Cardwell, J.S. Abell & A. Crisan, Artificial pinning centres in $YBa_2Cu_3O_{7-\delta}$ thin films by $Gd_2Ba_4CuWO_y$ nano-inclusions. Superconductor Science and Technology, **2009**. Volume 22, Issue 3, pp. 034020.

A. Crisan, **M. M. Awang Kechik**, P. Mikheenko, V. S. Dang, A. Sarkar, J.S. Abell Critical current density and pinning potential in $YBa_2Cu_3O_{7-\delta}$ thick films ablated from a $BaZrO_3$-doped nanocrystalline target. Superconductor Science and Technology, **2009.** Volume 22, Issue 4, pp. 045014.

A. Crisan, A. Sarkar, P. Mikheenko, V. S. Dang, **M. M. Awang Kechik**, J.S. Abell. Improvement of pinning force and critical current density in thick $YBa_2Cu_3O_{7-\delta}$ films grown on $SrTiO_3$ substrates decorated with $LaNiO_3$ nanodots. Superconductivity and Novel Magnetism, **2009**.

Mikheenko, P., Sarkar, A., Dang, V.S., Tanner, J.L., **M.M.Awang Kechik**, Abell, J.S., Crisan, A. Pinning centers induced in YBCO films by nano-dots in substrate decoration and quasi-superlattice approaches: IEEE Trans. Appl. Supercond. **2009.** Volume 19, Issue 3

P. Mikheenko, J. S. Abell, A. Sarkar, V.S. Dang, **M.M. Awang Kechik**, J.L. Tanner, P. Paturi, H. Huhtinen, N. Hari Babu, D. A. Cardwell, and A. Crisan. Self-assembled artificial pinning centres in thick YBCO superconducting films. Journal of Physics: Conference Series **2010.** 234

V.S. Dang, P. Mikheenko, A. Sarkar, **M.M. Awang Kechik**, J.S. Abell, A. Crisan. Increased critical current density and pinning in thick $Ag/YBa_3Cu_2O_{7-x}$ multilayers. Physica C: Superconductivity and Its Applications. **2010**. Volume 470, Issue 20, pp.1238

Adrian Crisan, Pavlo Mikheenko , Asis Sarkar, Van Son Dang, **Mohammed M. Awang Kechik**, John S. Abell, Petriina Paturi and Hannu Huhtinen. Artificial pinning in thick YBCO films: Pinning potential and c-axis correlation. Physica C: Superconductivity and Its Applications. **2010**. Volume 470, Issue 19, p.840-843

P. Mikheenko V.S Dang, Y. Y. Tse, **M.M. Awang Kechik**, P. Paturi, H. Huhtinen, J. S. Abell, A. Sarkar and A. Crisan. Integrated nanotechnology of pinning centres in $YBa_2Cu_3O_x$ films. Supercond. Science. Technol. **2010** Volume 23: p.125007.

A. Sarkar, V.S. Dang, P. Mikheenko, **M.M. Awang Kechik**, J.S. Abell, A. Crisan. Improved critical current densities in thick $YBa_2Cu_3O_{7-\delta}$ multilayer films interspaced with $YBa_2Cu_3O_x$ nano-dots. Journal of Thin Solid Films **2010**. Volume 519, Issue 2: p 876-879.

P. Mikheenko, V.S. Dang, **M.M. Awang Kechik**, Y. Wang, A. Sarkar, J.L. Tanner, J. S. Abell, & A. Crisan. Synergetic pinning centres in YBa_2Cu_3Ox films through a combination of Ag nano-dot substrate decoration, Ag/YBCO quasi-multilayers, and the use of $BaZrO_3$-doped target. IEEE Trans. Appl. Supercond. **2011** Volume 21: 3:p. 3184-3188

V.S. Dang, P. Mikheenko, A. Sarkar, **M.M. Awang Kechik**, J.S. Abell, P. Paturi, H. Huhtinen, A. Crisan. Combination of Ag substrate decoration with introduction of $BaZrO_3$ nano-inclusions for enhancing critical current density of $YBa_2Cu_3O_7$ films. Journal of Supercond. Nov. Magnetism **2011** Volume 24:p.505-509

A. Sarkar, P. Mikheenko, V.S. Dang, **M.M. Awang Kechik**, J.S. Abell, A. Crisan. Improved critical current densities in $YBa_2Cu_3O_{7-\delta}$ multilayer films interspaced with Palladium nano-dots. Journal of Supercond. Nov. Magnetism **2011** Volume 24:p.173–177

P. Mikheenko, V.S. Dang, **M.M. Awang Kechik**, Y. Wang, A. Sarkar, J.L. Tanner, J. S. Abell, & A. Crisan. Nano techniques for enhancing critical current in superconducting YBCO films. Journal of Supercond. Nov. Magnetism **2011.** Volume 24:p.1059–1064

TABLE OF CONTENTS

LIST OF FIGURES

LIST OF TABLES

LIST OF ABBREVIATIONS

AC	*Alternate current*
AFM	*Atomic force microscope*
Al	*Aluminium*
BaO	*Barium oxide*
BCC	*Body centred cubic*
BCS	*Bardeen-Cooper-Schrieffer*
Bi	*Bismuth*
Bi_2O_3	*Bismuth oxide*
BSCCO	*Bi-Sr-Ca-Cu-O*
CeO_2	*Cerium oxide*
CH_3CH_2OH	*Ethanol*
CH_3COCH_3	*Acetone*
Cr	*Chromium*
Cu	*Copper*
CCD	*Charge coupled detector*
CuO	*Copper oxide*
CuO_2	*Copper dioxide*
CVD	*Chemical vapour deposition*
EDS	*Energy dispersive spectrum*
EBSD	*Electron backscattered diffraction*
EDS	*Energy dispersive spectroscopy*
FWHM	*Full width half maximum*
GL	*Ginsburg Landau*
He	*Helium*
Hg	*Mercury*
HTS	*High temperature superconductor*
HTSCs	*High temperature superconductors*
IBAD	*Ion beam assisted deposition*
ISD	*Inclined substrate deposition*
LANL	*Los Alamos national laboratory*
LPE	*Liquid phase epitaxy*
MgB_2	*Magnesium diboride*
MgO	*Magnesium oxide*
MPMS	*Magnetic property measurement system*
MOD	*Metal organic deposition*
MOCVD	*Metal organic chemical vapour deposition*
NaCl	*Sodium chloride*
Nb	*Niobium*
Nb_3Ge	*Niobium-germanium intermetallic compound*
Ni	*Nickel*
PDF	*Power diffraction pattern*
PLD	*Pulsed laser deposition*
PPMS	*Physical property measurement system*
POM	*Polarised optical microscope*
PVD	*Physical vapour deposition*

RABiTS	*Rolling assisted biaxially textured substrates*
RE	*Rare earth*
RMS	*Root mean square*
SEM	*Scanning electron microscopy*
Si	*Silicon*
SPM	*Scanning probe microscopy*
SiO_2	*Silicon oxide*
$SrTiO_3$	*Strontium titanate*
STO	*Strontium titanate*
STM	*Scanning tunnelling microscope*
T	*Temperature (K or °C)*
t	*Time (second or hours)*
T_c	*Transition or critical temperature (Kelvin)*
TEM	*Transmission electron microscopy*
Tl	*Thallium*
XRD	*X-ray diffraction*
Y	*Yttrium*
Y_2O_3	*Yttria (yttrium oxide)*
YBCO	*Y-Ba-Cu-O*
YBCO-123	$YBa_2Cu_3O_{7-x}$
YSZ	*Yttria stabilised zirconia*
Z	*Vertical position of the scanner*
Zi	*The current Z value*
ZnO	*Zinc oxide*
2411W	$Gd_2Ba_4CuWO_y$

Symbols

A	*Area (cm^2)*
A_1	*Scaling parameter of A_1*
A_2	*Scaling parameter of A_2*
A_3	*Scaling parameter of A_3*
B	*Magnetic field*
B_{c1}	*Lower critical field in type-II superconductors*
B_{c2}	*Upper critical field in type-II superconductors*
$B_{//}$	*Magnetic field parallel to x-axis*
B_{ab}	*Magnetic field parallel to the a, b-plane of a HTS tape*
B_c	*Magnetic field parallel to the c-plane of a HTS tape*
B_p	*Field of full penetration*
B_{irr}	*Irreversibility field in type-II superconductors*
β	*Temperature dependent coefficient*
C_t	*Cooling rate (°C/min)*
d	*The interplanar spacing (nm)*
δT_c	*Related to spatial fluctuations of T_c*
δl	*Related to spatial fluctuations of the charge carrier*
D_t	*Distance between target and substrate (mm)*
κ	*Ginsburg Landau parameter*
$\Delta\kappa$	*Ginsburg Landau parameter*
e	*Electron charge*
ξ	*Coherence length*
E,	*Electric field*
E	*Laser energy (mJ/pulse)*
f	*Frequency of the applied AC current or external field(Hz)*
f_n	*Normal state free energy*
F	*Lorentz force*
F_p	*Flux pinning force (GN/m^3)*
γ	*Anisotropy of the critical current density*
h	*Planck's constant*
H	*Applied Magnetic field (Tesla)*
H_c	*Thermodynamical critical field in type-I superconductors*
H_{c1}	*Lower critical field in type-II superconductors (Tesla)*
H_{c2}	*Upper critical field in type-II superconductors (Tesla)*
H_{irr}	*Irreversibility field in type-II superconductors (Tesla)*
I_c	*Critical current (A/cm)*
J	*Current density (A/cm^2)*
J_c	*Critical current density (A/cm^2)*
$J_{c\theta}$	*The angle-dependent critical current density (A/cm^2)*
λ	*Penetration depth*
J_c	*Critical current density*
J_{c0}	*Critical current density without any magnetic field present*
m	*Electron mass*
M	*Magnetization*
N_s	*Density of superconducting electron pairs*

O_p	*Oxygen pressure (Torr)*
O_{ap}	*Annealing oxygen pressure (Torr)*
R	*Electric resistance (Ohm)*
T_c	*Critical temperature (K)*
T_s	*Substrate temperature*
t	*Time (mins)*
U_0	*Activation energy*
v	*Volume*
V	*Voltage*
V_f	*Volume of the pinning center*
x	*distance of the flux motion*
χ'	*Real susceptibility (dimensionless)*
χ''	*Imaginary susceptibility (dimensionless)*

Chapter 1

Introduction

Since the discovery of high temperature superconducting materials in 1986, researchers are attracted by their potential for high current-carrying capacity for potential use in electric power transmission systems [1]. Powder in tube (PIT) wires or tapes were the first ones available for power and magnet applications based on high temperature superconductors (HTS). Despite this, the PIT process can only be applied to Bismuth or Thallium based oxide superconductors since both will form plate-like microstructures after mechanical deformation. This first generation (PIT) of superconducting tapes suffers serious degradation of critical current density in high magnetic field. $YBa_2CuO_{7-\delta}$ (YBCO) is considered as a promising alternative material, which has an excellent ability to carry a high superconducting critical current in high magnetic fields even with a lower

superconducting transition temperature, T_c of 92 K as compared to Bi based ones (T_c = 132 K) [2]. The second generation of HTS of YBCO tapes, that is called coated conductors, which are based on thin film technology, has been studied worldwide. Significant progress has been focused on the development of $YBa_2CuO_{7-\delta}$ (YBCO) with attention on the fabrication processes of high quality temperature YBCO superconducting thin film such as by Pulsed Laser Deposition (PLD), Sputtering Thermal Co Evaporation (STCE), Chemical Vapour Deposition (CVD), Liquid Phase Epitaxy (LPE) and Metal Organic Deposition (MOD). These fabrication methods can produce highly oriented thick superconducting layers that are important for obtaining a high performance, and high critical current, I_c in coated conductors [3-6].

Recently, long tape processing for superconducting layers with good crystal grain alignment and high crystallinity has shown rapid progress and enough I_c for power device application[6]. In order to control the crystal grain alignment of the superconducting layer, two distinct technologies exist, including fabrication of textured metallic substrates such as Rolling Assisted Bi-axial Texture (RABiTs) [7, 8] and crystal alignment of a buffer layer on a non-textured high strength metallic substrate by Ion Beam Assisted Deposition (IBAD) or Inclines Substrate deposition (ISD) [9, 10].

At present the coated conductor R & D community is attempting to work out fabrication techniques which work cost effectively in a continuous process [11]. Preferences for pulsed laser deposition (PLD) as a versatile technique for preparation of thin films of complex materials is exponentially growing due to low capital cost involved. It has been found to be convenient and efficient for the synthesis of high T_c superconducting thin films [12].

Significant progress has been made by the research community to enhance critical current density (J_c) in YBCO in coated conductors for power applications. The strong increase of J_c can be achieved when the flux lines are pinned and their movement completely prevented. The flux lines could be pinned by introducing effective artificial pinning centers leading to high current density at higher fields and higher temperatures. The first cost-effective method in introducing artificial pinning centers is the so-called substrate decoration [13, 14], i.e., growing nanoscale islands (nano-dots) of certain materials on the substrate prior to the deposition of the superconducting thin film.

In this research another approach is used which has been shown to be successful in the nanotechnology of pinning centres: distributing a secondary phase in the film by modifying the target composition. Four target compositions were used: commercially available YBCO 123, YBCO with 1% mol $Gd_2Ba_4CuWO_y$ (2411W) nano-phase inclusions and nano-crystalline YBCO doped with 2% wt $BaZrO_3$ and 4% wt $BaZrO_3$ (BZO), respectively.

YBCO films using the three target compositions were deposited on $SrTiO_3$ (STO) single crystal substrates by PLD using a scanning laser beam. This method consumes the target material gradually and homogeneously and does not require frequent and intermediate polishing of the target, which makes the technique potentially suitable for large-scale production of superconducting coated conductors. In addition, the thickness, *d*, of the films is relatively large, which would make them suitable for potential high power applications that require high critical currents.

This work is focused on fundamental studies of both the fabrication and characterization of YBCO 123 thin films grown on Strontium Titanate (STO) substrate by Pulsed Laser Deposition method, with emphasis on optimizing the processing conditions.

The depositions were performed in a chamber which had not been used for superconductor material before. The superconducting properties of $YBa_2Cu_3O_{7-x}$ (Y123) films are very sensitive to the deposition conditions. In order to achieve good quality films, the effects of the deposition parameters such as deposition temperature (T_s), annealing oxygen pressure (O_{ap}) and cooling time (cooling rate) (C_t) in relation to superconducting transition temperatures and critical current density were observed.

This work is also to focus on the PLD fabrication technology of YBCO film with objectives of understanding the underlying mechanism of the T_c and J_c performance of YBCO films and the mechanism of superconducting properties enhancement by nano-inclusion additions to the film. It is well known that J_c is closely related to the flux pinning, thus it is important to study some flux pinning in YBCO films. The flux pinning mechanism is also addressed in this work. Extensive discussion is included on the flux pinning mechanism in films with nano-inclusions having different thickness, using the scaling function of Dew-Hughes. As a result we are able to solve an important issue in YBCO films, which is the observed rapid decrease in J_c under high magnetic field.

Chapter 2

Theory and literature review

2.1 Fundamentals of superconductivity

2.1.1 History of superconductors

Superconductivity was discovered by physicist H Kamerlingh Onnes in 1911 at University of Leiden, Holland when he measured the electrical resistance of solid mercury. Three years earlier he managed to develop a method to produce liquid helium. He had been using liquid helium to cool mercury below 4.2 K. Later, Onnes noticed that if he turned off the voltage below 4.2 K, the current continues to flow without loss for months and even years in this material (mercury) [15]. The resistance of this material had become zero and is known as the superconducting state at temperatures below a critical temperature or transition temperature T_c. Understanding of the basic mechanism of superconductivity was only found 46 years later by John Bardeen, Leon Cooper and Robert Schrieffer which is known as Bardeen-Cooper-Schrieffer (BCS) theory.

In 1973 Gavaler had produced films from Nb_3Ge alloys with the structure of binary A_3B, which is known as A15 with a critical temperature of T_c = 23.1 K. In the following years all efforts to find superconducting materials with higher critical temperature have failed. However in 1986 Bednorz and Müller, scientists at the IBM laboratory in Switzerland discovered superconductivity in the family of layered copper oxides with pervoskite like structure $(La, Ba)_2CuO_4$ with a T_c up to 35 K [16]. This discovery has opened a new era of superconductor research and researchers in the United States, Japan, Europe and China have been actively involved in research on high temperature superconducting (HTS) ceramics.

The main contribution in HTS was made by Paul Chu and colleagues at the University of Houston, Texas. Wu et al. [17] found a $YBa_2Cu_3O_x$ superconductor with T_c = 93 K which exceeds the boiling point of liquid nitrogen 77 K. This finding leads to the usage of liquid nitrogen as a cooling medium which is much cheaper than liquid helium. After a year of key findings by Chu and his group, the further work of Maeda et al. [18] reported the presence of superconducting phases with T_c about 110 K in the system Bi-Sr-Ca-Cu-O.

Shortly afterwards, Sheng and Hermann [19] found the thallium system Tl-Ba-Ca-Cu-O with T_c reaching 125 K. The bismuth system has been widely studied but less investigation has been done for thallium system because of its high toxicity. Research to obtain the highest value of T_c continues five years later with the publication by Schilling et al [20] showing that the substitution of bismuth and thallium by mercury increases the transition temperature up to 134 K. Figure 2.1 shows the evolution of the transition temperature of superconductors for 1911 onwards.

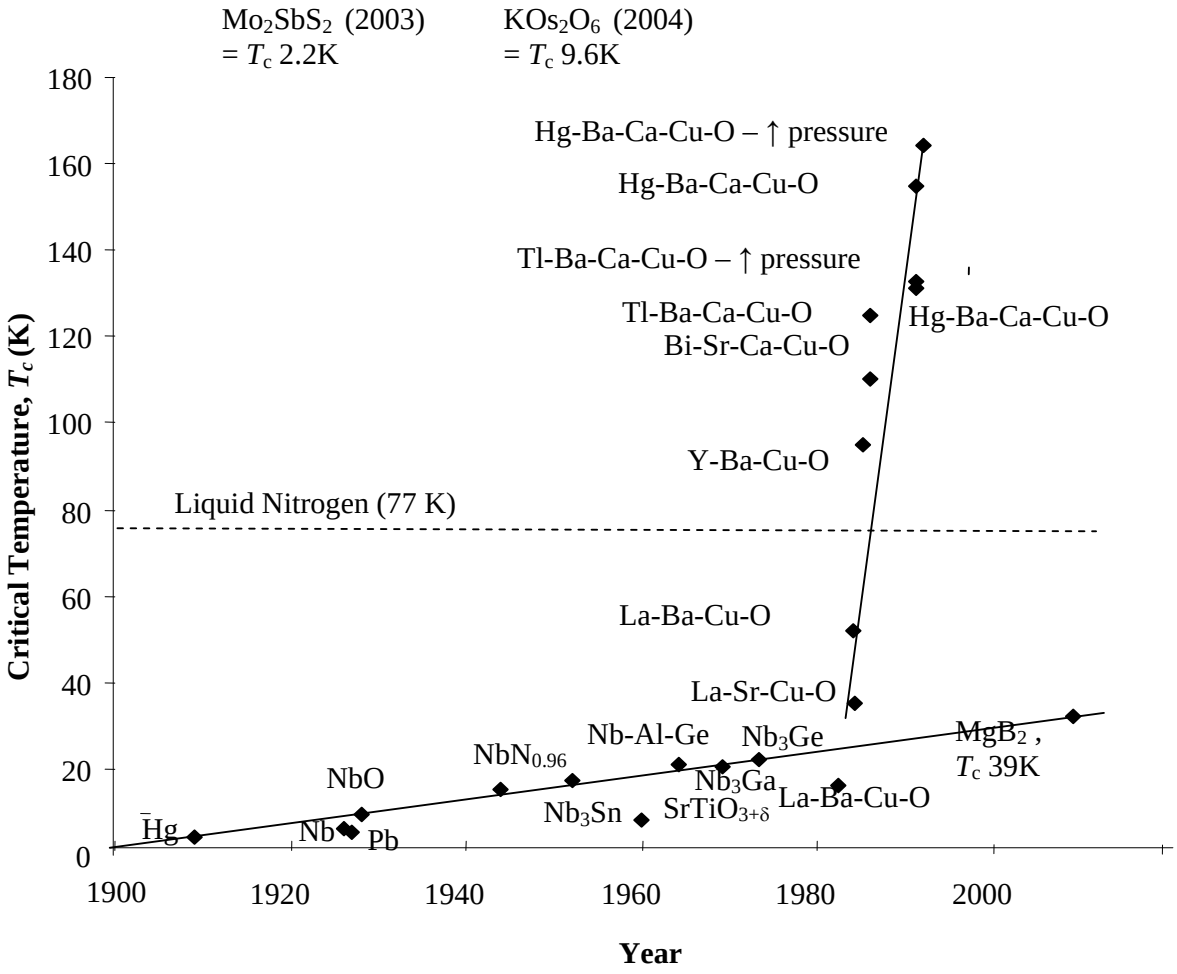

Figure 2.1: The evolution of critical temperature, T_c from 1911 [2].

2.1.2 Introduction to superconductor

Some metals such as titanium, aluminum, tin, lead and mercury that are in the superconducting state will exhibit zero resistance when they are cooled below the critical temperature [21]. These materials are the first superconductors to be discovered and named superconductor type I. Based on BCS theory, the loss of the electric resistance in a superconductor is because, at lower temperature the carrier charge consists of electron

pairs (super electron) which are called Cooper pairs, and can move without producing resistance. Cooper pairs are formed by an electron interaction with the vibration of the crystal lattice (phonon) [22].

In 1933, Meissner and Ochsenfeld found an interesting phenomenon for superconducting materials where it not only has zero resistance, but rejected the magnetic flux density (B = 0) in it when applied in magnetic field and cooled below the T_c i.e. it exhibits perfect diamagnetism as can be seen in Figure 2.2. This phenomenon is known as the Meissner effect in which the magnet could float on the superconducting material, which is another unique property of superconductors.

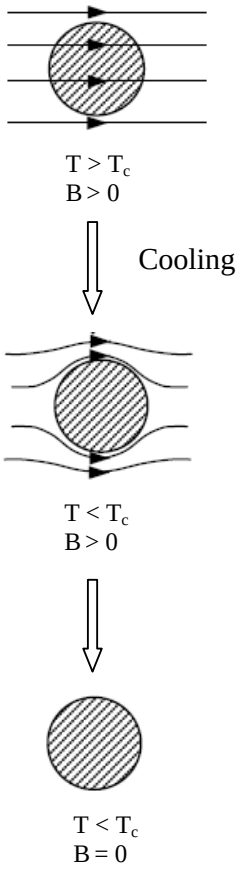

Figure 2.2: The flux is always expelled in a superconducting material type I so that B = 0 inside (Meissner effect).

2.1.3 Type I superconductors

The type-I superconductors allow no magnetic field at all to penetrate their interior. The shielding currents exist only on the surface. However, if the external magnetic field is too strong, the superconductor cannot shield it without surpassing its own critical current. Magnetic fields larger than this critical field, denoted B_c, will destroy the superconductivity in the material as shown in Figure 2.3. The externally applied magnetic field (H) is along the x-axis, while the field inside the superconductor (B) is along the y-axis. Above B_c, the material is not superconducting and the entire material becomes normal once the diamagnetic moment becomes zero and thus the entire external magnetic field which passes through the material and field outside, H and inside, B are equal. But as the external field drops below B_c, the material abruptly becomes superconducting and expels all magnetic field from its interior via the Meissner effect rendering $B = 0$ [15].

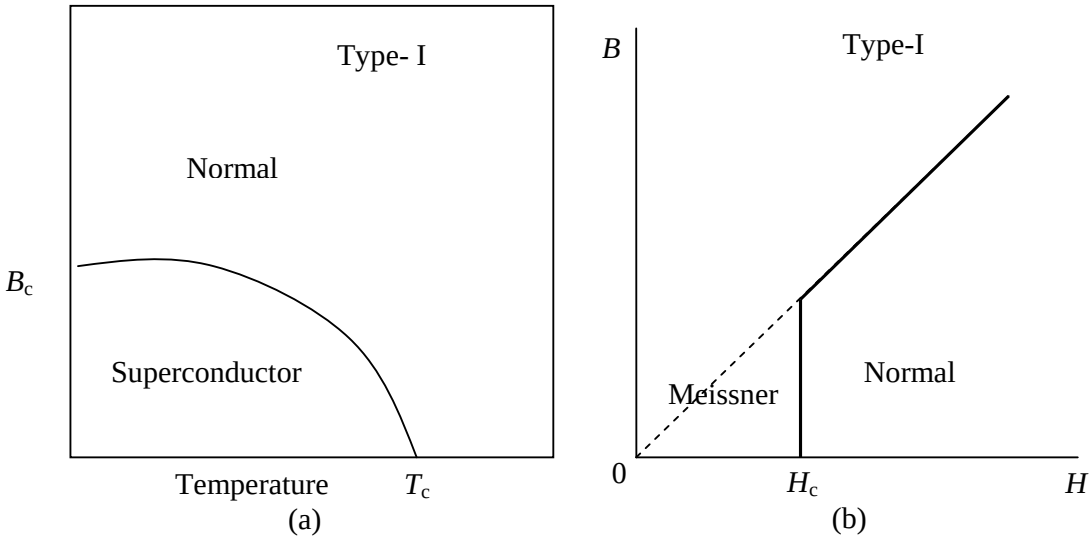

Figure 2.3. Type-I superconductor (a) B a function of temperature (b) The magnetic field within the material (B) as the function of applied magnetic field (H)

2.1.4 Type II superconductors

The type-II superconductor shows perfect diamagnetism or excludes all magnetic field lines below the lower critical field, B_{c1}. B_{c1} plays a very important role in determining the critical current. This is because between the critical fields, there is partial penetration of magnetic field known as a vortex. At field strength between B_{c1} and B_{c2}, the magnetic field begins to intrude into the material. The penetrating field forms cores that are non-superconducting. When this occurs, the material is said to be in the mixed state with some of the material in the normal state and the other still superconducting. The mixed (vortex) state is an intrinsic feature of type II superconductors and exists for magnetic fields such that $H_{c1} < H < H_{c2}$ as shown in Figure 2.4(a). The existence of the mixed state can be explained by the fact that the material always tends to assume the state with lowest total free energy and when the surface energy between normal and superconducting regions is negative, the appearance of normal regions will reduce the total free energy and lead to a more favourable energy state [21]. Above B_{c2}, magnetic field can penetrate into the material and form flux lines known as vortices forming a triangular flux lattice.

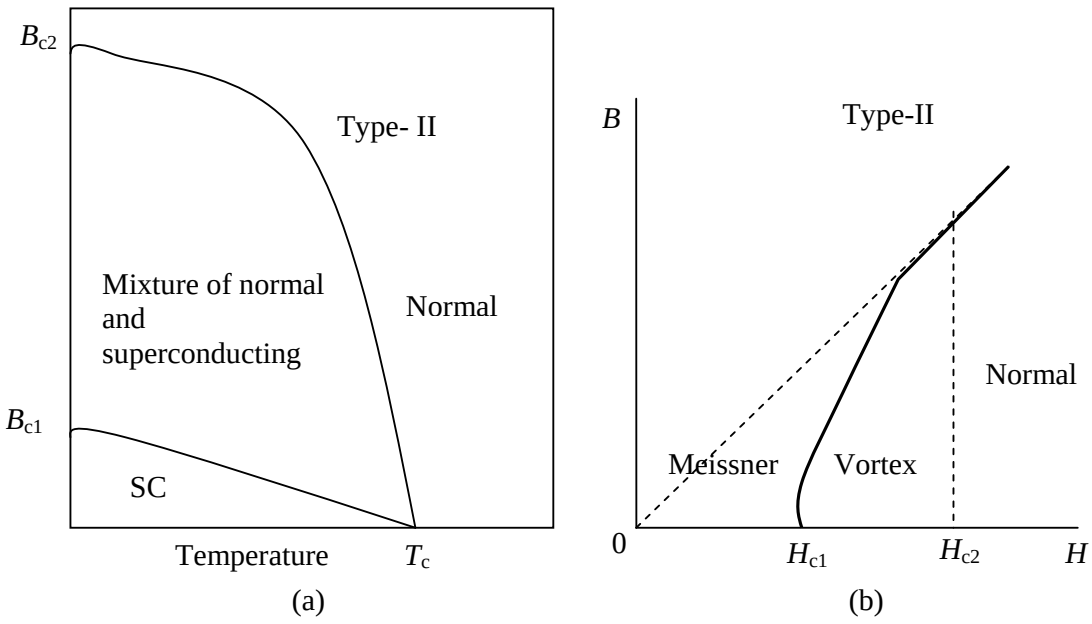

Figure 2.4: Type-II superconductor (a) *B* a function of temperature (b) The magnetic field within the material (*B*) as the function of applied magnetic field (*H*)

An important contribution to the theory of superconductivity was made by Abrikosov in 1957, describing a new phenomenon related to the Ginzburg-Landau theory. It was predicted by Abrikosov that the magnetic flux would penetrate in a regular array of flux tubes, named fluxons, each one having the quantum of flux $\Phi_0 = h/2e = 2.6678\times10^{-15}$ Wb (*h* = Planck's constant and *e* = electron charge). In a perfectly pure material, the flux lines would be able to easily move and adjust their density according to the applied field. However, due to impurities and inhomogeneities in type-II superconductors, the fluxons are pinned and an energy barrier is created that has to be overcome in order to move them [23].

The vortex is surrounded by magnetic field and the interior is non-superconducting. The radius of the vortex is about 100 nm for the conventional superconductors. As the

external magnetic field increases, the number of vortices increases until at the upper critical magnetic field B_{c2}, the material cannot support any more vortices, thereby destroying superconductivity. Abrikosov found that his theory actually predicted vortices narrow thread-like channels along which magnetism could penetrate the interior of the superconductor. These channels formed a lattice-like structure in the material. Abrikosov also provided a detailed prediction of how the number of vortices would grow as the magnetic field increases in strength and how superconductivity is lost when the field exceeds the upper threshold, causing the vortices to overlap.

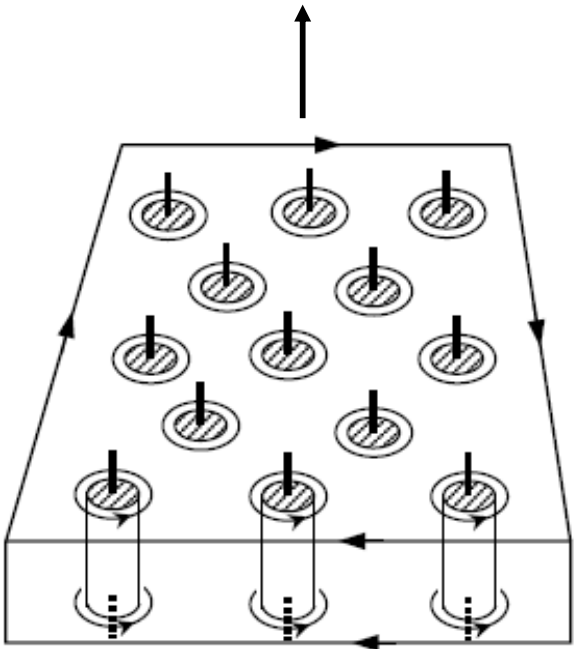

Figure 2.5: The mixed state, showing normal cores and encircling supercurrent vortices. The vertical lines represent the flux threading the cores. The surface current maintains the bulk diamagnetism [24].

2.1.5 Pinning mechanism in type II superconductors

In the vortices of an ideal type II superconductor, the magnetization is completely reversible and the very small critical current densities are obviously not interesting for applications [25]. The vortices in a type-II material repel each other, so they will arrange in a regular pattern to maximize the distance between nearest neighbours. When a current is applied to a type-II superconductor in the mixed state, the magnetic vortices feel a force (Lorentz force, $F = Jn\Phi_O$) that pushes the vortices at right angles to the current flow. This movement dissipates energy and produces resistance [26]. The interaction of current and the vortex determines the J_c of a type-II superconductor, and J_c is strongly related to the magnetic fields. Large current flow can interact with the vortex through the Lorentz law as shown in Figure 2.6, and can result in the motion of the vortex due to the Lorentz force, which can cause energy loss. The moving vortex can create an electric field, E and the energy loss when current with density, J is flowing, from the equation $J_c = E \bullet B$. B_{c1}, in the type-II superconductor is very low and so, theoretically, J_c is low in this type of superconductor. Flux pinning is also associated with J_c. J_c can be increased if the vortex is prevented from moving and this can be done by pinning the flux lines through introduction of suitable impurities as pinning centers. If the average pinning force is F_p, then for $F < F_p$ there is no flux flow and supercurrents persist. For $F > F_p$ the flux begins to move and the resistance is no longer zero. The critical force occurs when $F_p = J_c b$.

A carefully controlled introduction of impurities and inhomogeneities in the superconductor can be used to pin the flux lines as shown in Figure 2.7. However, suitable impurities must be identified in order to minimize breaking of the Cooper pairs, which destroys superconductivity. At absolute zero temperature, the flux only occurs when the

Lorentz force exceeds the pinning force. When $J < J_c$, current can flow without any losses. When $J > J_c$, the flux lines will move and electric field can be generated which eventually leads to a non-zero potential difference. Above absolute zero there is a finite probability that the flux lines may overcome the pinning energy and, although $J < J_c$ (T,B), there is flux flow and as a result the resistance is not zero. At absolute zero, the activation energy $U_o(0,B)$ can be written as

$$U_o(0,B) = J_c(0,B)BV_f x \qquad 2\text{-}1$$

where V_f is the volume of the pinning center and x is the distance of the flux motion.

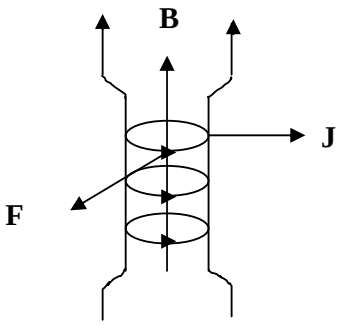

Figure 2.6: The Lorentz force $F = J \times B$ that resulted when current with density J interact on a flux line

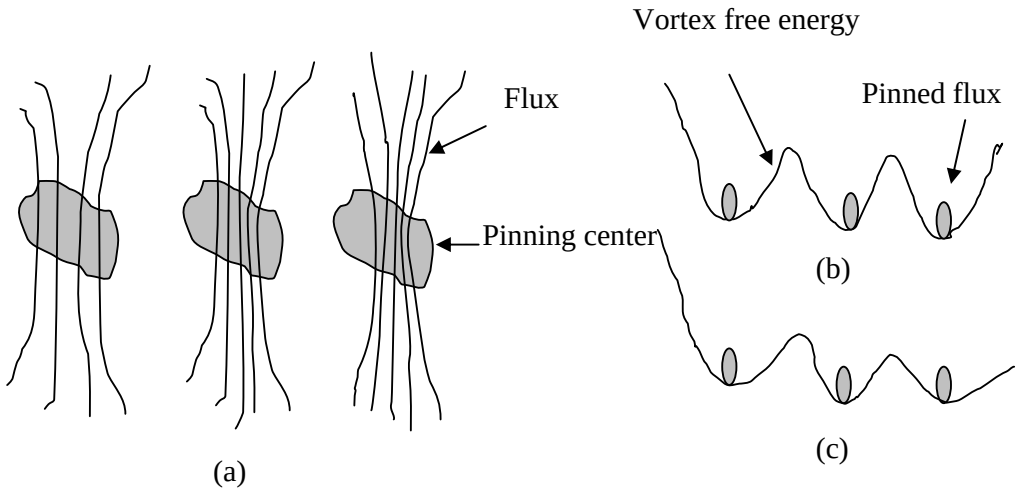

Figure 2.7. Impurities and defects can act as flux pinning centers. (a) impurities can interact and pin the flux (b) vortex free energy and the pinned flux (c) vortex in the presence of current flow [27].

2.1.5.1 Vortex structure

As explained earlier the magnetic field in mixed state of a Type II superconductor is present in the form of vortices. Abrikosov defined the relation of the lower (H_{c1}) and upper (H_{c2}) critical field to the thermodynamical critical field H_c as follows:

$$H_{c1} = H_c / \kappa$$
$$H_{c2} = \sqrt{2}\kappa H_c \qquad \text{2-2}$$

where κ is Ginzburg-Landau constant of the material.

$$\kappa = \frac{\lambda}{\xi} \qquad \text{2-3}$$

where λ is penetration depth, at which the magnetic flux enters a superconducting specimen and ξ is the coherence length, which corresponds to the distance between the super electrons according to Ginzburg-Landau (GL) theory. For superconductor type II,

where $\kappa \geq 1$, there is a negative surface energy which allows the entry of magnetic flux in a field $H \geq H_{c1}$ (the lower critical field).

The basic GL theory is that the free energy density of a superconductor can be expanded in a series of the form:

$$f_s = f_{n0} + \alpha|\psi|^2 + \frac{\beta}{2}|\psi|^4 + \frac{1}{4m}\left|\left(\frac{\hbar}{i}\nabla - \frac{2e}{c}\mathrm{A}\right)\psi\right|^2 + \frac{h^2}{8\pi} \qquad 2\text{-}4$$

where f_{n0} is the normal state free energy density, α and β are temperature dependent coefficients, m is the electron mass, e is the electron charge, c is the speed of light, A is the vector potential, h is the local magnetic field, ψ is the order parameter in the superconductor and $|\psi|^2 \propto n_s$, where n_s is the density of superconducting electron pairs in the superconductor. The first GL equation (2.12) can be solved to find ψ near an isolated vortex.

$$\alpha\psi + \beta|\psi|^2\psi + \frac{1}{4m}\left(\frac{\hbar}{i}\nabla - \frac{2e}{c}\mathrm{A}\right)^2\psi = 0 \qquad 2\text{-}5$$

As expected, ψ is zero in the center and recovers to its equilibrium value over a distance ξ. The vortex is described as a normal core $\pi\xi^2$. For $\kappa >> 1$, ψ can be approximated as a constant except over the small area of the normal core, so that the London Equation (equation 2.2)

$$h = -c\nabla \times \left(\frac{m}{n_s e^2} J\right) \qquad 2\text{-}6$$

can be used to determine the field distribution in the superconductor which gives

$$h(r) = \frac{\Phi_0}{2\pi\lambda^2} K_0\left(\frac{r}{\lambda}\right) \qquad 2\text{-}7$$

where $K_0(r)$ is zero order Hankel function. The limiting forms for $h(r)$ are:

$$h(r) = \frac{\Phi_0}{2\pi\lambda^2}\left(\frac{\pi}{2}\frac{\lambda}{r}\right)^{\frac{1}{2}} e^{\frac{r}{\lambda}} \qquad r \to \infty \qquad \text{2-8}$$

$$h(r) = \frac{\Phi_0}{2\pi\lambda^2}\left[\ln\left(\frac{\lambda}{r}\right)\right] \qquad \xi << r << \lambda \qquad \text{2-9}$$

The exponential decay of the field occurs over a characteristic distance λ. Using Maxwell's equation $\nabla \times h = \frac{c}{4\pi} J$, the field gradient implies that a supercurrent circulates around the vortex with spatial dependence $J_s \sim \partial h(r)/\partial r \sim 1/r$. The circulating supercurrent is the main contributor to the line energy of vortices, as well as the interactions between them.

2.1.5.2 Vortex line energy

Each vortex is line energy per unit length ε_1, which is given by (for $\kappa >> 1$):

$$\varepsilon_1 = \frac{1}{8\pi}\int\left(h^2 + \lambda^2\left|\nabla \times h\right|^2\right)dS \qquad \text{2-10}$$

where the first term is the field energy and the second term is the energy of the circulating supercurrents. A comparison of the two terms using the expression for $h(r)$ from equation 2.8 shows the second is larger by a factor of order $(\kappa/\ln\kappa)^2$. Evaluating the integral of equation 2.9 gives:

$$\varepsilon_1 = \left(\frac{\Phi_0}{4\pi\lambda}\right)^2 \ln\kappa = \frac{H_c^2}{8\pi} 4\pi\xi^2 \ln\kappa \qquad \text{2-11}$$

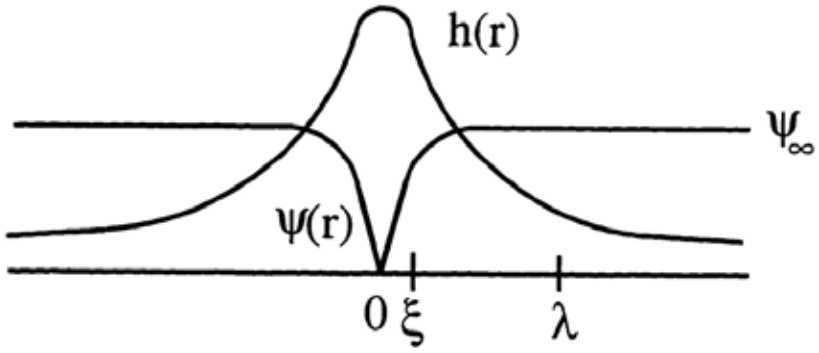

Figure 2.8. Structure of an isolated vortex for κ ~5 [28]. The order parameter $\psi(r)$ goes to zero in the center, producing a normal core of radius ξ. The magnetic field $h(r)$ decays approximately exponential over a distance λ.

This result shows that the energy associated with the supercurrent is of the same order of magnitude as the condensation energy lost in the core. Therefore, the pinning mechanism that uses the core energy (core pinning) and those that involve the supercurrent energy (surface pinning) can be of similar strength.

2.1.5.3 Flux pinning mechanisms in YBCO: Dew-Hughes Model

Vortex lines in the type II superconductors have a normal core diameter 2ξ, where ξ is coherence length. Pure YBCO has a calculated coherence length of 2 nm at 0 K. It is strongly suggested that nano precipitates smaller than 2ξ are the most important pinning centers in YBCO films [29]. To study the flux pinning in high temperature superconductors (HTS) more accurately at high temperatures such as 77 K, an improved method based on the Dew-Hughes model has been developed. The Dew-Hughes model of elementary pinning forces in flux pinning forces are caused by magnetic or core interaction. For HTS, we can safely assume that core pinning is dominant due to their large

κ values. This leaves two different sources of pinning: either by non-superconducting (normal) particles embedded in the superconducting matrix leading to a scattering of the electron mean free path (δl pinning) or by spatial variations of the Ginzburg parameter associated with fluctuations in the critical transition temperature T_c (δT_c or $\Delta\kappa$ pinning) [30].

The total pinning force is given by

$$F_p = \sum f_p \qquad 2\text{-}12$$

where f_p, is the force per unit length of pinned flux line. Dew-Hughes proposed the following general expression for the normalised pinning force density;

$$F_p(b) = F_p / F_p^{\max} \propto b^p (1-b)^q \qquad 2\text{-}13$$

where p and q depend on the specific characteristics of flux pinning in the superconductor, and b is the reduced magnetic field $\left(B/B_{c2}\ or\ B/B_{irr}\right)$. The different types of pinning centers are explained by different values of p and q.

In this Dew-Hughes model, there are six different pinning functions describing the core pinning using Eq. (2.3)[31].

1. p = 0, q = 2: normal core pinning, volume pins;
2. p = 1, q = 1: $\Delta\kappa$-pinning, volume pins;
3. p = 1/2, q = 2: normal core pinning, surface pins;
4. p = 3/2, q = 1: $\Delta\kappa$-pinning, surface pins;
5. p = 1, q = 2: normal core pinning, point pins;
6. p = 2, q = 1: $\Delta\kappa$-pinning, point pins;

This model is used for the YBCO films studied in this research to analyse the pinning type introduced by nanoparticle inclusion in every sample. The pinning force is calculated as

$$F_p(b) = J_c \times B \qquad 2\text{-}14$$

where J_c is the critical current density and B is an applied magnetic field. The $F_p(b)$ curves were fitted by Eq. 2.13 in order to obtain specific fitting parameters *p* and *q* that can be used to describe the type of pinning.

2.1.5.4 Types of pinning site

The critical current density is one of the most crucial properties of high temperature superconductor (HTS) for both physical understanding and applications [23]. A lot of work has been carried out on the question of how to enhance the critical current density of superconducting material. The property that determines the ability of not only coated conductors to carry supercurrent is referred to as flux pinning. There are a number of defect types that can act as artificial pinning centres (APC) which can be described as one-dimensional (1D-APC); dislocations [32-34] and nanorods [35], two-dimensional (2D-APC); such as grain boundaries [36, 37], anti-phase boundaries [38-40], surface roughness [41], and three-dimensional (3D-APC); such as nanoparticles and second phases [42] of size ξ or more. Figure 2.9 illustrates the various types of film defect that can be acted effectively at pinning center. The experimental route is another classification criterion that can lead to artificial pinning centres such as antidotes (holes) [43, 44], magnetic-dots [44-47] and substrate decoration [13, 48, 49] followed by deposition of superconducting phase by pulsed laser deposition (PLD), chemical solution deposition (CSD) and metalorganic chemical vapor deposition (MOCVD) and etc. Another route is the fabrication of alternate layer (multi layer) [50-56] of APC and superconductor.

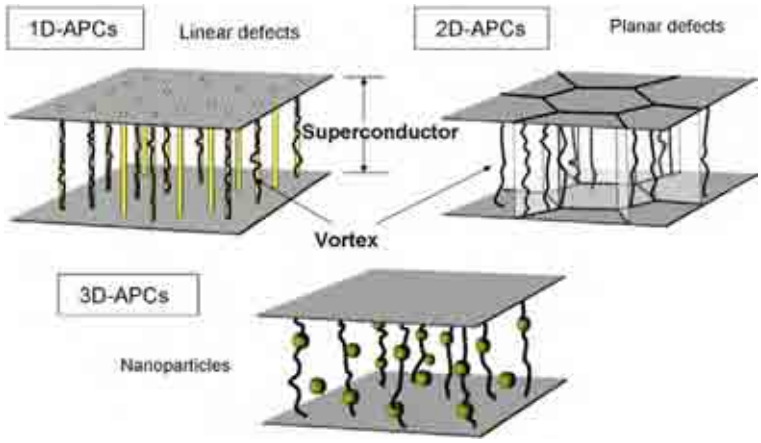

Figure 2.9. The dimensionality of artificial pinning centers (APC): 1D-APC, 2D-APC, and 3D-APC [42].

2.1.5.5 Vortex phase diagram

Figure 2.10 shows the vortex phase diagram plot of applied magnetic field strength versus the temperature, showing the Meissner state at low fields, below the H_{c1} (T) line, where no flux can enter the material, and regions between H_{c1} (T) and H_{c2} (T) lines, where the flux solid state exists for temperatures below the melting line; the flux liquid state is present for temperatures above the line.The variety of vortex phases, such as vortex lattice, vortex solid (glass), vortex liquid (fluid) and so on, have been proposed by many theoretical and experimental works. The vortex phases in HTS are determined by a delicate balance between the thermal energy, the vortex elastic energy and the vortex pinning energy. In the presence of strong thermal fluctuations, the thermodynamic phase-transition is shifted to the vortex melting line and the upper critical field H_{c2} (T) is no longer the sharp phase transition line between the normal and superconducting states [57-60]. The

melting transition of the vortex matter and the nature of the vortex solid are strongly affected by disorder.

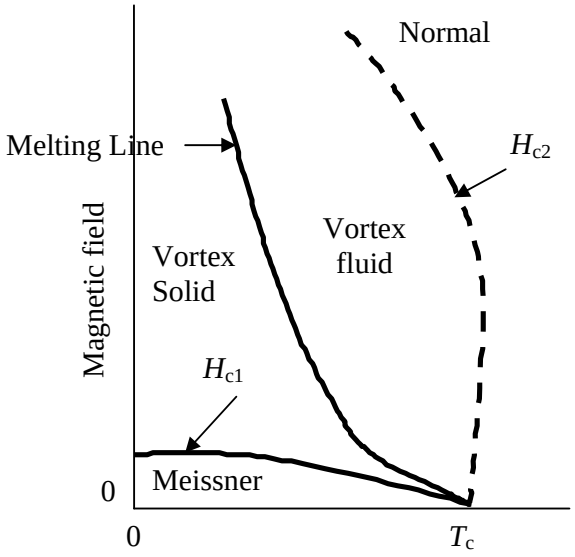

Figure 2.10. Vortex phase diagram of a Type II superconductor showing the Meissner region of excluded flux below the lower critical field curve H_{cl}(T), the flux solid and flux liquid phases separated by the flux melting line, and the normal region outside the upper critical field curve H_{c2}(T) [15].

Theorists predict a first-order transition for the melting in clean materials [61, 62] but if the material contains a large number of defects, grain boundaries, or twins that cause disorder of the vortex lattice, a second-order transition can occur. The physics of the vortex phase is complicated in accordance to the disorder, which grows with magnetic field and the concurrent number of vortices [63].

2.2 Superconducting properties of $YBa_2Cu_3O_{7-x}$

HTS cuprates based on $YBa_2Cu_3O_{7-x}$ are more practical for potential applications at liquid nitrogen temperatures (77K), which will dramatically improve performance while also lowering costs. The oxidised compound $YBa_2Cu_3O_{7-x}$, which is superconductive around 92 K, as seen in Figure 2.11, has an orthorhombic unit cell with the lattice parameter of a = 3.82 Å, b = 3.89 Å and c = 11.68 Å. This structure is like many other HTS, a complex variation of the perovskite structure, which has the general chemical formula of ABO_3. The central Y atom is sandwiched between Cu-O planes. These Cu-O planes are separated charge reservoir interleaved layers which allow a change in the carrier density available in the Cu-O plane. One of the main structural features of YBCO is that the charge reservoir layer of the latter is metallic and not insulating [64]. The CuO planes contain mobile charge carriers and there is where superconducting current flows. This is also a common feature in all the HTS cuprates, and is believed to be essential for superconductivity in this class of materials [64].

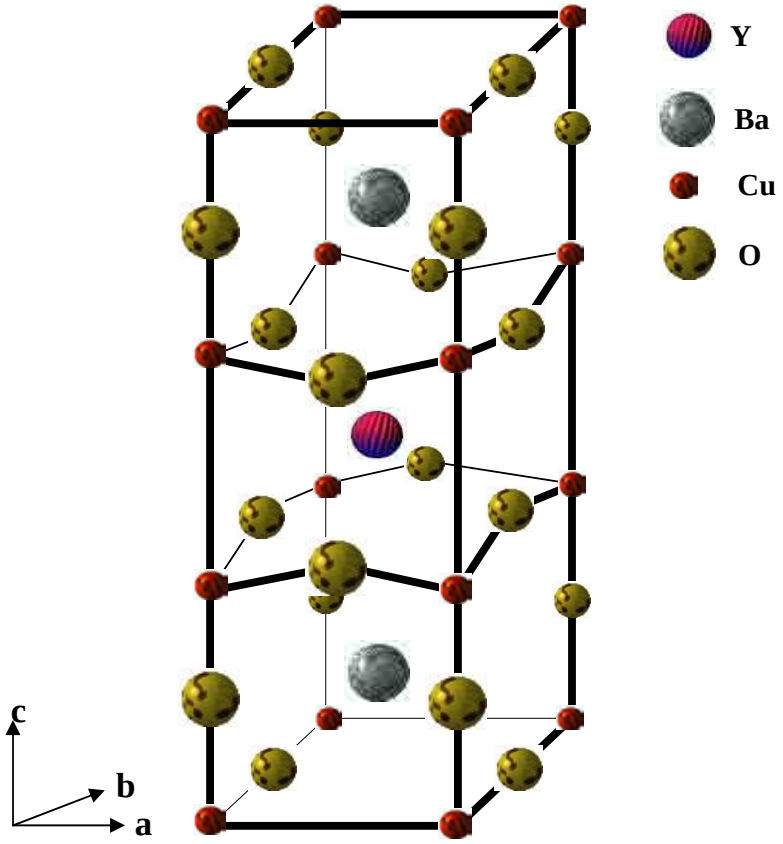

Figure 2.11. Structure of $YBa_2Cu_3O_{7-x}$ [65].

Since the cuprate superconductors exhibit strong anisotropy in the normal and superconducting properties, this anisotropy can produce significant differences in properties along the *a*-*b* plane and *c*-axis. The Cu-O planes define the *a*-*b* plane in all HTS crystal structures, with the *c*-axis of the crystal structure perpendicular to the Cu-O planes. Many results have shown that the current flow in the *a*-*b* plane of the HTS is much higher than the *c*-axis. This leads to higher critical current density along *a*-*b* plane than the *c*-axis [66]. Practically, to get a higher quality for superconducting films the *c*-axis has to be oriented perpendicular to the substrate, so that current can be applied easily along the *a*-*b* plane [66]. However, YBCO is still less anisotropic than other HTS.

2.2.1 $YBa_2Cu_3O_{7-x}$ films with nanoparticle inclusions

There are pinning centers such as oxygen vacancies and twins in YBCO single crystals but their J_c values are extremely low at 77 K. However, epitaxial YBCO films formed on single crystal substrates can have structural defects that are naturally present and have a high J_c at 77 K. This enhancement comes from various crystalline defects such as dislocations, grain boundaries, composition impurities, fine precipates, and voids existing in high density films [67], in addition to oxygen vacancies and twins [42]. The creation of dislocations along the *c*-axis of the films is believed to act as strong pinning centers [68]. This is because the dislocation core is a normal region and its diameter is about 1-3nm, comparable to the coherence length ξ, so that the dislocations can pin vortices effectively. On the other hand, it is incredibly difficult to control the density and the distribution of the dislocations in YBCO films to improve J_c under magnetic field at 77 K.

The breakthrough of nanoparticle inclusion in YBCO films has made a significant enhancement of flux pinning and this has become a mainstream research in HTS thin film and coated conductors' community. Incorporation of nano size oxide particles [69, 70] and nano size magnetic particles [71, 72] is proven to be useful in improving the current carrying capability and pinning, in YBCO thin films. The addition of $(Dy,Y)_2O_3$ particles has the effect of enhancing the critical current under magnetic fields applied perpendicular to the tape (the low-I_c configuration). These particles have a size distribution of 10–50 nm for $(Dy, Y)_2O_3$ and 10–25 nm for $BaZrO_3$, are approximately spherical, and are well dispersed [73]. The use of nanoparticles of Y_2O_3 [74, 75], rare-earth oxides [76, 77] has been observed to increase J_c. The introduction of these nanoparticles improves the I_c for magnetic-field angles away from the parallel direction, but there can be a reduction in

planar pinning. In the case of compositionally changed targets, $BaZrO_3$ (BZO) has been used most commonly as an impurity addition to $YBa_2Cu_3O_{7-\delta}$ (YBCO) targets [35, 78] and has been shown to be able to self-organize into correlated nano-rods within the film microstructure. More recently, $BaNb_2O_6$ and $BaSnO_3$ have been added as impurities to $ErBa_2Cu_3O_{7-\delta}$ targets [79, 80], $BaSnO_3$ has been added to YBCO [81], and RE_3TaO_7 (RE = rare earth = Er, Gd, Yb) was also added to YBCO targets [82].

2.2.2 Vortex pinning in $YBa_2Cu_3O_{7-x}$ films

The first straightforward and cheap method in creating extended defects as strong pinning centres in superconducting thin films was proposed by Crisan et al. initially in 2001 [13, 48, 83]. Nano-dots of Ag deposited on STO substrates prior to the growth of superconducting thin films have increased the critical current density J_c. The J_c of YBCO when metallic islands (nano-dots) of Ag were grown on a (001) YSZ surface using PLD at 780 °C was enhanced by up to 6-8 times relative to a control film [84]. Later, this method is called substrate decoration.

Nano-islands induce the formation of extended linear defects, such as dislocations, and nearly all the islands can induce dislocations inside a film. Studies that have investigated linear defects to improve J_c using decoration have employed Ag nano-dots on substrates for Tl-based thin films [13, 48, 83] and for YBCO films [84], an annealed CeO_2 buffer for YBCO films [70], Y_2O_3 nano-islands [85-87] and eventually iridium-sputtered particles for YBCO films [88]. In all these experiments, the decoration technique appears to effectively obtain high performance films. However, it is a very laborious and delicate process. The growth window for deposition is very narrow and even a small difference in

the number of laser shots can dramatically change the size and distribution of the nano-islands.

For thicker films and/or coated conductors, a variant of this technique is to produce the nano-islands during the entire film deposition process. By periodically switching two targets (the main YBCO target and the dopant target) during deposition, a fine multilayered distribution of the second phase and the superconducting phase into the film can be obtained [24, 51, 89, 90]. This modified technique has been employed to grow Y_2BaCuO_5 (Y-211)/YBCO, Y_2O_3/YBCO and $BaIrO_3$/YBCO quasi-multilayers.

Another common way to introduce artificial pinning centres is to ablate a target, which is comprised of a mixture of YBCO and nanoparticles of a non-superconducting phase, yielding a YBCO (or REBCO, RE = Er, Gd) thin film that incorporates non-superconducting nanodots and/or nanorods, which act as (1D) artificial pinning centers. Melt processed large, single-grain (RE)-Ba-Cu-O, where RE is Y or rare-earth element such as (Nd, Sm, Eu, Gd, Tb, Dy, Ho, Er, Tm, Yb) superconductors, which can trap magnet fields in excess of 14 T [91, 92] have significant potential for high magnetic field engineering applications. The field trapping ability of large grain bulk superconductors is associated directly with the critical current density J_c, and the grain size, so it is necessary to maximize J_c for a given sample dimension in order to maximize the trapped field. In high T_c, bulk (RE)BCO superconductors, on the other hand, it is well established that the presence of non-superconducting second-phase Y_2BaCuO_5 (Y-211) particles of size ~1 μm embedded in the superconducting $YBa_2Cu_3O_7$ (Y-123) phase matrix correlates with enhanced flux pinning in Y-Ba-Cu-O (YBCO).

By reducing the size of these particles, ideally to dimensions of the order of doubled(or twice) the coherence length ξ of the (RE)BCO system (around ~3 nm at 0 K),

increases their magnetic flux pinning potential further. It has been found by Sawh et al. 1998 that the addition of a small amount of uranium oxide to an initial composition of Y-123+30 mol % Y-211 with between 0 and 0.5 wt % Pt results in the formation of U-containing phase particles in a superconducting Y-123 matrix [93].

2.2.3 Dependence of critical current density on film thickness

Big efforts have been made to develop coated conductors using $YBa_2Cu_3O_{7-y}$ (YBCO) compounds with a high critical current density, J_c and high critical current, I_c [94]. Critical current density (J_c) is I_c per size area A of specimen. To obtain high- I_c superconducting films, it is necessary to fabricate thick films.

It is not clear about the cause of reduction of J_c with increasing film thickness as seen in Figure 2.12 . Thickness dependence of critical current density still is a controversial problem, and several explanations have recently been published [95-97]. It is reported that the J_c of YBCO films decreases with increasing film thickness because of mixing of *a*-axis orientation, impurities from the substrate or decrease of number of pinning sites [98]. As the thickness increases, the film morphology becomes much rougher, suggesting that the drop in J_c is related to a change in microstructure [94].

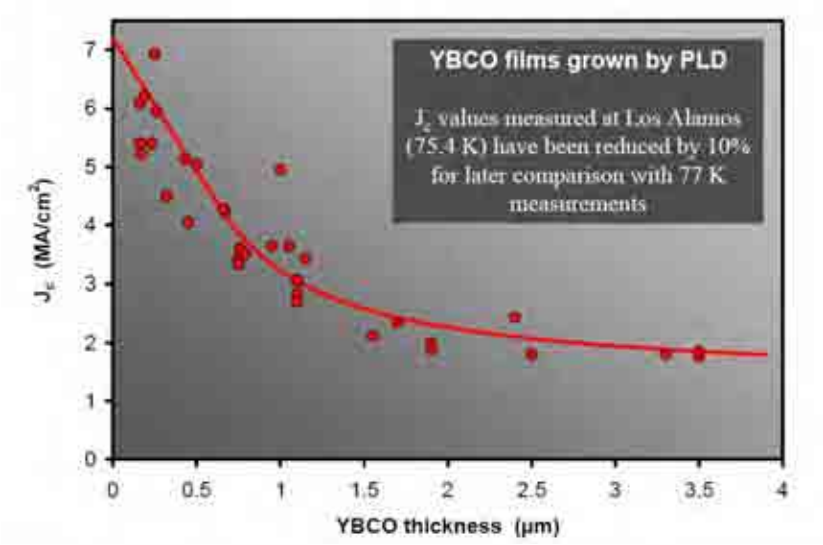

Figure 2.12. The J_c values of YBCO decreases sharply with film thickness and applied magnetic field [99].

2.3 Thin film growth technology

Over the years various techniques have been developed by scientists for the deposition of thin film superconductors. As a result these techniques can be broadly divided into two categories, namely chemical and physical methods. The chemical method is composed of the metal organic chemical vapour deposition (MOCVD), metal organic deposition (MOD)-solution methods and liquid phase epitaxy (LPE). The physical method consists of magnetron sputtering, pulsed laser deposition (PLD) and co-evaporation. It still remains a major challenge for most thin film groups to optimise the deposition method to produce high quality films.

2.3.1 Chemical methods

2.3.1.1 Metal organic chemical vapour deposition (MOCVD)

The first thin films of YBCO were prepared by the metal organic chemical vapor deposition (MOCVD) demonstrated by Berry et al. [100]. Since then MOCVD has been widely used for the deposition of HTS thin films for several reasons [101, 102]. The basic principle of MOCVD is rather simple. Atoms that form the film composition are brought in the vapour phase and combined with a complex organic gas and passed over a hot semiconductor wafer. The heat breaks up the molecules and deposits the desired atoms on the surface, layer by layer if proper conditions are used. By varying the composition of the gas, you can change the properties of the thin film crystal at an almost atomic scale [103]. This technique can grow high crystalline quality epitaxial heterostructures for semiconductor devices, because the growth is carried out near the equilibrium [104].

MOCVD has the potential of producing uniform (composition and thickness) films which grow as precisely controlled layers efficiently, as well as having the ability to be scaled up to industrial-scale production. Highly oriented films with both *a*- axis and *c*-axis directions can be grown by MOCVD [105]. Several numbers of groups [106, 107] have successfully deposited superconductive $YBa_2Cu_3O_{7-x}$ coatings by MOCVD on different substrate materials with high critical current densities in applied magnetic fields [108-110]. However, the rougher film surface and larger surface resistance are the disadvantages of this method.

2.3.1.2 MOD - Solution methods

Metal organic deposition (MOD) is one of the popular solution deposition methods, involving coating of an organic precursor solution on a substrate followed by thermal decomposition to form the final desired compound [111]. Solution deposition is a fast, cost efficient method and is applicable to large-area substrates. The most frequently used solution method approaches can be divided into two components; sol-gel process and Metalorganic Decomposition (MOD). The sol-gel process denotes its principle: a solution starting from precursors which are dissolved in a liquid phase, transformed to the solid state through a sequence of chemical reactions which involve polymerisation at ambient temperatures [112]. Metalorganic Decomposition (MOD) is a non-vacuum technique for processing of films of uniform thickness from liquid precursor solutions. For example, stoichiometric proportions of Ba, Y and Cu acetates are mixed in water with trifluoroacetic acid in an MOD process. This mixture is dried and re-dissolved in methanol to form an organic solution of trifluoroacetates which is used to dip coat or spin coat a textured substrate [113]. Several investigators have reported preparation of some oxide films like strontium titanate STO [7, 114] barium zirconate [14] which can act as buffer layers, and of Y123 films by MOD [115-117]. The advantages of MOD over other deposition techniques are rapid deposition rates and the ease with which films of uniform and controlled composition can be prepared. Even though the MOD solution methods greatly reduce the production cost they rarely obtain high J_c over 1 MA cm^{-2} (77 K, 0 T).

2.3.1.3 Liquid phase epitaxy (LPE)

Liquid phase epitaxy (LPE) is a solidification process from a liquid phase, either from solution or from the melt, of a crystalline layer onto a single crystal substrate in near-equilibrium processing conditions. The near-equilibrium growth process of the LPE

method is also preferred in obtaining high quality and a very flat surface [118, 119]. Although the preferred near-equilibrium mechanism is effective to obtain high quality films, it usually results in weaker flux pinning. Another pinning entity can be introduced by growing on substrate possessing a large lattice mismatch, such as MgO [120]. MgO, which has a thermal expansion coefficient larger than YBCO [121], and can also prevent crack formation in the YBCO film [122, 123].

All films can be grown over a large area with high growth rate (1-10μmin^{-1}) and control of the alignment can be achieved using appropiate substrate and growth condition. The LPE method has the advantage in the ability to fabricate a thick superconducting layer of YBCO and other rare earth cuprates (REBCO) [124-127]. However, some disadvantages include poor surface finish, poor large area uniformity and difficulty in varying stiochiometry [128].

2.3.2 Physical methods

2.3.2.1 Co-evaporation

The co-evaporation method is a process in which the vapour of metallic materials is created by electron beam or thermal evaporation sources in a vacuum chamber. The deposition by evaporation typically takes place in a low pressure background around 10^{-6} Torr. Because of that most of the in situ growth of HTS films requires much higher molecular oxygen pressures. The film is formed by evaporating the metallic ingredients of YBCO simultaneously from a resistively heated tungsten filament. From the filament sources the metal vapour spreads in the vacuum until it reaches the substrate. The substrates are placed on a rotating disc and alternated between a zone of the metal vapour and a molecular oxygen pocket. The passage transforms the metals into the required oxide

which grows as single crystalline film on a single crystal substrate surface. The co-evaporation deposition method has several advantages. It allows a rigorous control of the stoichiometry, as each element is evaporated independently of others. Besides, the relatively large distance between the metallic targets and the substrate allows for deposition of very homogenous thin films on large surfaces.

2.3.2.2 Magnetron Sputtering

Sputtering is the ejection of surface atomised material from an electrode surface to the energetic bombarded surface layers by ions in a vacuum of less than one ten millionth of an atmosphere [128]. The sputtering process is performed by applying a high voltage across a low pressure atmosphere to create plasma, which consists of electrons, gas ions and metals ions in a high energy state. There are several sputtering systems for the purpose of thin film deposition. Either the direct current (DC) or radio frequency (RF) sputtering is used to deposit HTS thin films. DC sputtering can be used only for conducting targets where RF sputtering can be used for both conducting and insulating targets.

Magnetron sputtering is another variant of sputtering sources which uses magnetic fields transverse to the electric fields at sputtering-target surfaces. Target-generated secondary electrons do not bombard substrates because they are trapped in cycloidal trajectories near the target, and thus do not contribute to increased substrate temperature and radiation damage [128]. The magnetron sputtering method has been widely used for MgB_2 [129, 130] and YBCO [131] thin films depositions because of their high deposition rates and relatively low temperature process. However, the critical current densities of YBCO films grown by sputtering are still lower than films prepared by pulsed laser deposition.

2.3.2.3 Pulsed Laser Deposition (PLD)

Pulsed laser deposition (PLD) is widely used for the deposition of YBCO thin films since 1987 by Dijkamp et al.[132]. They found that the films obtained by the PLD technique are higher in quality to those previously grown using other deposition methods and has opened worldwide interest in the technique. PLD is a versatile technique for the preparation of thin films of complex stoichiometry and the capital cost involved is low. It has been found to be most convenient and efficient for the synthesis of high T_c superconducting thin films [133]. In the PLD process of making YBCO thin films, a pulsed laser strikes a solid bulk YBCO target and removes material off the target in the form of a plume. The plume comes in contact with the surface of a heated substrate kept at a certain distance from the target. The plume containing the building blocks (neutrals, ion, and electron) of the YBCO lattice, covers the substrate. PLD is found to have significant advantages, including the capability for stoichiometric transfer of material from target to substrate, low contamination level, high deposition rate and non equilibrium processing. Other advantages include repeated generation of energetic species, hyperthermal reaction between the ablated cations and the background gas in the ablation plasma and compatibility with background pressures [134].

There are several variables for the synthesis of HTS thin films such as substrate temperature T_s, the energy of the atom flux, the relative and absolute arrival rate of the atoms forming the film and the oxygen pressure P_o in the deposition chamber. Even as we know that PLD is an evaporation process, the stoichiometry and the nature of the species are quite different from standard evaporation. The PLD can be divided into four regimes: (i) interaction of laser beam with the surface of target, (ii) interaction of the ablated material with the incident laser beam resulting in plasma formation and growth consisting

of positively charged and neutral particles, molecules, atoms and other species, (iii) anisotropic adiabatic expansion of the plasma leading to the characteristic laser deposition process and (iv) interaction of the plasma with background gas [135]. In the evaporation regime, the evaporation of the target is thermal in nature, while in the isothermal regime the plasma formation, heating, and expansion give rise to nonthermal deposition characteristics, like sharply forward peaked deposition with kinetic energy of the species much larger than the thermal energy.

2.3.2.3.1 Interaction of laser with target

Usually the target material is a sintered bulk superconductor with a varying degree of porosity depending on the fabrication conditions. The surface roughness of the target affects its coupling with the laser beam. The free-carrier collisions are the dominant mechanism for the absorption of the photon energy resulting in high target absorption. The surface roughness can enhance the diffraction of the laser radiation with consequent non-uniform spatial distribution of the energy and non-uniform, non-stoichiometric ablation of the material result in low vaporisation threshold. The vaporisation represents the energy required in heating the material to its evaporation temperature, the conduction heat losses in the target, and the losses due to the absorption of the laser energy by the expanding plasma. Figure 2.13 explains a basic thermal cycle induced by a laser pulse striking the target. Two separate heating regimes have been identified: (i) the surface heating regime in which the laser energy is deposited near the target surface, and (ii) the volume heating regime in which a volume of the solid material is heated by the laser pulse [136].

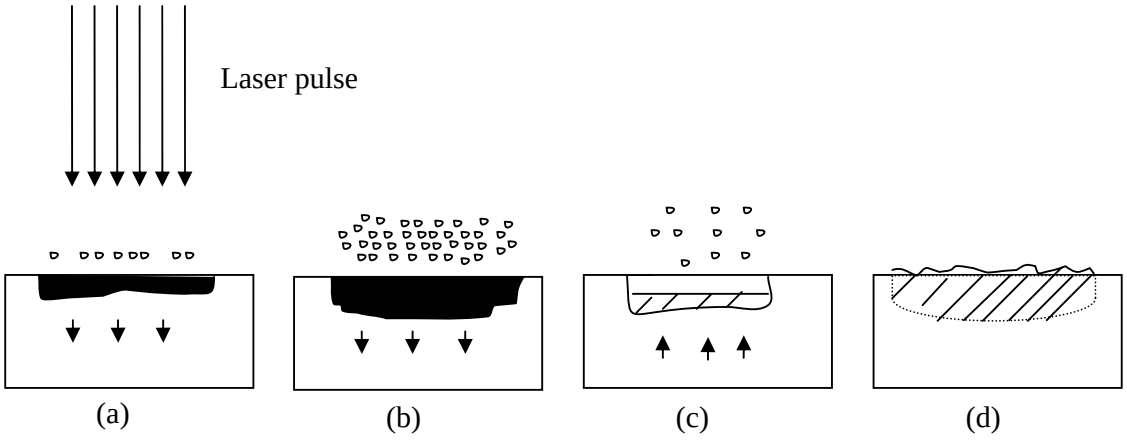

Figure 2.13: Schematic of thermal cycle induced by a laser pulse striking the target. (a) Light pulse is absorbed, melting and vaporization begin. (b) Melt front propagates into the solid, accompanied by vaporization. (c) Melt front recedes; cross-hatched area indicates resolidified material. (d) Solidification is complete showing frozen capillary waves on the surface [135, 137].

In the first regime the laser energy is absorbed in the surface layer, and the thermal diffusivity controls the heating and ablation characteristics. During ablation of the target, a planar vaporization interface may initiate from the surface and propagate into the target [138, 139]. However, at higher power densities, subsurface heating effects may become important which may lead to explosive removal of material from the target, and thus lead to non-linear ablation [140, 141].

In the volume heating regime, the thermal conductivity plays an insignificant role in controlling the laser-target interactions, and the ablation depth is determined mainly by the optical absorption depth which is given by the inverse of the optical absorption coefficient. In this regime, internal heating sub-surface effects may predominate leading to removal of particles from the target, and these particles may shield the target from the incoming laser beam [136]. The time after which the ablation front may change from a

planar to volume type depends on the degree of internal heating and the time required for formation of a subsurface gaseous phase [137].

2.3.2.3.2 Energy transfer through interaction

The interaction of nanosecond high-powered laser beams with the target leads to very high surface temperatures (> 2000 K), which results in emission of positive ions and electrons from the free surface [142, 143]. The flux of positive ions and electrons is produced at these high surface temperatures. The ablation of the target has been found to be accompanied by a brilliant glow (laser plasma) extending outward from the surface. The plasma constitutes both charged and neutral species of atoms and molecules. The expansion of the flume is driven by plasma pressure gradients, but there may be an additional contribution from Coulumb repulsion between ions if the net loss of more mobile electrons is significant.

2.3.2.3.3 Nucleation and growth of film

In general the crystal growth of films is governed by three modes, depending on the thermodynamics relating the surface energies of the film and the substrate to their interface energy. The three dimensional island growth (Volmer-Weber mode) (Figure 2.14b) is where small clusters are nucleated directly on the substrate surface and then grow into islands of the condensed phase. This occurs when the atoms (or molecules) of the deposit are more strongly bound to each other than to the substrate [144].

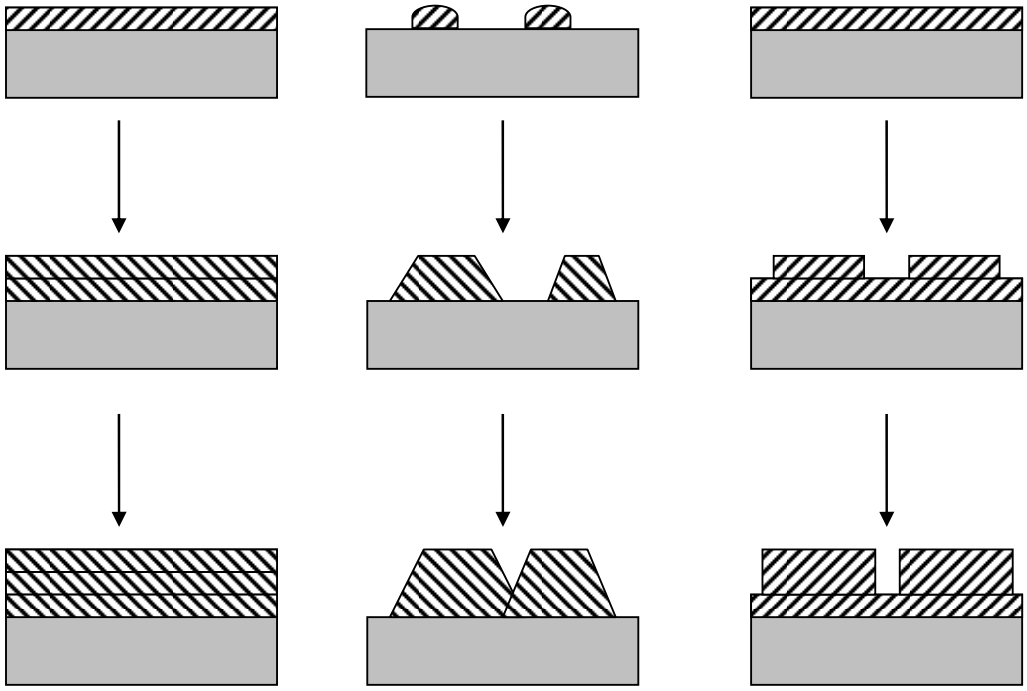

(a) Frank-Van der Merwe (b) Volmer-Weber (c) Stranski-Krastanow

Figure 2.14. Illustration of the three modes of nucleation and initial growth of epitaxial deposits proposed by Bauer et al. [145].

The two dimensional monolayer growth (Frank-van der Merwe mode) (Figure 2.14a) displays the opposite characteristics. When the atoms are more strongly bound to the substrate than to each other, the first atoms to condense form a complete monolayer on the surface, which becomes covered with a somewhat less tightly bound second layer. Provided that the decrease in binding is monotonic toward the value for a bulk crystal of the deposit, the layer growth mode is obtained [144].

The three dimensional island growth plus the two dimensional monolayer growth (Stranski-Krastanov mode) (Figure 2.14c) is an interesting intermediate case. After forming the first monolayer subsequent layer growth is unfavourable and islands are formed on top of this intermediate layer. There are reasons for this mode to occur, and almost any factor which disturbs the monotonic decrease in binding energy, characteristic of layer growth, may be the cause. For example, the lattice parameter of, or symmetry of, or molecular orientation in, the intermediate layer may not be able to be continued into the bulk crystal of the deposit. This results in a high free energy of the deposit-intermediate-layer interface which favours subsequent island formation [144].

2.4 Choice of substrate for HTS films

One of the most important issues in thin film growth is the choice of the right substrate. To grow high-quality HTS thin films, the substrate must have the basic requirement properties such as: no chemical interaction at the interface between HTS, crystallographic lattice match between HTS film and substrate, similar thermal expansivities of HTS and substrate, and low roughness.

The HTS cuprate oxides with a square-planar surface orientation, such as the (001) face of cubic oxide crystal, are ideal for *c*-axis-oriented HTS films. Typically, the in-plane

lattice spacing of the HTS film should closely match that of the substrate either aligned with or rotated 45° with respect to the principle axes. Significant differences in the thermal expansion coefficient should be avoided, as this will lead to cracking of the film during cooling or loss of adhesion. Any chemical reaction between the substrate and film will likely inhibit good epitaxy and may prevent the formation of the HTS phase. The substrate material should also be stable against thermal cycling with no significant phase transitions [64].

$SrTiO_3$ (100) and MgO (100) are generally the most attractive substrates in growing high quality epitaxial HTS films. But the main disadvantage of MgO substrates is the degradation of the hygroscopic surface in air [146]. These substrates also have a lattice mismatch of 9% with YBCO and a different crystal structure. These properties lead to a significant amount of in-plane 45° misoriented grains in the YBCO films deposited on MgO substrates, which significantly suppresses the average critical current density of the HTS films [147]. Several other substrates have been used such as $LaAlO_3$, $LaGaO_3$ and $NdGaO_3$ but the search is still on for the best that should not react with the film at the film deposition temperature.

Strontium Titanate $SrTiO_3$ has been widely used for making YBCO films, as it has superior properties over other types of substrates, including chemical compatibility, good thermal expansion matching, lack of reactivity in oxygen-rich ambient conditions, and good lattice matching with Y123 [148]. STO (lattice constant is 0.3905 nm) has a small lattice mismatch with YBCO (lattice constant is 0.3820 nm) and is able to support high quality YBCO films with the state of the art properties. All films studied in this thesis are deposited on STO single crystalline substrates using pulsed laser deposition and standard deposition parameters.

The quality HTS films grown to date, as determined by a multitude of metrics including critical current density, morphology, and stability over time, are epitaxial on their substrates. Epitaxial growth requires a controlled crystallographic orientation of the film with respect to the substrate [149].

The deposition of HTS material onto a number of technically interesting metallic substrate materials requires a buffer layer which provides epitaxial growth. Buffer layers can be grown epitaxially prior to the YBCO phase. The idea to use a buffer layer is to avoid inter diffusion of substrate and HTS material and to reduce the lattice mismatch between them. Choosing a buffer material with a lattice constant intermediate between the two materials may enhance the epitaxial quality of the grown layer.

Three techniques for growth on metallic substrates currently being studied are; ion beam assisted deposition (IBAD), rolling assisted biaxially textured substrate (RABiTS), and inclined substrate deposition (ISD). IBAD is a technique for obtaining biaxially textured films by simultaneous ion beam bombardment to the film surface during growth of the buffer layer (YSZ, $La_2Zr_2O_7$) on polycrystalline metallic substrates (hastelloy, stainless steel) [150]. The Fujikura group [6] developed the technique first and subsequently another group at the of Los Alamos National Laboratory (LANL) optimized the IBAD-YSZ/PLD-YBCO process and achieved J_c up to 1 MA/cm^2 at 77 K in short samples [151].

The well biaxially textured, smooth surface and small grain size (5-10nm) [152, 153] associated with IBAD can solve the weak-link problem of the YBCO and drive high performance in transport current property. The YBCO films grown on IBAD templates

have energised much attention because of its high critical current, length and reproducibility.

The second method in producing textured metallic substrate is called the RABiTS [154]. In the RABiTS process, pure nickel or nickel alloy (Ni-Cr or Ni-W) substrate itself is rendered highly biaxial textured by well-defined thermomechanical processes of rolling deformation, followed by annealing [114]. The resulting texture in the face-centered cubic (fcc) metal corresponds to the cube planes parallel to the tape surface and perpendicular to the tape's long axis. Yttria stabilized zirconia (YSZ) [155], cerium oxide (CeO_2) [104], lanthanum aluminate ($LaAlO_3$) [156], barium zirconate ($BaZrO_3$) [154, 157], and other ceramics in single constituent or multi-constituent layers have been used to provide a buffer layer and to protect the chemical barrier to the reaction with the YBCO. The third technique in producing textured metallic substrates is inclined substrate deposition (ISD)[158]. This approach achieves biaxial alignment of the YSZ buffer without assistance of an additional ion-beam using a high rate laser deposition and appropriate inclination of the metal substrate with respect to the laser plume [159].

Chapter 3

Experimental Details

3.1 Introduction

This chapter describes the experimental procedures to fabricate and characterise the pure YBCO, YBCO/Gd2411 and YBCO/BZO films. Substrate preparation prior to the film deposition is discussed in the beginning of this chapter, followed by a brief account of the deposition process of the films by pulsed laser deposition. Characterisation techniques of the film are discussed next.

3.2 Substrate preparation

All films studied were deposited on (100) SrTiO3 (STO) single crystalline substrates using pulsed laser deposition and standard deposition parameters were set by our group (refer 3.4.1). STO has been widely used for making Y123 films, as it has superior properties over other types of substrates, including chemical compatibility, good thermal

expansion matching, lack of reactivity in oxygen-rich ambient conditions and good lattice matching with Y123 [160]. STO also has a rather small lattice mismatch (its lattice constant is 0.3905 nm) with YBCO and is able to support high quality YBCO films. All substrates require cleaning before the film deposition to remove some dirt particles on the surface of the substrate which can adversely affect the film growth. The STO substrates (5mm × 5mm × 2mm) were put into a bath of acetone and ultrasonically cleaned for about 5 minutes. Then these substrates were washed once more by using iso-propanol. After that the samples were dried by compressed air.

3.3 Target preparation

Four types of target (Table 3.1) were used to grow thin films. The first target is pure Y123 target which is commercially available, the second is YBCO/Gd2411 which is solid state processed and provided by Prof. Dr. DA Cardwell, University of Cambridge, the third is YBCO/2% $BaZrO_3$ and the fourth target is YBCO/4% $BaZrO_3$ provided by Dr. Petriina Paturi, University of Turku, Finland.

Table 3.1. Targets details

Target	Details	Source
Pure YBCO	$Y_1Ba_2Cu_3O_{7-\delta}$	Commercially available from Praxair Surface Technology
YBCO/Gd2411	100 mol % Y123 + 1 mol % $Gd_2Ba_4CuWO_y$	Solid state process by Bulk Superconductivity Group, University of Cambridge, UK
YBCO/2%BZO	100 wt. % Y123 + 2 wt. % $BaZr_3O$	Citrate-gel method by University of Turku, Finland
YBCO/4%BZO	100 wt. % Y123 + 4 wt. % $BaZr_3O$	Citrate-gel method by University of Turku, Finland

The $Gd_2Ba_4CuWO_y$ (2411) phase particles are plausible candidates for engineering the microstructure of large grain (RE)BCO superconductors at the nanoscale level in order to achieve a large flux pinning effect [161]. A study of the effects of nano Gd 2411 on the performances of Y123 films is presented based on the optimised growth conditions for Y123 films. A target of composition $YBa_2Cu_3O_{7-\delta}$ (Y-123) + 1 mol% $Gd_2Ba_4CuWO_{12}$ was fabricated from Y-123 (Nexans Superconductors GmBH, purity 99.9%) and Gd-2411 phase powders. The latter were synthesized via solid-state reaction of Gd_2O_3, $BaCO_3$, CuO and W pre-reacted powders (purity 99.9%). The precursor powders were mixed in the

required molar ratio, and calcined at temperatures between 900 and 1100 °C with several intermediate grinding stages.

The nano-crystalline YBCO targets containing 2 wt% $BaZrO_3$ and 4 wt% $BaZrO_3$ were prepared using the citrate gel method. The important advantage of this method is the homogeneity at atomic level. The starting materials are water solutions of high-purity nitrate salts of Y, Ba, Cu and Zr that were mixed in molar ratios of YBCO + $BaZrO_3$. After evaporation of the water and directly heated at 500 °C to remove the organic compounds the obtained powder was first calcined at 790 °C for 96 h in flowing O_2 to convert it to the tetragonal YBCO phase. Then the powder was converted to the orthorhombic phase by annealing in Ar and cooling down in a O_2 atmosphere as described in [162]. This process leads to nanosize YBCO powder with an average grain width of 60–80 nm [162]. The PLD targets were prepared by pressing the powder at 300 MPa pressure into pellets of 20 mm diameter, sintering them in flowing O_2 at 900 °C for 4 h and finally oxygenating in flowing O_2 at 500 °C for 50 h and at 400 °C for 10 h.

3.4 Pulsed Laser Deposition System

All films were deposited on (100) $SrTiO_3$ (STO) single crystal substrates by PLD using a scanning laser beam. Scanning laser beam method consumes the target material gradually and homogeneously and does not require frequent and intermediate polishing of the target, which makes the technique potentially suitable for large-scale production of superconducting coated conductors. The laser deposition installation was constructed in the PLD Laboratory at School of Metallurgy and Materials, University of Birmingham. A

photograph is shown in Figure 3.1 with a schematic illustration of the equipment shown in Figure 3.2. The films are grown in the stainless steel chamber using a KrF excimer laser supplied by Lambda Physik, LPX 300 Germany with a wavelength of 248 nm. The laser beam is focused onto the rotating target by beam scan optical train.

3.4.1 Standard Deposition Parameter

Substrates were mounted on a heatable sample stage holder with silver paste. Prior to the deposition of a film the chamber is evacuated with a turbo molecular pump below the pressure of 10^{-5} torr. A collimated laser beam is directed at an incident angle of 45 º and scanned over the surface of the rotating target. The target was then cleaned and conditioned with a 1000 laser pulses under vacuum with a shutter being positioned over the substrate. The substrate was then heated to 780°C at a rate of 20°C/min. The distance between the target and the substrates is55 mm, and an oxygen background pressure of 450 mTorr (0.6 mbar) was employed during the deposition. 5000 pulses (based on film thickness needed) at pulse repetition rate of 4 Hz were employed for YBCO deposition. One of the best deposition conditions was obtained when the tip of the plume generated by the interaction of the laser beam with the target surface comes near to the substrate, with a pulse duration = 30 ns, repetition rate of 4 Hz, laser energy density of 1.0 mJ/cm^2, oxygen pressure of ≈ 450 mTorr, substrate temperature ≈ 780 ºC and the target-substrate distance ≈ 55 mm. After deposition, the oxygen loading of the films took place in 450 Torr O_2 in situ during cool-down at 8 °C min^{-1}. The other optimum conditions for high quality YBCO films have been obtained and will be discussed in chapter four.

The PLD system used for the present study has the following main features:

i) Spherical chamber

ii) Turbo pump

iii) Lambda Physik LPX excimer laser with a wavelength of 248nm.

iv) Six target holders allowing multi-layer deposition

v) Target rotation by an external motor

vi) Substrate temperatures up to 900 °C, adjustable by a digital controller

vii) Two gauges measuring the pressure from 1 atm to 10^{-9} Torr

Figure 3.1. Image of the PLD system

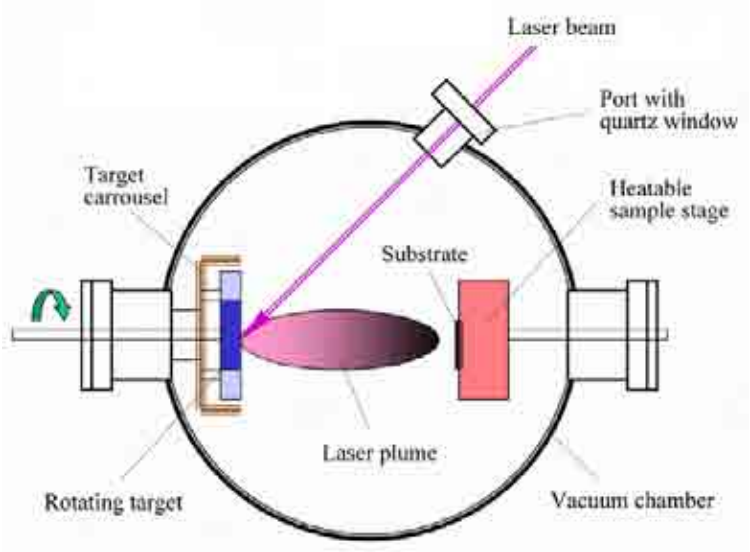

Figure 3.2. Schematic of PLD System [163].

3.5 Microstructure characterization

3.5.1 Scanning Electron Microscopy (SEM) observations

The scanning electron microscope (SEM) is often the preferred preliminary tool for analytical microscopy. Basically inside the SEM, an electron gun is used to generate the electron beam. There are two types of electron guns: the thermionic emission gun and the field emission gun. Scanning electron microscopy (SEM) was performed on a JEOL JSM 7000 field emission system equipped with an energy dispersive spectroscopy (EDS) system as seen in Figure 3.3. It has an electron emission gun which consists of three electrodes: a LaB_6 (lanthanum hexaboride) cathode filament, a Wehnelt cylinder and an anode. When an electron beam interacts with a film specimen, a variety of electron, photon, phonon and other signals can be generated as can be seen in Figure 3.4. Three

types of electrons can be emitted from the electron-entrance surface of the specimen: secondary electrons with energy < 50 eV, Auger electrons produced by the decay of the excited atoms, and backscattered electrons that have energy close to those of the incident electrons. No sample is required for gold coating since all of our films once oxygenated are conducting. So the films were just placed by silver paint paste in the specimen stage of the SEM.

Figure 3.3. A JEOL 7000 scanning electron microscope

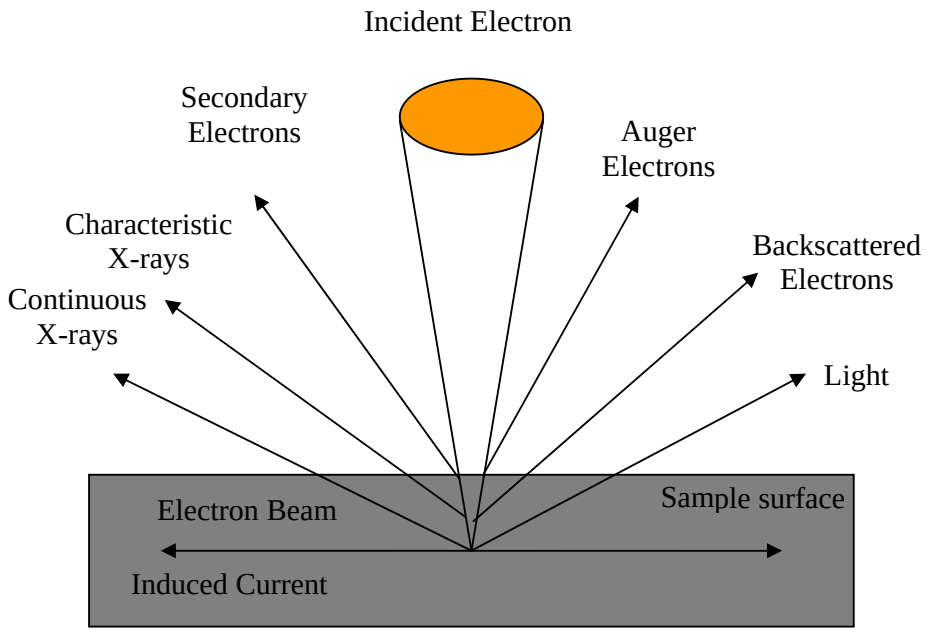

Figure 3.4. Schematic drawing illustrates the signals generated inside a scanning electron microscope when an electron beam interacts with a specimen [164].

3.5.2 Transmission electron microscopy

The best of the nano-inclusion films were analysed by imaging cross sections of the films by transmission electron microscopy (TEM). The cross section images of the film was taken by a Jeol JEM 2100 TEM (Figure 3.5) using a lanthanum hexaboride (LaB_6) crystal thermionic electron source. The TEM was operated at 200 kV and magnification of up to 200,000 times. The Tecnai F20 TEM using field emission electron source was also used in this study. Due to field emitter the Tecnai F20 was equipped with scanning transmission electron microscopy (STEM) and Oxford EDS system. High resolution images can be produced by the Tecnai F20 (HRTEM) and element mapping was also analysed in the STEM mode by the EDS system. Bright field image with (001) zone axis was selected in most of the TEM images in this work.

Figure 3.5. Jeol JEM 2100 LaB_6 TEM at Centre Electron Microscopy, University of Birmingham [165].

3.5.3 Energy dispersive spectroscopy (EDS)

Energy dispersive spectroscopy (EDS) is the most common type of general purpose SEMs and it is attached to the SEM JEOL JSM 7000 from LINK ISIS of the Oxford Instruments company. To perform EDS, the electron beam has to very finely focussed to execute an elemental analysis of a very small area on the sample surface. The sample surface was first observed with secondary electron imaging. The electron beam was positioned at the designated point on the sample.

Whenever a sample is irradiated by an energetic electron beam, some electrons from within the material will be excited into vacant higher-energy levels. A vacancy is thus created in one of the inner electron shells and the atom is effectively ionized. When an electron from

a higher orbital drops back down in energy to fill the vacancy, an x-ray is emitted having energy equal to the difference between the two levels. Because the energies of these emitted photons are characteristic of the ionized atoms, inspection of the emitted x-ray spectrum using energy dispersive spectroscopy (EDS) provides rapid identification of the elemental composition of the material. There are two types of information about the composition of samples that can be obtained from energy dispersive spectroscopy (EDS) [166]. Qualitative analysis: involves identification of the elements contained in the samples by analyzing the characteristic of the x-rays emitted. Quantitative analysis provides the relative weight or atomic concentration of the elements.

3.5.4 Electron backscattered diffraction (EBSD)

Electron backscatter diffraction (EBSD) allows the crystallographic information to be obtained from samples in the SEM. EBSD determines of the orientation of individual grains in the sample, and consequently gives the degree of misorientation between grains. EBSD is the diffraction of backscattered electrons produces from a focussed incident electron beam, by the crystal planes in the samples. A schematic of a typical experimental setup is shown in Figure 3.6.

The EBSD pattern is collected with the specimen surface normal making an angle of around 70° with the incident electron beam. The diffracted backscattered electrons are recorded by a phosphor screen and charge coupled detector (CCD camera) to produce a pattern similar to a Kikuchi pattern. The pattern contains crystallographic data on both the crystal structure and the orientation of the specimen surface. The entire indexing pattern is routinely carried out by a computer.

The texture measurement requires thousands of measurements so that the distribution of orientations may be acquired. Scanning beam requires the electron beam to be held stationary and the sample is rastered by moving the sample stage so that automated orientation mapping can be accomplished. Usually this method gives recognition of the EBSD patterns which allows automated mapping of the orientation over fairly large areas, up to mm dimensions, which is important when statistically significant data on real samples are required [167]. An analysis of crystal orientation or grain boundary misorientations maps were built according to the orientation and colour coded for easy recognition.

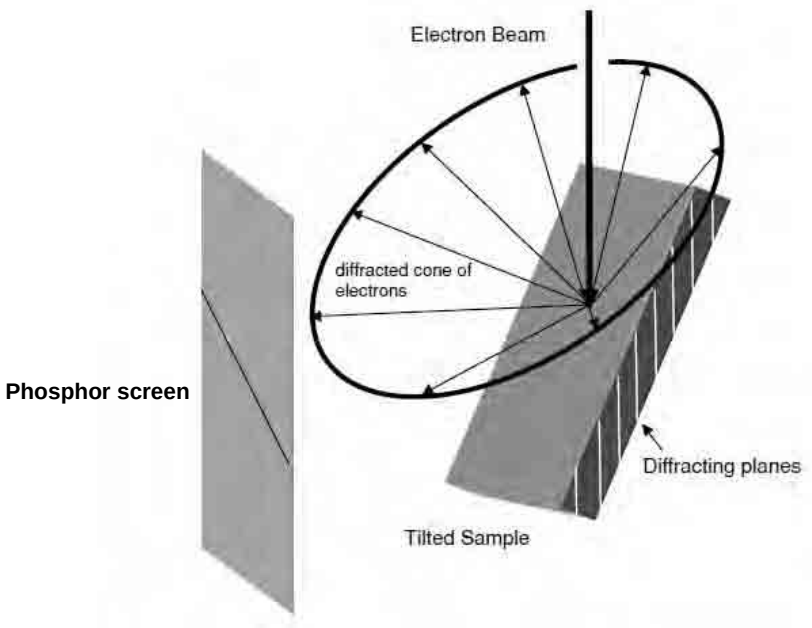

Figure 3.6. EBSD experimental configuration which is showing the electron beam, the tilted sample and the phosphor screen [167].

3.5.5 Surface topography by AFM

Scanning probe microscopes (SPM) is in a class of instruments that enable precise surface topography measurements to be performed in two forms: scanning tunnelling microscopy (STM) and atomic force microscopy (AFM). AFM was introduced about 20 years ago. AFM have revolutionised surface analysis by providing high resolution visualization of structures at the atomic and nanometer scales. The structure and morphology of the surface of the tin films were investigated using AFM in this research. The detailed information from this AFM images can be used to model the growth process. The atomic force microscopy uses a fine ceramic cantilever (silicon nitride) to probe the surface of the sample. There is no electrical current flow between the probe and the surface hence the AFM is suitable for use with non-conducting material. In AFM, mechanical force interactions acting between a sharp probe and a sample are used for surface imaging.

There are three primary imaging modes available in AFM; contact mode, non contact mode AFM and tapping mode. Contact mode was used in this work. The cantilever with a sharp tip at one end, is brought into interaction with the sample surface. The interaction level between the tip apex and the sample is determined through precise measurements of the cantilever displacements. The deflection of the cantilever is measured by a laser beam, projected at the tip of the cantilever and reflected towards a pair of closely spaced photo detectors mounted on the scanning head. By measuring the relative signal intensities from these detectors, the magnitude and direction of the deflection of the probe can be monitored, and an image of the sample surface can be constructed.

3.5.6 X-ray diffraction (XRD)

X-ray diffraction is one of the versatile methods in identifying the crystalline phases present in films and analyses the structural properties such as grain size, phase composition, crystal orientation etc. A Philips x-ray diffractometer with Cu K_α was used to detect diffraction peaks in a θ-2θ scan. The x-ray wavelength is 0.154 nm with a beam size of 3 mm. The x-rays are diffracted (according to Bragg's law at equation 3.1) as they are reflected from successive planes formed by the crystal lattice of the material.

$$2d \sin\theta = n\lambda \qquad 3\text{-}1$$

where n is an integer and called the order of diffraction, λ is the wavelength of an incident monochromatic x-ray beam, d is the interplanar spacing and θ is called the diffraction angle (the angle between the incident x-ray beam and the particular crystal plane under consideration). The pattern is identified by comparing it with an internationally recognized data base powder diffraction file (PDF) reference patterns. In order to obtain good XRD results the film surface must be well aligned in the diffraction plane of the x-ray source. The diffraction signal from the $SrTiO_3$ substrate was used as a guide for alignment.

3.5.7 Thickness measurements

For film thickness measurements, the film was broken in cross section by a diamond cutter. The two parts of cross section sample were polished by using 0.5 μm size of diamond paper. Then, the thickness of the films was measured using SEM or POM (Polarised Optical Microscope). Thicknes measurements are best obtained by taking several measurements along the sample from the centre to the edge and averaging the

results. Films with a thickness of less than 1 μm were measured by SEM while the thicker film was measured by POM.

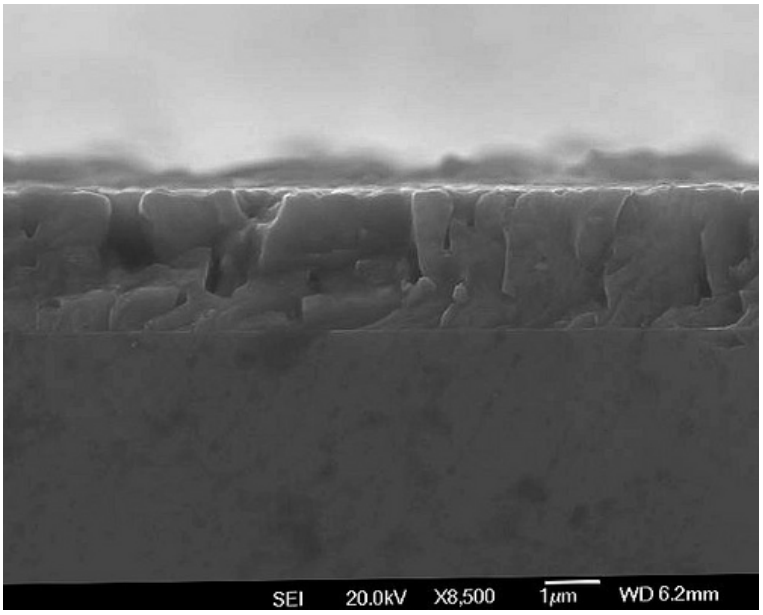

Figure 3.7. Cross section of YBCO/ $Gd_2Ba_4CuWO_y$ film with average thickness of 2.6 μm

3.6 Superconducting properties

3.6.1 Measurements of T_c and J_c

The superconducting transition temperatures, T_c were measured by magnetic AC susceptibility in a Quantum Design Magnetic Property Measurement System (MPMS-XL). T_c was defined as the onset of diamagnetism by measuring the real part of the AC susceptibility. In most cases, the error in determining T_c was smaller than 0.2 K. The sample was located in a system consisting of a primary and secondary coil. The primary coils produce an excitation field set to 0.05 Oe. The sample was placed in the secondary

pick up coils, where the change of the induction voltage across the coils due to the shielding current can be measured by the lock-in amplifier.

The critical current density J_c was determined by DC magnetisation loops measured in the Quantum Design MPMS-XL. In order to measure the value of DC magnetisation, a DC field is applied up to 4.5 T, and the sample was moved through the entire detection coil. The pick up coil detects a waveform signal versus the position of the sample.

The J_c can also be calculated from AC susceptibility while a DC field is applied to the sample or no applied field. The dependence of DC field, temperature and AC frequency on J_c can be estimated by AC susceptibility measurement. By choosing ACMS option from Quantum Design Physical Properties Measurement System (PPMS) (Figure 3.8) in DC magnetic field up to 6 T, AC field amplitude h_{ac} up to 10 Oe, and ac field frequency f between 47 and 9997 Hz, the dependence of χ" on AC frequency and DC applied field was plotted and hence J_c was calculated as can be seen in Figure 6.29.

Figure 3.8. Quantum Design Physical Properties Measurement System at School of Chemistry, University of Birmingham [168].

3.6.2 Lithography for the patterning microbridge

Transport measurement can only be made on film that has patterned with current tracks and current and voltage tabs. The lithography techniques allow the patterning of superconducting microbridges upon a substrate material carried out in the well equipped clean room operated by Electronic, Electrical and Computer Engineering School. Patterning using etching is facilitated in this work. It is important to start with a clean film. The film was put into a bath of acetone and ultrasonically cleaned. Then this film was washed once more by using iso-propanol. After that the film was dried by compressed air. The film was placed on a speed controllable spinner, while rotating with speed of 4000 rpm, 2 or 3 photoresist S1818 droplets was applied on the surface of the sample for 30 seconds to a minute. Particular care needed to be taken to ensure a smooth resist layer and it is often necessary to spin the resist several times before baking.

The film then was baked for 3 minutes at temperature of 120^{o}C. The next step of patterning was performed in a Karl Suss MJB3 mask aligner (Figure 3.9). The film was mounted on the mask aligner and put into direct contact with the mask. The film was then exposed to an UV400 Exposure Optics (for 365nm and 405nm exposure) UV source through the mask. The film is then stirred in diluted developer (Microsposit MF-319) solution for a few minutes; the time may be varied according to the exposed sample quality. Diluted Nitric acid 0.1% was used to etch the developed sample. The film was put in the diluted acid for several minutes; the time is varied according to the thickness of the sample. For 1 μm thick film it will take in 10 minutes etching. Less than 1 μm thick film is the easiet and quick to etch. The etched film then was cleaned by acetone again to remove the photoresist layers and remaining acid by ultrasonic. Figure 3.10 shows a device patterned from YBCO which was subsequently used to produce and investigate the properties of sub-micron superconducting bridges. The square pads around the edge of the substrate are used to make contact between the sample and the measurement apparatus.

Figure 3.9. Karl Suss MJB3 Mask Aligner system.

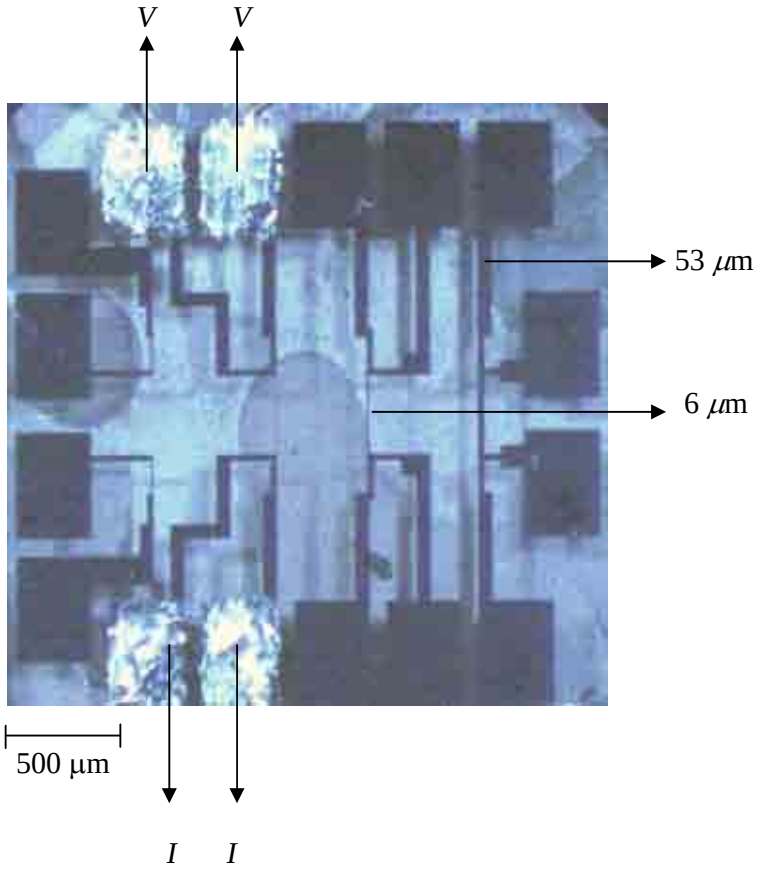

Figure 3.10. Optical image of the bridges (53 μm-biggest and 6 μm-smallest) patterned using photolithography

3.6.3 Field orientation dependent transport measurements

Transport measurements of films were carried out using the so called four point probe technique. This method consists of attaching four contacts to the film by indium solder through gold wires as seen in Figure 3.10 . The two outermost contacts are for the current (I) and two inner contacts are for the voltage (V). For critical current (I_c) measurements, the standard value of 1μV/cm is used as a criterion for I_c. In the transport measurement, not only the angle between applied field and the *c*-axis of the sample (θ) can be changed but also applied field (B) and temperature (T) can be controlled, so one can get

$J_c(\theta, B, T)$ instead of only $J_c(\theta)$. In this measurement, the rotating range of -10^o to 370^o were used.

Chapter 4

Fabrication and Characterisation of $YBa_2Cu_3O_{7-x}$ films

4.1 Introduction

The superconducting properties of $YBa_2Cu_3O_{7-x}$ (Y123) films are very sensitive to deposition conditions. In order to achieve good quality films, the effects of the deposition parameters such as deposition temperature (T_s), annealing oxygen pressure (O_{ap}) and cooling time (cooling rate) (C_t) in relation to superconducting transition temperatures were observed.

The plume behaves in a different manner in vacuum and in the presence of an ambient background gas. A picture of the plume captured during deposition is shown in Figure 4.1. Ambient oxygen scatters and attenuates the plume, changing its spatial distribution, deposition rate, and kinetic energy distribution of the different species. Oxygen pressure also has an influence on the length of the plume and it is often the easiest parameter that can be slightly modified during the deposition. The annealing oxygen

pressure plays an important role in determining the oxygen stoichiometries to achieve good quality YBCO films. The relationships between parameters are plotted in Figure 4.2, Figure 4.7 and Figure 4.8.

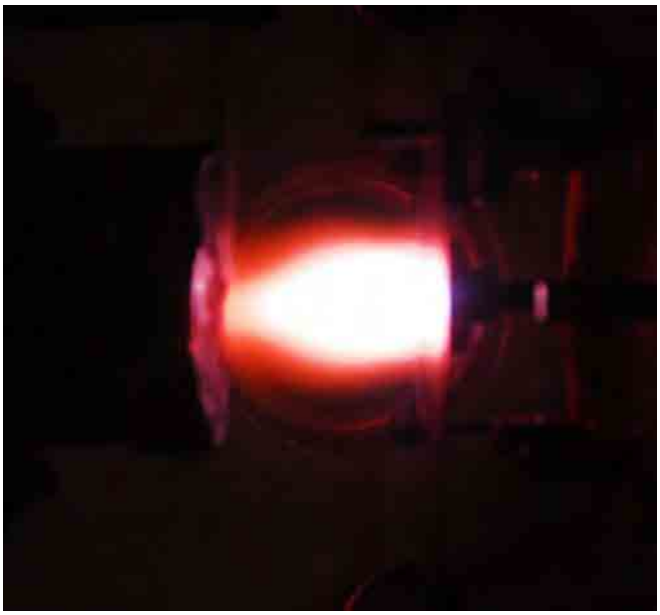

Figure 4.1. An optical image showing the shape of the visible plume resulting in the best films.

4.1.1 The correlation between T_c and deposition temperature

The growth was carried out at an optimum distance (D_s) between target and the substrate, which is about 55 mm [169], using a laser repetition rate of 4 Hz, 5000 of laser pulses, laser energy (E) of 218 mJ/pulse and under other fixed conditions as indicated in the inset Figure 4.2. After deposition, the Y123 film was annealed at 780° C at a pressure (O_p) of 450 Torr of oxygen with a cooling rate of 8° C /min until room temperature is reached. It can be seen that the T_c of the films has a close relation with those variables. The T_c decreases when the deposition temperature (T_s) rises from 780 ° C to 820 ° C. This shows that T_c is correlated with the substrate temperature with the optimum value at 780° C.

The deposition or substrate temperature is one of the most important parameters governing the crystallization process [170, 171]. The deposition temperature should be sufficiently high to increase the surface mobility of the adatoms and to promote formation of the correct crystalline phase [172]. It was reported by Huhtinen et al.[173] that no superconductivity was observed when the Y123 film was grown at $T_s \leq 625°$ C. By increasing the deposition temperature up to 780° C, films with T_c = 91 K ± 0.2 K could be obtained.

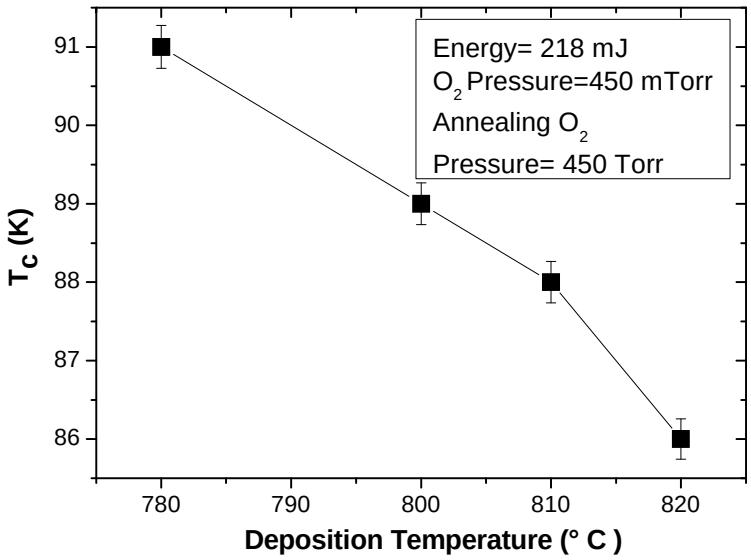

Figure 4.2. The correlation between T_c and deposition temperature with other conditions fixed: laser energy 218 mJ; deposition oxygen pressure 450 mTorr.

4.1.2 Surface morphology by AFM at different deposition temperatures

AFM images are widely used to look at the surface morphology of various structures or at different stages of the fabrication process [174]. The AFM images of films made using those conditions; laser energy (E) 218 mJ, deposition oxygen pressure (O_p) 450 mTorr and annealing oxygen pressure (O_{ap}) 450 Torr, but with different deposition temperatures (T_s) are shown in Figure 4.3 to Figure 4.6. Histograms of height distribution which show average film width also can be seen in all these figures. All the AFM images of films exhibited a clear texture of growth islands. The trenches apparent between growth islands are irregular at various dimensions for films with different deposition temperature. The deepest trenches were found for the film deposited at 820° C in Figure 4.6.

The surface roughness of the YBCO films is mainly affected by the growth temperature and the oxygen pressure [175]. The smoothest root mean square (RMS) roughness of the film is given in Figure 4.3 showing the minimum value of approximately 2.403 nm for the film grown at T_s of 780° C with a peak width of 2.832 nm. All the grains seem to be well connected. The RMS roughness of the growth islands is increased to about 14.935 nm for the film T_s at 800° C in Figure 4.4. The peak width also increased up to 21.865 nm for the same film. The surface roughness in the film deposited at 810° C becomes higher at approximately 30.278 nm and the peak width is also slightly higher at approximately 36.701 nm.

The above mentioned optimization of deposition conditions resulted in an apparent increase of surface roughness (RMS > 100.7 nm) with degradation of superconducting transition temperature as shown in Figure 4.2. This poor superconductivity might be due to a poor inter-grain connection between the *c*-axis crystallites [176].

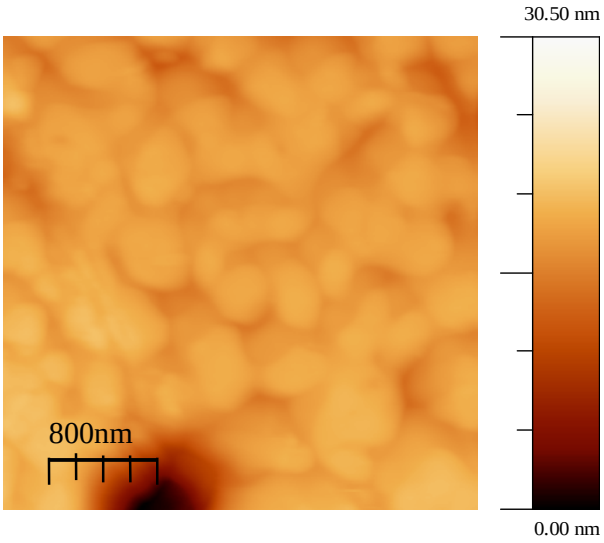

(a)

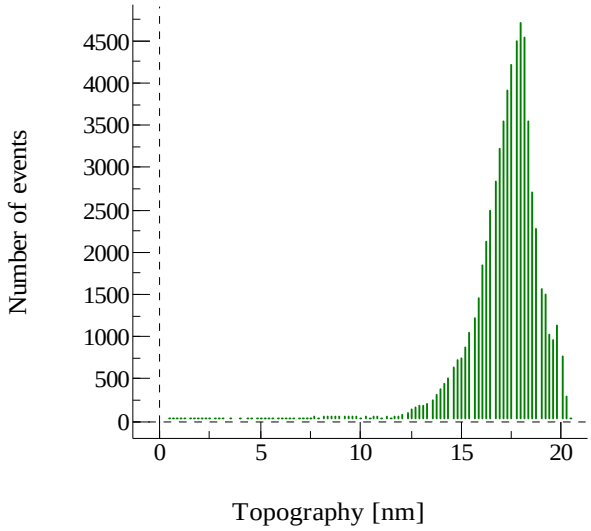

(b)

Figure 4.3. (a) AFM image of film made using the following conditions; Deposition temperature 780° C with other conditions fixed: laser energy 218 mJ; deposition oxygen pressure 450 mTorr. (b) Histogram of height distribution with a peak width of 2.832 nm.

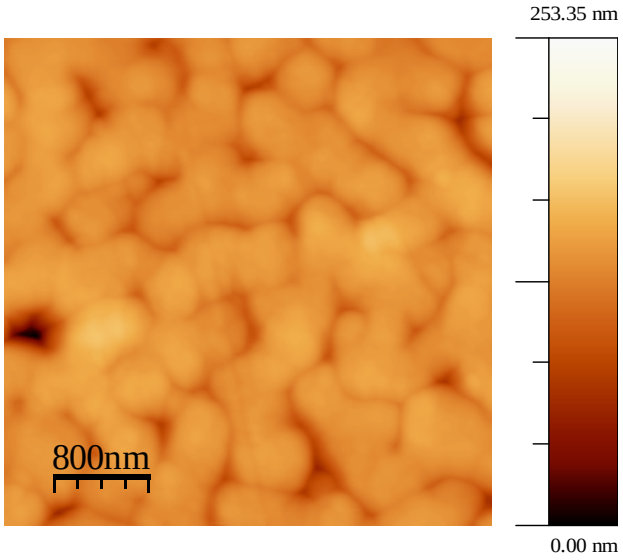

(a)

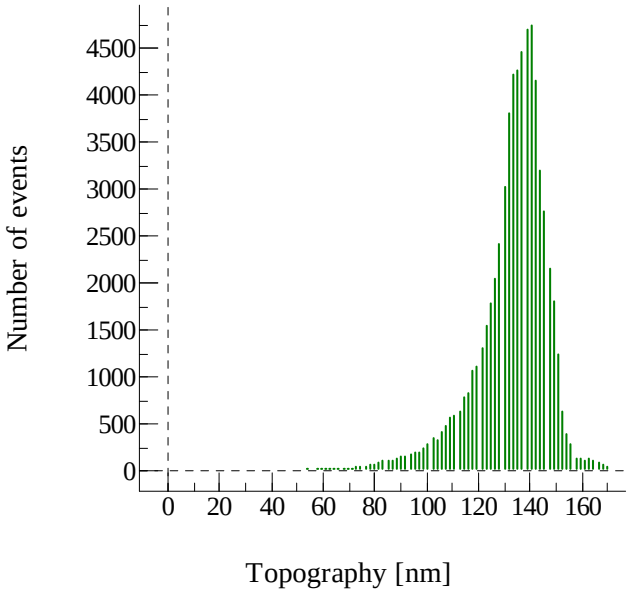

(b)

Figure 4.4. (a) AFM image of film made using the following conditions; Deposition temperature 800° C with other conditions fixed: laser energy 218 mJ; deposition oxygen pressure 450 mTorr. (b) Histogram of high distribution which shows peak width of 21.865 nm.

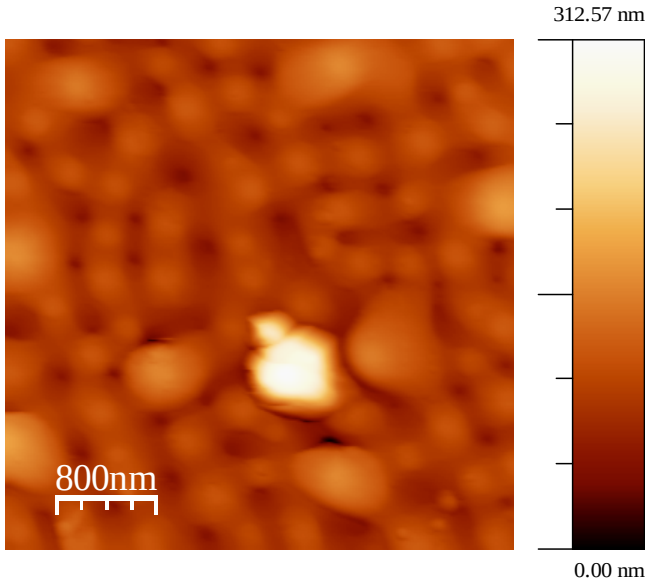

(a)

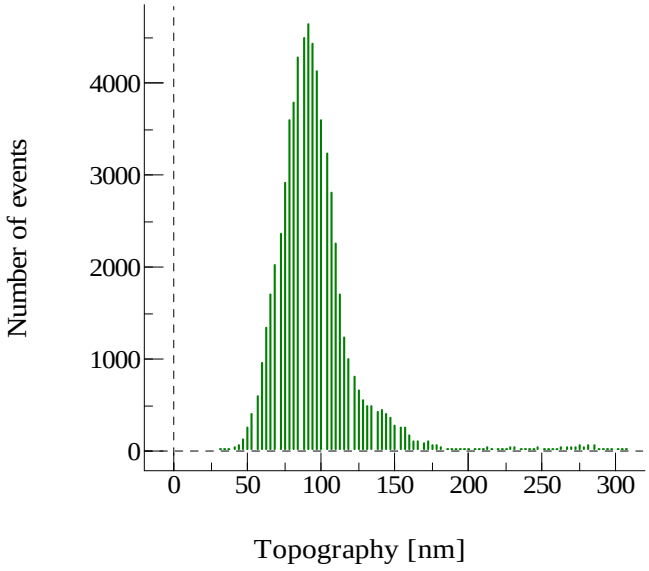

(b)

Figure 4.5. (a) AFM image of film made using the following conditions; 810° C deposition temperature with other conditions fixed: laser energy 218 mJ; deposition oxygen pressure 450 mTorr. (b) Histogram of high distribution which shows peak width of 36.701 nm.

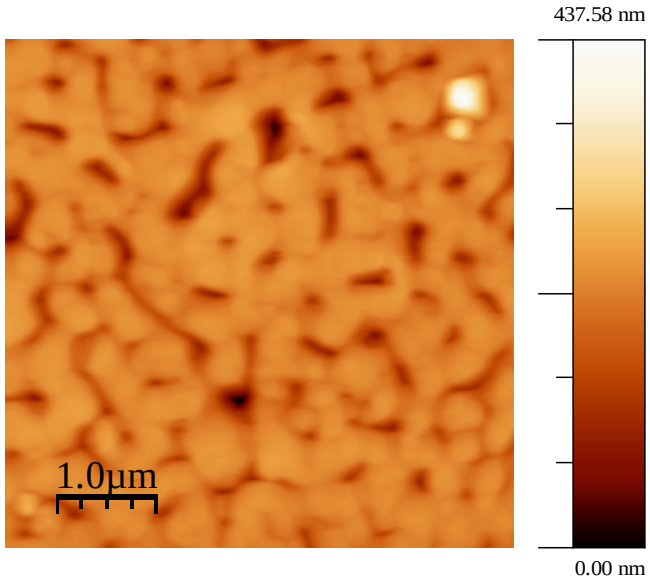

(a)

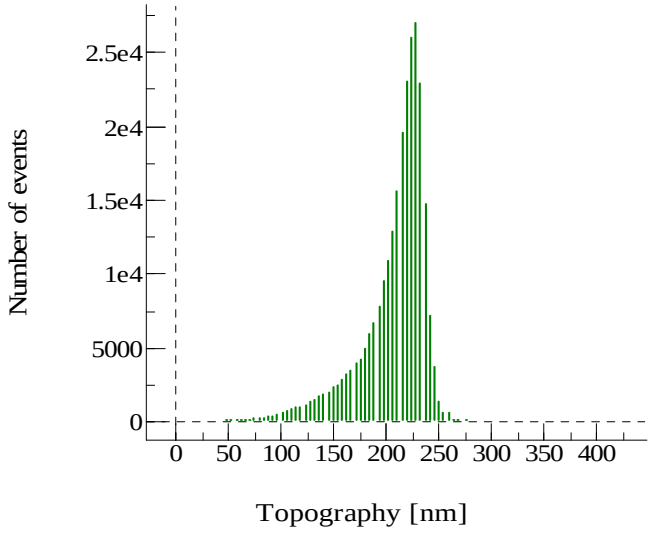

(b)

Figure 4.6. (a) AFM image of film made using the following conditions; 820° C deposition temperature with other conditions fixed: laser energy 218 mJ; deposition oxygen pressure 450 mTorr. (b) Histogram of high distribution which shows peak width of 42.185 nm.

4.1.3 The correlation between T_c and *in situ* annealing

It was found that the pressure of the oxygen atmosphere and cooling time during annealing time could also be crucial to the T_c of the Y123 films. In this experiment, the annealing oxygen pressure was first varied with the other conditions fixed at the optimum (T_s = 780° C, O_p = 450 mTorr, E = 218 mJ) condition. Significant changes in the T_c with annealing oxygen pressure (O_{ap}) are shown in Figure 4.7. It can be seen that the T_c gradually increases with O_{ap}, but it begins to drop when the O_{ap} exceeded 450 Torr. It has been found that the annealing oxygen pressure with 450 Torr gives the best T_c of 91 K ± 0.2K. It seems that the value of T_c can be substantially increased by annealing with sufficient oxygen. Although deposition of these films was carried out under identical conditions, different annealing oxygen pressures during cooling causes differences in the extent of crystallization in the film and in crystal orientation [177].

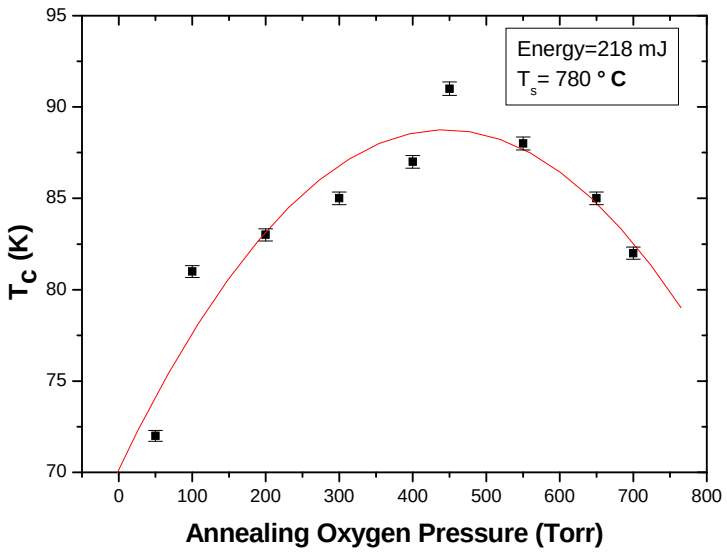

Figure 4.7. The correlation between T_c and annealing oxygen pressure with other conditions fixed: laser energy 218 mJ; deposition temperature 780° C. The trend is shown by the line, which was constructed by a polynomial function of the experimental data.

Then the annealing cooling time was varied with the other parameters fixed at optimum (T_s = 780° C, O_p = 450 mTorr, O_{ap} = 450 Torr and E = 218mJ) condition. Shown in Figure 4.8 is the relationship between T_c and cooling time. The film with the shortest cooling time has a lower T_c, which is 72 K ± 0.2 K. It is clear that with longer cooling time, the T_c increases and the film with 97.5 minutes cooling time shows a good T_c, which is 91 K ± 0.2 K. However, the suppression of T_c was observed after 190 minutes. The lower T_c at fast cooling time is not favourable for the phase formation of Y123. The suppression of T_c at long cooling time can be attributed to the increase in the amount of impurities that are formed when the sample is kept longer at high temperatures. It also suggests that poor crystallisation always results if the duration of cooling time is too short. Based on the results described above, it is considered that the optimal in situ annealing conditions for Y123 films are 450 Torr for oxygen pressure and 97.5 minutes for cooling time (cooling rate at 8 °/min).

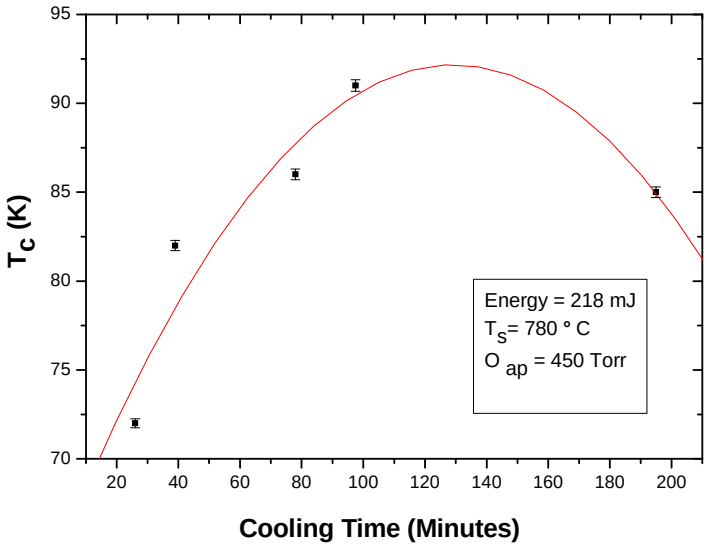

Figure 4.8. The correlation between T_c and cooling time with other conditions fixed: laser energy 218 mJ; deposition temperature 780° C. The trend is shown by the line, which was constructed by a polynomial function of the experimental data.

Analysis of the magnetic transitions in these samples was conducted and is shown in Figure 4.9. The transition curves of the films obtained with O_{ap} of 450, 550 and 650 Torr show not only higher T_c but also have a sharper transition ΔT, whereas films with lower oxygen pressure have lower T_c and more broadened ΔT. The narrower ΔT of the former films implies that they are more homogeneous. It suggests that impurity phases with lower T_c are broadening the transition in M-T measurements. The film which has highest T_c (91 K ± 0.2 K), has an O_{ap} of 450 Torr. When oxygen pressure was increased up to 700 Torr, suppression of T_c was observed. At very high oxygen pressures oxidation of metal atoms could also occur in the vapour phase, which is probably detrimental to ordered YBCO growth [178].

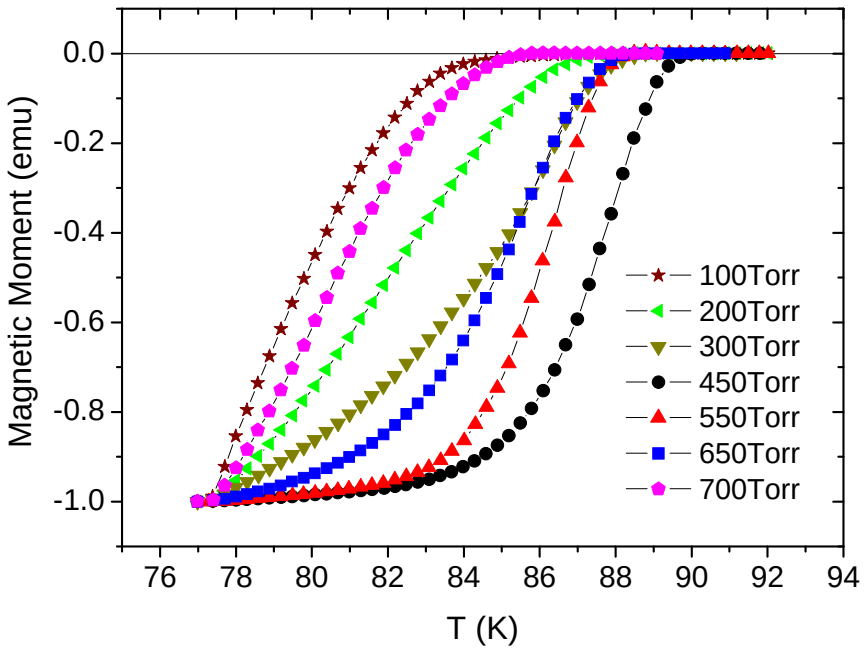

Figure 4.9. Normalised magnetic (*M-T* measurements) transition curves of films with different annealing oxygen pressure O_{ap} with other conditions fixed: laser energy 218 mJ; deposition temperature 780° C. The lines connecting the data points are for guiding the eye

4.1.4 SEM morphologies of *in situ* annealing

The SEM surface morphology of the Y123 film annealed under different oxygen pressure (O_{ap}) conditions were examined and are shown in Figure 4.10 to Figure 4.14. It can be seen that the surface of films seem to be dense but with numerous visible white spots. These white spots are found on both films in Figure 4.10 (O_{ap}= 100 Torr) and Figure 4.11 (O_{ap}= 200 Torr), similar to those commonly present in Y123 films made by using the PLD technique [10]. The presence of white spots with maximum diameter of approximately 0.5 μm is typical in all areas of these films. It is likely that these particles originate from the targets. However the white spots become lesser and lesser for the films with O_{ap}= 450 Torr and O_{ap}= 650 Torr. Films (Figure 4.12 to Figure 4.14) with high annealing oxygen pressure exhibit droplets with a granular surface, spherically shaped features and irregular pores with sizes of 150-350 nm. Smaller size and reduced number of pores were observed at low oxygen pressures [179].

Porosity may affect the transport current density because of the decreased connectivity of grains in the YBCO film [180]. However, a porous structure may sometimes improve the superconducting critical current density by strain relief, depending on the size and shape of the pores [97, 181]. Since oxygen diffusion is known to be much faster along the *ab* plane of YBCO than in the *c*-axis direction [182] it is expected that a porous film can be oxygenated more easily than a dense and smooth film. This is confirmed by Develos et al. [183] who showed that a porous film is already well-oxygenated in the as-grown state and further annealing will result to minimal, if any, improvements in the overall film property. However the surface morphology changes in all films deposited under the same condition remain unexplained.

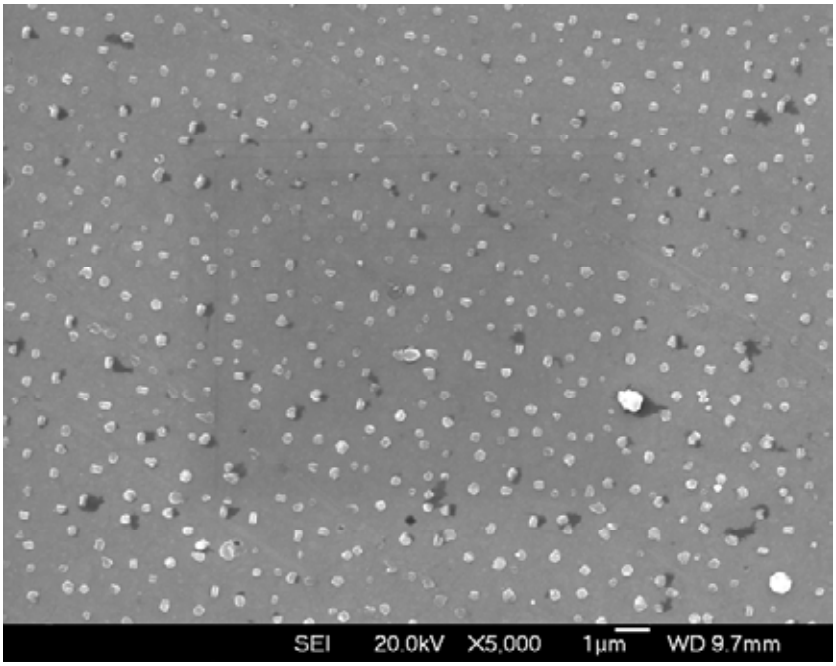

Figure 4.10. SEM image of Y123 film annealed at 100 Torr annealing oxygen pressure (O_{ap})

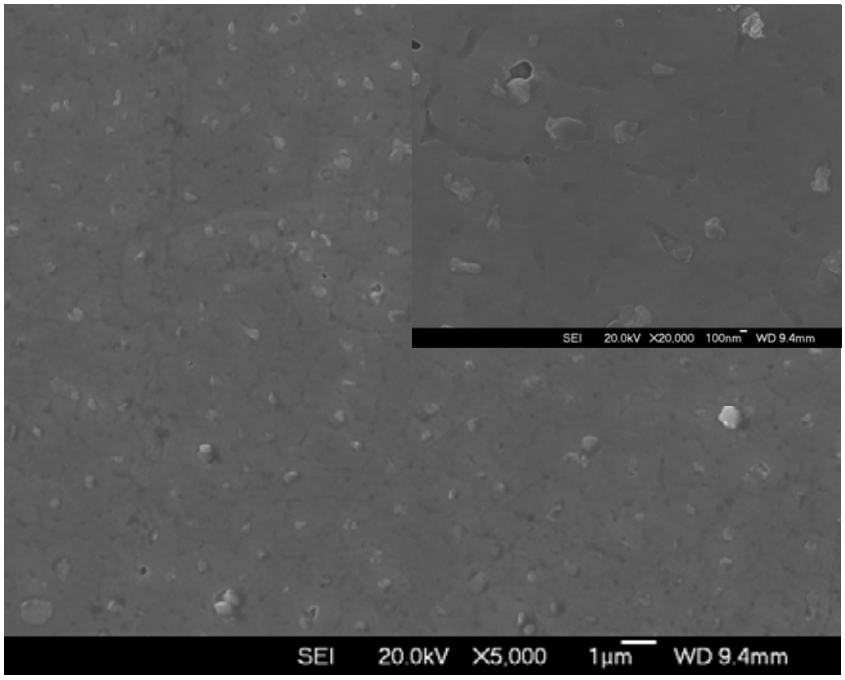

Figure 4.11. SEM image of Y123 films annealed at 200 Torr annealing oxygen pressure (O_{ap})

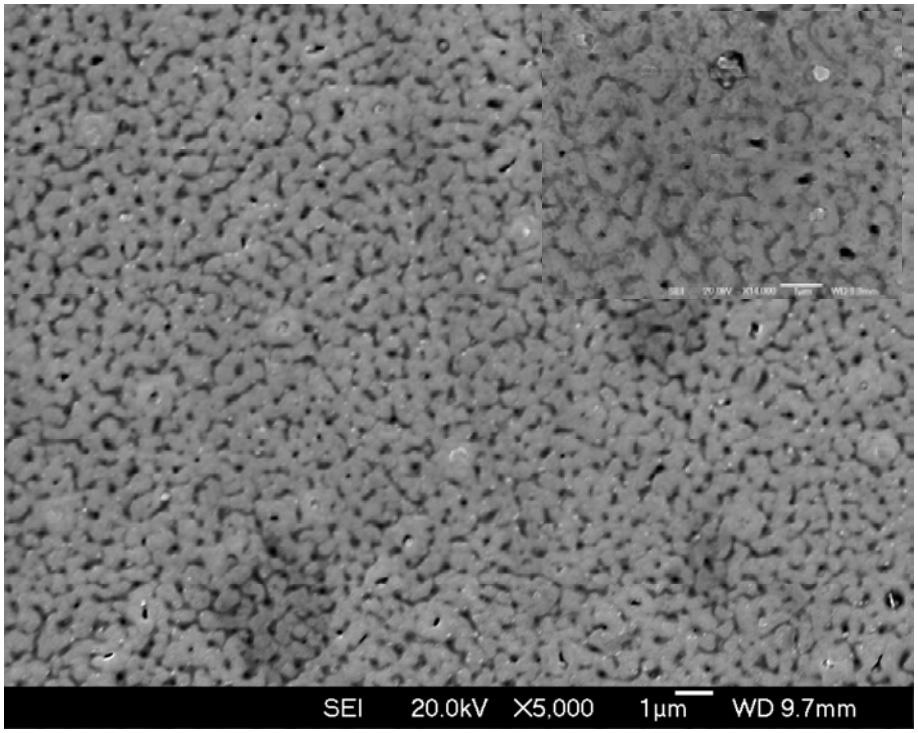

Figure 4.12. SEM image of Y123 films annealed at 300 Torr annealing oxygen pressure (O_{ap})

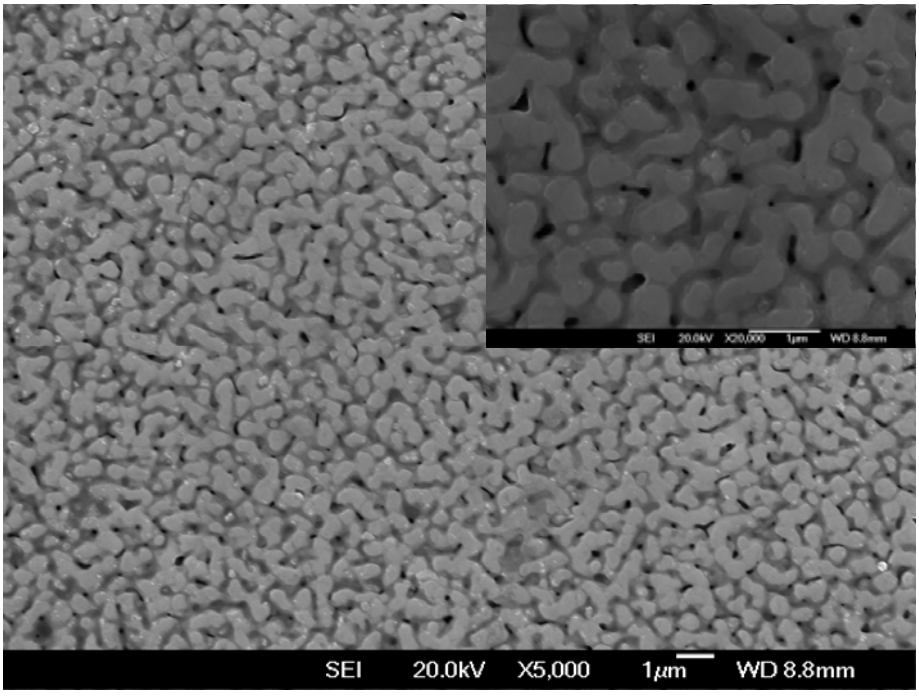

Figure 4.13. SEM image of Y123 films annealed at 450 Torr annealing oxygen pressure (O_{ap})

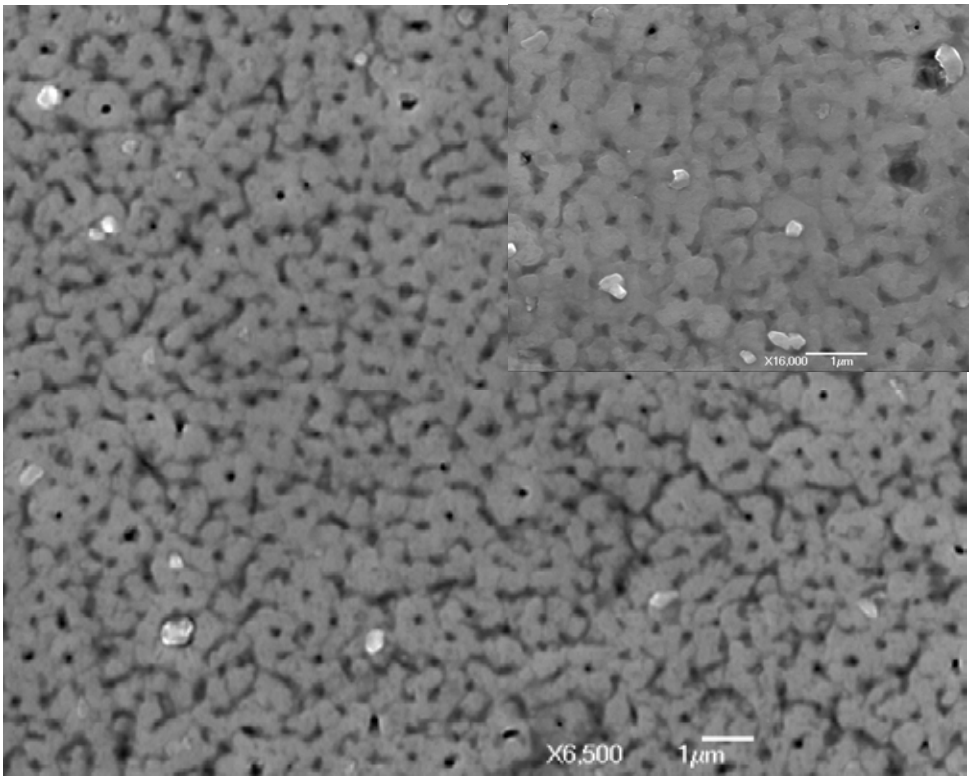

Figure 4.14. SEM image of Y123 films annealed at 650 Torr annealing oxygen pressure (O_{ap})

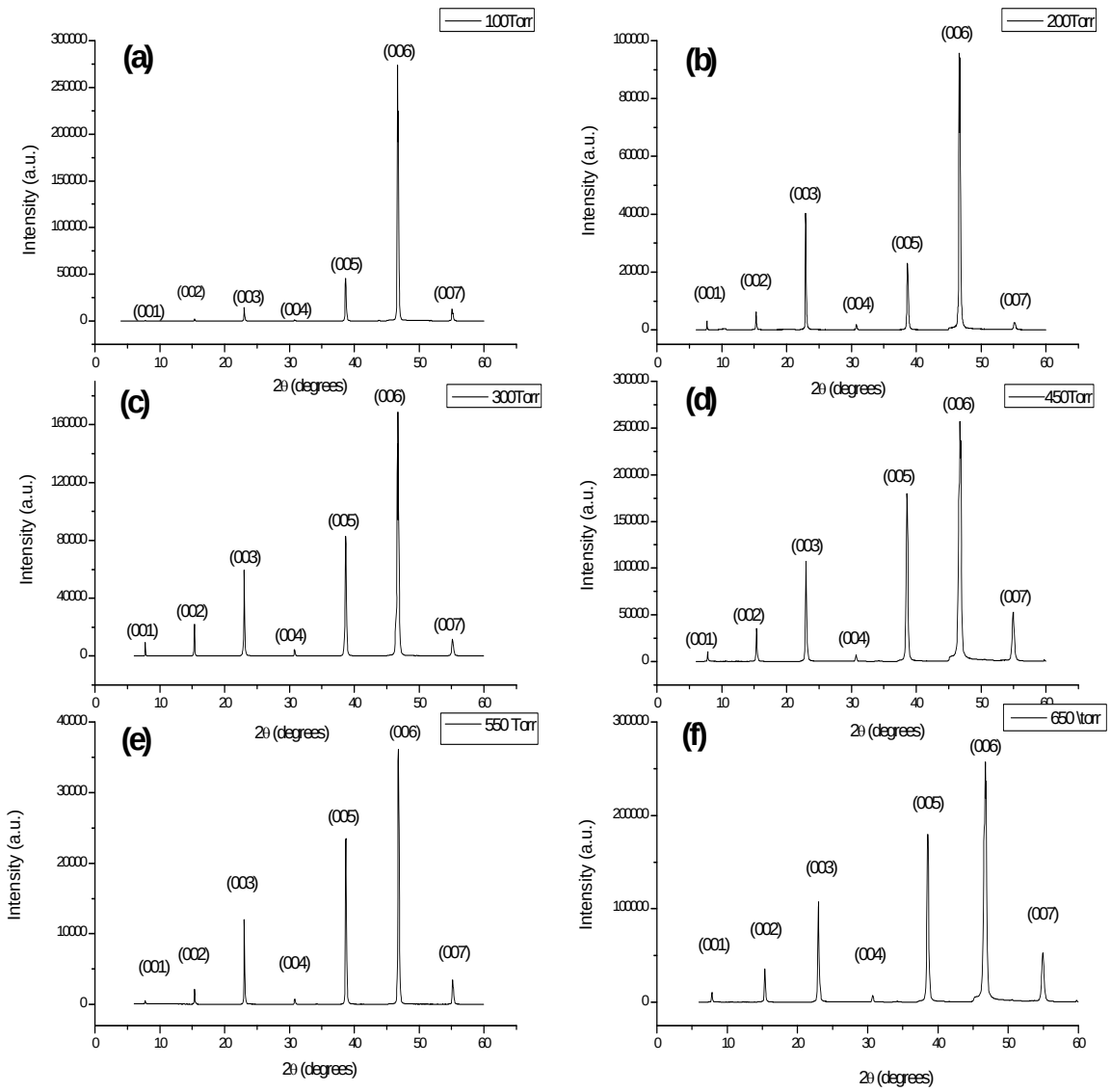

Figure 4.15. Typical XRD patterns for films prepared under different annealing oxygen pressure (O_{ap}) with other conditions fixed: laser energy 218 mJ; deposition temperature 780° C

4.1.5 Structure of oxygen annealed films

To determine the structure of the films, x-ray θ-2θ scans for several films annealed under different oxygen pressure (O_{ap}) conditions were performed and shown in Figure 4.15. The θ - 2θ scan maintains its angle with the sample, detector and x-ray source.

The peaks indicate (by hkl), that the films belong to the 123 phase. The (00l) XRD peaks especially (001), (002), (003), (004), (005), (006) and (007) appear in all films in Figure 4.15, indicating strong epitaxy in all films. The (001) and (002) peaks of STO substrate coincided with the (003) and (006) peaks of YBCO. No a-axis orientation growth peaks were found. For the good T_c films, the diffraction pattern mainly show Y123 (003), (005) and (006) peaks at 22.92°, 38.55° and 46.75° (2-theta), whereas in the other films these peaks are not as strong. In the higher T_c films, strong peaks were observed at 38.55° and 46.75° for the film with high O_{ap} (450 Torr). This might be because when the oxygen pressure is increased, O_2 are easily dissolves into YBCO film and enhance the growth of Y123 grains during the film crytallisation process. These strong peaks indicate high quality epitaxy. The lower T_c shows weak intensities at 22.92°(003) and 38.55°(005) for the film with low O_{ap} (100 Torr). Another possible factor could be the oxygen content that could play a role in the decrease of the 003 and 005 peaks intensity. On the other hand, the film with high O_{ap} (550 Torr) shows low intensity value in all peaks because of the film positioning during the XRD measurement. Film position is very sensitive in XRD measurement.

The oxygen deficiency, δ, of the thin films can be precisely determined from the intensity ratios of (005) and (004) peaks [185] where I (005)/I (004) < 20 gives δ < 0.1. All the pure YBCO films at different Oap have I (005)/I (004) < 19 and the variation of YBCO

c-axis is due to varying oxygen content. The films with O_{ap} = 450 Torr and above show c-axis = 1.160 nm, which is quite close to the theoretical value. However a larger *c*-axis = 1.169 nm is exhibited for films below O_{ap} = 450 Torr.

4.1.6 Critical current densities (J_c)

Magnetic measurements were made by the MPMS and the critical current density (J_c) of the films was deduced from magnetisation at 5 K and 77.3 K. Measurements for all films annealed under different oxygen pressure (O_{ap}) conditions were performed and shown in Figure 4.16 and Figure 4.17. The inductive critical current density (J_c) of the samples has been calculated using Eq. 4-1:

$$J_c = \frac{4m}{a^2 bd(1-\frac{a}{3b})} \qquad 4\text{-}1$$

which is derived in SI units from a critical state model applied to thin films [185]. In Eq.4-1, m is the irreversible magnetic moment, or the half-width of the magnetisation loop, a and b ($a \leq b$) are the planar dimensions of the film, and d is the thickness. Wherever possible, square planar films of side length $a = b$ = 5 mm were measured. The calculated magnetic J_c values at 5 K are presented in Figure 4.16 for different values of oxygen pressure. Basically, weak links are responsible for the sudden decrease of J_c in low fields due to many weak links between the grains being progressively switched-off as the field increased, while the slow reduction in J_c at higher fields is due to strong links [186] and can be clearly seen in all films in Figure 4.16.

The lowest J_c value in the film with O_{ap} = 200 Torr in near zero field is about 1.9×10^7 Acm^{-2}. As O_{ap} increases from 200 to 450 Torr, J_c increases in near zero fields. For all

the films, J_c monotonically decreases with increasing applied field. The decline in J_c for O_{ap} = 450 Torr is somewhat less than that of the other annealed oxygen pressure films, and the magnetic field is about 4.8 Tesla, which implies that the high oxygen pressure annealed film may have stronger flux pinning. However, the J_c decreases obviously when O_{ap} was increased up to 650 Torr.

A similar trend in J_c at a higher temperature of 77.3 K, shown in Figure 4.17, was revealed with films prepared at different oxygen pressure (O_{ap}). It can be seen that the J_c values systematically changes with the change of O_{ap}. Measurement of Jc reaches a maximum at O_{ap} = 450 Torr and the film gives values of 2.8 $MAcm^{-2}$ at self-field and 0.8$MAcm^{-2}$ at 1 Tesla. It is obvious that the J_c of film with O_{ap} of 650 Torr decreases to 0.4 $MAcm^{-2}$ in 1.2 T magnetic fields. There is no doubt that the superconductivity of film with O_{ap} = 450 Torr is enhanced greatly. Strickland et al. found that J_c clearly increases monotonically with increasing partial pressure of O_2 during annealing [187]. It believed that the increase in oxygen pressure while the sample is at high temperature transforms the crystal from a tetragonal to orthorhombic structure [188]. The optimum O_{ap} seems to be 450 Torr, producing optimum J_c at 5 K and 77.3 K.

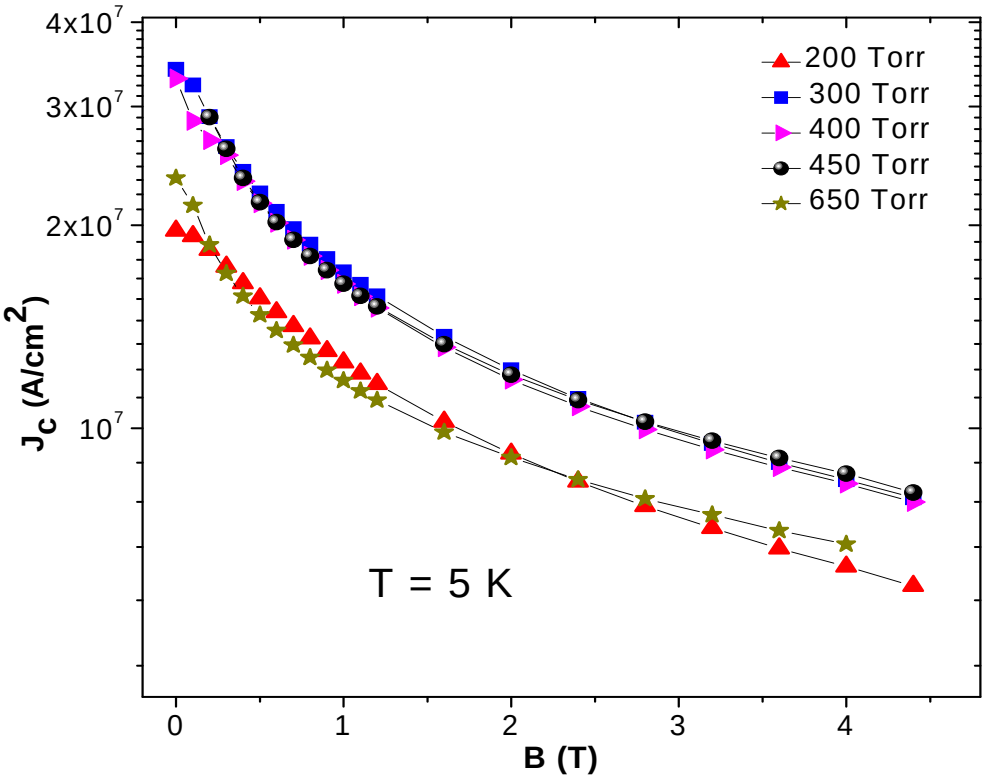

Figure 4.16. Magnetic field dependence of J_c at 5 K for films under different annealing oxygen pressure (O_{ap}) with other conditions fixed: laser energy 218 mJ; deposition temperature 780° C. The field is applied perpendicular to the plane of the film. The lines connecting the data points are for guiding the eye

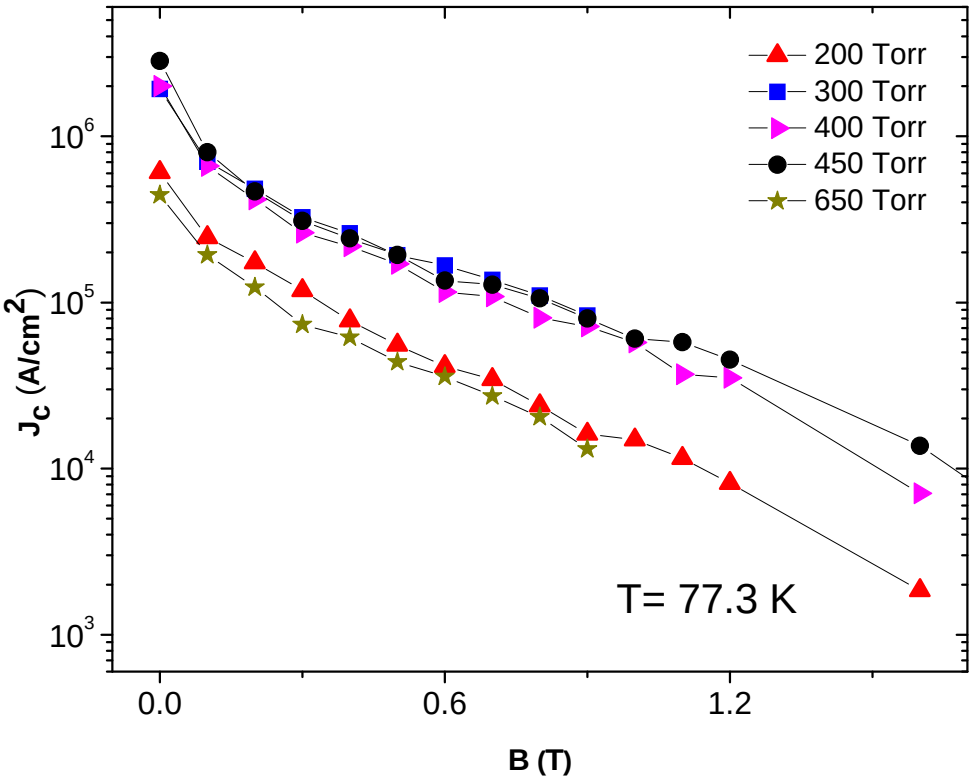

Figure 4.17. Magnetic field dependence of J_c at 77.3 K for films under different annealing oxygen pressure (O_{ap}) with other conditions fixed: laser energy 218 mJ; deposition temperature 780° C. The field is applied perpendicular to the plane of the film. The lines connecting the data points are for guiding the eye

4.1.7 Variation of pinning force with oxygen pressure

Figure 4.18 shows the field dependence of pinning force density F_p ($F_p = J_c \times B$) and its evolution with O_{ap} at 77.3 K. The film with low O_{ap} (200 Torr) exhibited a reduced F_p in the ranges of magnetic field shown. Pinning force density at high O_{ap} of 650 Torr is also shifted to a lower value. It is interesting that the O_{ap}= 300 Torr shows the highest value of F_p. The film with the optimum O_{ap}= 450 Torr shows improvement in J_c but not in

F_p. This indicates that the oxygen pressure influences the pinning force density in YBCO film in a different way than the effect on the current density.

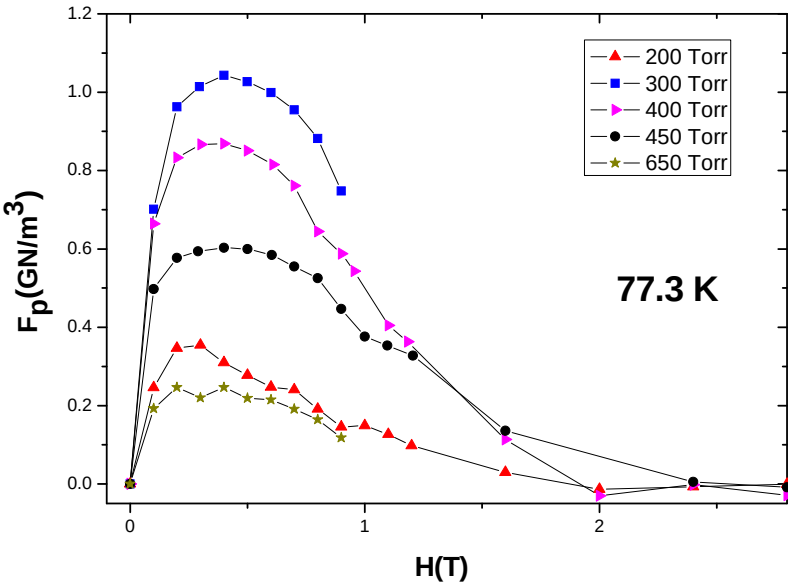

Figure 4.18. Field dependence of the pinning force at 77.3 K of the films prepared under different annealing oxygen pressure (O_{ap}) with other conditions fixed: laser energy 218 mJ; deposition temperature 780° C. The field is applied perpendicular to the plane of the film. The lines connecting the data points are for guiding the eye

4.1.8 EDS Analysis

In order to clarify the composition ratio of the Y:Ba:Cu:O, energy dispersive spectroscopy (EDS) analysis was carried out for the best film made using the optimum conditions; laser energy (E) of 218 mJ, deposition temperature (T_s) of 780° C, deposition oxygen pressure (O_p) of 450 mTorr and annealing oxygen pressure (O_{ap}) of 450 Torr. The analysis was performed in the position as seen in Figure 4.19. Table 4.1 shows quantitative data of EDS. The EDS results show the elemental composition ratio of the

YBCO in atomic percentage which is very close to the composition ratio of the real $YBa_2Cu_3O_{7-x}$. From the EDS analysis it can be concluded that there is no evidence of impurity traces in the YBCO film and reconfirms that all elemental compositions are in a good ratio.

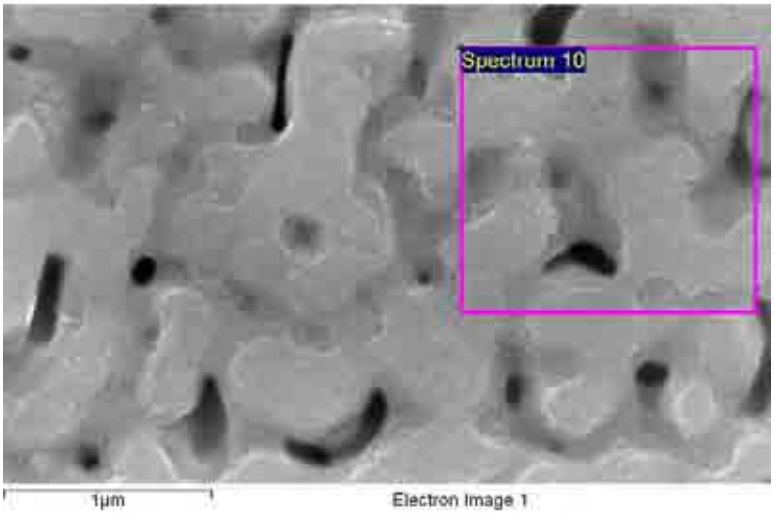

Figure 4.19. EDS spectrum position of the optimised YBCO film

Table 4.1. Quantitative elemental analysis of optimised YBCO film obtained by EDS analysis.

Element	Atomic %	Error %
O	53.63	3.4
Cu	22.28	2.1
Y	7.69	1.4
Ba	16.40	2.0

4.2 Summary

The values of T_c are highly dependent on several important conditions, such as the laser energy (E), oxygen pressure (O_p), substrate temperature (T_s), annealing oxygen pressure (O_{ap}) and cooling time (cooling rate) (C_t). The effects of the deposition parameters such as deposition temperature (T_s), annealing oxygen pressure (O_{ap}) and cooling time (cooling rate) (C_t) in relation to superconducting transition temperatures were observed. A proper combination of these parameters could lead to high quality films. It is found that a condition with T_s of 780° C, E ~ 218 mJ/pulses, O_{ap} of 450 Torr and C_t of 8° /min makes good films with T_c 91 K. The XRD results have revealed 100 % (00l) orientation. At 77.3 K, the highest J_c gives values of 2.8 $MAcm^{-2}$ at self-field and 0.8$MAcm^{-2}$ at 1 Tesla. In situ high temperature annealing carried out immediately after the deposition with optimum oxygen pressure and cooling rate has been proven to be effective to obtain high T_c and J_c. This condition has also been used in growing all other films relating to the effect of Gd2411 and BZO additions on the flux pinning that is to be reported in the following chapters.

Chapter 5

Fabrication and Characterisation of $YBa_2Cu_3O_{7-x}$ films containing $Gd_2Ba_4CuWO_{12}$ nanoinclusions

5.1 Introduction

In order to improve the performance of $YBa_2Cu_3O_{7-x}$ films, enhancement of critical current density (J_c) and flux pinning force in this system is crucial. Incorporation of nano-inclusion particles is proven to be an alternative economic approach to enhance J_c for Y123 films [90, 189, 190]. In this chapter, it is shown that a small amount of 1 mol % $Gd_2Ba_4CuWO_y$ addition in $Y_1Ba_2Cu_3O_{7-\delta}$ films improves the J_c and flux pinning force values in films with various thicknesses. The growth was carried out at an optimum distance (D_s) between the target and the substrate, which is about 55 mm, using a laser repetition rate of 6 Hz, and laser energy (E) of 218 mJ/pulse. After deposition, the Y123 film was slow-cooled from 780° C to room temperature at a pressure (O_p) of 450 Torr of oxygen with cooling rate (C_t = 97.5) of 8°C /min. Several films were fabricated with thickness ranging from 0.78 μm to 2.65 μm.

5.2 Superconducting properties

5.2.1 Transition temperature, T_c

The magnetic moment (M) is normalised to eliminate the effect of difference in demagnetisation factors and thickness. The T_c transitions of all the films are shown in Figure 5.1. The highest T_c of 90.7 K ± 0.2 K has been achieved in film YG2 with thickness of 0.96 μm. This YG2 film was also measured and compared to $YBa_2Cu_3O_{7-}x$ (Y1= 0.96 μm) to calculate the J_c at different temperatures of 5, 50, 70 and 77.3 K, as shown in section 5.2.2.

Basically ΔT_c (T_c onset - T_c offset) for all films is small as shown in Figure 5.2. T_c onset is defined as the onset of diamagnetism and T_c offset as the temperature of complete diamagnetic signal. The transition is sharper for thicker films YG3 and YG5 (1.29 and 2.1 μm), with a width of ~ 0.4 K. The film YG4 and YG6 exhibits a secondary, smaller broader transition (not complete diamagnetic signal) between 89 and 88 K. This secondary phase may provide some additional pinning centres of δTc-type, although this is not studied further in this work. ΔT_c is slightly increased for the thinner films, YG1 (0.78μm) and YG2 (0.96μm), with a width of ~ 0.9 K. It is suggested that the transition broadening on these films is most probably due to the substitution of compatible atoms between YBCO and 2411W (e.g., Gd for Y, as will be discussed in more details in section 5.3.3) during the film growth process to produce small quantities of a second phase composition with lower T_c.

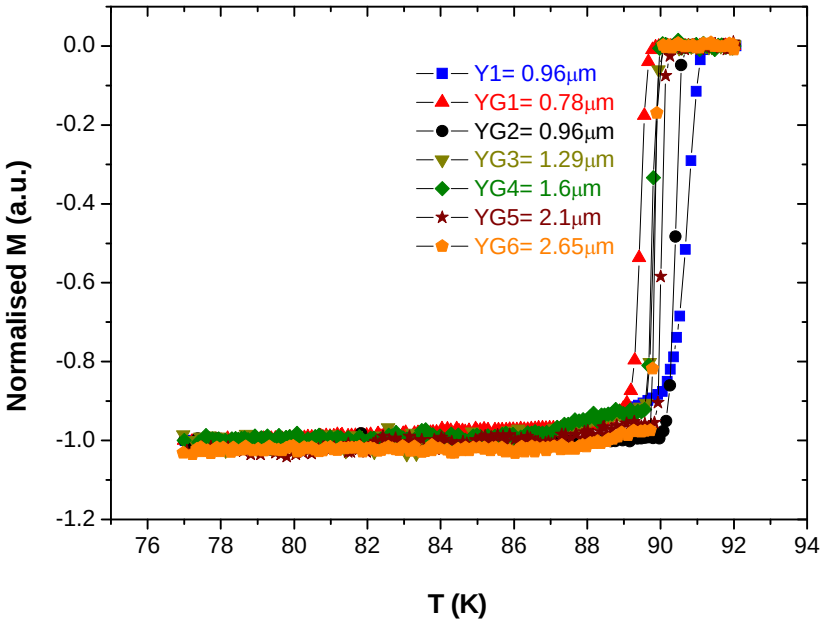

Figure 5.1. Normalised M as a function of temperature for $YBa_2Cu_3O_{7-x}$ / $Gd_2Ba_4CuWO_{12}$ films with various thicknesses.

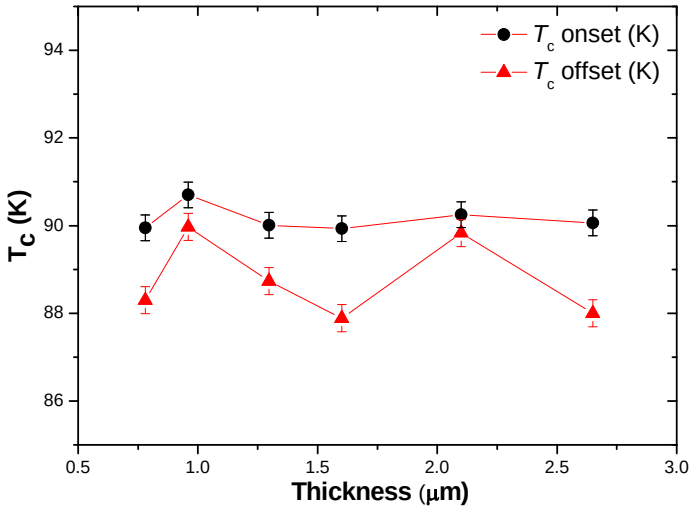

Figure 5.2. Dependence of critical temperatures, T_c onset and T_c offset, on the thickness.

5.2.2 Critical current densities, J_c

Figure 5.3 depicts the field-dependent critical current densities of the two films (YG2 and Y1), estimated from the DC magnetization loops measured at various temperatures in the range of 5 to 77 K. Both compared films have the same thickness of 0.96 μm. The critical current densities of the two films (YG2 and Y1) are essentially the same at low temperatures, whereas the film containing nano-inclusions exhibits a consistently higher J_c than the reference film (Y1) at temperatures above 50 K. In addition, the relative difference in J_c between the two films increases with increasing temperature. At 77 K, and fields between 0.5 and 2.5 T, the nano-inclusions lead to an increase in J_c by a factor of 2–3 times. This behaviour is not consistent with that reported for other films containing artificial pinning centres, in which the increase in J_c occurs typically at all temperatures. The results of this study can be explained by considering the nature of flux pinning by the nano-inclusions.

Magnetic flux pinning by secondary phase inclusions is most effective (i.e. strong) when their size is comparable with the (temperature-dependent) coherence length, ξ, which is small at low temperatures (about 2 nm at 5 K) compared to the size of the 2411 inclusions (mostly between 30 nm and 100 nm) [191]. As a result, the associated pinning force provided by the nano-inclusions is relatively weak at low temperatures. ξ increases with increasing temperature, however, it eventually becomes comparable with the dimensions of the smaller nano-inclusions. The number of inclusions of size comparable to $\xi(T)$ increases as the temperature increases further, as does the number of strong pinning centres, and hence J_c.

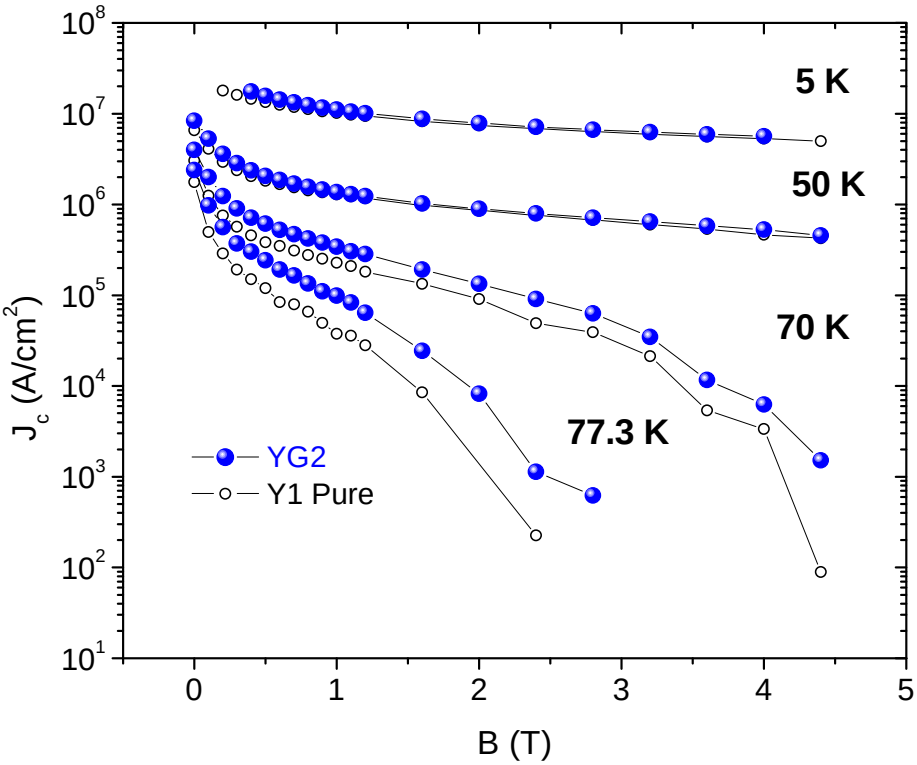

Figure 5.3. Field dependence of the critical current densities J_c of one best film prepared from the YBa2Cu3O_{7-x} / Gd_2 Ba_4CuWO_{12} (YG2) and from the $YBa_2Cu_3O_{7-x}$ (Y1) at 5, 50, 70, and 77.3 K. Solid lines are to guide the eye.

Since no significant changes were found in J_c at low temperature, J_c was only measured at temperatures of 65, 70 and 77.3 K for other films. Two of the best $YBa_2Cu_3O_{7-x}$ /Gd_2 Ba_4CuWO_{12} films with thicknesses of 0.78 μm (YG1) and 0.96 μm (YG2) were selected to compare their J_c at 70 and 77.3 K only. The field dependence of critical current density of YG1 and YG2 films is shown in Figure 5.4. At 70 K and in self-field, J_c of the YG1 film is about 4.7×10^6 A/cm^2, slightly larger than that of theYG2 film, which is about 3.9×10^6 A/cm^2. At 77 K in self-field, J_c of YG1 (2.7×10^6 A/cm^2) is again slightly larger than that of YG2 (2.4×10^6 A/cm^2). In higher fields, YG1 film has a higher J_c at both temperatures.

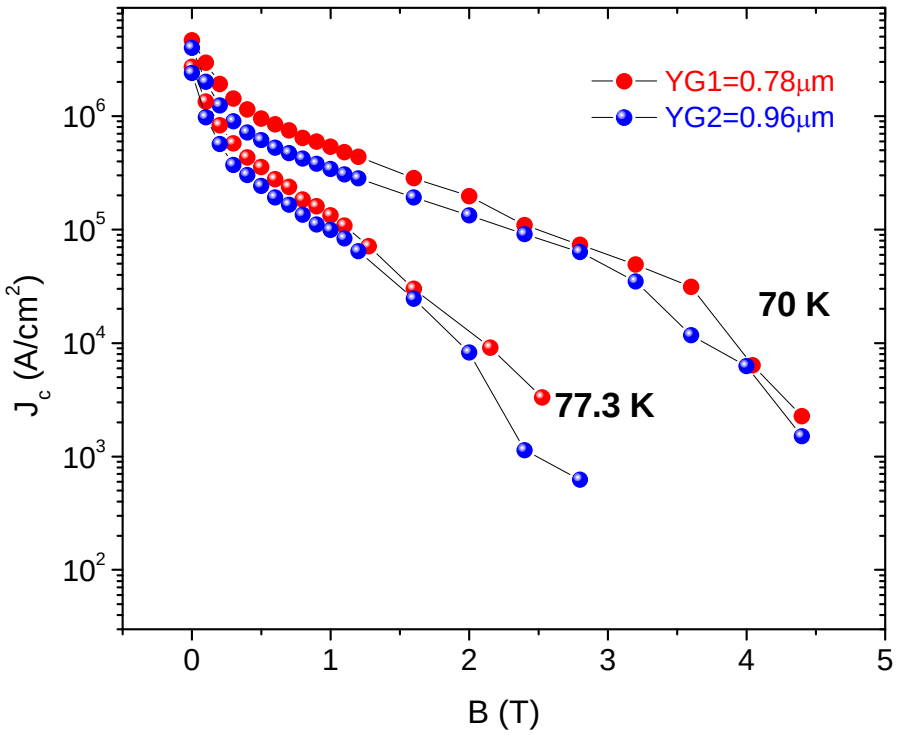

Figure 5.4. Field dependence of the critical current densities J_c of the YG1 and YG2 at temperatures 70 and 77.3 K. Solid lines are drawn for eye guidance.

Field dependences of the critical current densities of other films from a different batch with thicknesses from 1.29 to 2.65 μm, at 65 K are shown in Figure 5.5. At 65 K, quite high J_c in magnetic fields of up to 4 T was observed in all films.

In self-field, J_c of the thinnest YG3 film (1.29 μm) is about 2.9×10^6 A/cm^2, which is higher than the other films. The J_c in self-field decreases to 1.7×10^6 A/cm^2 as the thickness increases to 1.6 μm (YG4). The lowest J_c of 1.44×10^6 A/cm^2 and 1.46×10^6 A/cm^2 in self-field were obtained for thicker films both on YG5 (2.1 μm) and YG6 (2.65 μm),

respectively. This result clearly shows that the J_c in self field decreases as the film thickness increases, which is similar to the results observed for YBCO films [98]. It is reported that the reduction in J_c of YBCO films is related to a change of microstructure because the film surface grows much rougher as the film thickness increases [94].

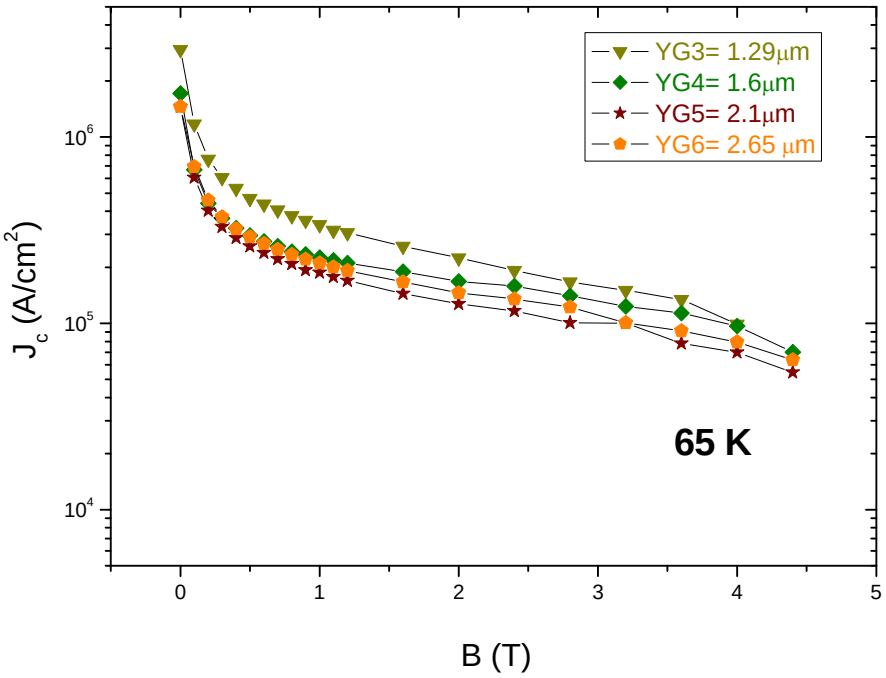

Figure 5.5. Magnetic field dependence of critical current densities of films with thickness of 1.29, 1.60, 2.10 and 2.65 μm at 65 K. Solid lines are drawn for eye guidance.

Figure 5.6 shows the magnetic field dependence of critical current densities of the same films measured at 77.3 K. In self-field, J_c remains at as high as 2.7×10^6 A/cm^2 at a thickness of 0.78 μm (YG1). The self-field J_c decreases from 2.4×10^6 A/cm^2 to 1.5×10^6 A/cm^2 for films YG2 (1.29 μm) and YG3 (1.60 μm). The same trend of self-field J_c suppression was found in the films YG4, YG5, and YG6 with values of 8.8×10^5 A/cm^2, 7.6×10^5 A/cm^2, and 7.4×10^7 A/cm^2, respectively. It is clearly shown that a monotonic decrease in J_c is observed as the thickness increases.

At high field (Figure 5.7) above 1.6 T, the critical current density of the thinnest film (YG1) decreases rapidly with increasing magnetic field in comparison with thicker films, which is a possible confirmation of scenario of two-dimensional pinning at high temperature and field, as suggested by Jha et al. [193].

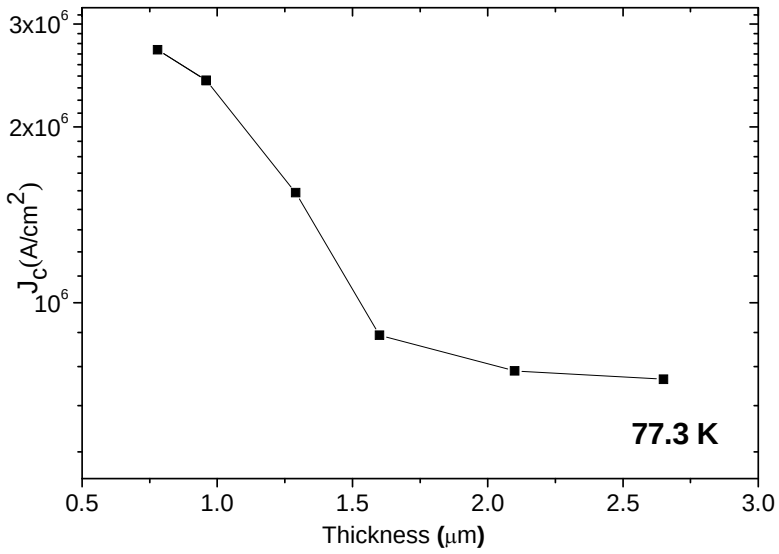

Figure 5.6. Thickness dependence of critical current densities of films at 77.3 K, self field. Solid lines are drawn for eye guidance

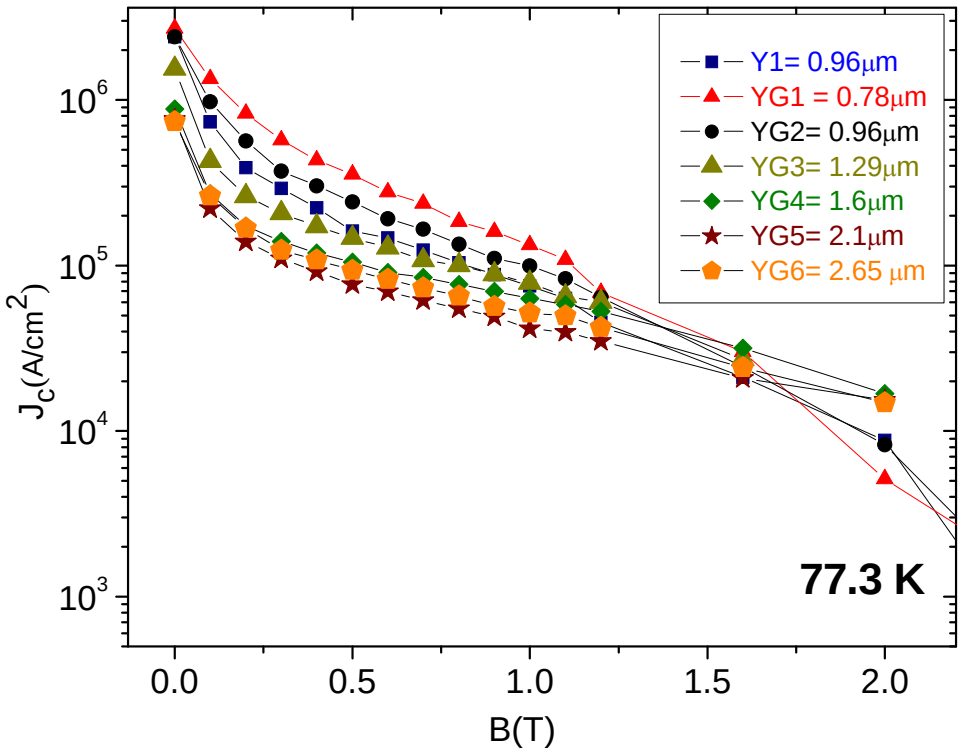

Figure 5.7. Magnetic field dependence of critical current densities of YG films with thickness of 0.78 to 2.65 μm at 77.3 K. Solid lines are drawn for eye guidance.

Figure 5.8 shows the magnetic field dependence of the critical current per cm width, at 77.3 K, for the same films in Figure 5.6. In fields higher than 0.6 T, all nano-inclusion films have a higher critical current than the reference film. In lower fields and self-field, few nano-inclusion films have a lower critical current than the reference film.

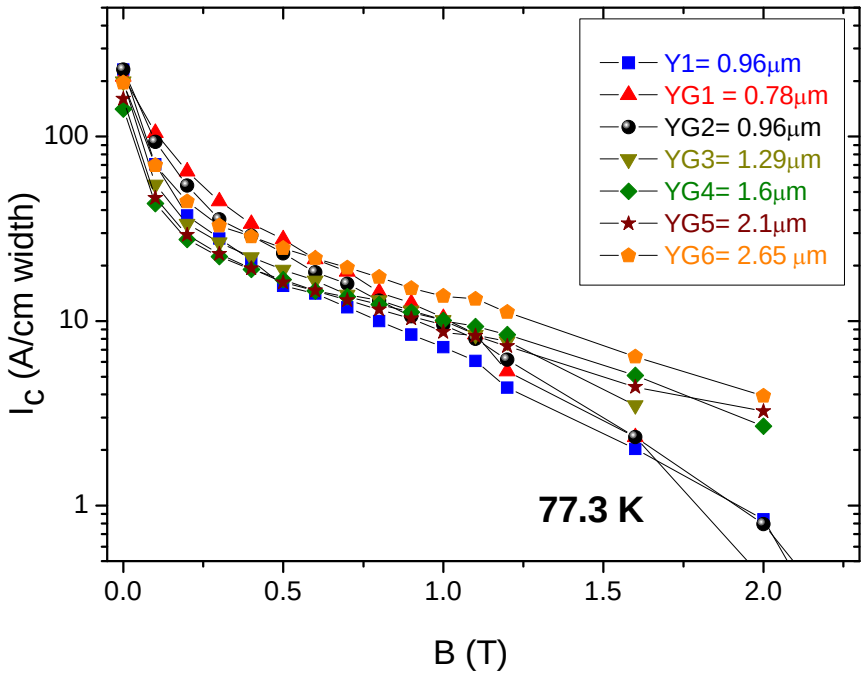

Figure 5.8. Magnetic field dependence of critical current of films with thickness of 0.78 to 2.65 μm at 77.3 K. Solid lines are drawn for eye guidance.

5.2.3 Flux pinning force, F_p

Figure 5.9 shows the magnetic field dependence of the flux pinning force, $F_p = J_c \times B$ for the films of various thicknesses at 77.3 K. The J_c data used to calculate F_p are as shown in the earlier Figure 5.7. Similarly to J_c, pinning force is higher in the case of thinner films. The magnitude of the F_p max increases as the thickness decreases because of the contribution of the strong-pinning interface layer. F_p, max = 1.77 GN/m^3 is more than two times higher for the thinnest film YG1 (0.78 μm) as compared with F_p, max = 0.51 GN/m^3, for thickest film YG6 (2.65 μm). It is also observed that the peak in F_p shifted to higher magnetic fields as the thickness was increased. This is possibly due to different dominating pinning mechanisms at different thickness in $YBa_2Cu_3O_{7-x}$/Gd_2 Ba_4CuWO_{12} films.

The enhancement in the flux pinning force in the $YBa_2Cu_3O_{7-x}$/Gd_2 Ba_4CuWO_{12} films (compared with the pure YBCO film) can be explained as a result of the presence of $Gd_2Ba_4CuWO_{12}$ nano-inclusions in the intergrain regions. This in turn causes the increase of intergrain contact surface [194] (decreasing the intergrain resistance) and increases the number of flux pinning centres due to the presence of $Gd_2Ba_4CuWO_{12}$ particles in the intergrain regions and results in the enhancement of J_c even in the presence of higher magnetic field.

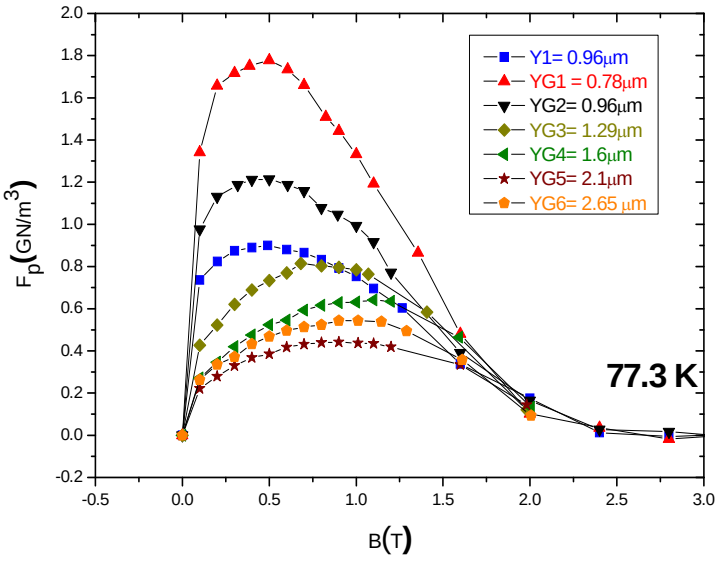

Figure 5.9. Field dependence of the pinning force of films with thickness of 0.78 to 2.65 μm at 77.3 K. Solid lines are drawn for eye guidance.

5.2.4 Pinning mechanisms

The interaction of the flux line lattice with pinning centres induced by the 2411 nano particles in YBCO film is responsible for the higher critical current density. Following the analysis of Dew-Hughes [32] pinning centres are considered to arise from two phenomena: (i) small differences in κ, arising from changes in the normal state resistivity due to composition fluctuations, or non-uniform distributions of dislocations, and (ii) non superconducting particles, which may be normal metal, insulator or void [32].

The two types of pinning centres will be referred to as '$\Delta\kappa$ pinning' and 'normal pinning'. The pinning centres are notably named as point pins, surface pins and volume pins in relation with the number of their respective dimensions (1,2 or 3) that are large compared with the inter-flux-line spacing d $\left(=1.07(\Phi_0 / B)^{0.5}\right)$ where Φ_0 denotes the flux

quanta [195]. Point pins are regions whose dimensions in all directions are less than *d*, surface pins have two dimensions greater than *d* and volume pins have all dimensions larger than *d*.

It is known that high T_c superconductors accommodate several types of pinning centres which may be active simultaneously. The model of Dew-Hughes is a direct summation model of the elementary pinning forces and predicts many forms of pinning types. The Dew-Hughes model was employed because there are various pinning mechanisms acting concurrently in YBCO film and it is important to find the dominating one. This dominating pinning mechanism will be in turn responsible for the location of the maximum peak in $F_p(b)$ where $b = B/B_{irr}$ [196].

In the Dew-Hughes model, there are six different pinning functions $F_p(b)$ describing the core pinning:

$$F_p = Ax^p(1-x)^q \qquad 5\text{-}1$$

where F_p is the pinning force density, *A* is a parameter associated with the pinning strength, *x* is the normalised applied magnetic field and *p* and *q* are parameters describing the actual pinning mechanism. The values of *p* and *q* depend on geometry of pinning site (volume, surface or point) and type of pinning center (normal or $\Delta\kappa$). To simplify the procedure, only three different pinning functions were taken into account, giving:

$$F_p = A_1x^p(1-x)^q + A_2x^{p1}(1-x)^{q1} + A_3x^{p2}(1-x)^{q2} \qquad 5\text{-}2$$

Each term describes one type of flux pinning centre, while parameters A_1, A_2 and A_3 reflect the weighting of each type of pinning centre. The normalised flux pinning force $F_p / F_p^{\max}$ at 77.3 K has been plotted as a function of reduced field $b = B/B_{irr}$ for the films

described above, in Figure 5.10 to Figure 5.15. The irreversibility field (B_{irr}) was determined using a criterion of 10^3 A/cm^2 for all films throughout this study. The irreversibility field, a characteristic field at which the critical current density reduces to zero, is one of the important parameters of the superconductor for its application [197].

In all films from YG1 to YG6 the normalized pinning force shows a typical curved shape and all sets of data produce a good fit to the scaling law. In Figure 5.10 and Figure 5.11, the solid fitting curves represents the result of calculation using Eq. 5.1 with only two types of pinning centres: one with p = 0.5 and q = 2, which describes normal surface pinning centres, and a $\Delta\kappa$ point pinning with the values of p = 2 and q = 1. The position of the peak in F_p in the thin films of 0.78 μm and 0.96 μm is the same at the reduced field b (0.2). From the data, we can deduce that normal surface pinning centre is dominant, thus being responsible for maximum peak $F_p(b)$ = 0.2 position. These results are also supported by the values of scaling parameters A_1 and A_2 in Figure 5.16, where A_1 parameter here refers to the normal surface pinning and A_2 refer to the $\Delta\kappa$ point pinning. Since A_1 is larger than A_2, the dominating pinning mechanism in those two films is the normal surface pinning.

In thicker films, (from 1.29 to 2.65 μm) three different pinning mechanisms were detected. From the best fits, normal surface pinning (p = 0.5 q = 2), $\Delta\kappa$ point pinning (p = 2, q = 1) and Δk volume pinning (p = 1, q = 1) were deduced in the 1.29 μm - thick film (Figure 5.12) and, respectively in the 1.69 μm-thick film (Figure 5.13). From the position of the maximum at b = 0.5, the main pinning mechanism seems to be the $\Delta\kappa$ point pinning. It is worth mentioning that with increasing film thickness of over 1 μm, the number of relevant pinning mechanisms has increased from 2 to 3. For the thickest films of 2.1 μm (Figure 5.14) and 2.65 μm (Figure 5.15), the normal surface pinning (p = 0.5 q = 2),

$\Delta\kappa$ point pinning (p = 2, q = 1) and normal point pinning (p = 1, q = 2) were observed from the best fit of experimental data, with the $\Delta\kappa$ point pinning still dominant in these films with peak position at b = 0.67, and the normal point pinning mechanism giving only a minor contribution as shown by the smallest scaling parameter being $A_{3,}$ as can be seen in Figure 5.16.

For films thicker than 1.0 μm, it can be concluded that $\Delta\kappa$ point pinning is the dominant pinning mechanism. In this case, the source of $\Delta\kappa$ point pinning could be from the variation distribution of T_c. Several researchers found evidence for δT_c or $\Delta\kappa$ point pinning mechanisms in Pr-doped YBCO and (K,Ba)BiO_3 single crystal film [198].

Table 5.1. Summary of elementary pinning force of films at various thicknesses.

Films	$Ax^p(1-x)^q$	Type of centre
YG1	p = 0.5, q = 2	Surface normal
0.78 μm	p = 2, q = 1	Point Δk
YG2	p = 0.5, q = 2	Surface normal
0.96 μm	p = 2, q = 1	Point Δk
YG3	p = 0.5, q = 2	Surface normal
1.29 μm	p = 2, q = 1	Point Δk
	p = 1, q = 1	Volume Δk
YG4	p = 0.5, q = 2	Surface normal
1.6 μm	p = 2, q = 1	Point Δk
	p = 1, q = 1	Volume Δk
YG5	p = 0.5, q = 2	Surface normal
2.1 μm	p = 2, q = 1	Point Δk
	p = 1, q = 2	Point normal
YG6	p = 0.5, q = 2	Surface normal
2.65 μm	p = 2, q = 1	Point Δk
	p = 1, q = 2	Point normal

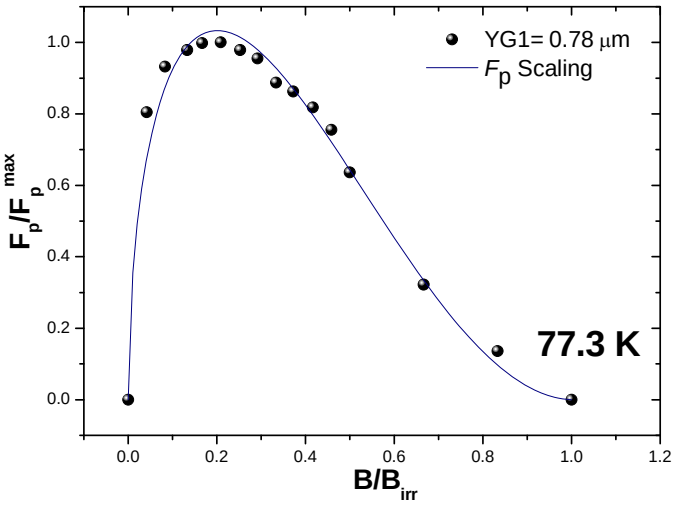

Figure 5.10. Normalised pinning force as a function of magnetic field of the YG1 film at 77.3 K with the scaling parameter of A_1, A_2 and A_3 shown in Figure 5.16. The solid line represents theoretical curve by Eq. 5.1.

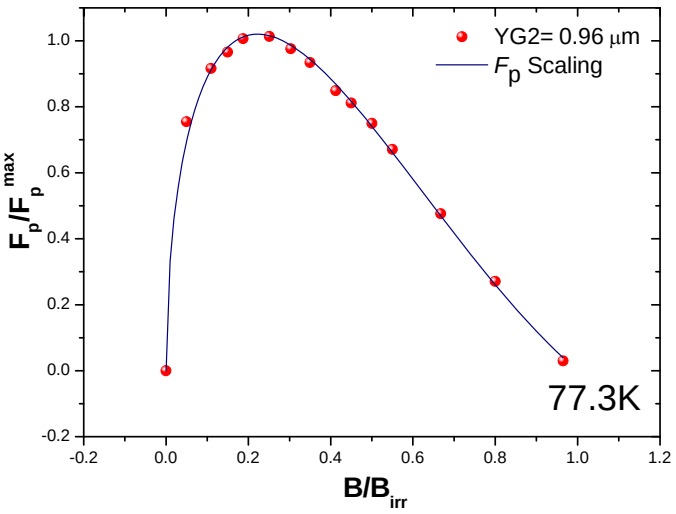

Figure 5.11. Normalised pinning force as a function of magnetic field of the YG2 film at 77.3 K with the scaling parameter of A_1, A_2 and A_3 shown in Figure 5.16. The solid line represents theoretical curve by Eq. 5.1

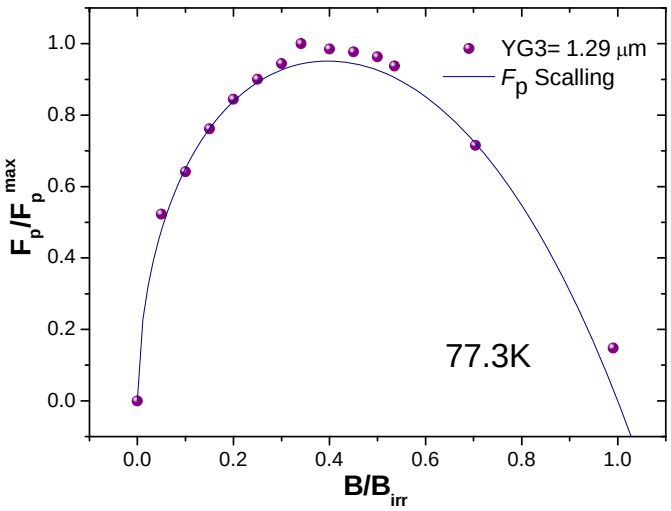

Figure 5.12. Normalised pinning force as a function of magnetic field of the YG3 film at 77.3 K with the scaling parameter of A_1, A_2 and A_3 shown in Figure 5.16. The solid line represents theoretical curve by Eq. 5.1

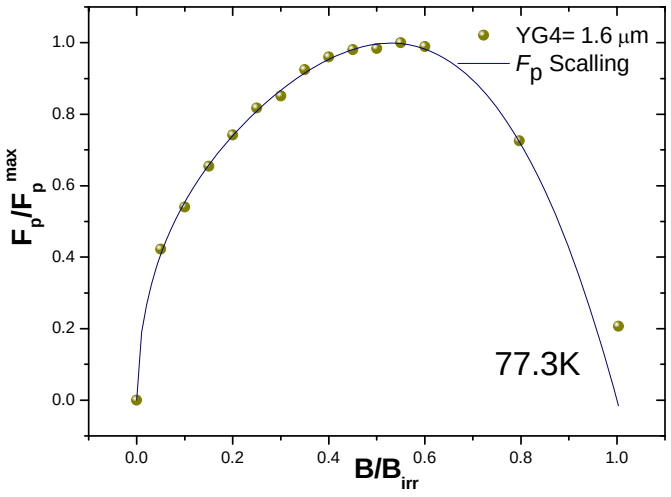

Figure 5.13. Normalised pinning force as a function of magnetic field of the YG4 film at 77.3 K with the scaling parameter of A_1, A_2 and A_3 shown in Figure 5.16. The solid line represents theoretical curve by Eq. 5.1

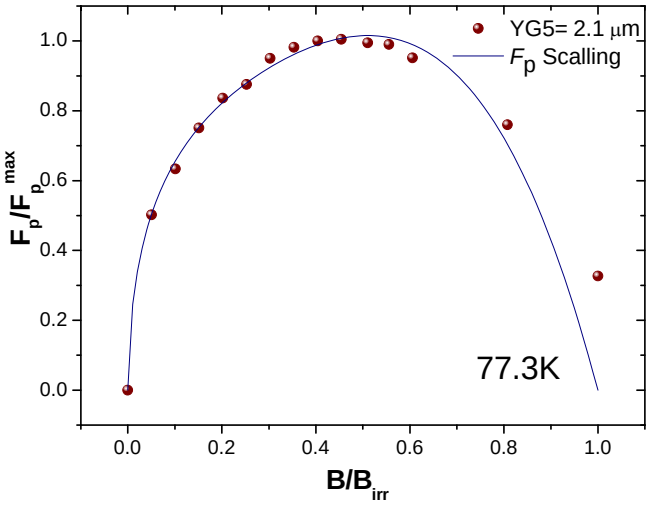

Figure 5.14. Normalised pinning force as a function of magnetic field of the YG5 film at 77.3 K with the scaling parameter of A_1, A_2 and A_3 shown in Figure 5.16. The solid line represents theoretical curve by Eq. 5.1.

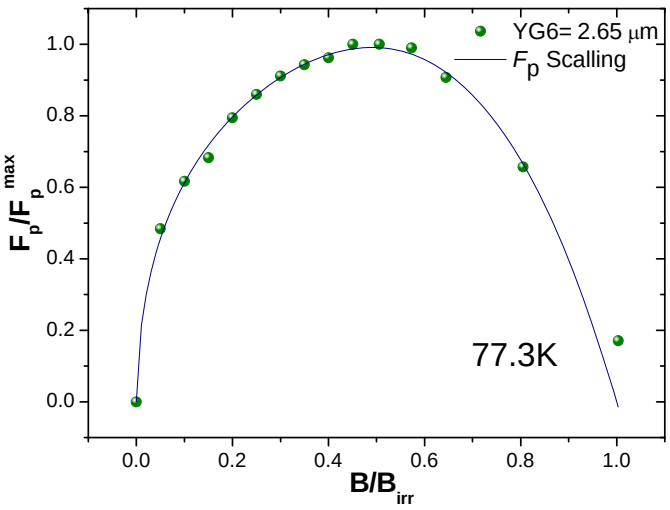

Figure 5.15. Normalised pinning force as a function of magnetic field of the YG6 film at 77.3 K with the scaling parameter of A_1, A_2 and A_3 shown in Figure 5.16. The solid line represents theoretical curve by Eq. 5.1

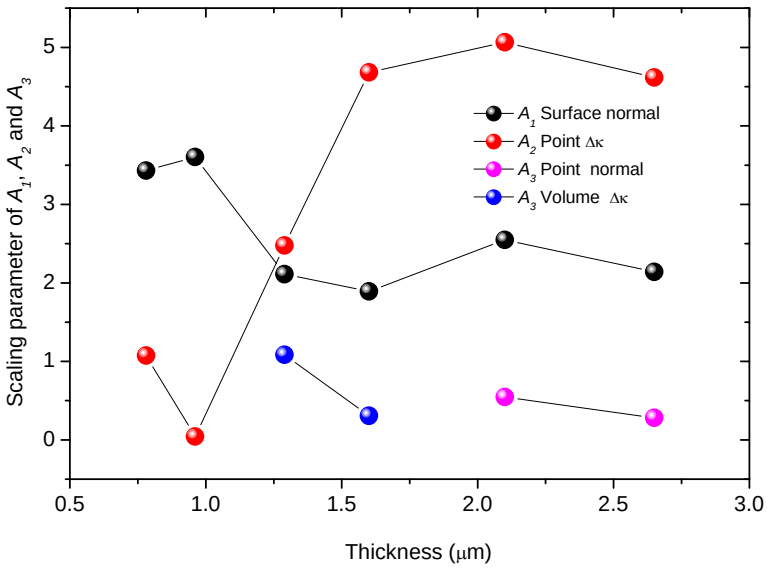

Figure 5.16. Scaling parameter of A_1, A_2 and A_3 (eq. 5.2) of $YBa_2Cu_3O_{7-x}$ / $Gd_2Ba_4CuWO_{12}$ films at various thicknesses.

5.2.5 Angular dependence of J_c

Particularly valuable information can be obtained from the analysis of dependence of J_c on the orientation of H, including eventual anisotropy of pinning centres (c-axis correlation) [199]. The YG2 film with thickness of 0.96 μm was selected for this particular study. The isotropic/anisotropic character of the strong artificial pinning centres induced by Gd2411 nano-inclusions can be investigated by performing angle-dependent transport measurements [158]. In the rescaling approach of Blatter et al. [200] within an anisotropic Ginzburg-Landau theory, the angle-dependent critical current density $J_c(\theta)$ is described by

$$J_c(\theta)/J_c(90°) = \left(\sin^2\theta + \gamma^2\cos^2\theta\right)^{-\frac{1}{2}} \qquad 5\text{-}3$$

where θ is the angle between the magnetic field and the c-axis, $J_c(90°)$ is the critical current density of the sample with the magnetic field in the *a-b* plane and γ is the anisotropy of the critical current density in the anisotropic Ginzburg-Landau theory.

Figure 5.17 shows the angle dependence of the critical current density of the YBCO/Gd2411 (YG2) film, at 77 K and in an applied field of 1 T, in a maximum Lorentz force configuration (transport current perpendicular to the magnetic field throughout the sample rotation in field). The measurements were taken on a microbridge patterned into the thin film as described in chapter 3. The full line represents the fit with Eq. 5.3 for the experimental data far from the perpendicular configuration (to minimize the effect of *c*-axis correlated pinning centres) and not too close to the parallel configuration (to eliminate the intrinsic pinning provided by the *a-b* planes). In these circumstances, the best (one parameter) fit was obtained for the anisotropy factor γ = 1.52, which is very small in comparison with the usual 5-7 in pure YBCO films. As demonstrated by Gutierrez et al. [158], this is a clear indication of strong, isotropic pinning centres. On the other hand, the difference between the experimental data and the theory at angles close to perpendicular field is due to the existence of some *c*-axis correlated pinning centres.

Figure 5.18 shows the field dependence of the critical current in the bridge for the two extreme configurations, perpendicular and parallel. It can be clearly seen that, for fields in the *a-b* plane, the decrease in J_c with increasing field is quite small, unlike the perpendicular configuration. This dependence is another indication of strong, isotropic pinning centres, with very few *c*-axis correlated pinning centres to support J_c in the perpendicular configuration.

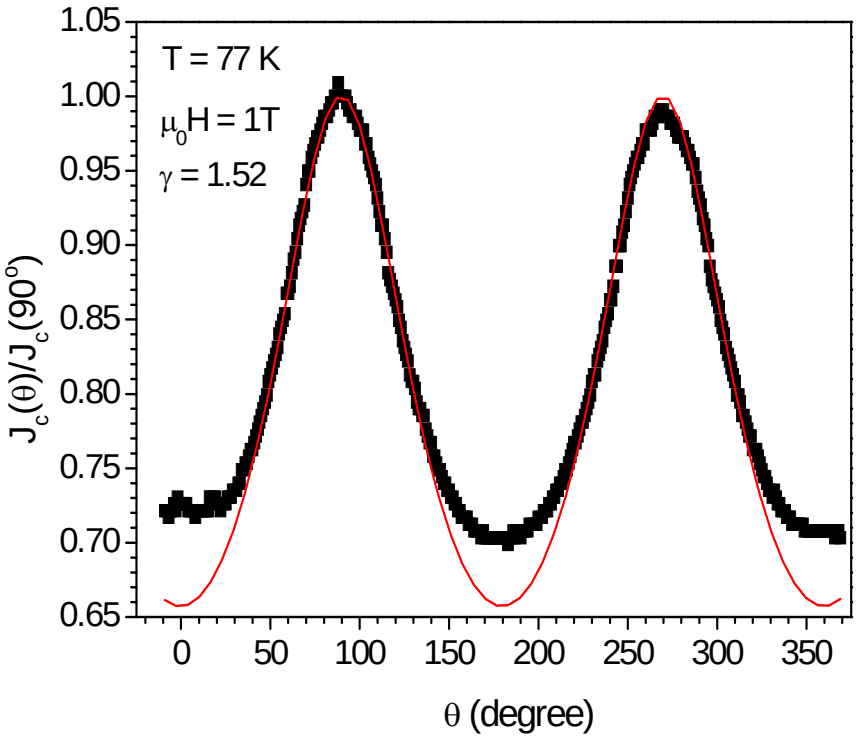

Figure 5.17. Angle dependence of the normalized critical current density at 1T and 77 K of the YG2 film. Solid line is the fit with Eq. 5.3

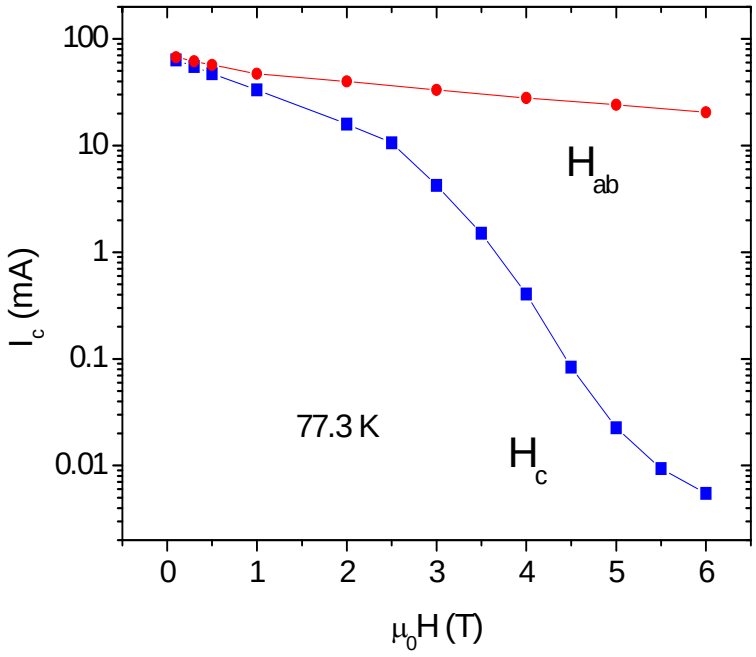

Figure 5.18. Field dependence of the critical current in the YBCO/Gd2411 (YG2) bridge for fields oriented along the *a*-*b* plane (circles) and along *c*-axis (squares). Solid lines are drawn for eye guidance

5.3 Microstructure analysis

5.3.1 XRD analysis

Figure 5.19 shows the XRD patterns of films with different thicknesses ranging from 0.78 to 2.65 μm. It can be seen that only the *(00l)* lines of YBCO are present in the diffraction pattern, which indicates the high crystalline quality of the film. None of *a*-axis orientation growth or polycrystalline peaks were found. For the high quality epitaxial films, the diffraction pattern mainly show Y123 (003), (005) and (006) peaks at 22.92°, 38.55° and 46.75° (2-theta). The thin films with thickness of 0.78 μm (YG1) and 0.96 μm (YG2), show strong intensities at 22.92° (003) and 38.55° (005). However in the thickest film of 2.65 μm (YG6), weaker peaks at 22.92° and 38.55° were observed, as can be seen in Figure 5.19(f).

Indeed there is no evidence to indicate the presence of Gd2411W since the amount of Gd2411W phases is very small, unlike the case in which XRD indicated the presence of Y2411Nb phase in a composite film with a much larger amount (15 mol%) of secondary phase[201]. In this case the XRD pattern of the resulting film measured using a three-circle system with a two-dimensional (2D) detector clearly indicates the presence of the (220) line (which is the most intense) of the Y2411Nb phase.

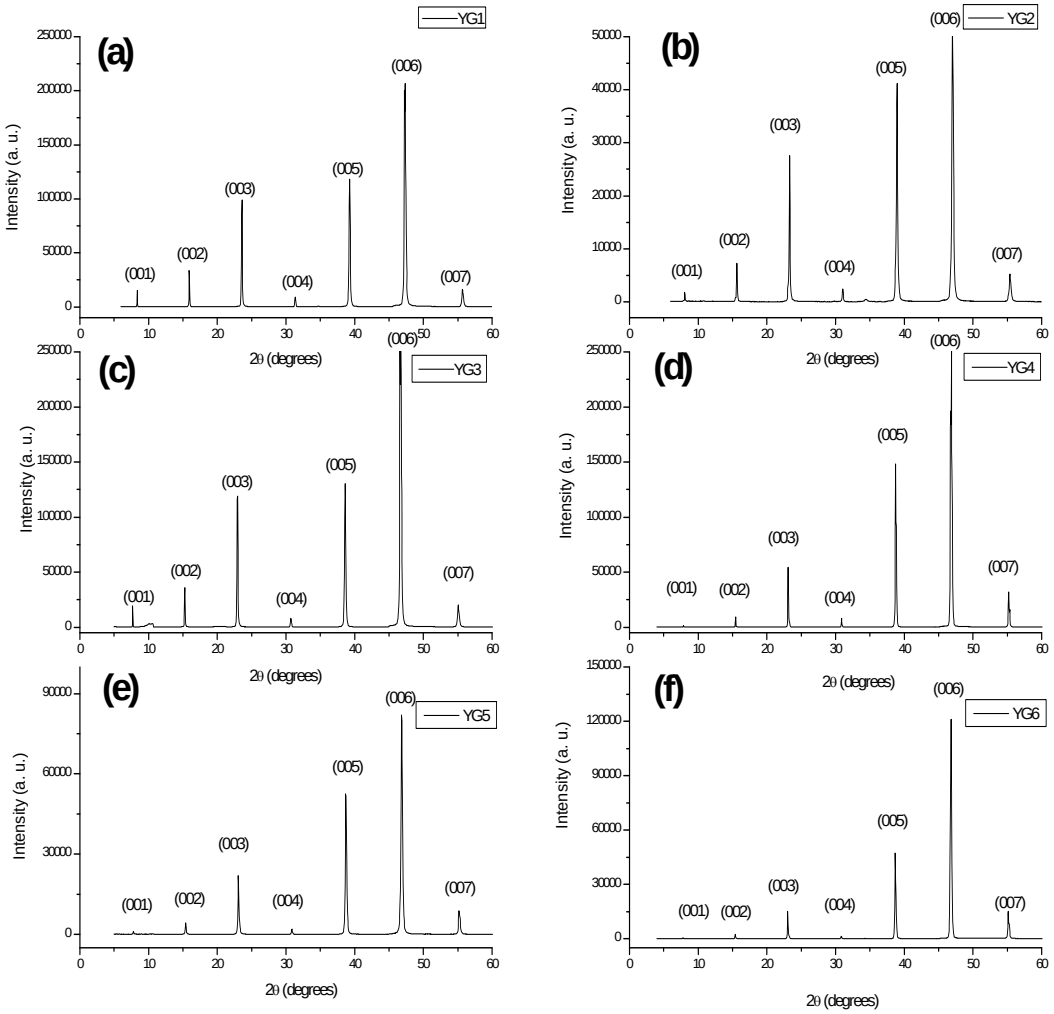

Figure 5.19. Typical XRD patterns for films of various thicknesses (YG1 = 0.78 μm, YG2 = 0.96 μm, YG3 = 1.29 μm, YG4 = 1.60 μm, YG5 = 2.1 μm, and YG6 = 2.65 μm)

5.3.2 SEM morphologies

Figure 5.20 to Figure 5.25 shows the SEM surface morphologies of the six YG films with various thicknesses ranging from 0.78 to 2.65 μm at different magnification. The basic morphology shows a distinct island growth structure that is preserved even up to micrometre thickness. Analysis of all the SEM images shows that the surface roughness and the number of pores increase as the film thickness is increased.

The average size of submicron pores is about 200 nm for the film YG1 with 0.78 μm thickness and increases gradually to about 1000 nm for the 2.65 μm-thick film YG6. Comparison of all these submicron pores can be seen in Figure 5.26. As the film thickness increases, there is an increase in submicron pores in the growing film due to the effects such as shadowing and reduced adatom mobility. These submicron pores block the superconducting current paths, reducing J_c , and this eventually becomes severe enough that there is no continuous current path through the upper layers of the film in very thick films [95].

The SEM morphologies of the films also reveal that the average grain size becomes larger when the film thickness increases. The average grain size is only 300 nm for the 0.78-μm thick film YG1 and increases moderately to about 1300 nm for the 2.65 μm-thickYG6 film. The increase of the grain size can lead to a decrease of J_c since a smaller grain size is more beneficial for the enhancement of grain boundary pinning. These results are in agreement with the report of Wang et al. which proposed that the poor grain connectivity and the large grain size that occurs with the increase of film thickness are responsible for the decrease of J_c with increasing thickness [200].

Another important factor that is believed to be directly related to the high J_c observed in the thinnest films is the smooth surface features of the films, which may further indicate a good connectivity and thermal conductivity between the grains of the film.

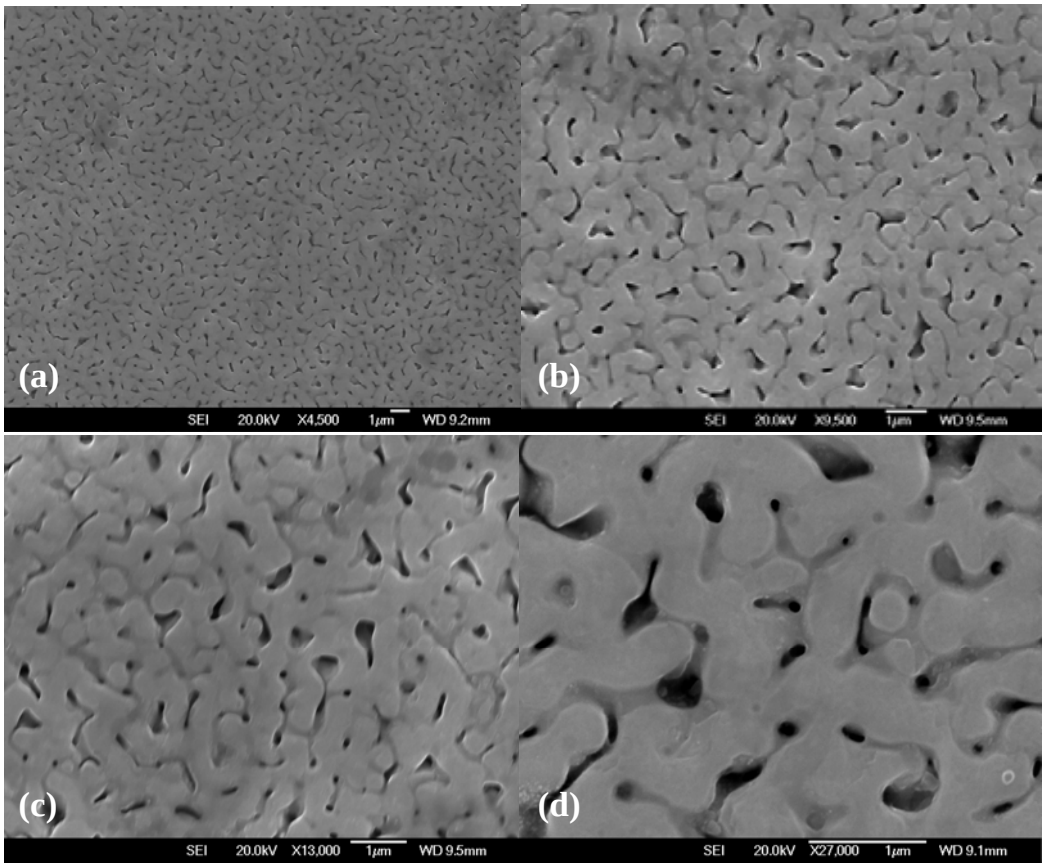

Figure 5.20. SEM images of YG1 with 0.78 μm thick film, taken at magnifications (a) 4500x, (b) 9500x, (c) 13 000x and (d) 27 000x

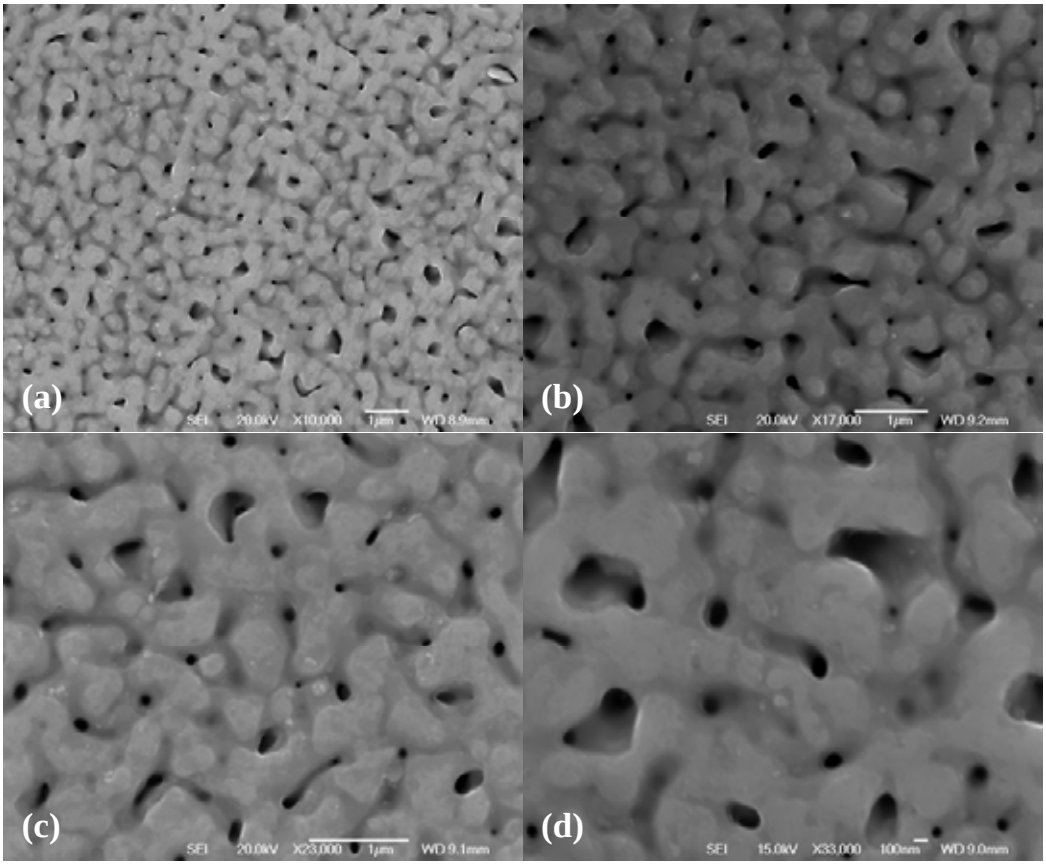

Figure 5.21. SEM images of YG2 with 0.96 μm thick film, taken at magnifications (a) 10 000x, (b) 17 000x, (c) 23 000x and (d) 33 000x

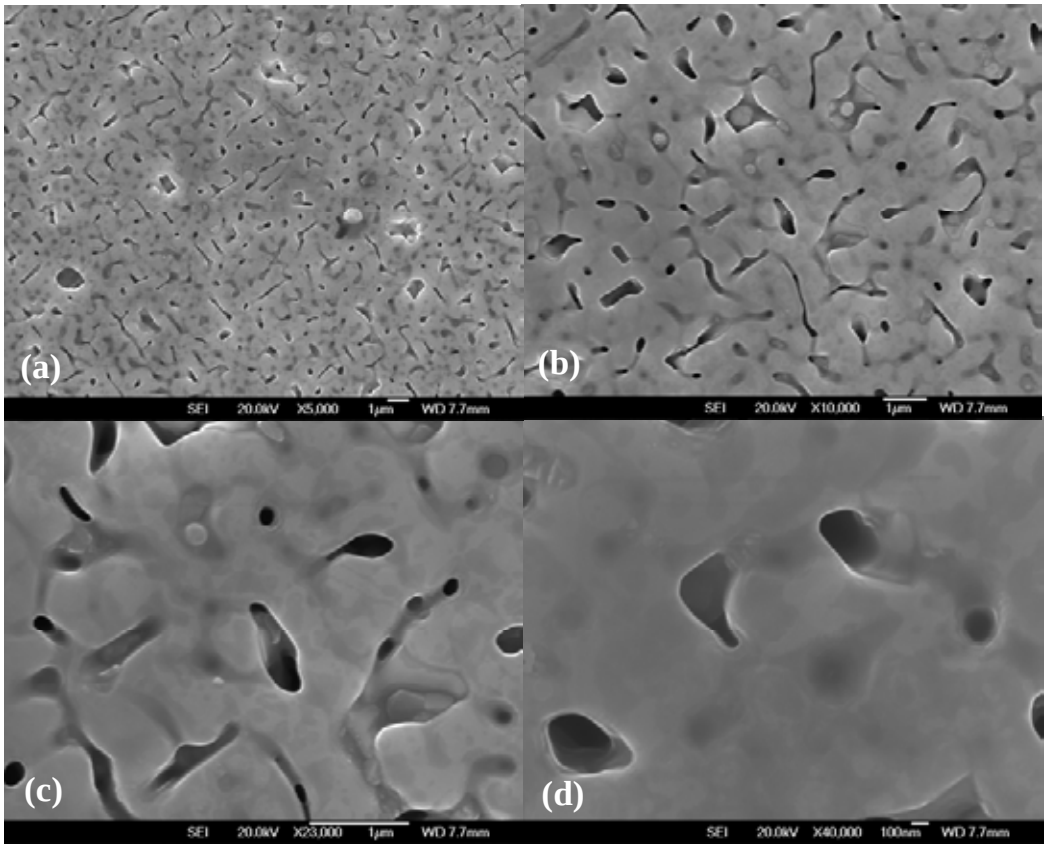

Figure 5.22. SEM images of YG3 with 1.29 μm thick film, taken at magnifications (a) 5000x, (b) 10 000x, (c) 23 000x and (d) 40 000x

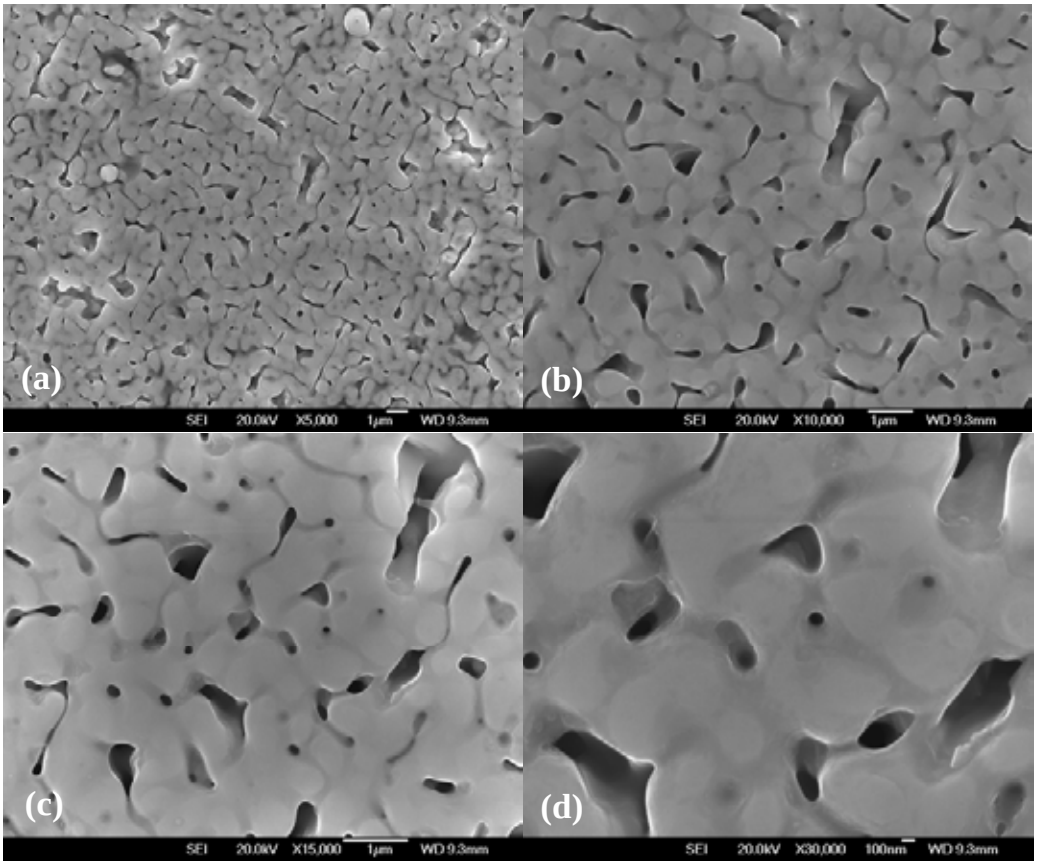

Figure 5.23. SEM images of YG4 with 1.6 μm thick film, taken at magnifications (a) 5000x, (b) 10 000x, (c) 15 000x and (d) 30 000x

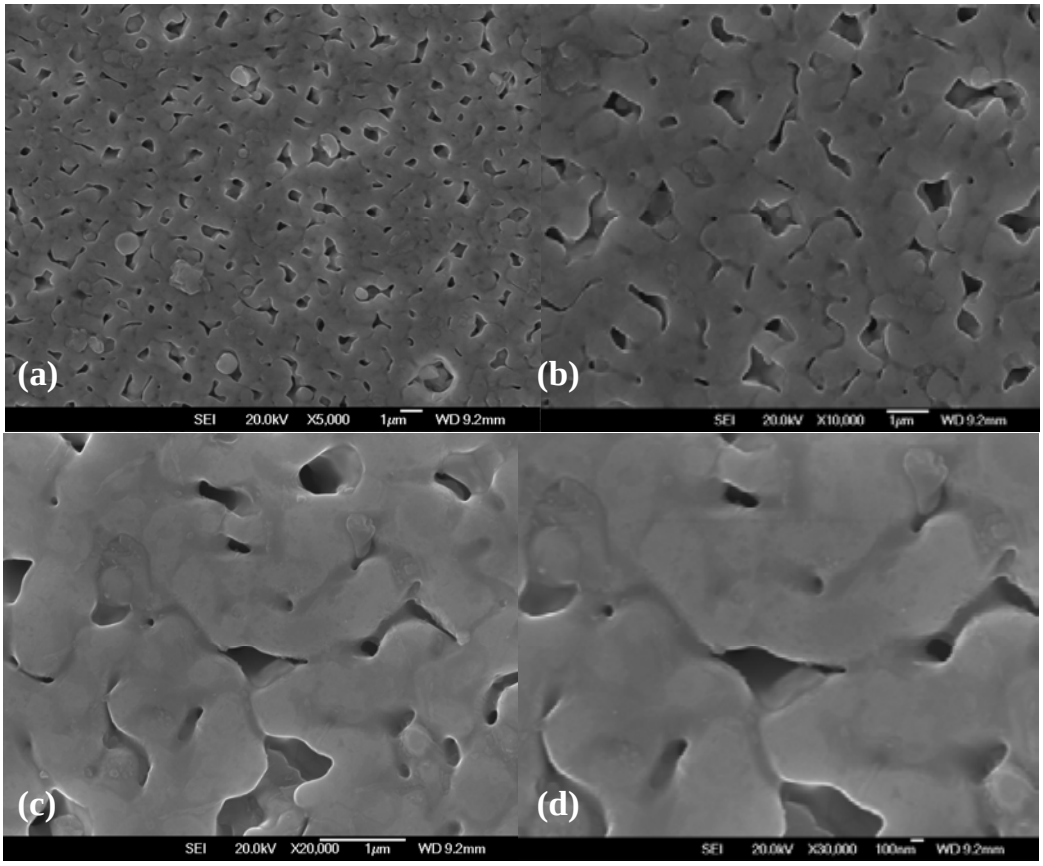

Figure 5.24. SEM images of YG5 with 2.1 μm thick film, taken at magnifications (a) 5000x, (b) 10 000x, (c) 20 000x and (d) 30 000x

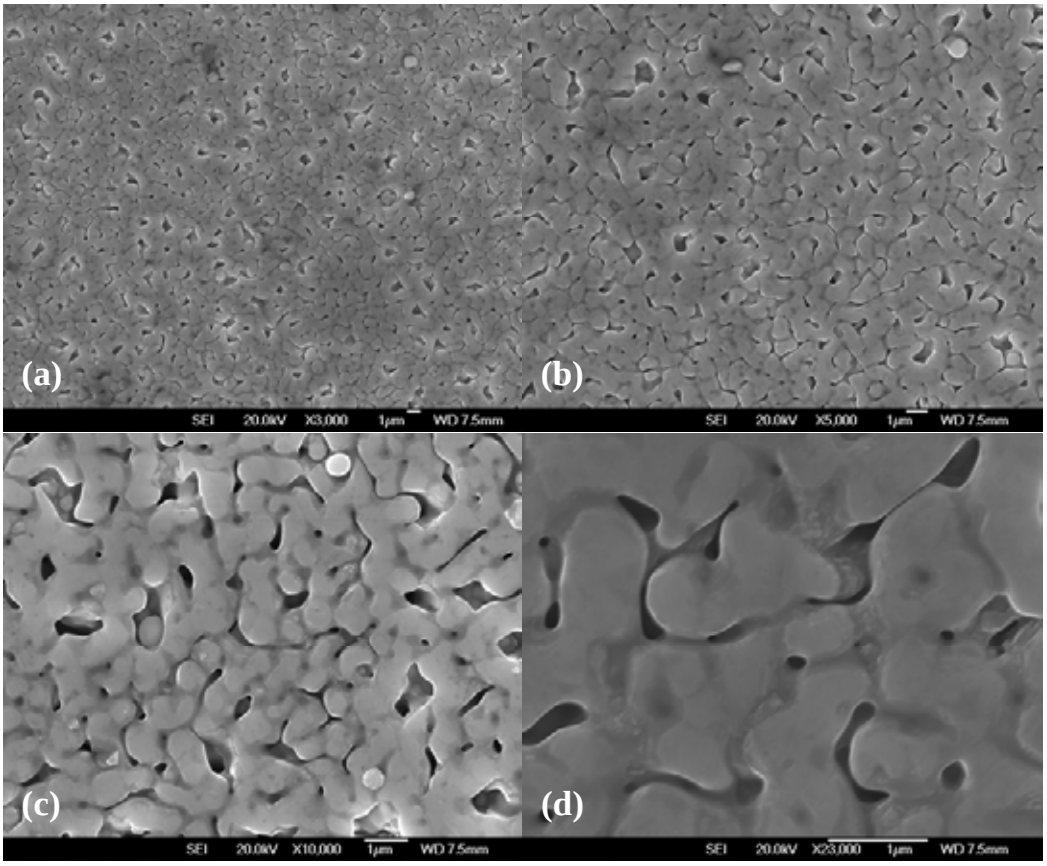

Figure 5.25. SEM images of YG6 with 2.65 μm thick film, taken at magnifications (a) 3000x, (b) 5000x, (c) 10 000x and (d) 23 000x

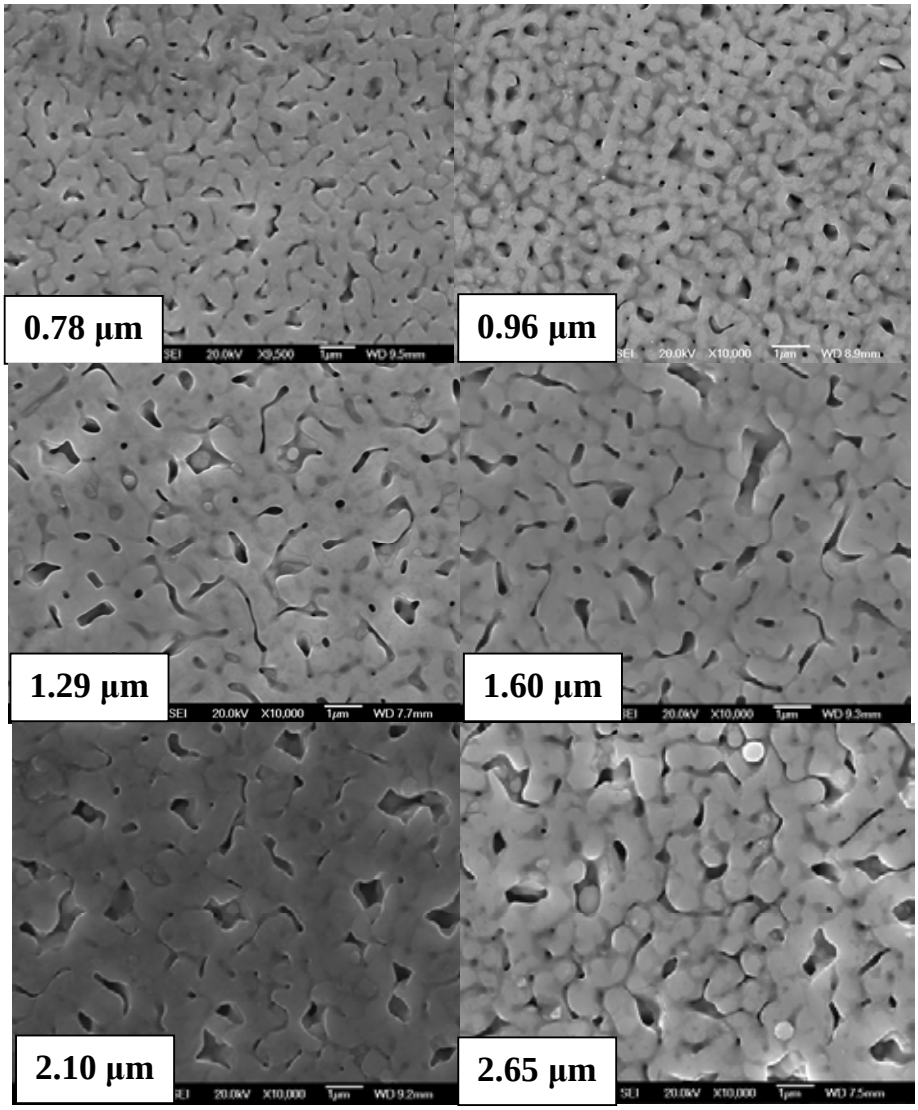

Figure 5.26. SEM images of YG films at various thicknesses, taken at 10 000x magnification.

5.3.3 EDS Analysis

Figure 5.27 shows an SEM image of the surface morphology of the YG2 film. In addition to the presence of submicron pores, closer inspection reveals nanosized particles of the 2411W phase (slightly brighter-in-contrast dots in the higher magnification micrograph) within the well-defined YBCO grains. The size of the observed 2411W phase nano-inclusions ranges between 30 and 100 nm (although smaller inclusions might also be present that are undetectable within the resolution of the SEM). The squares in the SEM image in Figure 5.27 indicate the presence of such nano-inclusions.

To further investigate the nature and distribution of the observed nano-inclusions EDS analysis has been performed on the YG2 film on various areas. On a smaller scale (e.g., the dotted small squares in the SEM image of Figure 5.27) centred around nanoscale inclusions, as small as 0.01 μm^2, the concentration of W is always higher, between 2.5 and 4 at .%, indicating that W is indeed located within the brighter nano-inclusions. On a larger scale of several μm^2, as seen in Figure 5.28, the resulting chemical composition for W is always around 1 at.%, very close to the nominal value, as shown in Table 5.3. Surprisingly, on both small and larger scales, compositional analysis shows a Gd concentration of several times smaller than the nominal value.

This can be explained by the substitutions of Gd by Y in the 2411W phase during the film growth (and by a large amount of Gd atoms entering the Y sites in the YBCO). However, given the ratio Gd/Y of only 1 at.%, it is expected that less then 1% of the YBCO unit cells becomes Gd-123, so the mean distance between nearest neighbours in the very diluted Gd lattice is too high for the EDS resolution. In the case of W, their presence could be detected because the W atoms ‘stick together’ in the 2411W nano-inclusions.

One can argue that the brighter nano-inclusions might not be the 2411W phase, but simply agglomerations of metallic W that segregates during the film growth. However, if this were the case, one also would expect a much higher concentrations of W in the small regions centred around such nano-inclusions. Moreover, as was demonstrated by the XRD patterns in [201], the 2411 phase exists as nano-inclusions in the YBCO film matrix.

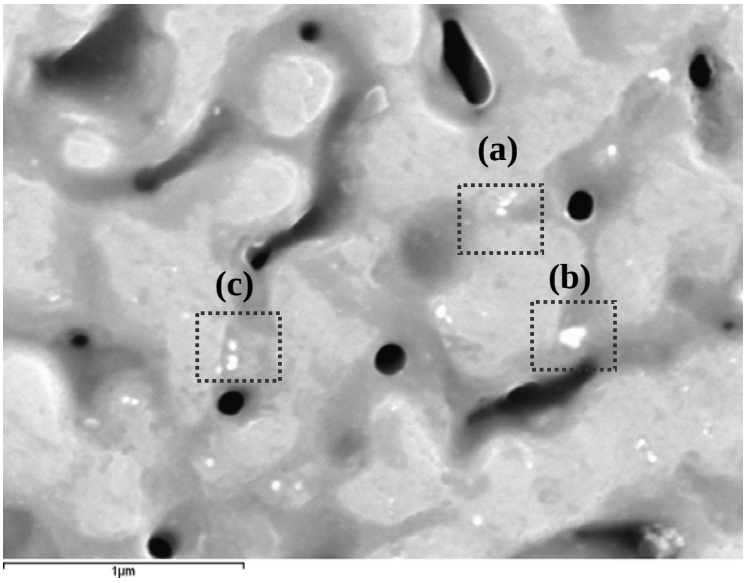

Figure 5.27. SEM image of nanosized inclusions of the 2411W (YG2) phases, indicated by (a), (b) and (c), where the the dotted squares represent small areas surrounding such nano-inclusions used for EDS analysis.

Table 5.2. Quantitative elemental analysis of YG2 film obtained by EDS analysis as seen in Figure 5.27

Element	Atomic %	Error %
O	60.85	3.0
Cu	16.06	1.6
Y	9.21	1.3
Ba	10.86	1.0
Gd	0.26	0.4
W	2.76	0.9

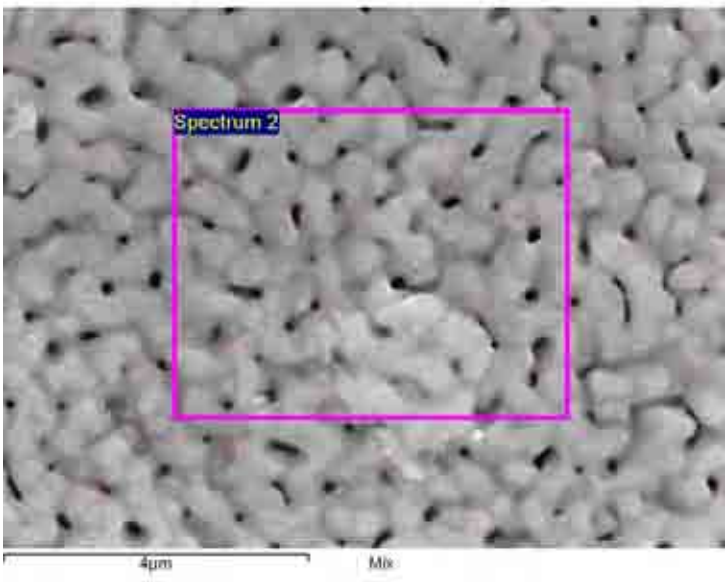

Figure 5.28. SEM-EDS spectrum position of YG2 film at a larger scale.

Table 5.3. Quantitative elemental analysis of YG2 film obtained by EDS analysis from SEM-EDS spectrum as seen in Figure 5.28.

Element	Atomic %	Error %
O	52.92	3.0
Cu	20.39	1.9
Y	9.49	1.2
Ba	15.64	1.7
Gd	0.40	0.7
W	1.15	0.9

The cross-sectional SEM/EDS analysis results revealed a few very interesting details. First of all, the submicron pores evident in Figure 5.29 do not nucleate at the STO/YBCO interface; they appear inside the film and extend towards the surface. Regarding the distribution of 2411W phase inside the film, EDS analysis performed on the W concentration on three distinctive areas (first third of the film close to the substrate in Figure 5.29, second third in the middle of the film in Figure 5.30, and the last third of the top in Figure 5.31) shows that the concentration of 2411W nano-inclusions is higher close to the STO/YBCO interface, and decreases towards the surface (W decreases from 3.7 at.% close to the interface as seen in Table 5.4 , to 2 at.% in the middle of the film, and, finally, to 1.3 at.% near the surface).

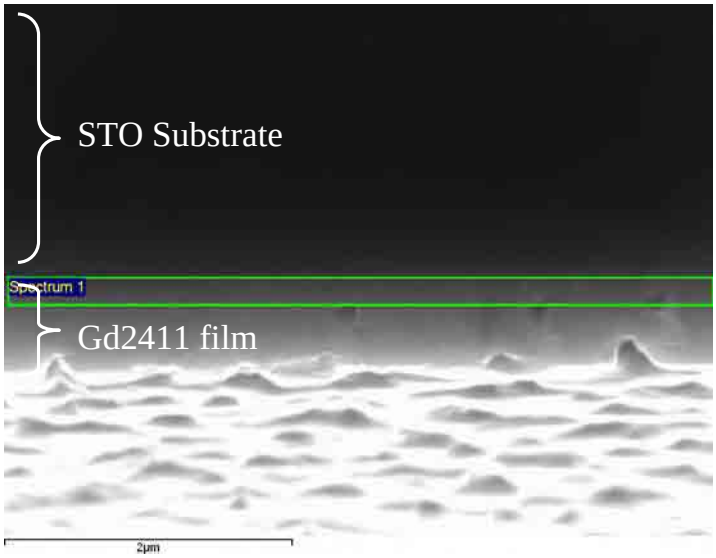

Figure 5.29. EDS analysis of the cross section of the first third of the YG2 film close to the substrate.

Table 5.4. Quantitative elemental analysis of the cross section for the first third of the YG2 film close to the substrate.

Element	Atomic %	Error %
O	63.95	3.9
Cu	14.36	1.9
Y	5.05	1.0
Ba	12.81	1.7
Gd	0.17	0.6
W	3.66	0.9

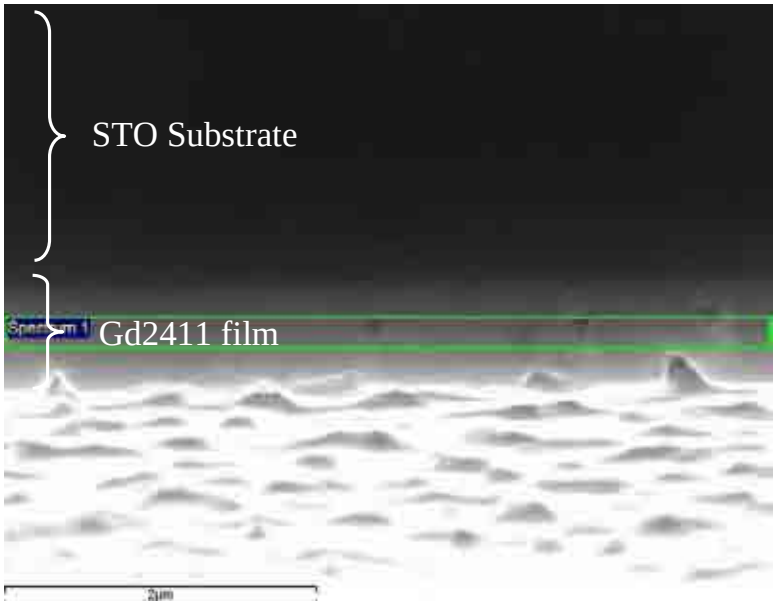

Figure 5.30. EDS analysis of the cross section of the second third of the middle YG2 film.

Table 5.5. Quantitative elemental analysis of the cross section for the second third of the middle YG2 film.

Element	Atomic %	Error %
O	65.06	2.9
Cu	15.00	1.7
Y	6.11	0.8
Ba	11.72	1.3
Gd	0.10	0.8
W	2.01	0.9

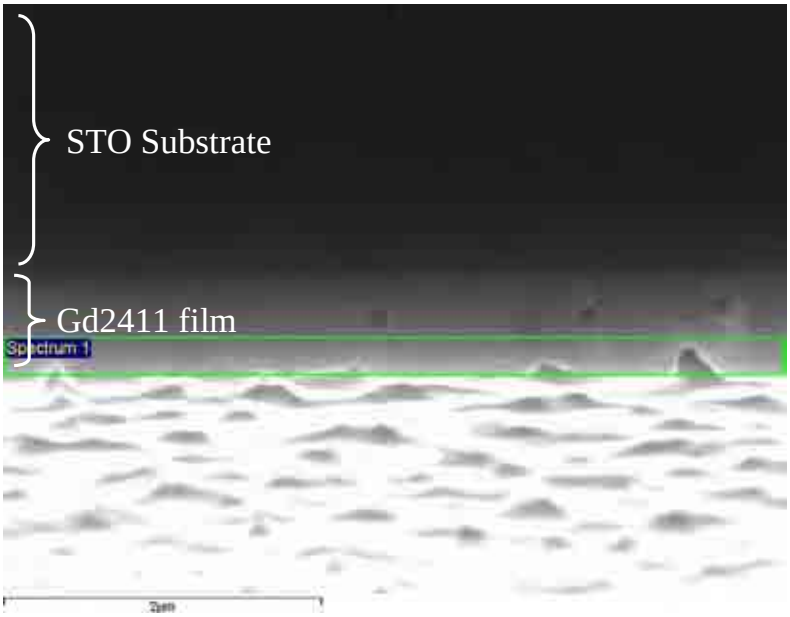

Figure 5.31. EDS analysis of the cross section of the last third of the YG2 film.

Table 5.6. Quantitative elemental analysis of the cross section for of the last third of the YG2 film

Element	Atomic %	Error %
O	67.77	3.5
Cu	14.00	1.7
Y	6.46	1.1
Ba	10.22	1.5
Gd	0.16	0.9
W	1.39	0.8

Figure 5.32 and Figure 5.33 show AFM images of the YBCO/Gd2411 films with different magnifications. Nanosized 2411W inclusions on the surface of the YG1 and YG2 films, which are apparent in SEM images, can also be observed in the AFM images. Similar features are not present in the pure YBCO (Y1) film as shown previously in Figure 4.3.

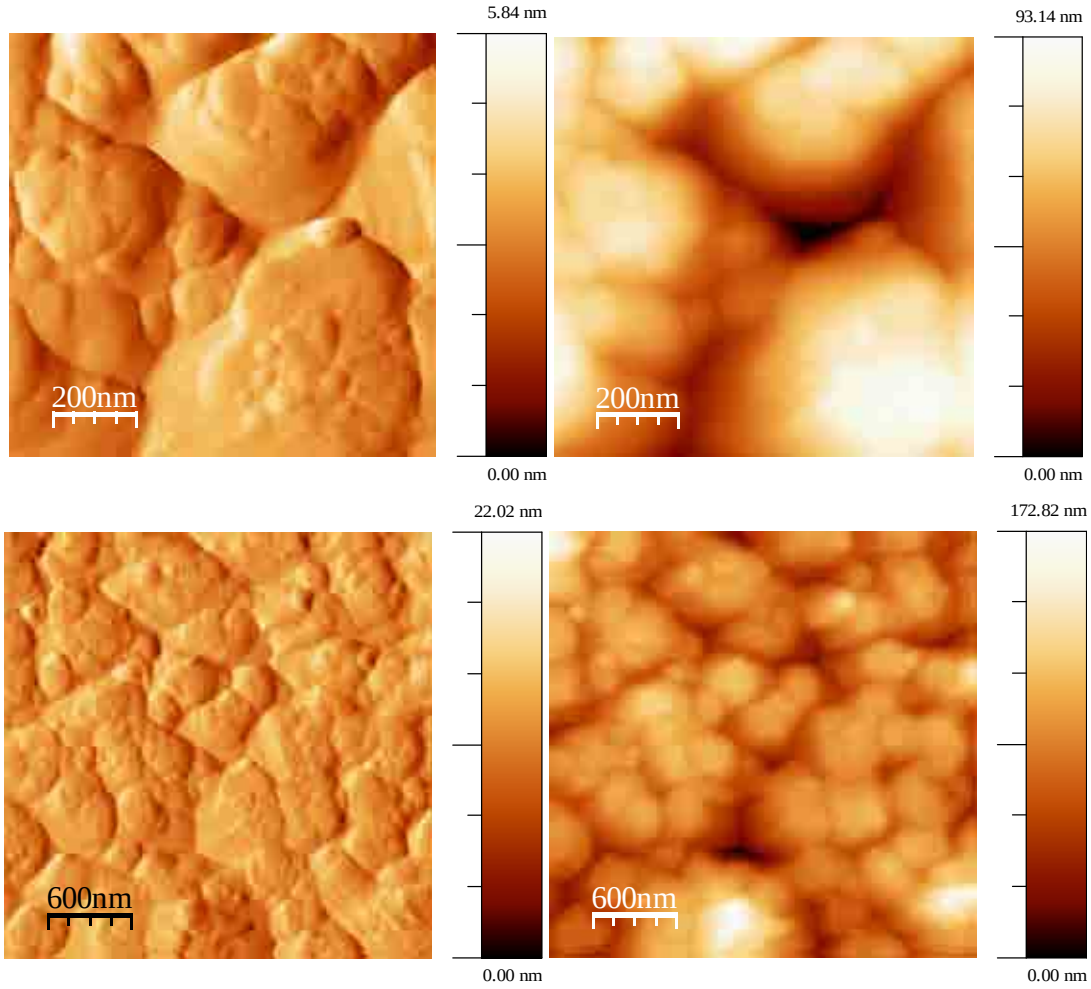

Figure 5.32. AFM images of YG1 with 0.78 μm thick film at different scale.

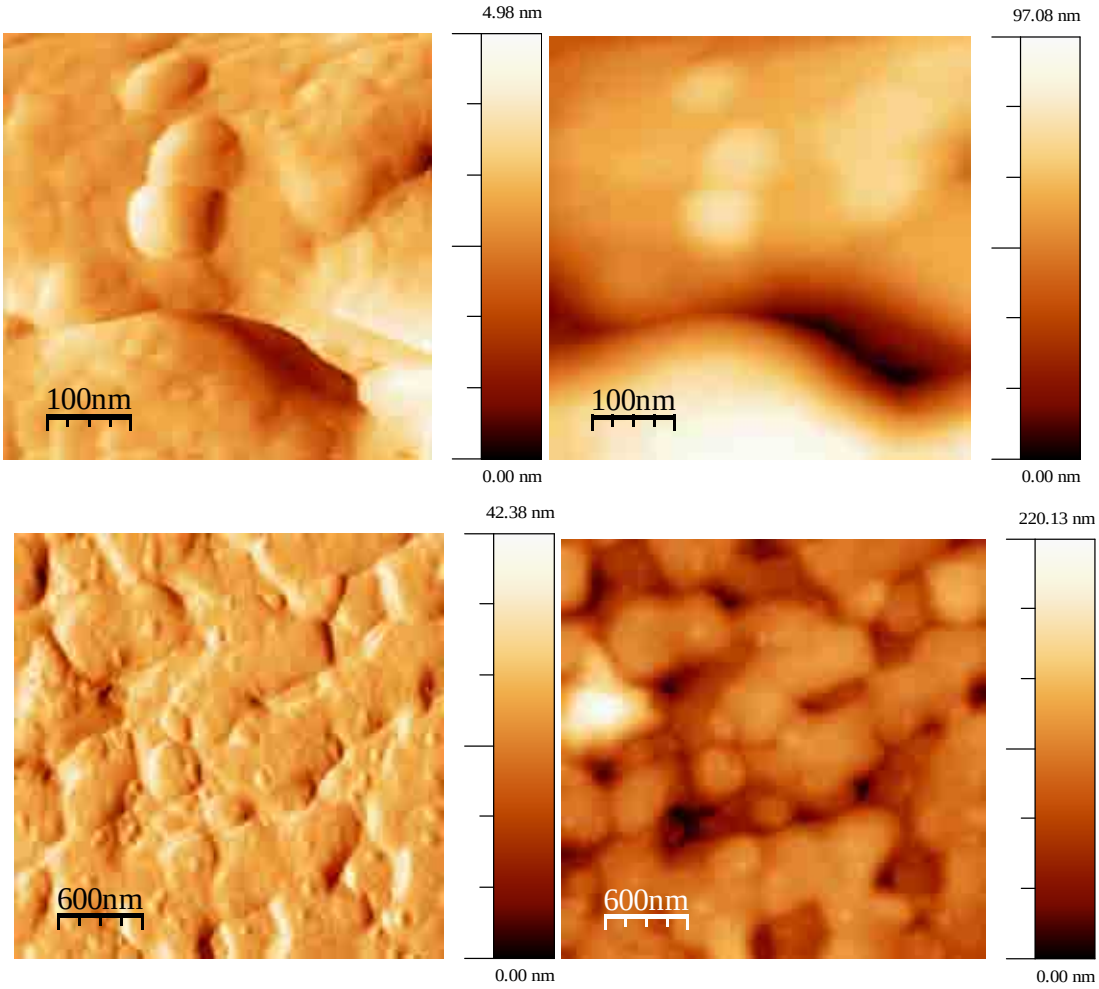

Figure 5.33. AFM images of YG2 with 0.96 μm thick film at different scale.

5.4 Summary

In summary, the $YBa_2Cu_3O_{7-x}$ / $Gd_2Ba_4CuWO_{12}$ films grown on STO single crystal substrates revealed an enhancement in the critical current density at temperatures exceeding 50 K compared to pure YBCO films. This enhancement of J_c in high fields is due to the artificial pinning centres induced by the $Gd_2Ba_4CuWO_{12}$ nano-inclusions. However, as the film thickness increases above 1 μm, a significant reduction of J_c was observed in all Gd2411 films which become even lower than the J_c of the 0.96 μm-thick pure YBCO film.

The position of the peak in pinning force F_p dependence on the reduced field is at b = 0.2 for the thinner film (0.78 μm and 0.96 μm), meaning that the normal surface pinning centre is dominant. This is also supported by the larger value of the scaling parameter A_1 as compared with A_2. The results of pinning force scaling in the Dew-Hughes model for the thicker films (1.29 μm to 2.65 μm) show that $\Delta\kappa$ point pinning is the dominant pinning mechanism. In this case, the source of $\Delta\kappa$ point pinning could be from the small-scale variations n of T_c. Several researchers found evidence for δT_c or $\Delta\kappa$ point pinning mechanism in Pr-doped YBCO and $(K,Ba)BiO_3$ single crystal film [198]. Several possible explanations for this behaviour have been proposed: a minority secondary superconducting phase with a slightly lower critical temperature appears to form during the PLD growth process and is due probably to the substitution of compatible atoms between YBCO and 2411W, (Gd with Y, as suggested also from EDS analysis). This phase may provide some additional pinning centres of δT_c-type, in addition to those associated with the Gd2411W nano-inclusions.

Angle-dependent transport measurements revealed a very small value of anisotropy of about 1.5 at 77.3 K and 1 T,, indicating that Gd2411 nano-inclusions induced strong, mainly isotropic pinning centres.

Chapter 6

Fabrication and characterisation of $YBa_2Cu_3O_{7-x}$ films with $BaZrO_3$ nanoinclusions

6.1 Introduction

The introduction of nano-inclusions $Gd_2Ba_4CuWO_{12}$ for artificial pinning centers presented in the previous chapter has positive effects in enhancing the J_c and flux pinning force, $F_{p.}$ $BaZrO_3$ (BZO) is the first and most common compound used as an impurity addition to $YBa_2Cu_3O_{7-x}$ targets [36] and has been shown [79] to be able to self-organize into correlated nanorods within the film microstructure. Using targets with nanometer-sized grains prepared by a citrate-gel method it was shown that critical current densities in high magnetic field are greatly improved in YBCO thin films, with and without BZO addition (although J_c is further increased by BZO addition), as compared with thin films ablated from microcrystalline (standard) targets [203, 204]. Similar to the case of microcrystalline targets [79], in thin films ablated from BZO-doped nanocrystalline targets,

BZO forms nanorods, usually surrounded by several dislocations [205], both acting as strong *c*-axis correlated pinning centres that lead to a much smaller value of the anisotropy of critical current density, as proven by the angle-dependent transport measurements [206].

In this chapter the critical temperature, critical current densities, pinning force and pinning potential in YBCO films ablated by PLD from a nanocrystalline target doped with 2 wt% BZO and 4 wt% BZO are shown, and the results were compared with those obtained in the case of a pure YBCO film grown from a commercial microcrystalline YBCO target. The growth was carried out under optimum conditions as mentioned in chapter 5. All films were fabricated with variable thickness ranging from 1.29 to 3.45 μm for 2 wt% BZO and from 1.2 to 2.5 μm for 4 wt% BZO.

6.2 Superconducting properties of $YBa_2Cu_3O_{7-x}$ / 2 wt% $BaZrO_3$ films

6.2.1 Transition temperature, T_c

T_c values of all the $YBa_2Cu_3O_{7-x}$ / 2 wt% $BaZrO_3$ films are slightly depressed from the reference YBCO (Y1) film as shown in Figure 6.1. The T_c was observed to be increased in a fairly linear relationship with increasing film thickness from 1.59 to 2.51 μm. The highest T_c , 89.6 K ± 0.2 K, from all the BZO doped films was found on a film with 2.51 μm thickness. However, the T_c was lowered to 88.3 K ± 0.2 K for the thickest film with 3.45 μm. The T_c values shown in Figure 6.2 were determined from the experimental curves where diamagnetic signal starts to occur and the width, ΔT_c, of the superconducting transition is given by $\Delta T_c = T_c$ onset - T_c offset. The transition width (ΔT_c) between ~ 0.5 and 1.3 K is almost the same in all BZO doped films.

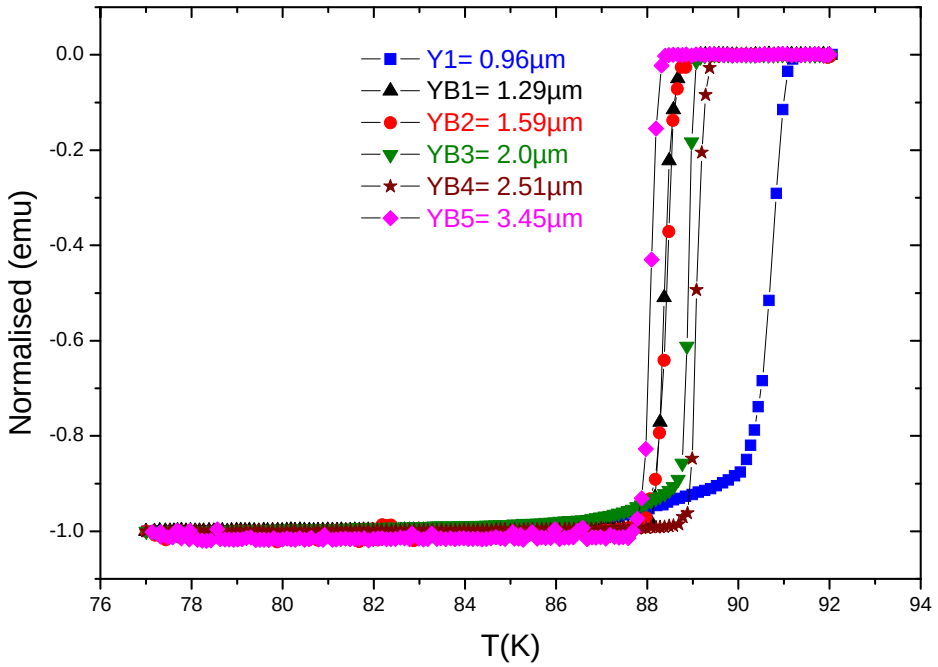

Figure 6.1. Normalised *M* as a function of temperature for $YBa_2Cu_3O_{7-x}$ / 2 wt% $BaZrO_3$ films with various thicknesses. Y1 is a pure YBCO film for reference. Solid lines are drawn for eye guidance.

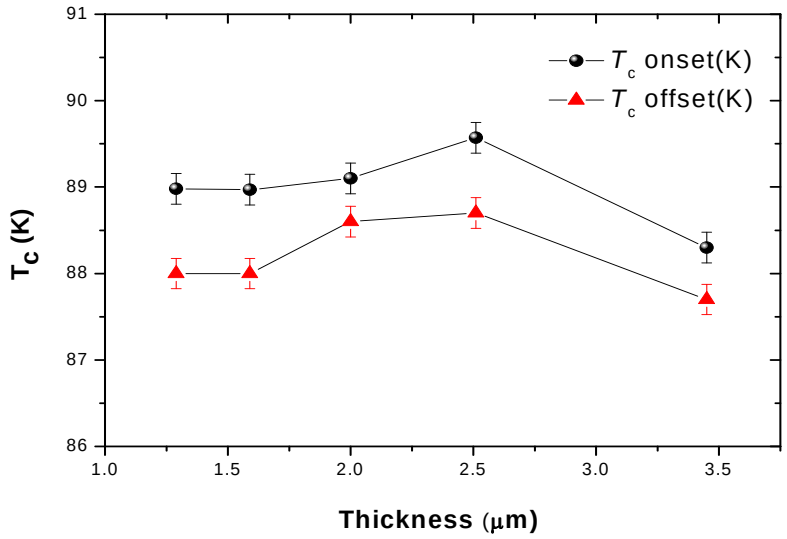

Figure 6.2. Dependence of critical temperature T_c onset and T_c offset on thicknesses of the films

6.2.2 Critical current densities, J_c

The magnetic field dependence of J_c at 65 K for all BZO doped films with thickness of 1.29, 1.59, 2.04, 2.51 and 3.45 μm is shown in Figure 6.3. As expected, self-field J_c is higher in the thinnest film of 1.29 μm thick with 4.24×10^6 Acm^{-2}. No significant changes in self-fied J_c was found for films with other thicknesses (1.59 to 3.45 μm). The attempts to grow even thicker films resulted in a drop in J_c. The difference in the J_c in all BZO doped films becomes smaller under high magnetic fields > 2 T. On the other hand, J_c at 4 T for thickness 1.59 to 3.45 μm does not exhibit much difference as shown in Table 6.1.

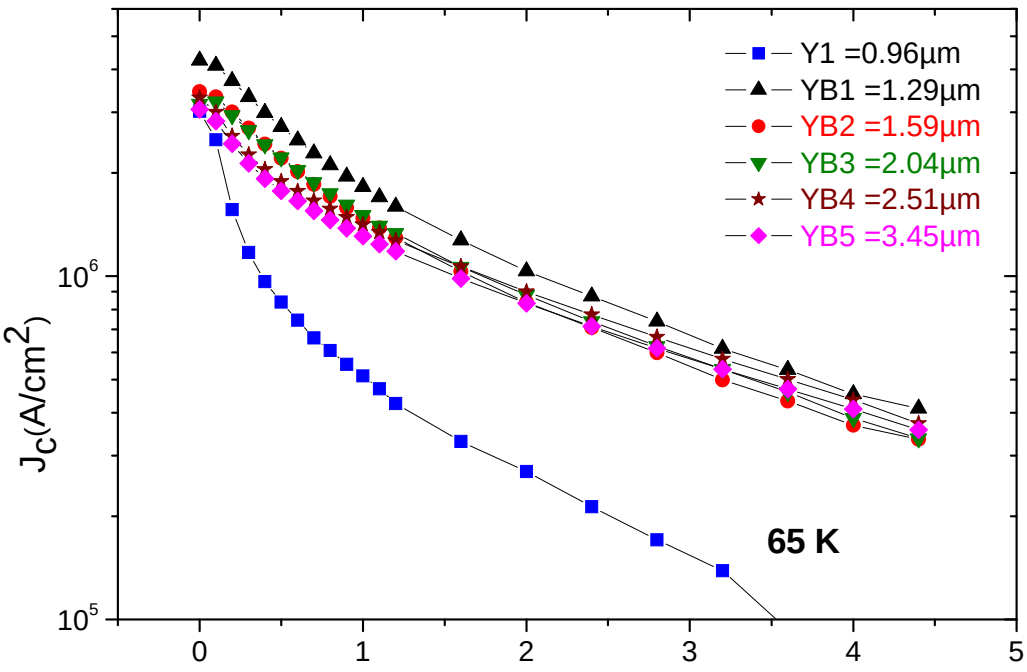

Figure 6.3. Magnetic field dependence of critical current densities of $YBa_2Cu_3O_{7-x}$ / 2 wt% $BaZrO_3$ films with thickness of 1.29 , 1.59 , 2.04 , 2.51 and 3.45 μm at 65 K. Y1 is a pure YBCO film for reference. Solid lines are drawn for eye guidance.

Table 6.1. Summary of $YBa_2Cu_3O_{7-x}$ / 2 wt% $BaZrO_3$ films with various thicknesses in magnetic field of 1 T and 4 T at 65 K.

Film Thickness	J_c at (65 K, 1 T)	J_c at (65 K, 4 T)
YBCO(Y1)		
0.96 μm	5.1×10^5 Acm^{-2}	7.7×10^4 Acm^{-2}
YBCO/BZO		
1.29 μm	1.8×10^6 Acm^{-2}	4.5×10^5 Acm^{-2}
1.59μm	1.5×10^6 Acm^{-2}	3.7×10^5 Acm^{-2}
2.0 μm	1.5×10^6 Acm^{-2}	3.9×10^5 Acm^{-2}
2.51μm	1.4×10^6 Acm^{-2}	4.3×10^5 Acm^{-2}
3.45 μm	1.3×10^6 Acm^{-2}	4.1×10^5 Acm^{-2}

The J_c at 77 K as a function of magnetic field of $YBa_2Cu_3O_{7-x}$ / 2 wt% $BaZrO_3$ films with different thicknesses compared with 0.96 μm-thick YBCO (Y1) is shown in Figure 6.4. The difference in the J_c between YB1 (1.29 μm) and pure YBCO (Y1) film becomes more pronounced with an increase in the applied magnetic field. There is no significant degradation of self-field J_c (Figure 6.5) in $YBa_2Cu_3O_{7-x}$ / 2 wt% $BaZrO_3$ films when the thickness is increased from 1.29 to 3.45 μm. The 1.59 μm-thick film has a J_c that is more than three times higher over a range of fields in comparison with the reference sample. In addition, the 3.45 μm YB5 film ($J_c > 1.3\times10^5$ Acm^{-2}) shows more than ten times increase

in J_c at 1.6 T compared to the J_c of a 0.96 μm thick YBCO film (J_c =1.1×10^4 Acm^{-2}). The results also show that the thicker films can maintain their J_c very well especially at higher fields up to 3.6 T. The J_c at 3.6 T of the 3.45 μm thick film is almost the same as the 2.51 μm thick film indicating that there is no loss of J_c with thickness when measured at this field.The improvement of the in-field J_c is seen for the BZO doped films, probably caused by the self-assembled stacks of BZO nanodots oriented on average parallel to the *c*-axis of the film [207].

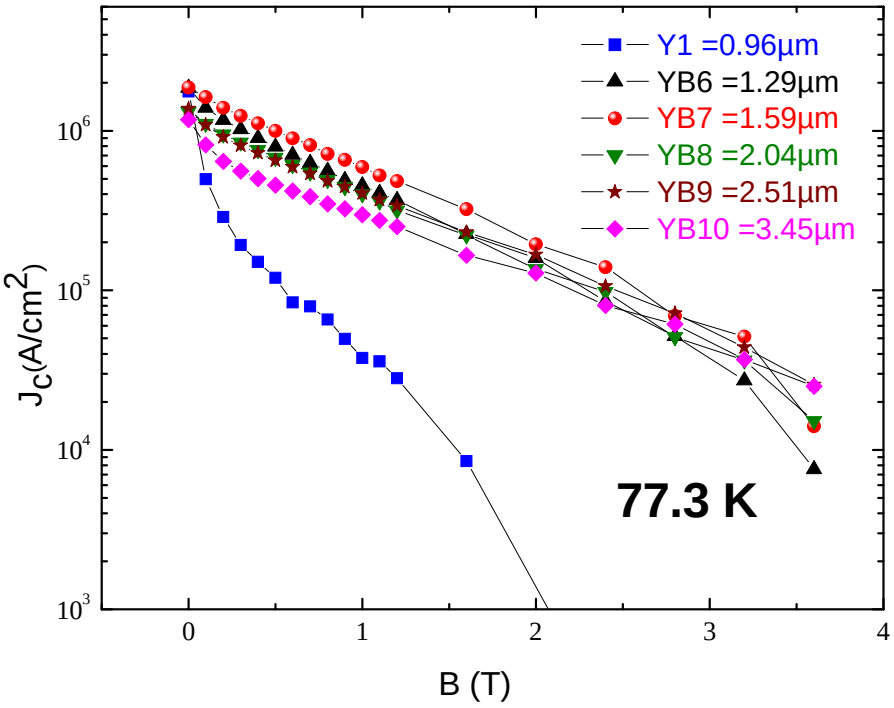

Figure 6.4. Magnetic field dependence of critical current densities of $YBa_2Cu_3O_{7-x}$ / 2 wt% $BaZrO_3$ films with thickness of 1.29 , 1.69 , 2.04 , 2.51 and 3.45 μm at 77.3 K. Y1 is a pure YBCO film for reference. Solid lines are drawn for eye guidance.

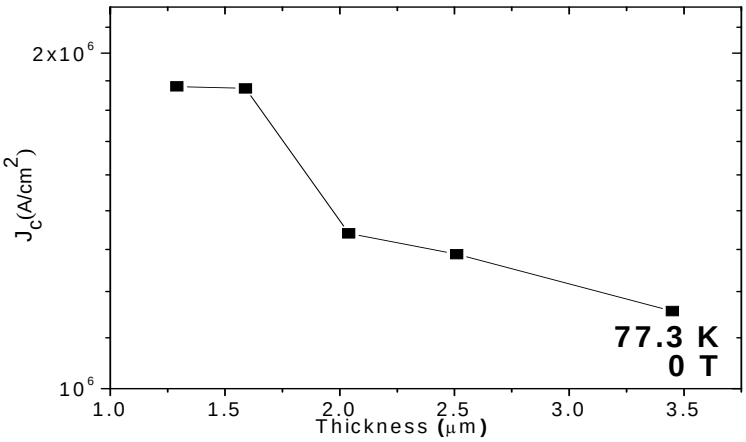

Figure 6.5. Thickness dependence of critical current densities of films at 77.3 K, self field. Solid lines are drawn for eye guidance

6.2.3 Critical current, I_c

In order to investigate the capability of critical current of the 2 wt% BZO doped films with increasing film thickness, the field dependence of critical current per cm width I_c at 77.3 K was analysed as can been seen in Figure 6.6. I_c values in all BZO doped films of different thickness are much higher than the Y1 of YBCO film, and the general trend shows an increase of I_c with increasing thickness over a wide range of magnetic field.

Figure 6.7 shows the I_c per cm width for 2% BZO doped films as a function of thicknesses in self-field and 77.3 K. As expected, it was found that with increasing film thickness from 1.29 to 3.45 μm, I_c increases from about 200 A to 400 A, with a small discontinuity due to sample properties scattering (possibly due to the inhomogeneity of the superconducting phase, inhomogeneous distribution of the nanoparticles and inhomogeneous density of defect distribution). The improvement of I_c with the increasing

film thickness was also previously reported by Kang et al. [207], who found that by increasing the YBCO+CeO_2 film thickness up to 4.3 μm thick, I_c reaches 300 A/cm width.

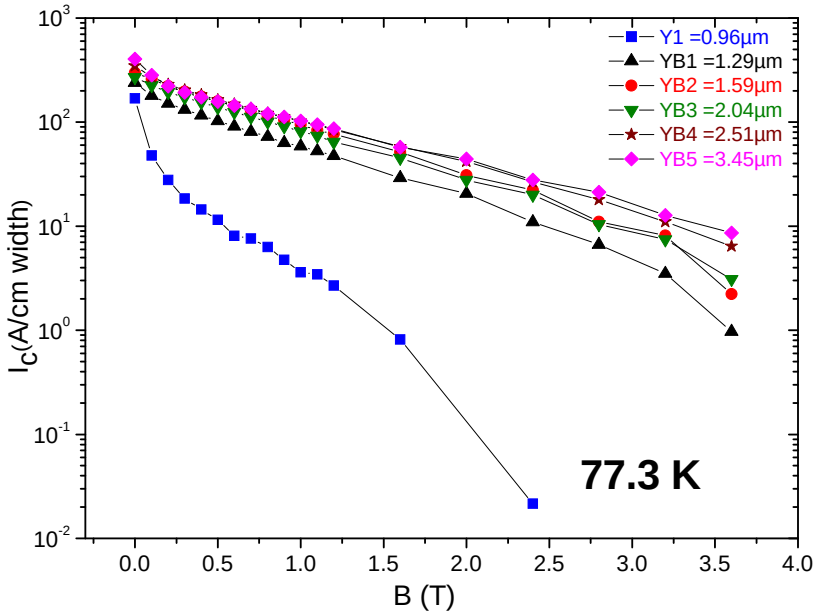

Figure 6.6. Magnetic field dependence of critical current of films with thickness of 1.29 to 3.45 μm at 77.3 K. Solid lines are drawn for eye guidance.

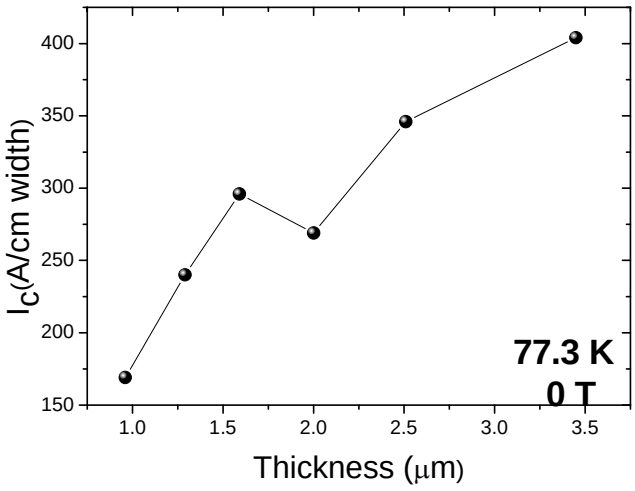

Figure 6.7. Thickness dependence of critical current (I_c) in self-field at 77.3 K.

6.2.4 Flux pinning force, F_p

The bulk flux pinning force, $F_p = J_c \times B$, for the films at various thicknesses at 65 K and 77 K are illustrated in Figure 6.8 and Figure 6.9. The figures also include data from the YBCO (Y1) film as a reference at both temperatures. A record value of F_p, max = 5.9 GN/m^3 was observed for YB2, 1.59 μm-thick film at B around 1.1 T and 77 K, that is more than four times higher than the YBCO 0.96 μm thick film. A more remarkable pinning force of F_p, max = 21 GN/m^3 is found for YB1, 1.29 μm thick film at 65 K in a wide magnetic field region (from 2 to 3.2 T), that is more than four times higher than the typical YBCO 0.96 μm thick film.

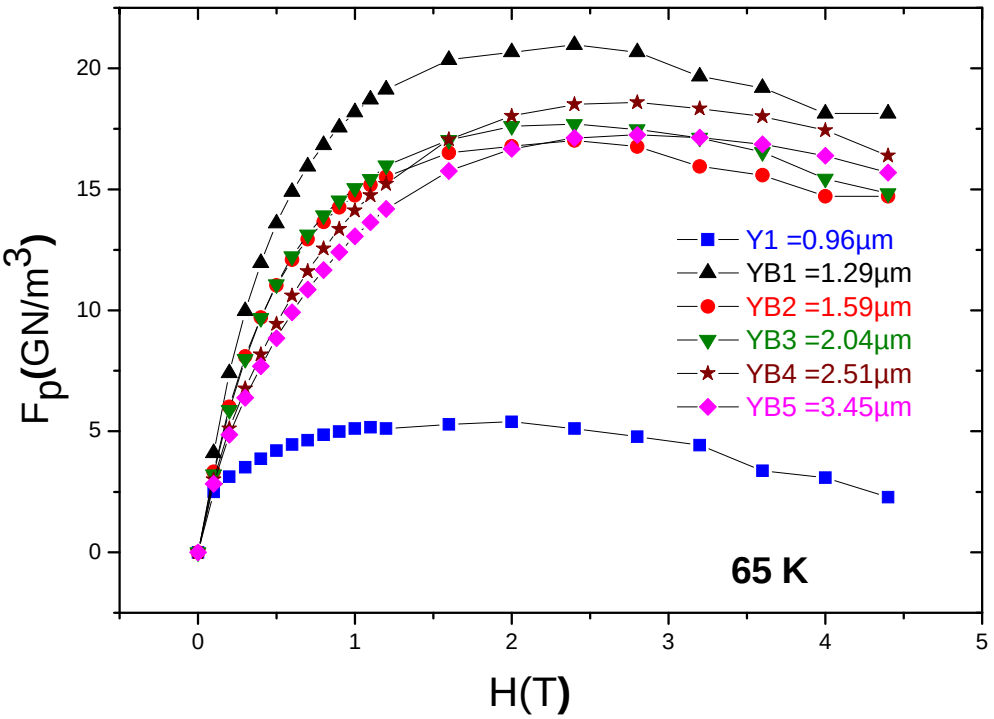

Figure 6.8. Magnetic field dependence of the pinning force F_p of $YBa_2Cu_3O_{7-x}$ / 2 wt% $BaZrO_3$ films with thickness of 1.2 , 1.61 , 2.0 , 2.2 and 2.5 μm at 65 K. Y1 is a pure YBCO film for reference. Solid lines are drawn for eye guidance.

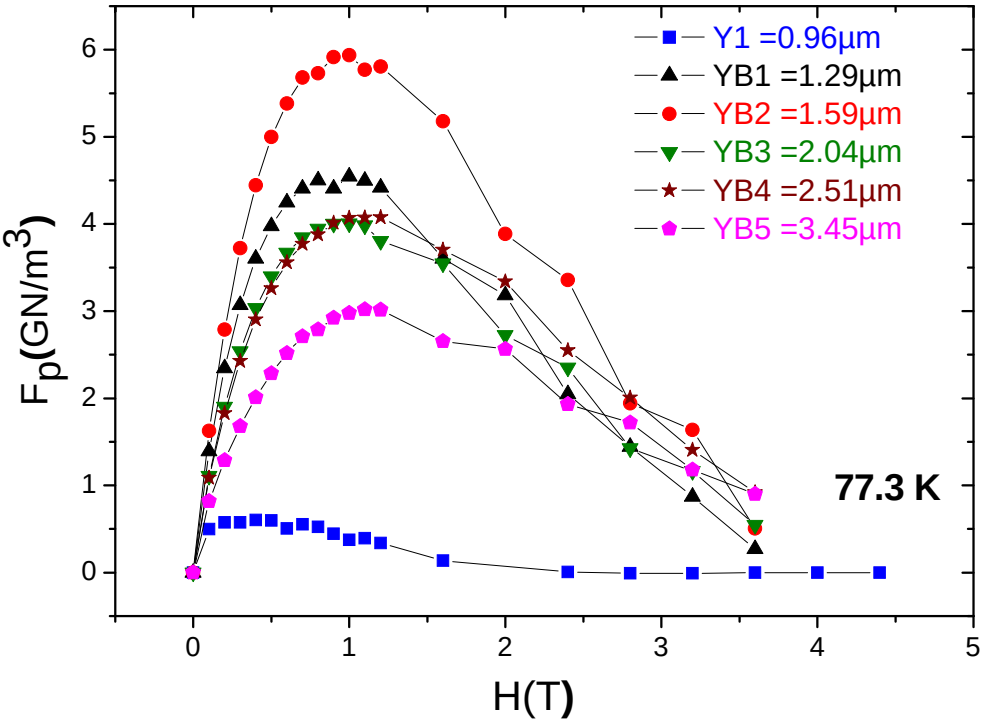

Figure 6.9. Magnetic field dependence of the pinning force F_p of $YBa_2Cu_3O_{7-x}$ / 2 wt% $BaZrO_3$ films with thickness of 1.2 μm, 1.61 μm, 2.0 μm, 2.2 μm and 2.5 μm at 77.3 K. Y1 is a pure YBCO film for reference. Solid lines are drawn for eye guidance.

6.2.5 Pinning mechanism

The volume pinning force, F_p, is mainly determined by the pinning centre size because the pinning centre size determines the total length of interacting flux lines and the geometrical nature of the interaction [208]. In order to understand the pinning mechanism in the studied films, the normalised flux pinning force F_p / F_p^{max} at 77.3 K has been plotted

as a function of reduced field $b = B / B_{irr}$ for different thickness as shown in Figure 6.10 to Figure 6.14. The normalising irreversibility field (B_{irr}) was determined using a criterion of 10^3 A/cm^2 for all films throughout this study. To further clarify the underlying pinning mechanism, the Dew Hughes model was used. As described in section 2.3, the Dew Hughes model proposed the pinning force density for elementary pinning forces $y = Ax^p(1-x)^q$ where y is a type of pinning function, A is the numerical parameter that reflects the weighting and p and q are parameters describing the actual type of pinning centre. The values of p and q depend on the geometrical nature of interaction (volume, surface and point) and the type of pinning center (normal and Δκ- as explained in chapter 5).

All films from YB1 to YB5 reveal a typical curved shape and all sets of data produce a good fit to the scaling law. The maximum peaks in pinning force are found to be at the same position for all films, at b = 0.33. In Figure 6.10, the solid fitting curve represents the result of a calculation using Eq. 5.1 with p = 0.5 and q = 2, which are associated with normal surface pinning centres, and a contribution of normal point pinning with the values of p = 1 and q = 2. It was found that the fitting curves from both of the two fitting functions (p = 0.5,1 and q = 2,2) agree well with their experimental data for film thicknesses from 1.29 (Figure 6.10) to 2.61 μm (Figure 6.14). The effective pinning mechanisms for the 2 wt% $BaZrO_3$ doped films with different thicknesses are listed in Table 6.2. However, in the 3.45 μm thick film, three different mechanisms were observed, with values p = 0.5 and q = 2 for normal surface pinning, p = 1 and q = 2 for normal point pinning and p = 2 and q = 1 for $\Delta\kappa$ point pinning. It was found from the fitting procedure using the Dew-Hughes model that the pinning properties involve more than one pinning

mechanism at the same time. There are many different pinning mechanisms active simultaneously in high-T_c superconductors [195].

To compare the difference in magnitude between normal point pinning and normal surface pinning, the scaling parameter of A_1 and A_2 were used. The A_1 parameter here refers to the normal surface pinning and A_2 refers to the normal point pinning. It was found that the values of A_2 increase with increasing film thickness as shown in Figure 6.15. On the other hand, the values of A_1 decrease with increasing film thickness. Based on the relative ratio of A_1 and A_2, it is indicated that the main pinning mechanism for 1.29 to 2.61 μm films is normal point pinning, and normal surface pinning as the second mechanism. These results imply that the 2 wt% $BaZrO_3$ doped films have two types of pinning centre and the magnitude of the scaling parameter of A_1 and A_2 changes with thickness. Based on the above pinning analyses, normal point pinning is the more dominant mechanism than surface point pinning to all 2 wt% $BaZrO_3$ doped films.

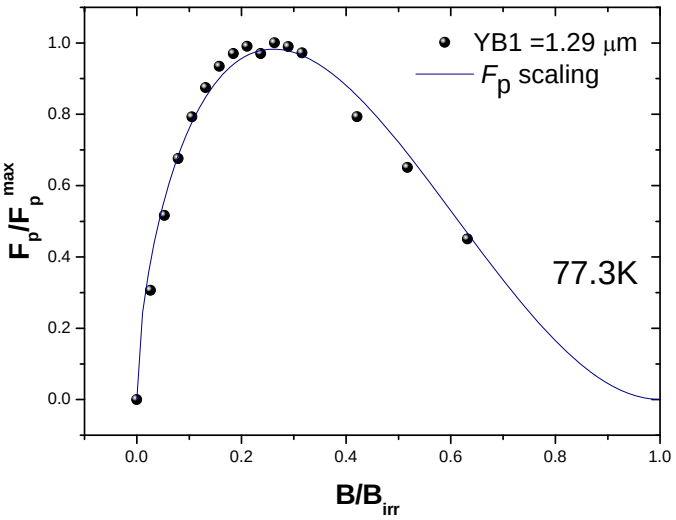

Figure 6.10. Normalised pinning force as a function of magnetic field of the YB1 film at 77.3 K with the scaling parameter of A_1, A_2 and A_3 shown in Figure 6.15. The solid line represents theoretical curve by Eq. 5.1.

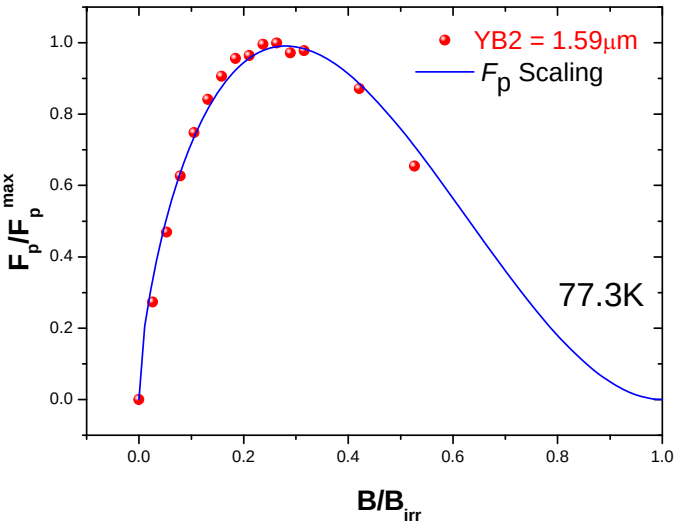

Figure 6.11. Normalised pinning force as a function of magnetic field of the YB2 film at 77.3 K with the scaling parameter of A_1, A_2 and A_3 shown in Figure 6.15. The solid line represents theoretical curve by Eq. 5.1.

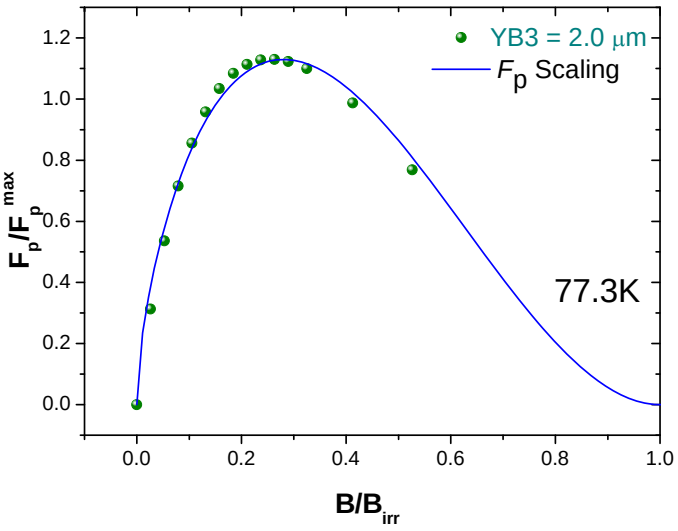

Figure 6.12. Normalised pinning force as a function of magnetic field of the YB3 film at 77.3 K with the scaling parameter of A_1, A_2 and A_3 shown in Figure 6.15. The solid line represents theoretical curve by Eq. 5.1.

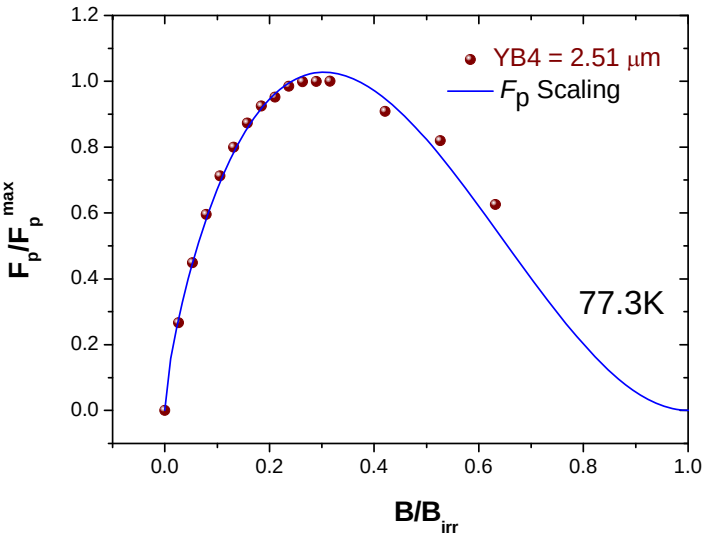

Figure 6.13. Normalised pinning force as a function of magnetic field of the YB4 film at 77.3 K with the scaling parameter of A_1, A_2 and A_3 shown in Figure 6.15. The solid line represents theoretical curve by Eq. 5.1.

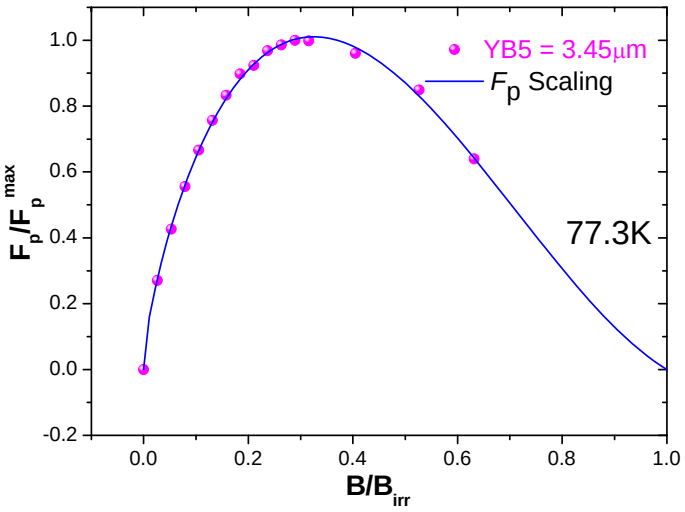

Figure 6.14. Normalised pinning force as a function of magnetic field of the YB5 film at 77.3 K with the scaling parameter of A_1, A_2 and A_3 shown in Figure 6.15. The solid line represents theoretical curve by Eq. 5.1.

Table 6.2. Summary of elementary pinning force of films at various thicknesses.

Films	$Ax^p(1-x)^q$	Type of centre
YB1	p = 0.5, q = 2	Surface normal
1.29 μm	p = 1, q = 2	Point normal
YB2	p = 0.5, q = 2	Surface normal
1.59 μm	p = 1, q = 2	Point normal
YB3	p = 0.5, q = 2	Surface normal
2.04 μm	p = 1, q = 2	Point normal
YB4	p = 0.5, q = 2	Surface normal
2.51 μm	p = 1, q = 2	Point normal
YB5	p = 0.5, q = 2	Surface normal
3.45 μm	p = 1, q = 2	Point normal
	p = 2, q = 1	Point $\Delta\kappa$

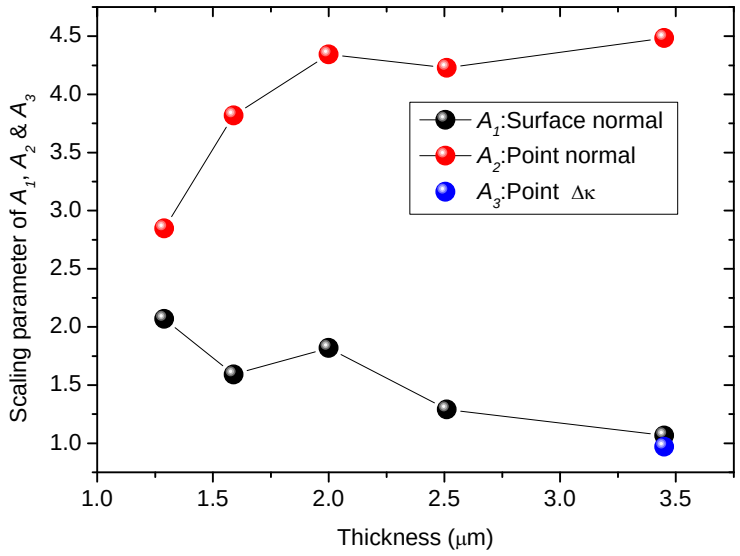

Figure 6.15. Scaling parameter of A_1, A_2 and A_3 (Eq. 5.2) of $YBa_2Cu_3O_{7-x}$ / 2 wt% $BaZrO_3$ films at various thicknesses.

6.3 Superconducting properties of $YBa_2Cu_3O_{7-x}$ / 4 wt% $BaZrO_3$ films

6.3.1 Transition temperature, T_c

Figure 6.16 shows T_c for 4 wt% $BaZrO_3$ doped films with different thicknesses from 1.2 to 2.5 μm, as determined by AC susceptibility measurements. The T_c value of 91 K ± 0.2 K for the thinnest film of YB6 (1.2 μm) decreases gradually as the thickness increases, down to 87.4 K ± 0.2 K for the thicker film YB10 (2.5 μm). The exact cause of the descrease in T_c is unclear. Campbell et al. suggested that an increase of intrinsic strain on the YBCO layer thickness with increasing volume fraction addition of Y_2O_3 can cause T_c reduction [156]. The thinnest film (YB6) exhibits not only a higher T_c but also a sharper

transition ΔT, whereas thicker films have lower T_c and more broadened ΔT, which is around 3.4 K as seen in Figure 6.17. The transition widths ΔT remain at a reasonable sharpness for film YB7 (1.6 μm), YB8 (2.0 μm) and YB9 (2.2 μm), which is around 1 K.

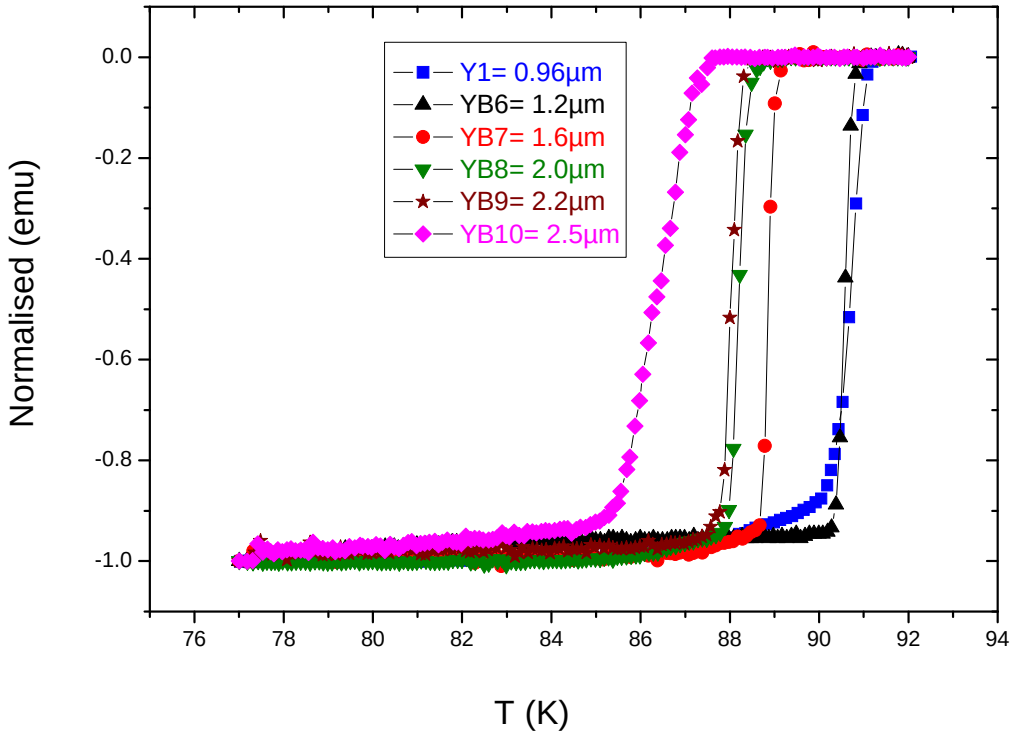

Figure 6.16. Normalised M as a function of temperature for $YBa_2Cu_3O_{7-x}$ / 4 wt% $BaZrO_3$ films with various thicknesses. Y1 is a pure YBCO film for reference.

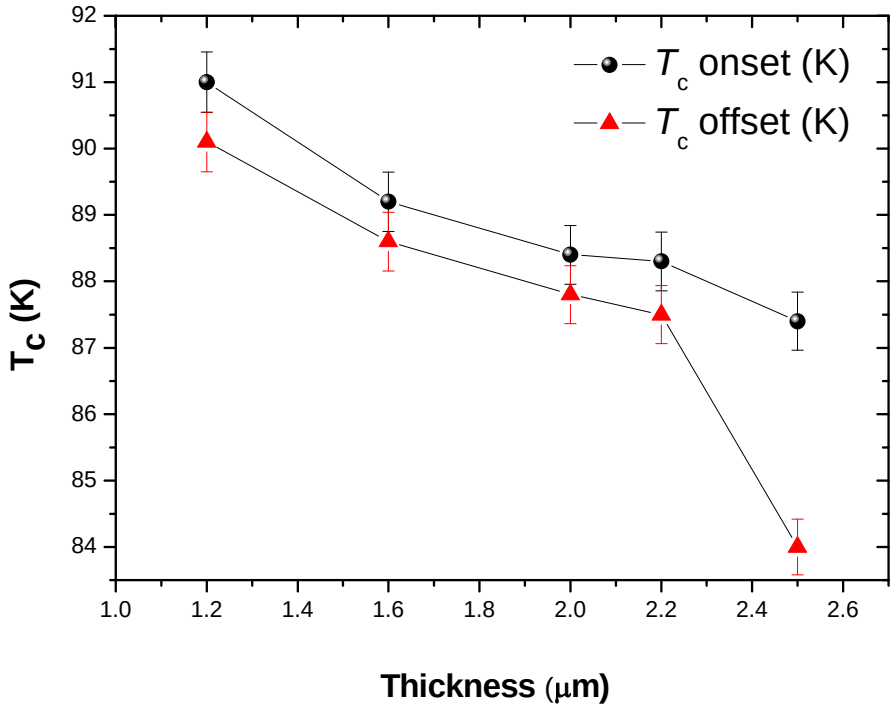

Figure 6.17. Dependence of critical temperature (T_c onset and T_c offset) on thicknesses of the films.

6.3.2 Critical current densities, J_c

Figure 6.18 shows DC field dependence of the critical current densities for several typical thicknesses (1.2 to 2.5 μm) of YB (YBCO/4 wt% BZO) films, and the reference 0.96 μm-thick Y1 (YBCO) film, at 65 K. It can be seen that, even if YB6 is 32% thicker (1.2 μm) than the YBCO thick film, the YBCO/ 4 wt% BZO thick film has a critical current density of five to six times higher, within a wide range of DC magnetic fields, at 65

K. In fact, as compared to the Y1 film of 0.96 μm thickness, the YB10 of 2.5 μm thick films hada J_c that is more than three times higher over a range of magnetic fields.

The J_c at 0 T field values for both YB1 and YB2 BZO films increases compared with the undoped (Y1) film. The YB6 film has the highest J_c, about 4.5×10^6 Acm^{-2} in a 0 T field, 1.6×10^6 Acm^{-2} in a 1 T field and 4.4×10^5 Acm^{-2} in a 4 T field as shown in Table 6.3. All films with a thickness ranging from 1.2 to 2.2 μm can sustain a critical current density of more than 1.0×10^6 Acm^{-2} in a 1 T field. It can be seen that the J_c at 4 T in all YBO/BZO (YB6 to YB10) films are in a good range from 2.2×10^5 to 4.4×10^5 Acm^{-2} and is nearly three orders of magnitude higher as compared to 0.96 μm thick YBCO (Y1) film.

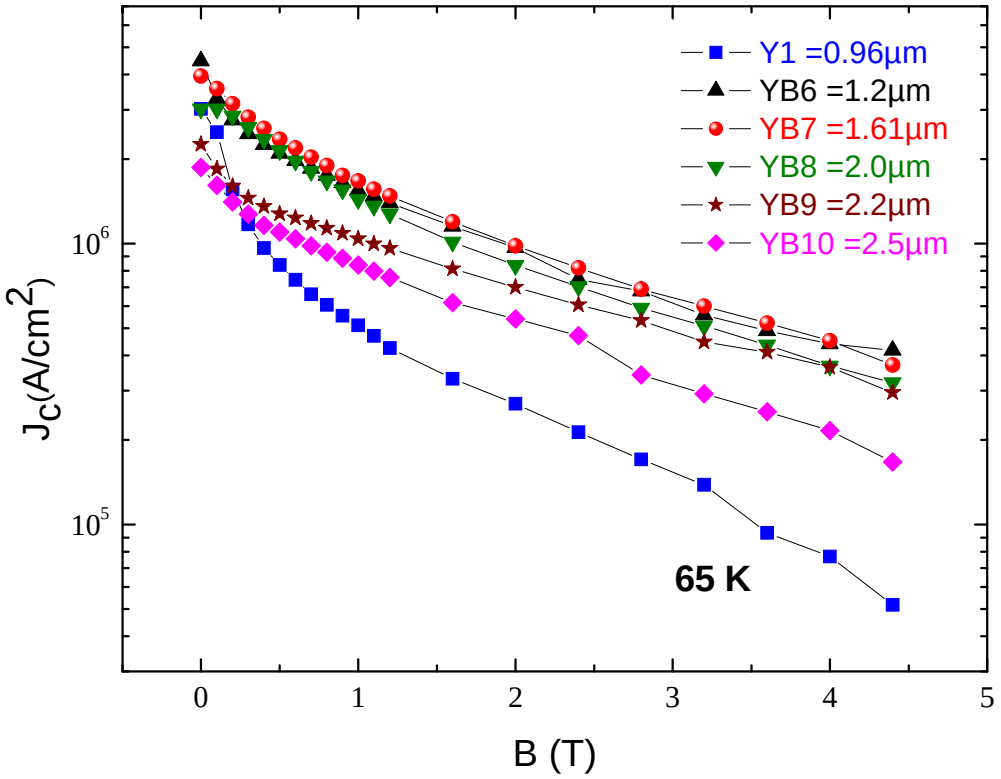

Figure 6.18. Magnetic field dependence of critical current densities of $YBa_2Cu_3O_{7-x}$ / 4 wt% $BaZrO_3$ films with thickness of 1.2 , 1.61 , 2.0 , 2.2 and 2.5 μm at 65 K. Y1 is a pure YBCO film for reference. Solid lines are drawn for eye guidance.

Table 6.3. Summary of $YBa_2Cu_3O_{7-x}$ / 4 wt% $BaZrO_3$ films with various thicknesses in magnetic field of 1 T and 4 T at 65 K.

Film Thickness	J_c at (65 K, 1 T)	J_c at (65 K, 4 T)
YBCO(Y1)		
0.96 μm	5.1×10^5 Acm^{-2}	7.7×10^4 Acm^{-2}
YBCO/BZO		
1.2 μm	1.6×10^6 Acm^{-2}	4.4×10^5 Acm^{-2}
1.6 μm	1.7×10^6 Acm^{-2}	4.5×10^5 Acm^{-2}
2.0 μm	1.4×10^6 Acm^{-2}	3.7×10^5 Acm^{-2}
2.2 μm	1.0×10^6 Acm^{-2}	3.6×10^5 Acm^{-2}
2.5 μm	8.4×10^5 Acm^{-2}	2.2×10^5 Acm^{-2}

The magnetic field dependence of J_c at 77 K for YBCO/4 wt% BZO films with different thicknesses is compared to 0.96 μm thick YBCO film in Figure 6.19. In the entire field range, the BZO-doped (YB6 to YB10) samples show higher critical current densities than the undoped YBCO film (Y1). It can be clearly seen that in self-field, J_c of the thinnest YB6 (1.29 μm) film is about 1.8×10^6 A/cm^2, which is higher than other films. However, there is no significant degradation of self field J_c in YBCO/4 wt% BZO films when the thickness is increased from 1.2 to 2.0 μm. These ranges of thickness show a similar trend of J_c as seen in the YBCO/2wt% BZO films in Figure 6.4. The lowest J_c of 8.5×10^5 A/cm^2 in self-field was recorded for the 2.2 μm thick film. On the other hand, there

are no drastic changes in J_c for the 1.2, 1.61 and 2.0 μm thick films at low magnetic field. However, there is some reduction in J_c evident at very low fields for the 2.2 and 2.5 μm thick films and there appears a slight improvement at the higher fields for the 1 μm range.

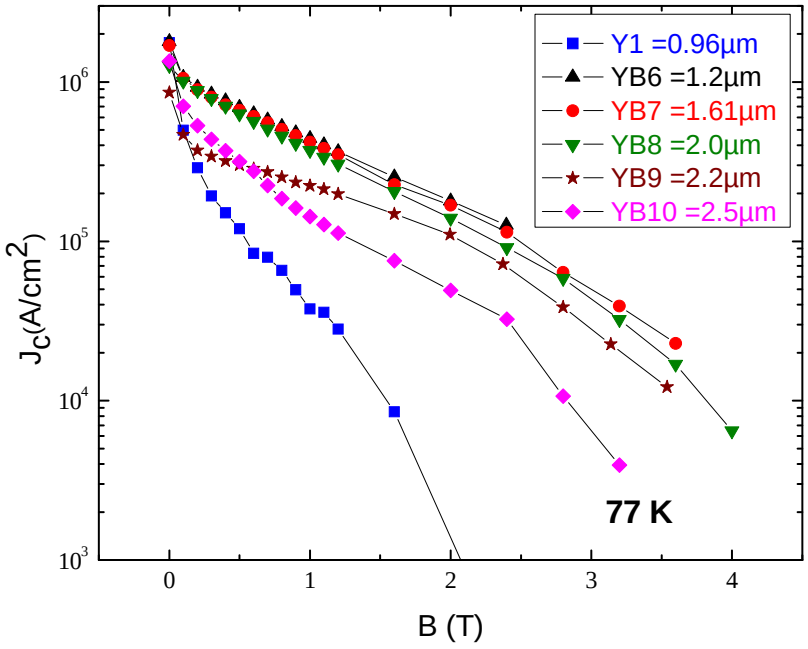

Figure 6.19. Magnetic field dependence of critical current densities of $YBa_2Cu_3O_{7-x}$ / 4 wt% $BaZrO_3$ films with a thickness of 1.2 , 1.61 , 2.0 , 2.2 and 2.5 μm at 77.3 K. Y1 is a pure YBCO film for reference. Solid lines are drawn for eye guidance.

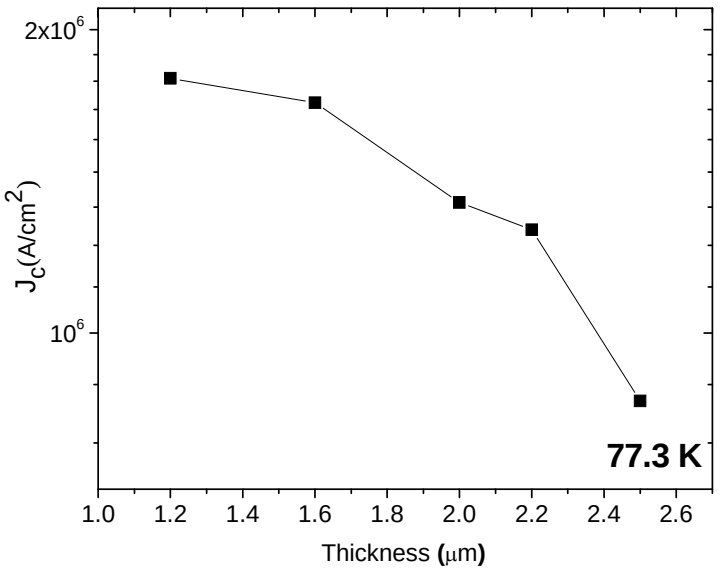

Figure 6.20. Thickness dependence of critical current densities of films at 77.3 K. Solid lines are drawn for eye guidance

6.3.3 Critical current, I_c

Figure 6.21 illustrates the magnetic dependence of critical current (I_c) of 4% BZO doped films with various thickness at 77.3 K. The largest I_c was obtained for the 2.0 μm thick film over all magnetic fields. However, the thickest film (2.5 μm) resulted in a gradual decrease in I_c over a wide range of magnetic field. On the other hand, the thickest (2.5 μm) film exhibited a notably improved I_c in self-field compared to other films. This improvement can be seen in Figure 6.22 which shows the self-field I_c at 77.3 K as a function of the film thickness. It can also be seen that the I_c is nearly unchanged for the films with thickness 1.29, 1.6 and 2.2 μm in the range of 1 T to 3.5 T.

The self-field I_c at 77K is 337 A/cm-width for the 2.5 μm thick film, 253 A/cm-width for the 2.0 μm thick film and 214 A/cm-width for the 1.29 μm thick film.

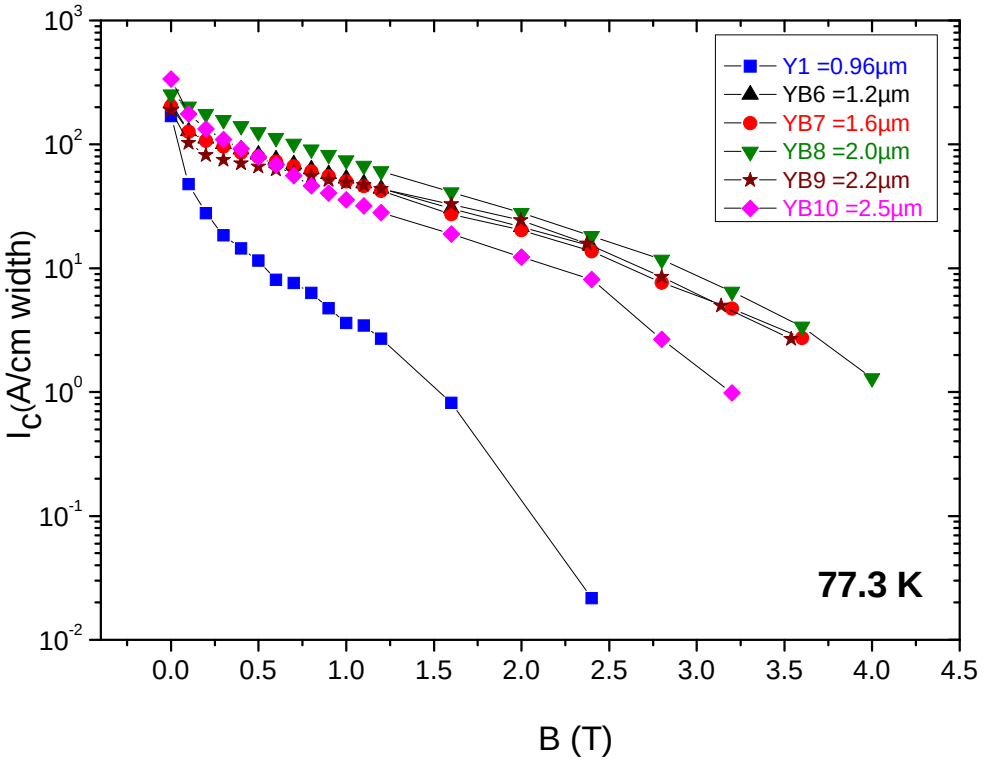

Figure 6.21. Magnetic field dependence of critical current of films with thickness of 1.2 to 2.5μm at 77.3 K. Solid lines are drawn for eye guidance.

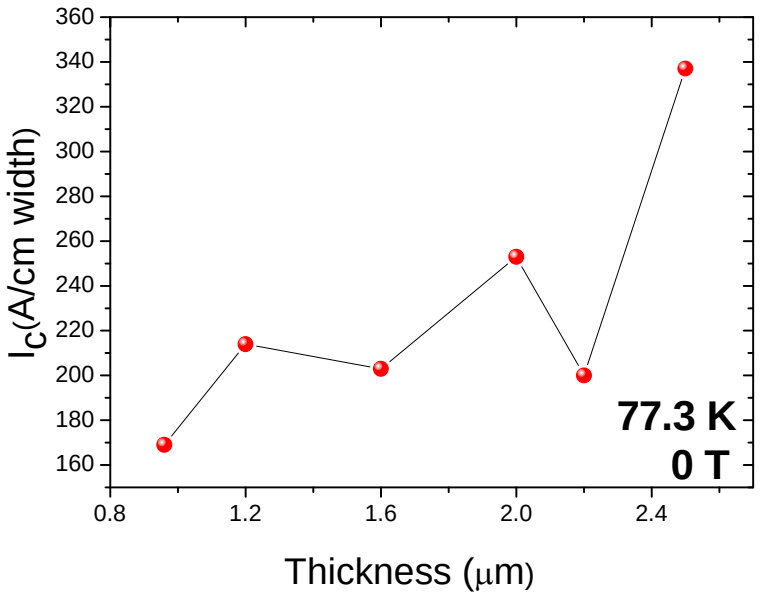

Figure 6.22. Thickness dependence of critical current, I_c in self-field at 77.3 K.

6.3.4 Flux pinning force, F_p

The thickness-dependent flux pinning force (F_p) curves are shown in Figure 6.23 and Figure 6.24 at 65 K and 77.3 K, respectively. F_p has a well-defined maximum in the mid-field region (from 2 to 3 T) at 65 K. However, the F_p well-defined maximum in the mid-field region (from 0.5 to 1.5T) at 77 K is degraded. The general trend for films is that the overall F_p increases as thickness decreases, eventually reaches a maximum, then decreases once again as can be easily seen in both temperatures. F_p, max = 19.3 GN/m^3 is nearly twice higher for the thinnest film (YB6 = 1.2 μm) than F_p, max = 10.1 GN/m^3 for the thickest (YB10 = 2. 5 μm) film at 65 K. At 77 K, F_p, max of the thinnest film (YB6) with 4.4 GN/m^3 is nearly three times higher than for the thickest film (YB10).

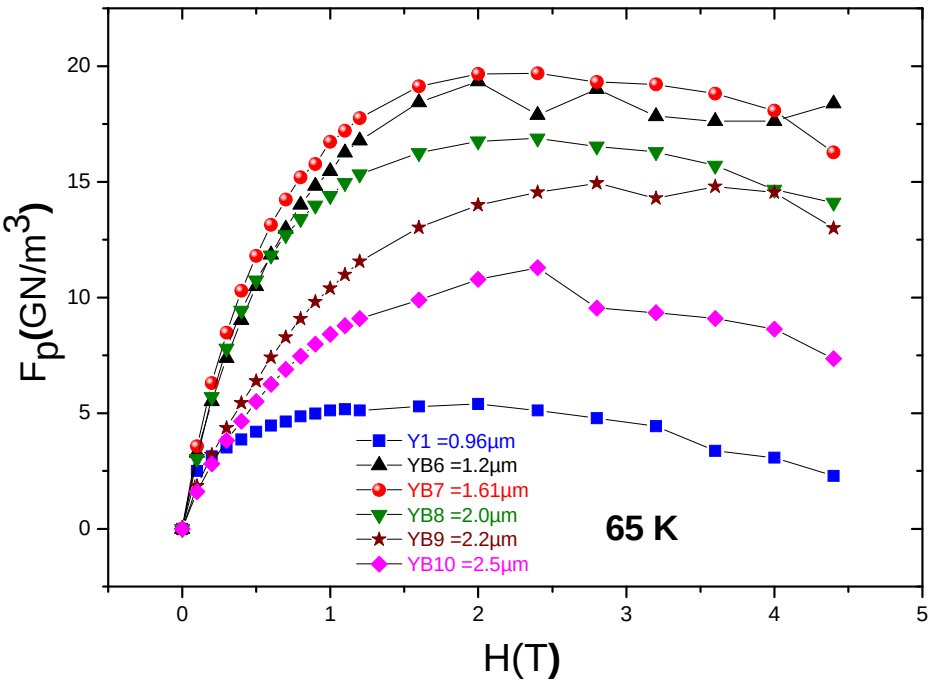

Figure 6.23. Magnetic field dependence of the pinning force (F_p) of $YBa_2Cu_3O_{7-x}$ / 4 wt% $BaZrO_3$ films with thickness of 1.2 , 1.61 , 2.0 , 2.2 and 2.5 μm at 65 K. Y1 is a pure YBCO film for reference. Solid lines are drawn for eye guidance.

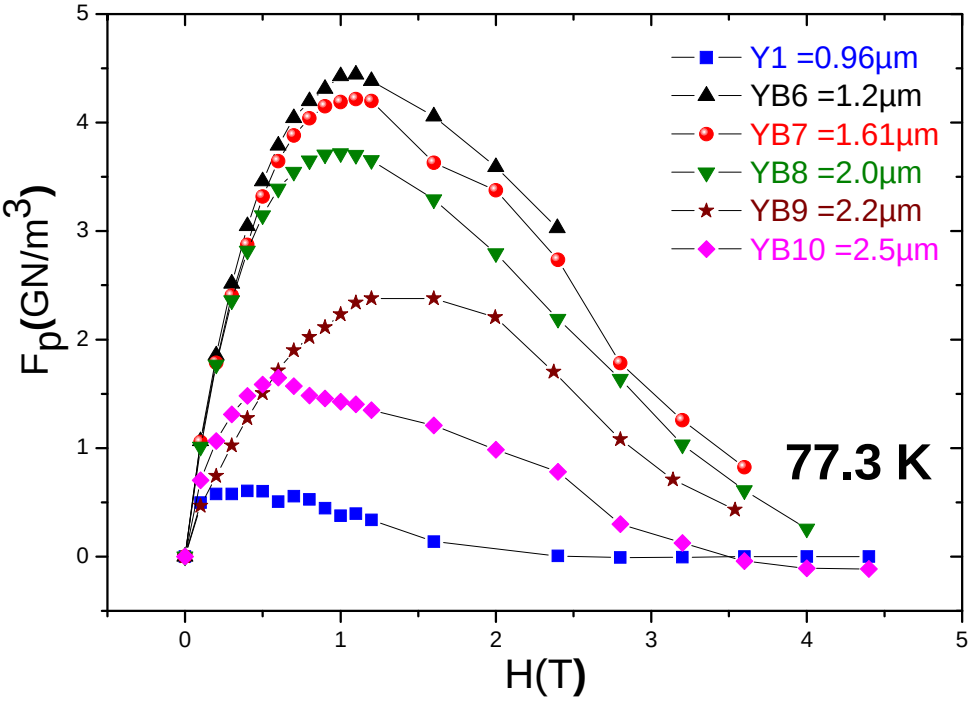

Figure 6.24. Magnetic field dependence of the pinning force (F_p) of $YBa_2Cu_3O_{7-x}$ / 4 wt% $BaZrO_3$ films with thickness of 1.2 , 1.61 , 2.0 , 2.2 and 2.5 μm at 77.3 K. Y1 is a pure YBCO film for reference. Solid lines are drawn for eye guidance.

6.3.5 Pinning mechanisms

The flux pinning force has been analysed in 4 wt% $BaZrO_3$ doped films in order to study the aspect of the pinning mechanism. The Dew-Hughes model is a direct summation model of elementary pinning proposed by a general equation as used before (Eq. 5.1) for the normalised pinning force density where the parameters p and q depend on the specific characteristics of pinning centre. In Figure 6.25 to Figure 6.29, the scaling normalised flux pinning force $F_p / F_p^{\max}$ at 77.3 K is plotted as a function of reduced field $b = B / B_{irr}$ for

films with different thicknesses. Figure 6.25 shows the multi-elementary pinning mechanisms appeared in the 1.2 μm (YB6) film with the best fits for normal surface (p = 0.5, q = 2), normal point (p = 1, q = 2) and $\Delta\kappa$ point (p = 2, q = 1). This curve also indicates that $F_p / F_p^{\max}$ has a maximum peak at b = 0.5 which is in good agreement with the Dew-Hughes model prediction for $\Delta\kappa$ point pinning (where $\Delta\kappa$ represents a change in the Ginzburg-Landau parameter (κ) due to change in T_c). This $\Delta\kappa$ point pinning becomes dominant compared to other pinning mechanisms (normal point and normal surface), which is in good agreement with the value scaling parameter of A_1 being larger than other values of A_2 and $A3$ as seen in Figure 6.30. The multi-elementary (normal point, normal surface and $\Delta\kappa$ point) scaling pinning mechanisms were observed also in films with other thicknesses (1.61 μm to 2.2 μm). These are evident from the solid line fit of the p and q values to the experimental data (see Table 6.4). The normal point pinning mechanism is the most dominant in these films (YB7 to YB9). The $\Delta\kappa$ point pinning mechanism only gives minor contributions as the lower scaling parameter values of A_3 can be seen in Figure 6.30. It was found that the maximum peak of $F_p / F_p^{\max}$ shifted from h = 0.5 to 0.33 with the increase of film thickness from 1.61 μm (Figure 6.26) to 2.2 μm (Figure 6.28).

For the thickest film YB10, (2.5 μm) only two pinning mechanisms resulted from the fit (the solid curve in Figure 6.29 calculated from Eq. 5.1): normal surface pinning (p = 0.5, q = 2) and $\Delta\kappa$ volume pinning (p = 2, q = 1). The pinning mechanism in this film is totally different from other films mentioned before. It was also found that the normal surface pinning for YB10 is the dominant mechanism, which is indicated by the peak position of $F_p / F_p^{\max}$ having a maximum at b = 0.2. The result is in good agreement with

the scaling parameter (Figure 6.30) values, A_1 (normal surface) being larger than A_2 ($\Delta\kappa$ volume) calculated from Eq. 5.2

Table 6.4. Summation of elementary pinning force of films at various thicknesses.

Films	$Ax^p(1-x)^q$	Type of centre
YB6	p = 0.5, q = 2	Surface normal
1.2 μm	p = 1, q = 2	Point normal
	p = 2, q = 1	Point $\Delta\kappa$
YB7	p = 0.5, q = 2	Surface normal
1.61 μm	p = 1, q = 2	Point normal
	p = 2, q = 1	Point $\Delta\kappa$
YB8	p = 0.5, q = 2	Surface normal
2.0 μm	p = 1, q = 2	Point normal
	p = 2, q = 1	Point $\Delta\kappa$
YB9	p = 0.5, q = 2	Surface normal
2.2 μm	p = 1, q = 2	Point normal
	p = 2, q = 1	Point $\Delta\kappa$
YB10	p = 0.5, q = 2	Surface normal
2.5 μm	p = 1, q = 1	Volume $\Delta\kappa$

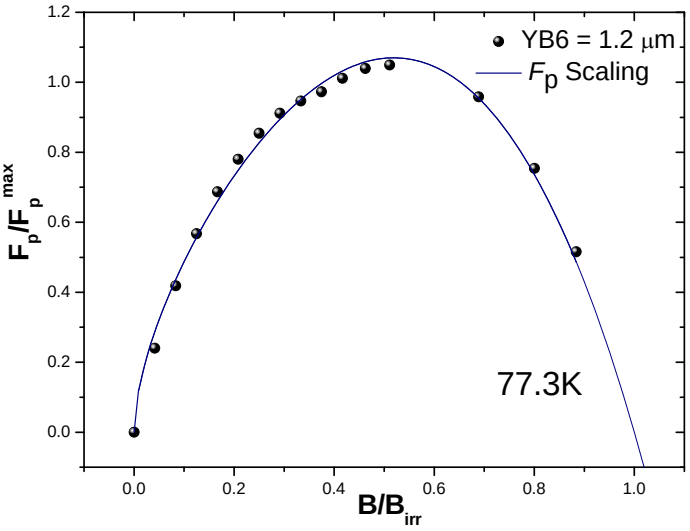

Figure 6.25. Normalised pinning force as a function of magnetic field of the YB6 film at 77.3 K with the scaling parameter of A_1, A_2 and A_3 shown in Figure 6.30. The solid line represents theoretical curve by Eq. 5.1.

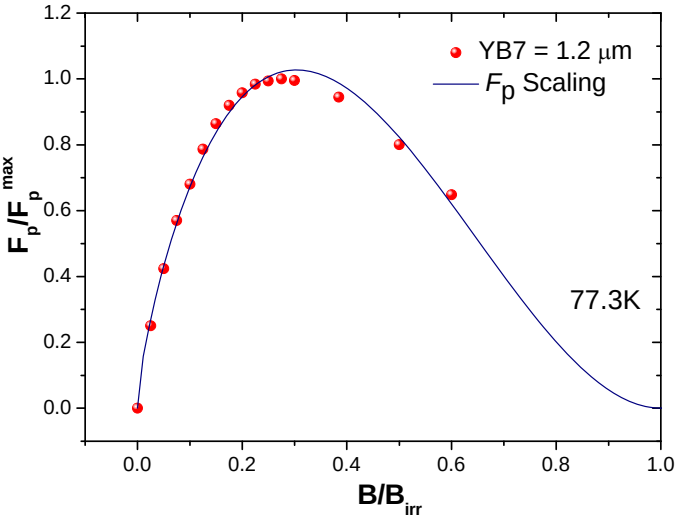

Figure 6.26. Normalised pinning force as a function of magnetic field of the YB7 film at 77.3 K with the scaling parameter of A_1, A_2 and A_3 shown in Figure 6.30. The solid line represents theoretical curve by Eq. 5.1.

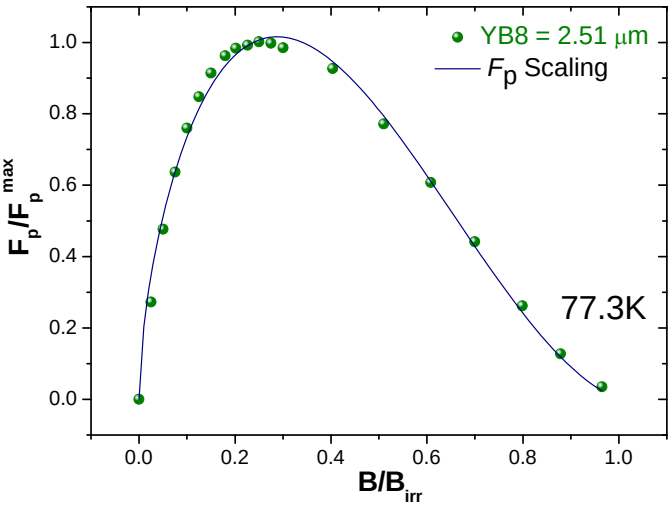

Figure 6.27. Normalised pinning force as a function of magnetic field of the YB8 film at 77.3 K with the scaling parameter of A_1, A_2 and A_3 shown in Figure 6.30. The solid line represents theoretical curve by Eq. 5.1.

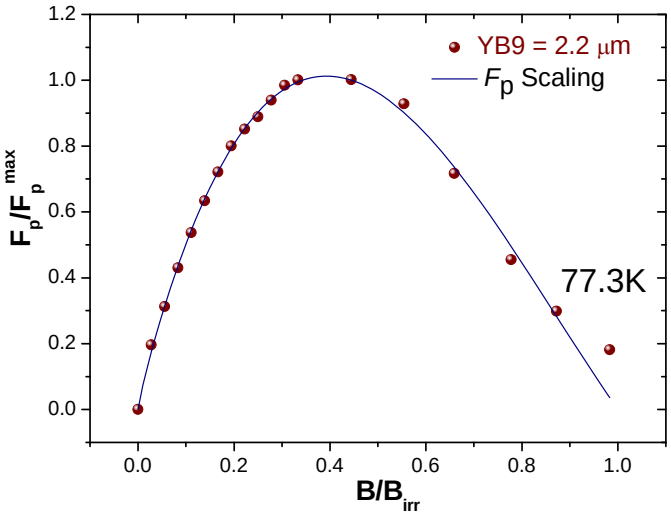

Figure 6.28. Normalised pinning force as a function of magnetic field of the YB9 film at 77.3 K with the scaling parameter of A_1, A_2 and A_3 shown in Figure 6.30. The solid line represents theoretical curve by Eq. 5.1.

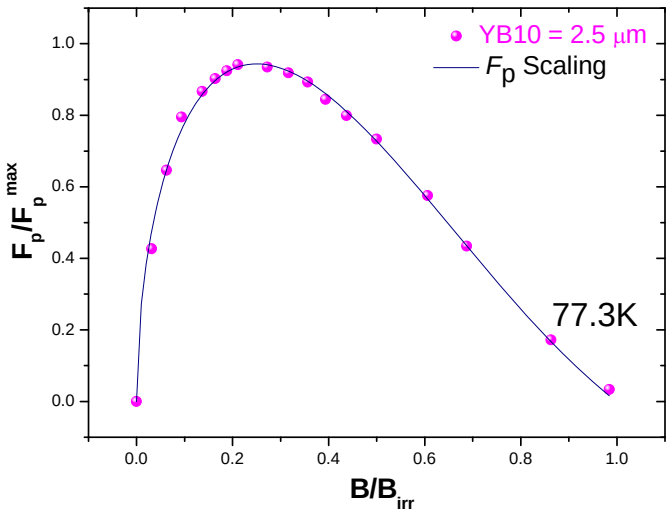

Figure 6.29. Normalised pinning force as a function of magnetic field of the YB10 film at 77.3 K with the scaling parameter of A_1, A_2 and A_3 shown in Figure 6.30. The solid line represents theoretical curve by Eq. 5.1.

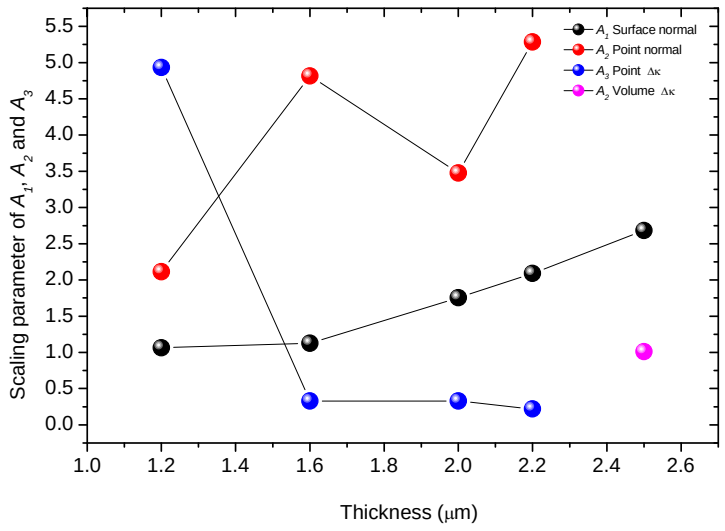

Figure 6.30. Scaling parameter of A_1, A_2 and A_3 (Eq. 5.2) of $YBa_2Cu_3O_{7-x}$ / 4 wt% $BaZrO_3$ films at various thicknesses.

6.3.6 Frequency dependence of critical current density J_c; pinning potential

Figure 6.31 shows the AC field amplitude dependence of the out-of-phase susceptibility response of the 1.2 μm thick BZO doped film YB6, at 77.3 K and $\mu_0 H_{DC}$ = 4 T, for 10 frequencies f between 47 and 9997 Hz equally distributed in a logarithmic scale (47, 85.26, 154.66, 280.56, 508.94, 923.22,1674.7, 3038, 5511 and 9997 Hz). The curves χ" (h_{ac}) shift towards higher AC field amplitudes with increasing frequency (i.e. from left to right in Figure 6.31, the curves correspond to the frequencies listed above). From calculations of Brandt [209] on the flux penetration in superconductors with one dimension much smaller than the other two (disks, squares, stripes) in a perpendicular configuration (suitable for thin films with magnetic field perpendicular to the film surface), it is shown that the position h^* of the maximum χ"(h_{ac}) is related to the critical current density governed by Equation 6.1.

$$J_c = \frac{h^*}{\alpha d}, \qquad 6\text{-}1$$

where d is the film thickness and α is a constant between 0.8 and 0.9 that depends slightly on the geometry (disks, squares, stripes). As can be seen from Figure 6.31, h^* and hence J_c are frequency-dependent due to the different time scale of the thermally-activated flux creep that is the main dissipation mechanism at this temperature and in this range of dc magnetic fields.

Figure 6.32 shows the frequency dependence of J_c, J_c vs. ln(f_0/f), where f_0 is a macroscopic attempt frequency of about 10^6 Hz [59], at 77.3 K and several DC fields in the two films (YB6 and Y1), calculated from equation 6.1 with h^* determined experimentally from the χ"(h_{ac}) curves and α = 0.8. It should be noted that the experimental window in

which J_c can be estimated in this way is limited by the experimental range of both AC field amplitudes and frequencies.

From the frequency (time) dependence of critical current density the pinning potential can be estimated. Experimental data from this study could not be well described by neither the power-law current density dependence of the pinning potential from the weak collective pinning theory [28] (that worked very well in the case of Tl-based thin films in moderate magnetic fields [48]), nor the linear Anderson-Kim's [210]. Instead, as can be seen in Figure 6.32, the data are very well described by a straight line in a double logarithmic plot:

$$\ln J_c = a - b\ln\left(\frac{f_0}{f}\right). \qquad 6\text{-}2$$

The above dependence is consistent with a logarithmic dependence of the effective pinning potential on the current density, as proposed by Zeldov and co-workers based on magneto-resistivity [212] and current-voltage characteristics [213] measurements on YBCO thin films, and explained theoretically [214] by a potential well having a cone-like structure exhibiting a cusp at its minimum and a broad logarithmic decay with distance:

$$U_{eff} = U_0 \ln\left(\frac{J^*}{J}\right), \qquad 6\text{-}3$$

where J^* is a "critical current" at which the effective pinning potential U_{eff} approaches zero (cross-over between flux creep and flux flow). It can be proven that, by using Eq. 6.3 for the current dependence of effective pinning potential, U_0 can be related to the slope b in Eq. 6.2 of the experimental data (complete derivation is given in the Appendix):

$$U_0 = k_B T\left(1+\frac{1}{b}\right) \qquad 6\text{-}4$$

Figure 6.32 shows the values of the pinning potential (U_0) calculated from the slopes in Figure 6.31 making use of Eq. 6.4, in K (k_B = 1), at 77.3 K and several DC fields, for the two thick films. It can be seen that the average pinning potential of the 1.2 μm-thick BZO doped film (YB6) is higher and, even if the increase does not seem impressive, the exponential dependence of dissipation (Eq. 6.5 in Appendix) implies a much lower dissipation caused by thermally activated flux creep in the film with artificial pinning centres induced by BZO.

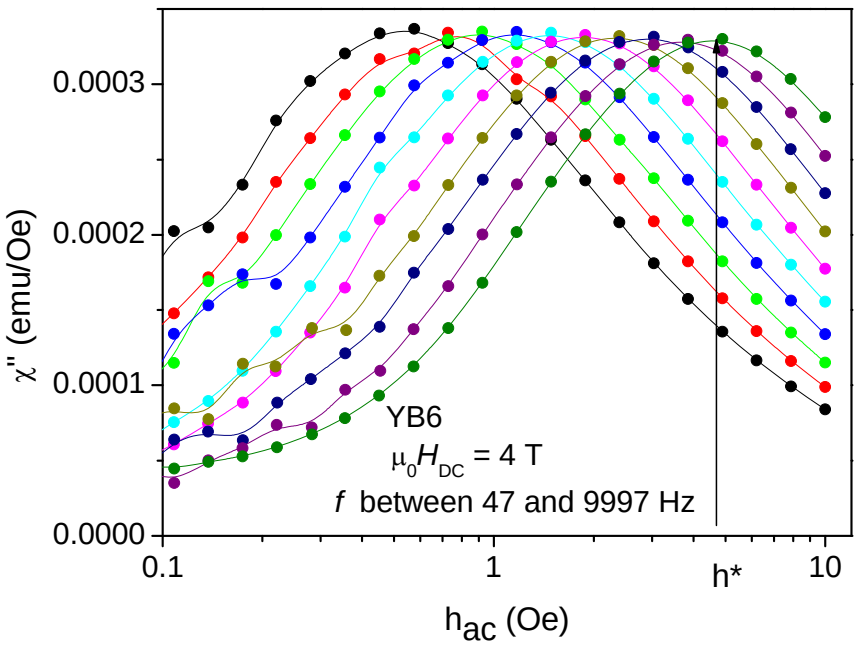

Figure 6.31. AC field amplitude dependence of the out-of-phase susceptibility response of the YB6 1.2 μm film, at 77.3 K and 4 T, for ten AC field frequencies between 47 and 9997 Hz. The arrow indicates the position (h*) of the maximum in χ"(h_{ac}) for 9997 Hz, used to estimate the frequency-dependent critical current density, as described in the text.

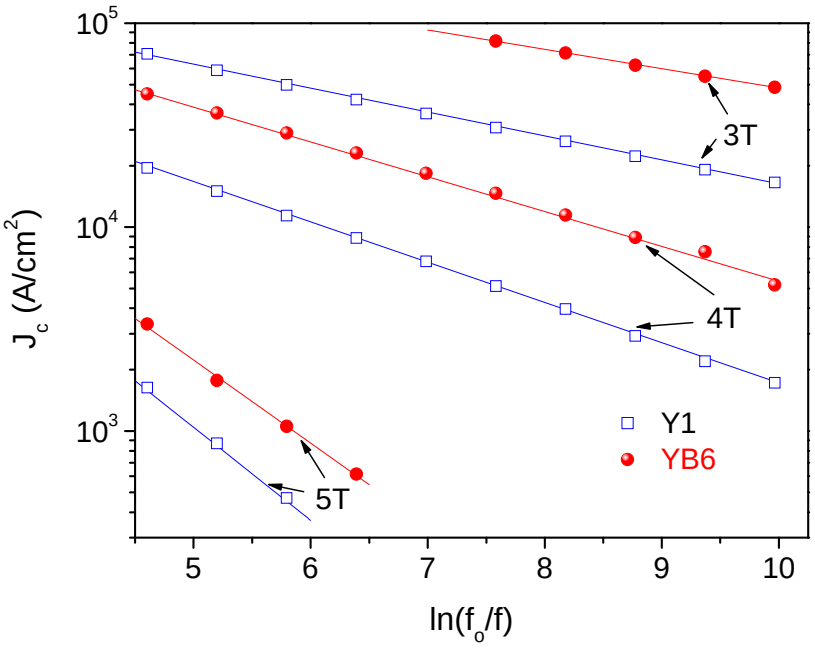

Figure 6.32. Frequency dependence of critical current densities of the two thick films (YB6 and Y1) at 77.3 K and in 3, 4, and 5 T, respectively. Full lines are linear fits in a double-logarithmic scale. Y1 is pure YBCO.

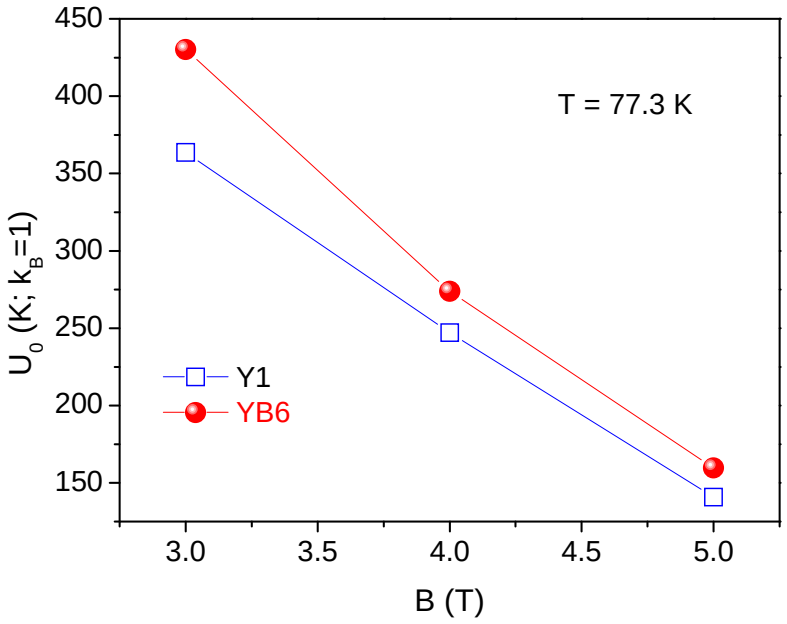

Figure 6.33. Pinning potentials at 77.3 K and in DC magnetic fields of 3, 4, and 5 T of the two thick films, in K (k_B = 1), estimated from the slopes of the curves in Figure Figure 6.32, and Eq. 6. Lines are for eye guidance.

6.4 Microstructure analysis of $YBa_2Cu_3O_{7-x}$ / 2 wt% $BaZrO_3$ films

6.4.1 XRD analysis

Figure 6.34 shows the θ-2θ diffraction pattern of the 2 wt% BZO doped films with high diffraction intensity for films with different thicknesses. In these patterns, the major peaks correspond to the (00*l*) reflections of the YBCO phase, which indicates that the YBCO film has a strong c-axis texture. The strongest peak with the highest intensity, located at 2θ = 46.6° belongs to the (006) peak. It can be seen that the BZO phase, which is

visible in the XRD at 2θ = 43.2° is represented by the (200) peak. It can be seen from these XRD scans that (003) and (006) peaks of the films overlap with STO substrate peaks because of very similar inter-planar spacings. There are no other film peaks present except the holder peak at 2θ = 11.2°. The BZO (002) peak value width increases with inreasing film thickness. More quantitative analyses of long range lattice ordering made from the broadening $\Delta\omega$ of the $\langle 005 \rangle$ rocking curve need to be done as suggested by Gauzzi et al. [222].

The oxygen deficiency, δ, of all films can be confirmed from the intensity ratios of (005) and (004) peaks where $I(005)/I(004) < 20$ gives $\delta < 0.1$. All of the 2 wt% BZO doped films have $I(005)/I(004) < 17$, indicating a variation of YBCO *c*-axis constant. In YB1 film with thickness of 1.29 μm, the main (005) peak gives a *c*-axis = 1.162 nm, a value close to the theoretical value. A higher value of *c*-axis, which is 1.164 nm for the thicker film (YB3) was observed.

Although for the pure YBCO, a large variation of *c*-axis parameter means a large deviation from the optimum oxygen content, this is not the case in nanostructrued YBCO when variations in *c*-axis parameter results from the internal stress induced by nanoinclusions [215].

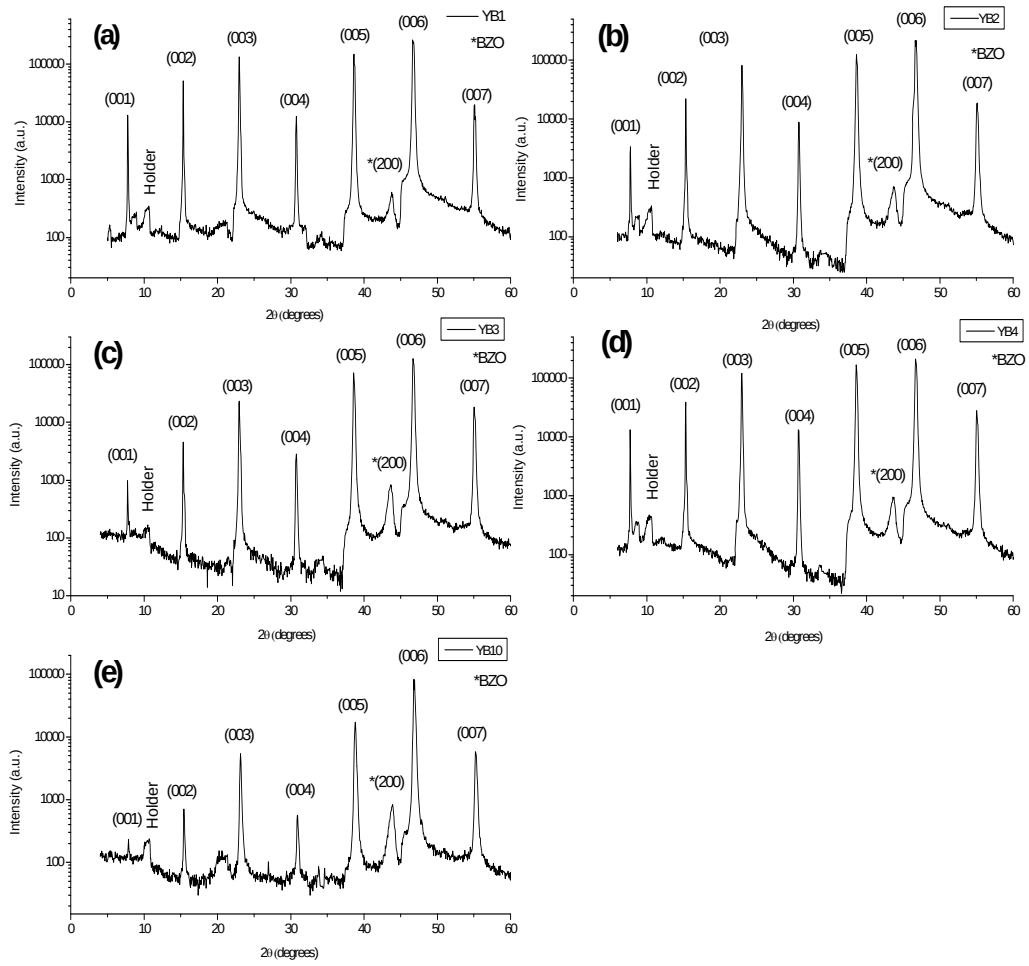

Figure 6.34. Typical XRD patterns of $YBa_2Cu_3O_{7-x}$ / 2 wt% $BaZrO_3$ films with thickness of (a) 1.29 μm, (b) 1.59 μm, (c) 2.0 μm, (d) 2.51 μm and (e) 3.45 μm.

6.4.2 SEM morphologies

In order to investigate the decrease of J_c for $YBa_2Cu_3O_{7-x}$ / 2 wt% $BaZrO_3$ films with increasing film thickness, the morphological properties of films were analysed by scanning electron microscopy (SEM). Figure 6.35 to Figure 6.39 illustrates the surface morphological evolution of 2 wt% $BaZrO_3$ films as a function of film thickness at different magnification. The 1.29 μm thickness film, YB1, shows a dense, quite smooth surface, irregular pores and reasonable grain connectivity. The submicron pores are about 300 nm for film YB1 with 1.29 μm thickness and increases regularly to about 1000 nm for the 3.45 μm-thick YB5 film. It can be seen that the shape of the pores is quite different in all films. For thicknesses between 2.65 and 3.45 μm, the density of submicron pores in 2 wt% $BaZrO_3$ films is more or less a constant. Comparison of all these films can be seen in Figure 6.40.

The supercurrent flow is significantly reduced due to the development and the coarsening of grain boundaries, and possibly an increased porosity [217]. Zhou et al. [217] also suggested that at sufficient thickness current flow will be eventually limited by microstructure imperfections such as rough grain boundaries, voids, cracks, etc, which increase with thickness.

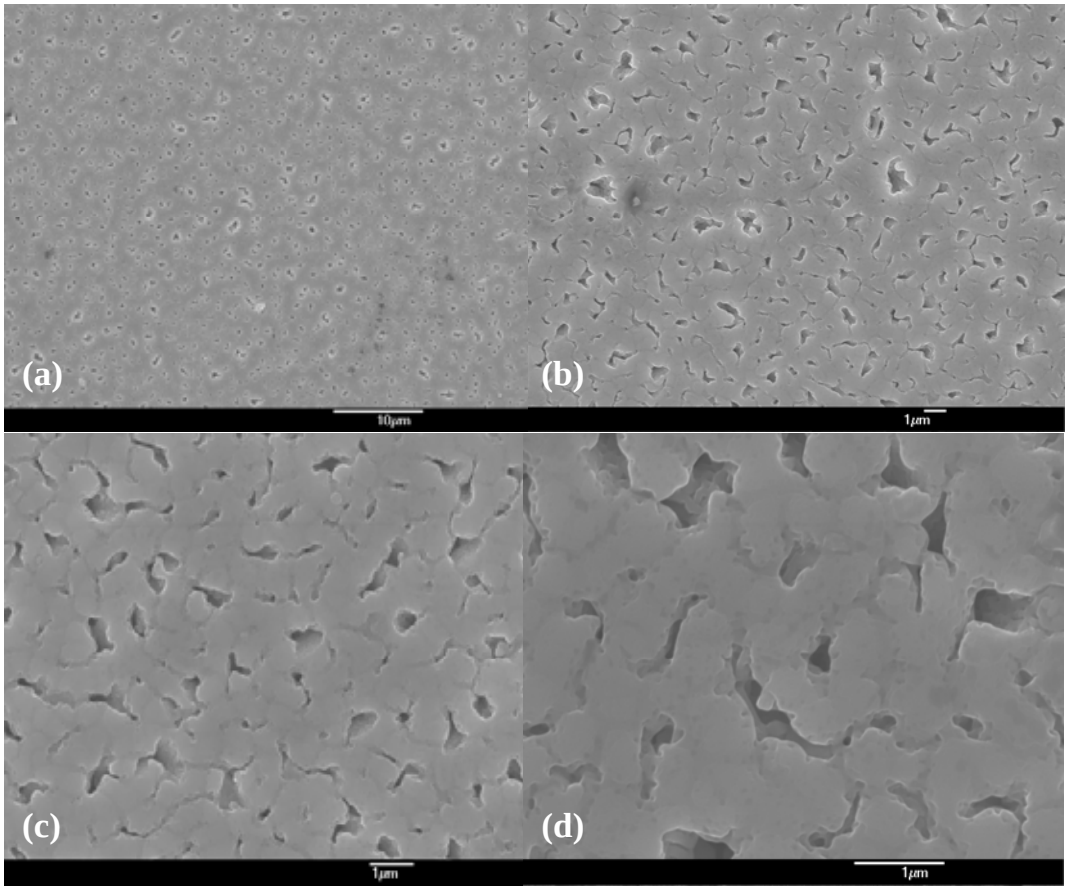

Figure 6.35. SEM images of YB1 with 1.29 μm thick film, taken at magnifications (a) 5000x, (b) 10 000 x, (c) 15 000 x and (d) 20 000 x

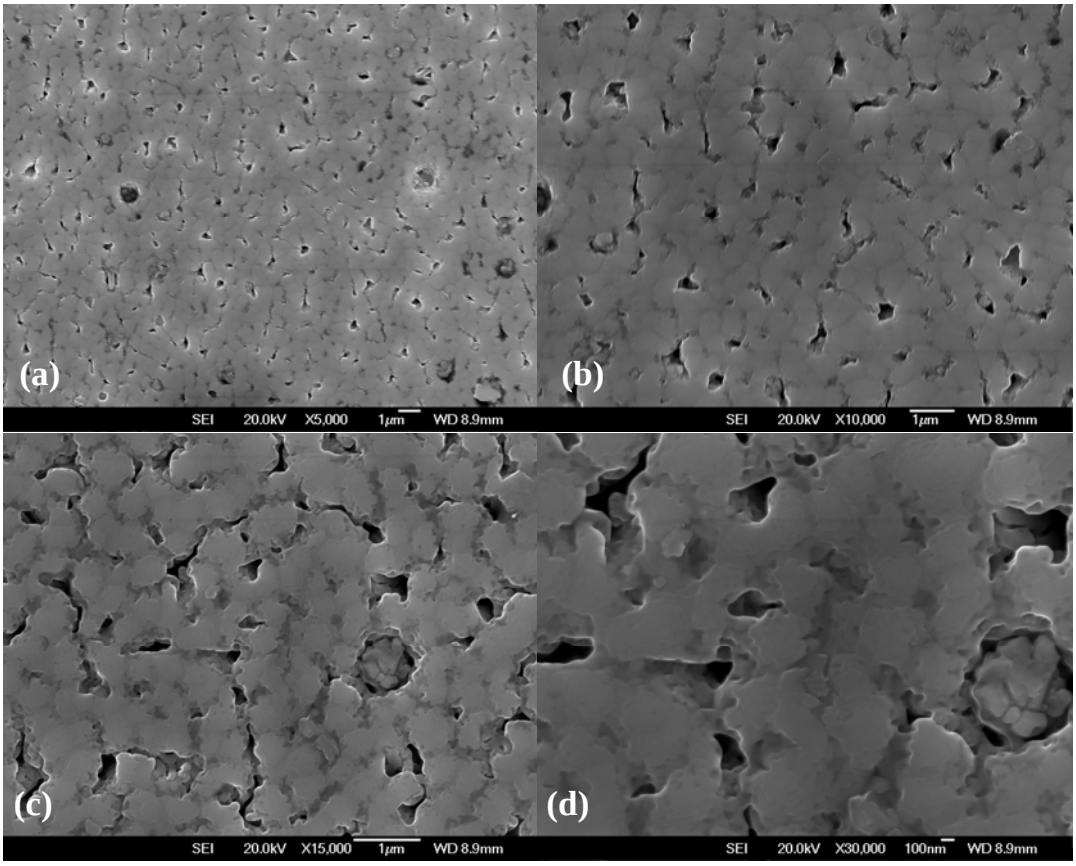

Figure 6.36. SEM images of YB2 with 1.59 μm thick film, taken at magnifications (a) 5000x, (b) 10 000x, (c) 15 000x and (d) 30 000x

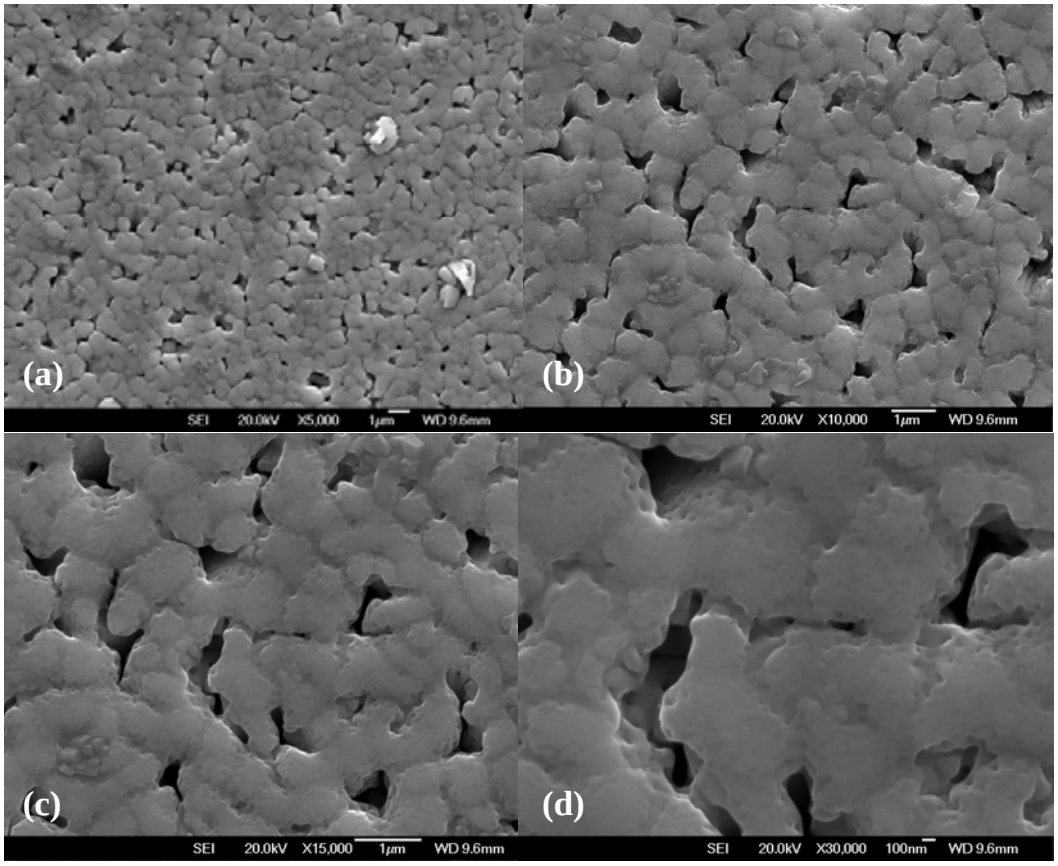

Figure 6.37. SEM images of YB3 with 2.0 μm thick film, taken at magnifications (a) 5000x, (b) 10 000x, (c) 15 000x and (d) 30 000x

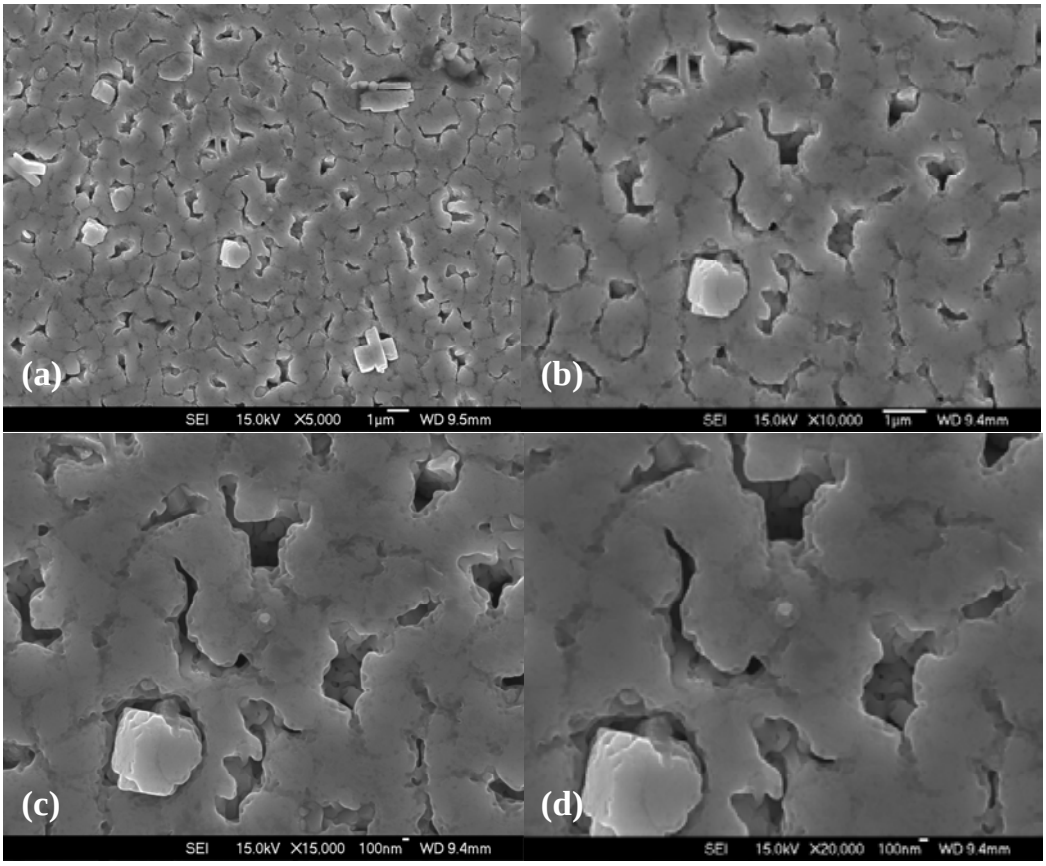

Figure 6.38. SEM images of YB4 with 2.51 μm thick film, taken at magnifications (a) 5000x, (b) 10 000x, (c) 15 000x and (d) 20 000x

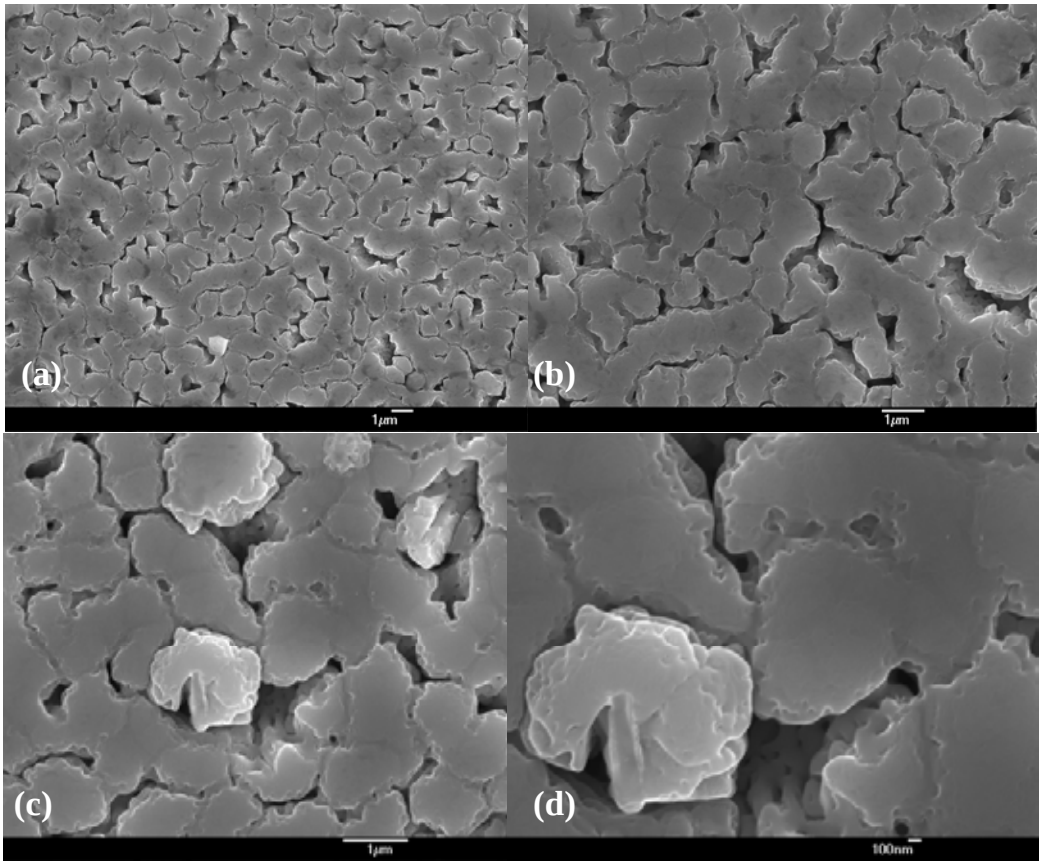

Figure 6.39. SEM images of YB5 with 3.45 μm thick film, taken at magnifications (a) 5000x, (b) 10 000x, (c) 20 000x and (d) 35 000x

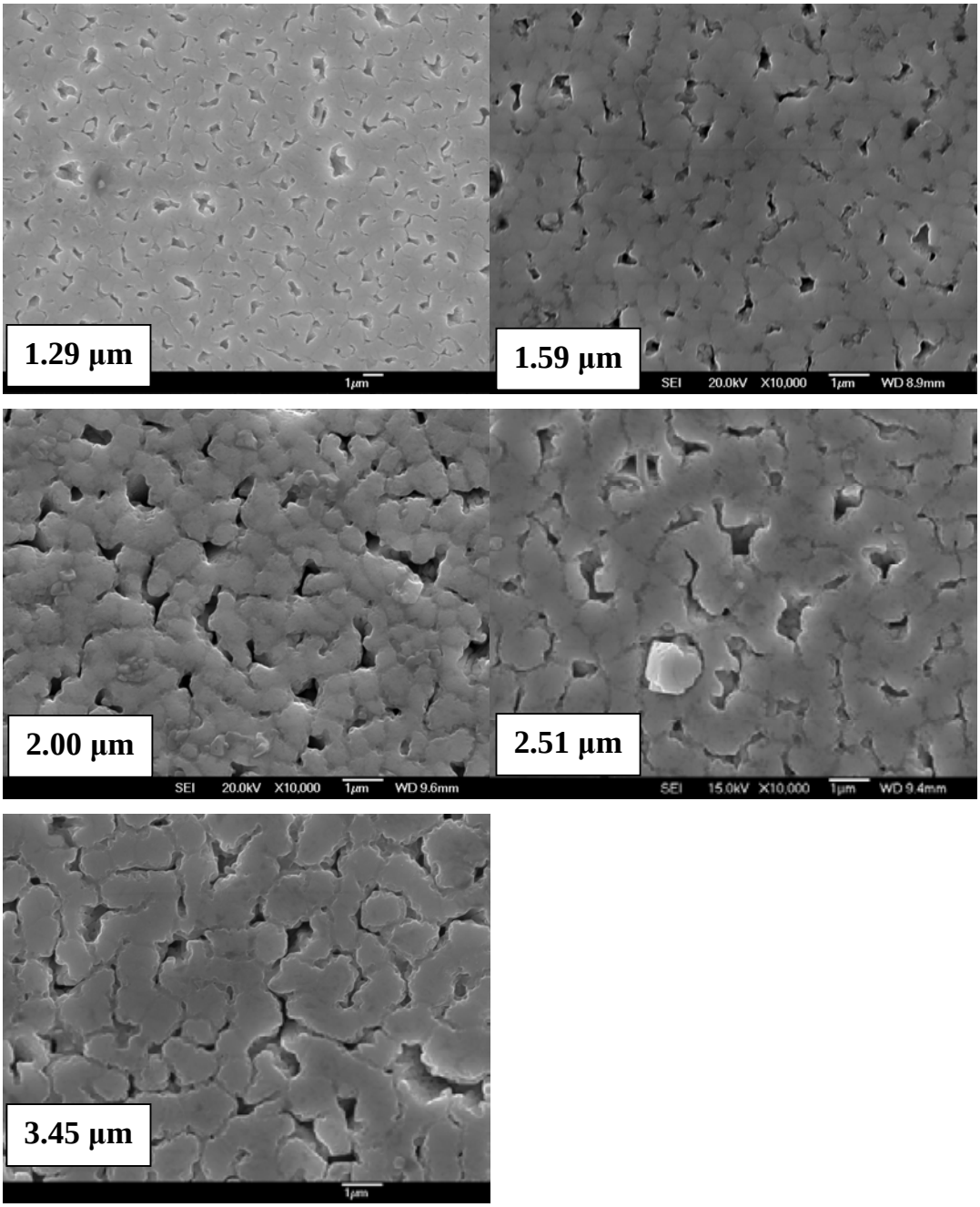

Figure 6.40. SEM images of YB1 to YB5 films at various thicknesses.

6.4.3 EDS analysis

The EDS results of the elemental composition ratio of the YB1 $YBa_2Cu_3O_{7-x}$ / 2 wt% $BaZrO_3$) film (Figure 6.41) in weight percentage are shown in Table 6.1. From the EDS analysis it can be seen that the Zr concentration is around 1.2 wt. % and a bit smaller compared to the 2 % in the nominal value. The values obtained here is slightly lower from nominal values could be lead by two factor. The value obtained here is slightly lower from the nominal value because of two possible factors. One factor is because the composition value is not identical within the limited amount of analysis. The other factor is agglomeration of the fine particles and the inhomogeneous distribution during and after the formation of Y123 grains [221]. There are no other impurity traces in the film and the analysis confirms that all the elemental compositions are in correct ratio.

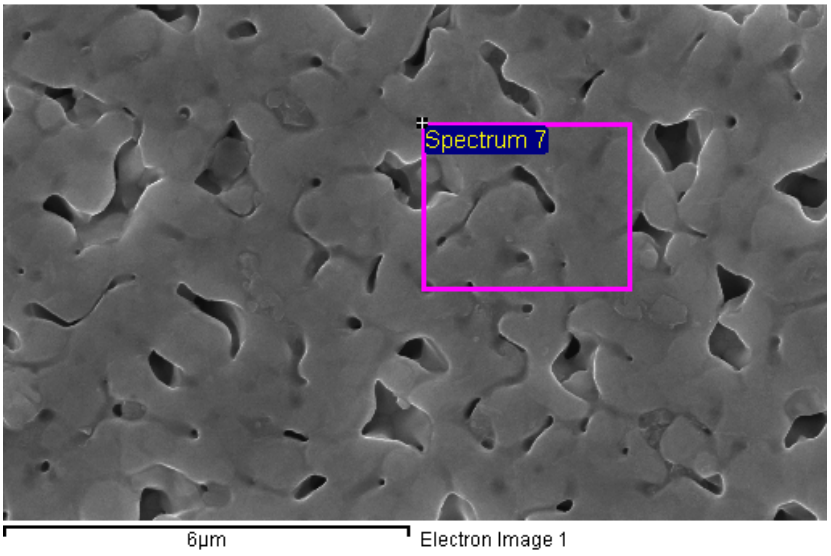

Figure 6.41. SEM-EDS spectrum position of YB1 film.

Table 6.5. Quantitative elemental analysis of YB1 film obtained by EDS analysis from SEM-EDS spectrum as seen in Figure 6.41.

Element	Weight %	Error %
O	19.44	1.7
Cu	24.86	2.1
Y	14.97	1.9
Zr	1.19	1.0
Ba	39.55	3.4

6.4.4 TEM analysis

TEM is the most important technique to determine the formation of nano rods or nano particles of BZO phase in the YBCO film. TEM images were taken at high resolution as shown in Figure 6.42 taken from film YB1. It should be noted that this TEM study was only performed for selected films only. A BZO nano-rods (marked by white arrow) structure can clearly be seen with width 5-10 nm along the *c*- axis in the YBCO matrix. Scattered BZO nano-particles (marked by red arrow) in the YBCO matrix were also detected. All of these nano rods and nano particles have not appeared on pure YBCO film as shown on Figure 6.43. These microstructural results are evidence of potential artificial BZO flux pinning centres and are consistent with the observed enhancement of J_c in these doped YBCO films.

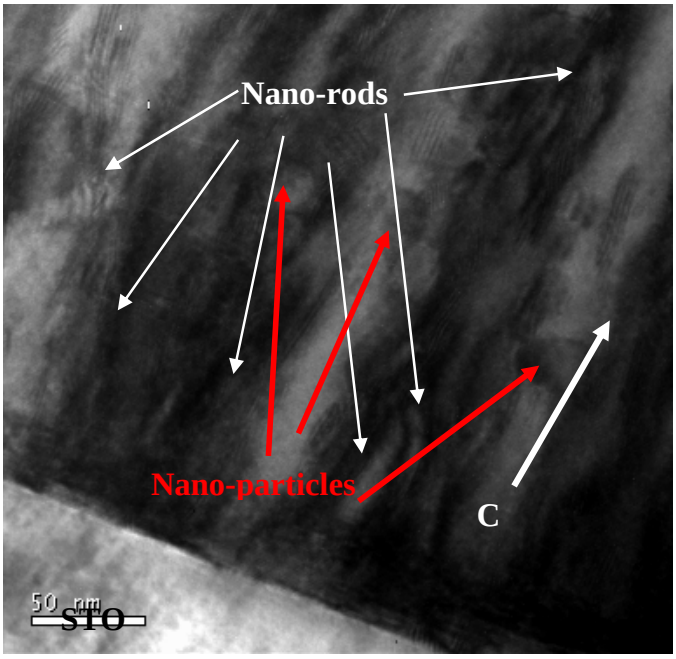

Figure 6.42. TEM image of cross-sectional area inside YB1 film. The *c*-axis direction is shown in the right corner.

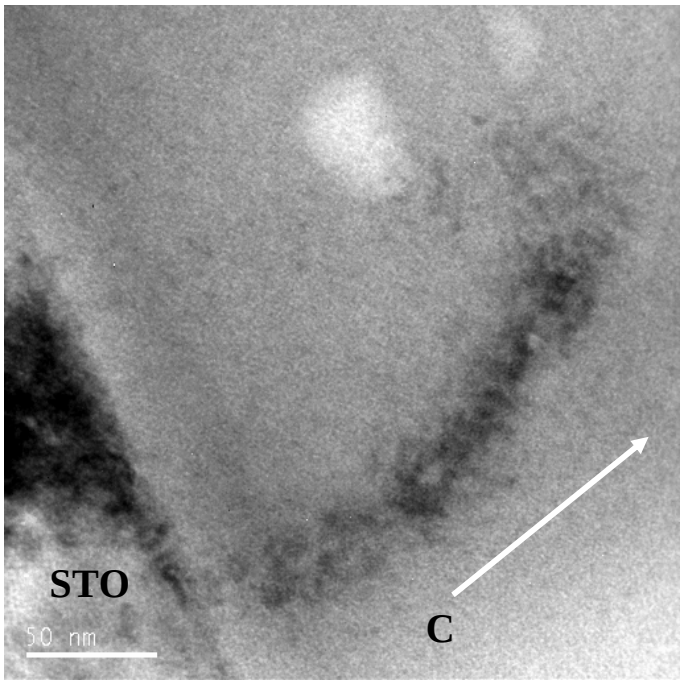

Figure 6.43. TEM image of cross-sectional area inside Y (Pure YBCO) film. The *c*-axis direction is shown in the right corner.

6.4.5 EBSD mapping analysis

EBSD was applied to identify $BaZrO_3$ crystals incorporated in the matrix of $YBa_2Cu_3O_{7-\delta}$. The $BaZrO_3$ file for EBSD analysis was created from high-resolution XRD data taken from the deposited films that reveal exact lattice parameters of $BaZrO_3$ necessary for the analysis of Kikuchi patterns in EBSD. Due to small planar size of $BaZrO_3$ inclusions (typically 5 to 10 nm as found by TEM) and low percentage of incorporated $BaZrO_3$, this crystal phase is expected to be seen as isolated pixels on high-resolution EBSD maps. In identifying this phase, large differences in crystal lattices of cubic $BaZrO_3$ and orthorhombic $YBa_2Cu_3O_{7-\delta}$ were relied on.

Additionally to identifying $BaZrO_3$, EBSD maps provide useful information about crystallographic orientations of all phases on the surface of $YBa_2Cu_3O_{7-\delta}$ + 2 wt% $BaZrO_3$ films. The spatial distributions of the phases ($YBa_2Cu_3O_{7-\delta}$ and $BaZrO_3$) of particular orientation are mapped by different colours based on theoretical analysis of the measured diffraction patterns. The EBSD scan of YB1 film is presented in Figure 6.44. The mapping analysis was performed to evaluate the distribution of 2 wt% $BaZrO_3$ phase in the film. The first map shown in Figure 6.44(a) is the so-called image quality map at 200,000 magnifications with a scale of 200 nm. The image quality is not relatively good as the magnification images are too large but this is the best way to optimize the mapping in this scale. Figure 6.44 (b) shows the detected 1.6% content of $BaZrO_3$ phase in pink colour. It is evident that the $BaZrO_3$ nano particles are randomly distributed with reasonable percentage of detected $BaZrO_3$ in this film deposited from $YBa_2Cu_3O_{7-\delta}$ + 2 wt% $BaZrO_3$ target. The third map of Figure 6.44 (c) is the phase map in which the YBCO-123 phases of different orientations are shown in red and blue (not all $YBa_2Cu_3O_{7-\delta}$ is perfectly

oriented with c-axis perpendicularly to the surface of the film) and the $BaZrO_3$ phase in green. The black hole appearing at the bottom left of this photo is porous area of the film.

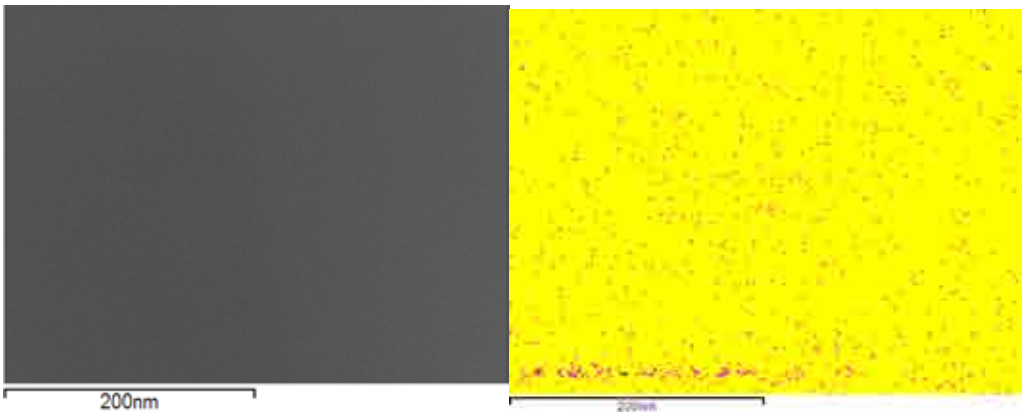

(a) (b)

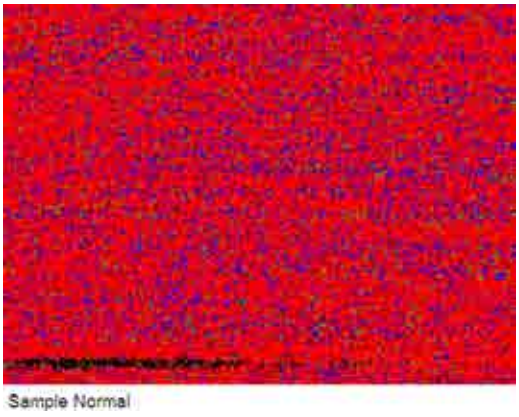

(c)

Figure 6.44. EBSD of $BaZrO_3$ mapping of 2 wt% $BaZrO_3$ (YB1) film (a) the image quality, (b) the $BaZrO_3$ phase in pink, (c) the YBCO phase in red and blue

6.5 Microstructure analysis of $YBa_2Cu_3O_{7-x}$ / 4 wt% $BaZrO_3$ films

6.5.1 XRD analysis

The results of XRD patterns for the 4 wt% BZO doped films show that only (00*l*) peaks are present (Figure 6.45) with high diffraction intensity for films at different thicknesses. This is similar to what has been observed for 2 wt% BZO doped films in section 6.4.1. This indicates that all these films have only *c*-axis orientation and well textured although weak 110 peaks 2θ = 34.2° were obtained on YB7 and YB9. These weak 110 peaks 2θ = 34.2° are not detectable on other films. The formation of this weak YBCO (110) peak is believed to be a nucleation problem during deposition.

The (001) and (002) peaks of STO substrate coincided with the (003) and (006) peaks of YBCO.The highest intensity peaks, located at 2θ = 38.6° and 46.6°, are the (005) and (006) peaks. The BZO (200) peaks, which are detected in the XRD at 2θ = 43.2° are similar to the 2 wt% BZO doped films (Figure 6.35). It seems that it is hard to find any difference in the four XRD pattern films with different thicknesses and different wt % BZO content.

YB6 and YB7 films have the intensity ratios of (005) and (004) peaks where $I(005)/I(004) < 19$, showing a variations of *c*-axis constant. In the YB8 to YB10 films, where the thickness is relatively thick, the main (005) peak give a *c*-axis = 1.162 nm, close to the theoritical value. The extra broadening of the (005) peaks on this film was also observed. It can be concluded that the (005) peaks become broader when the film thickness is thicker.

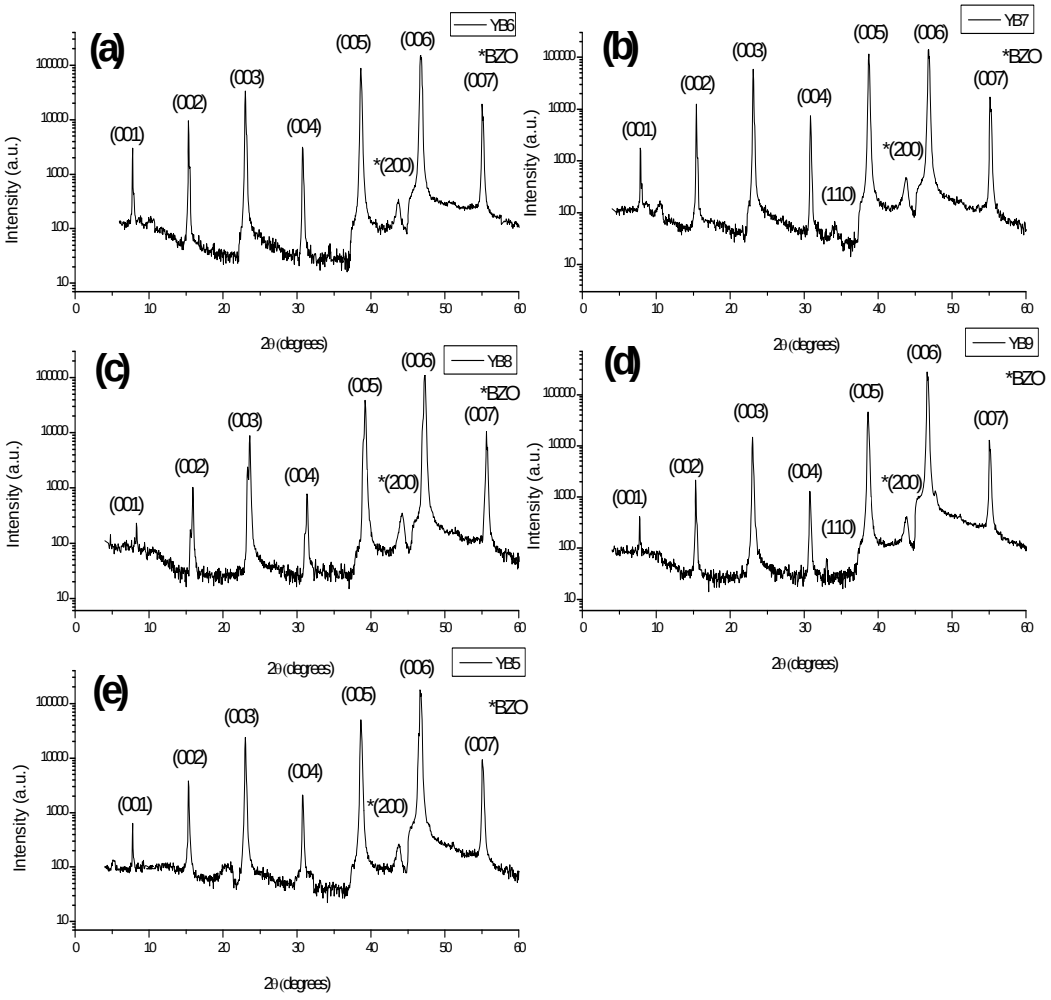

Figure 6.45. Typical XRD patterns for of $YBa_2Cu_3O_{7-x}$ / 4 wt% $BaZrO_3$ films with thickness of (a) 1.2 μm, (b) 1.61 μm, (c) 2.0 μm, (d) 2.2 μm and (e) 2.5 μm.

6.5.2 SEM morphologies

SEM images for the 4 wt% BZO doped film surface for various thicknesses are presented in Figure 6.46 to Figure 6.50. All of these films have microcrack-free surfaces and are formed by *c*-axis oriented grains. The surface of the smooth *c*-axis oriented film is quite dense for the YB6 film as can be seen in Figure 6.46. It should be mentioned that the submicron pores size in the thinnest 4 wt% BZO doped film surface (Figure 6.46) at high magnification is not comparable to the 2 wt% BZO doped film surface (Figure 6.35). However, differences in submicron pores morphologies are clearly noticeable in thicker films.

The submicron pore diameters remain nearly constant over the 2.0 and 2.2 μm film thicknesses and a range of 300 to 400 nm in each sample. It was observed that the shape of the pores is quite different for the thickest YB10 film with 2.65 μm. Above 2.65 μm film thickness, the films show a gradual microstructure transition (Figure 6.49) from well connected grains to segregated grains, which may have weaker grain connectivity, as shown in Figure 6.50. This significant microstructure degradation is similar to that reported by Zhou et al. [217], when the thickness approaches 3.6 μm. They also said the current carrying ability from the part of the film beyond 6.5 μm is significantly reduced, indicating a ‘dead layer’ above this thickness. The ‘dead layer’ is associated with the top surface of the film that carries little or no current due to the greatly deteriorated local microstructure [95]. Comparison of all these films can be seen in Figure 6.51.

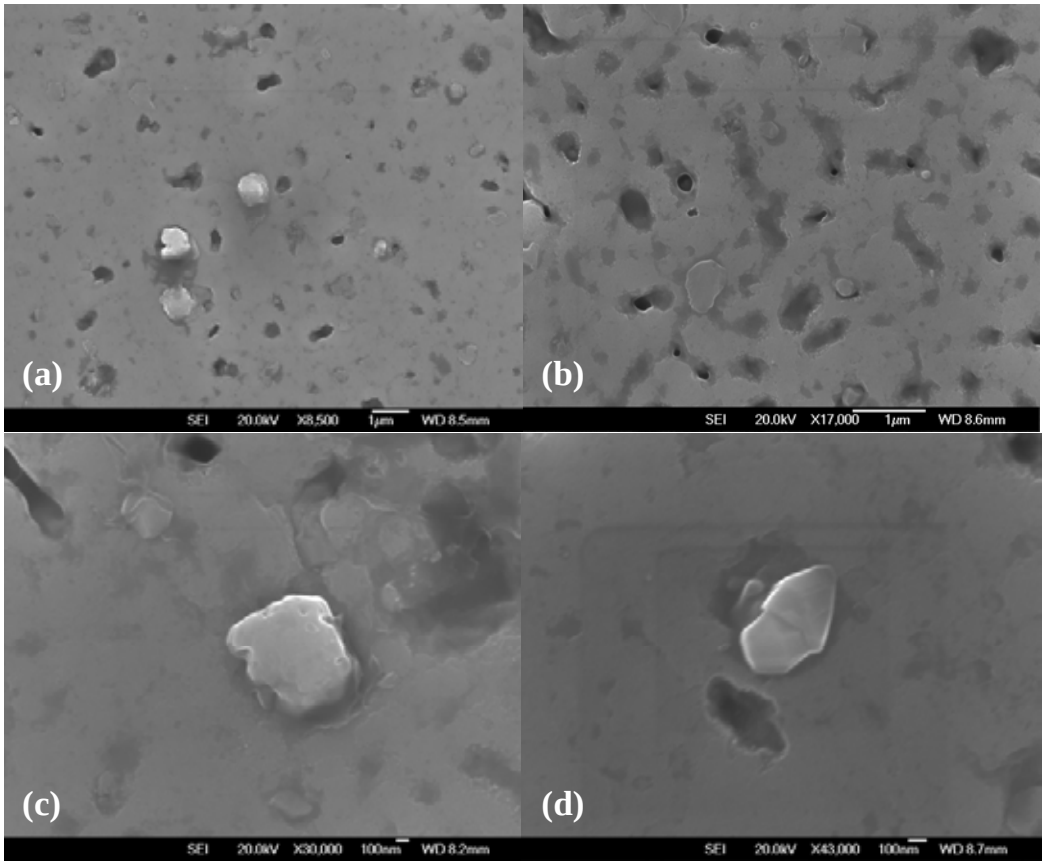

Figure 6.46. SEM images of YB6 with 1.2 μm thick film, taken at magnifications (a) 8500x, (b) 17 000x, (c) 30 000x and (d) 43 000x

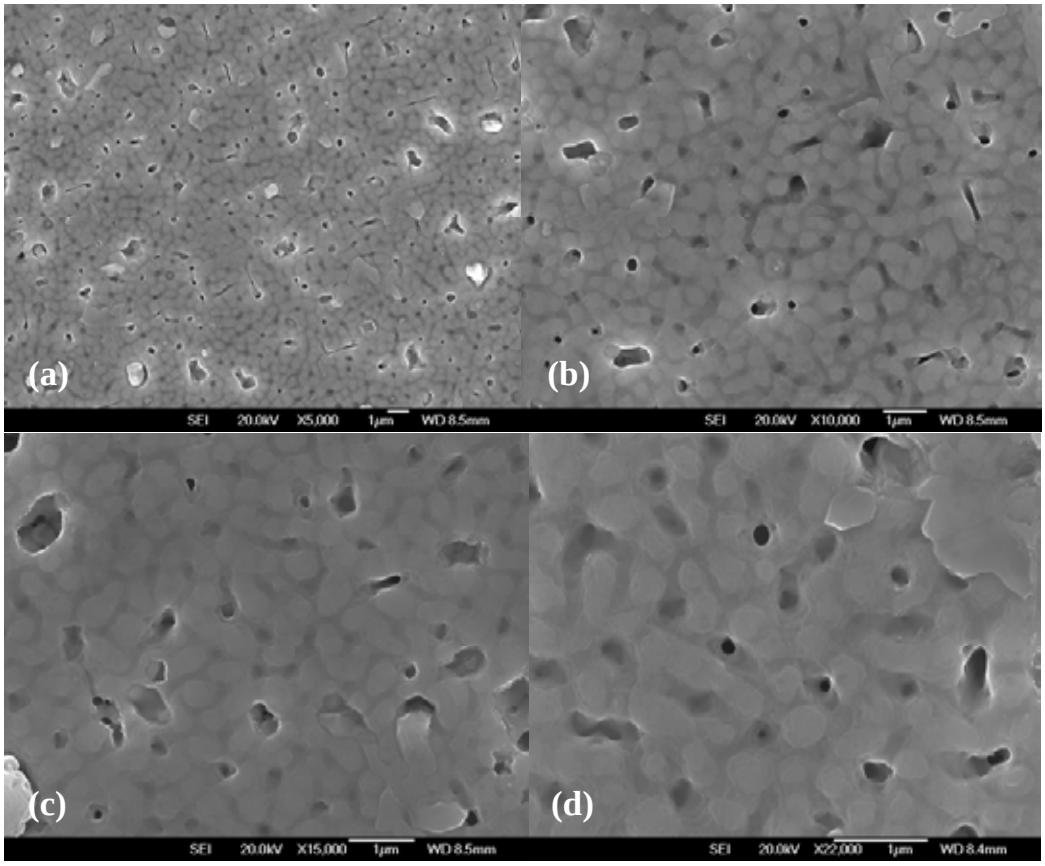

Figure 6.47. SEM images of YB7 with 1.6 μm thick film, taken at magnifications (a) 5000x, (b) 10 000x, (c) 15 000x and (d) 22 000x

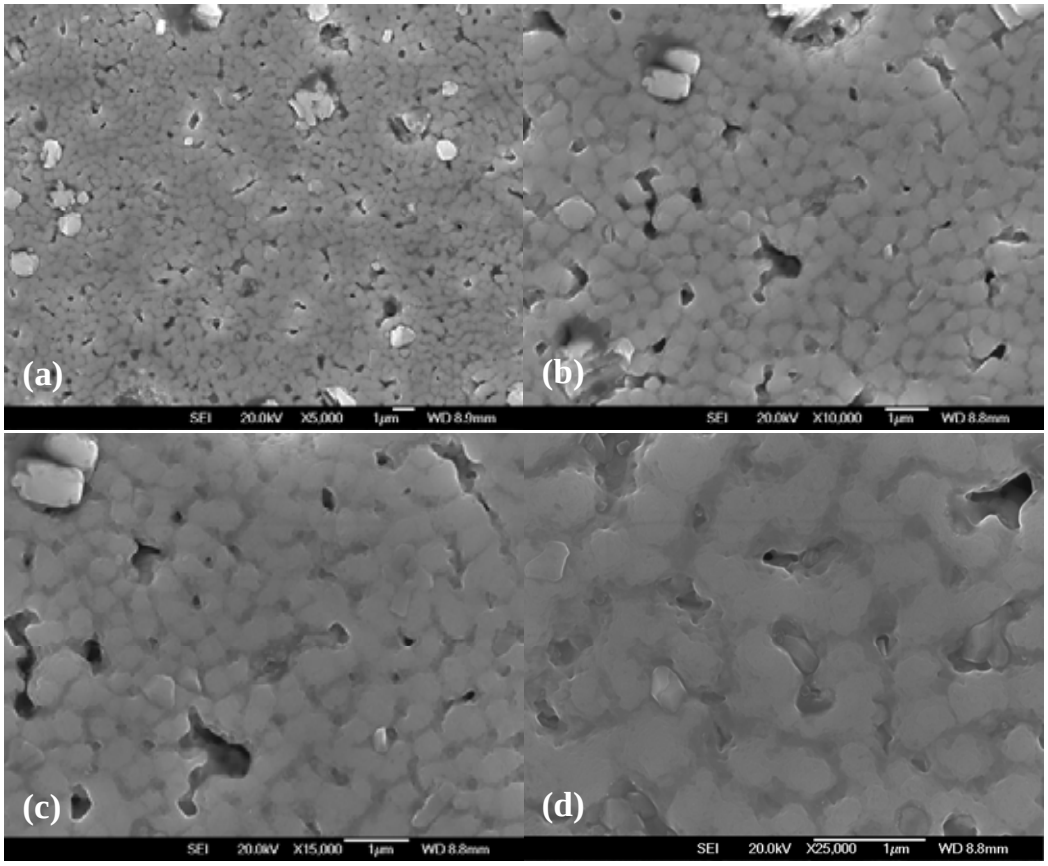

Figure 6.48. SEM images of YB8 with 2.0 μm thick film, taken at magnifications (a) 5000x, (b) 10 000x, (c) 15 000x and (d) 25 000x

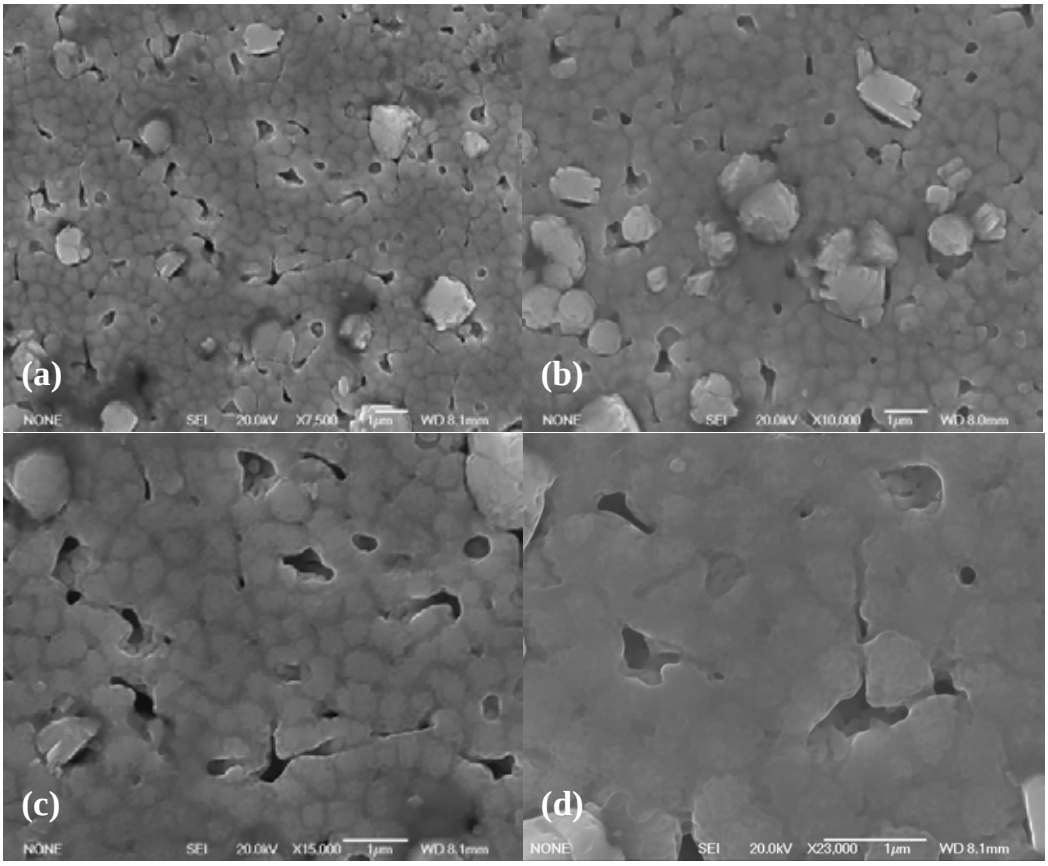

Figure 6.49. SEM images of YB9 with 2.2 μm thick film, taken at magnifications (a) 7500x, (b) 10 000x, (c) 15 000x and (d) 23 000x

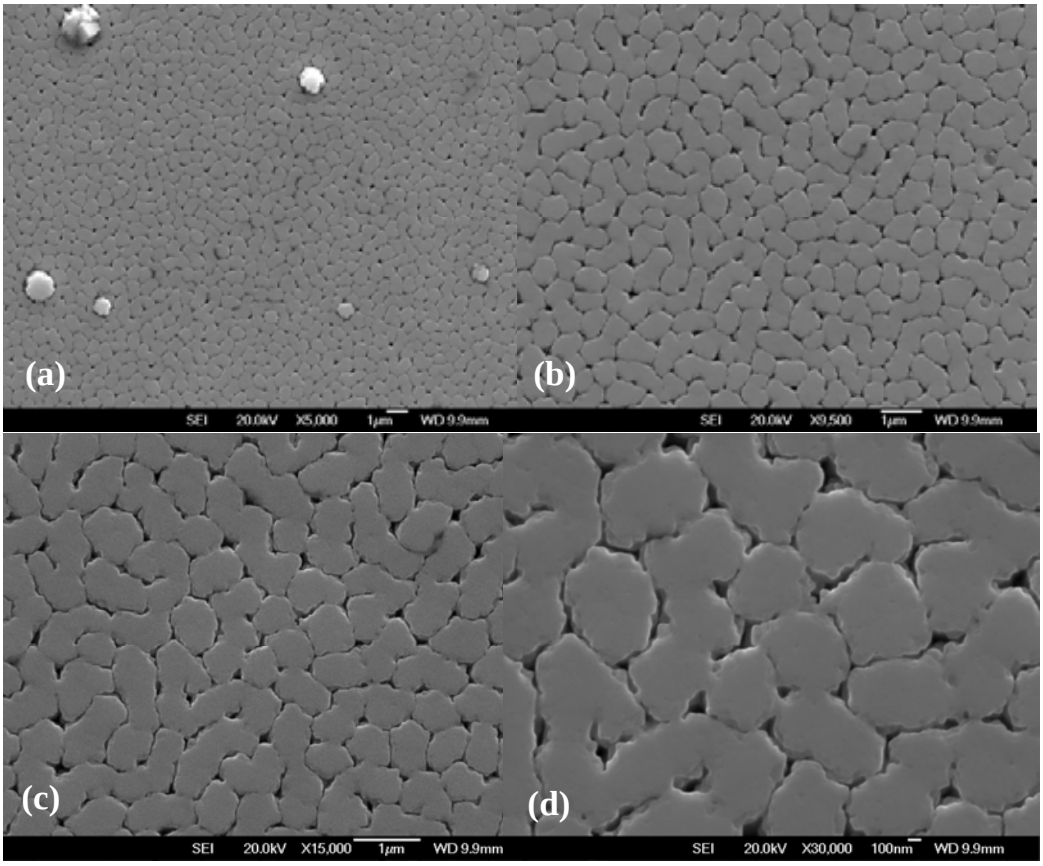

Figure 6.50. SEM images of YB10 with 2.65 μm thick film, taken at magnifications (a) 5000x, (b) 9 500x, (c) 15 000x and (d) 30 000x

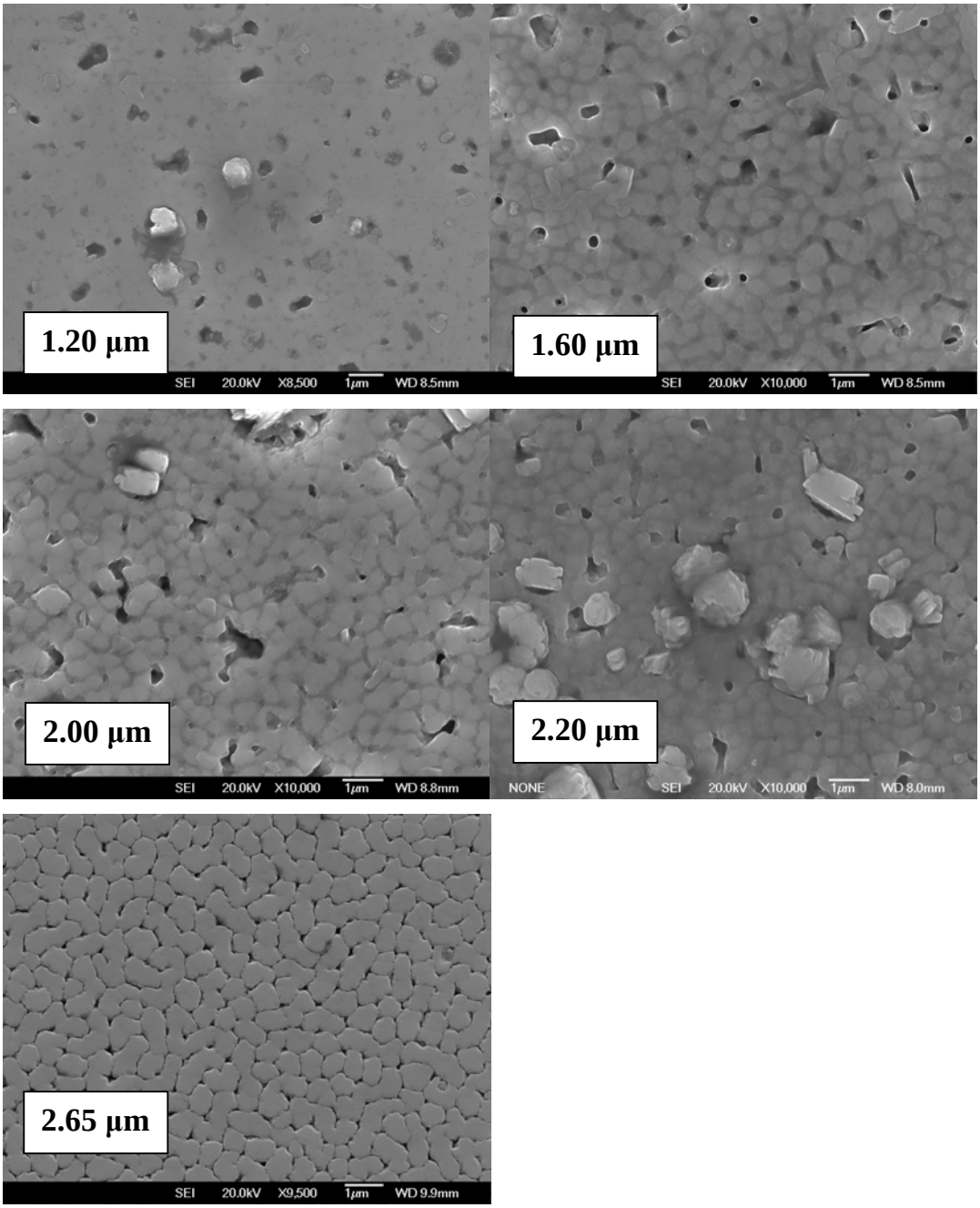

Figure 6.51. SEM images of YB6 to YB10 films at various thicknesses

6.5.3 EDS analysis

To investigate the elemental concentration in the BZO doped films, EDS analysis was performed on one of the best films YB6 (1.2 μm) which has the highest J_c. As seen in Table 6.6, the resulting chemical composition for Zr is around 1.5 wt. %. The compositional analysis shows a Zr concentration smaller than the nominal value. It may be caused by the gathering of the fine particles of BZO between grains. This is similar to what has been observed for 2 wt% BZO doped films. Further investigation and analysis need to be done by using electron backscattering diffraction, EBSD.

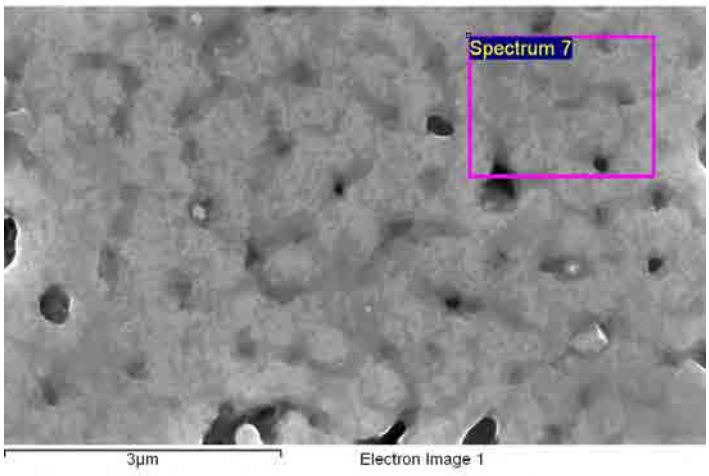

Figure 6.52. SEM-EDS spectrum position of YB6 film

Table 6.6. Quantitative elemental analysis of YB6 film obtained by EDS analysis from SEM-EDS spectrum as seen in Figure 6.52.

Element	Weight %	Error %
O	15.87	1.5
Cu	26.68	2.2
Y	14.54	1.6
Zr	1.54	1.0
Ba	41.37	3.5

6.5.4 TEM analysis

Figure 6.53 shows a cross-sectional TEM image of the 4 wt% $BaZrO_3$ doped YB6 film with a thickness of 1.2 μm. The $BaZrO_3$ nano-rod (marked by white arrow) structures are much more clearly observed in the YBCO film. The $BaZrO_3$ nano-rods are visible as long dark features of a width of about 5–10 nm. The dense $BaZrO_3$ nano-rods align along the c-axis of YBCO (marked by arrow). The dense nano-rods are not clearly observed in 2 wt% $BaZrO_3$ doped film in Figure 6.42. This result agrees with a study of Atura et al. where the density of the $BaZrO_3$ nano-rods was confirmed to increase with increasing $BaZrO_3$ content in the ablation target [216].

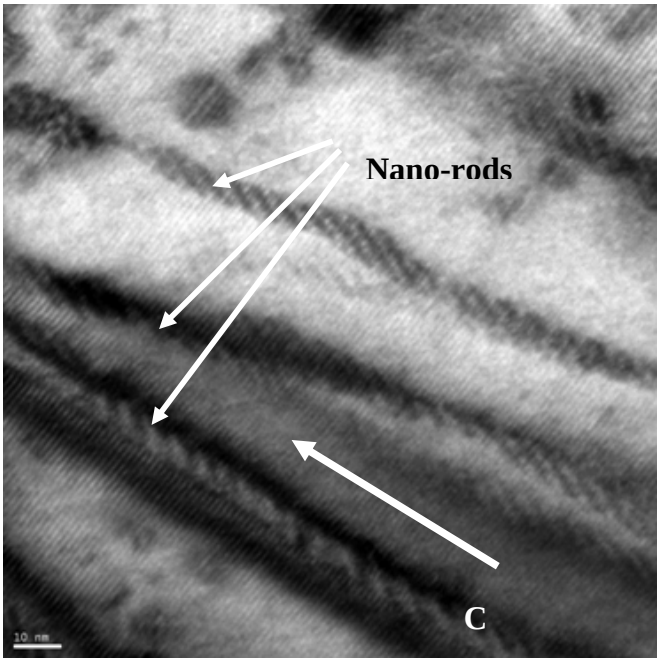

Figure 6.53. TEM image of cross-sectional area inside YB6 film. The *c*-axis direction is shown in the right corner.

6.5.5 EBSD mapping analysis

In order to investigate the phase distribution, the film surface of YB7 was scanned at 200,000 magnifications with a scale of 200 nm. The mapping analysis has been performed to analyse the distribution of the 4 wt.% $BaZrO_3$ in the film. The first map shown in (a) is a so-called image quality map.

Figure 6.54(b) presents the $BaZrO_3$ phase distribution map in pink with a content of 3.6 %. This result reveals that the $BaZrO_3$ phase distribution is close with the nominal value of 4 wt.%.

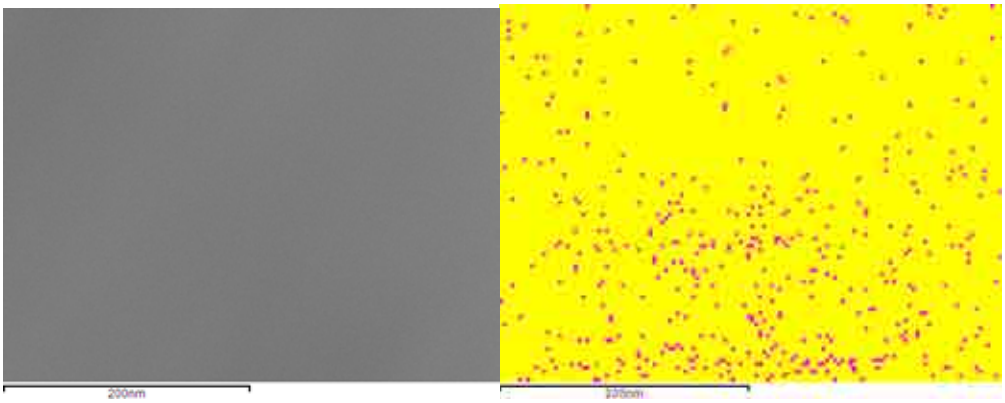

(a) (b)

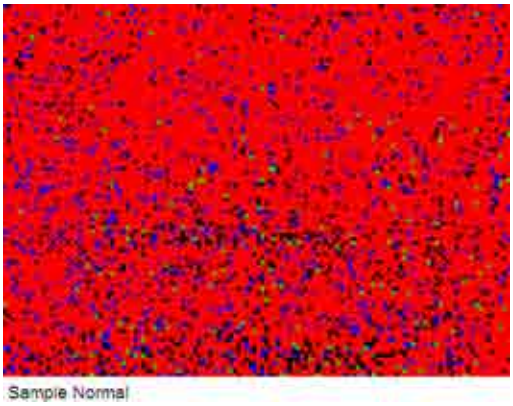

(c)

Figure 6.54. EBSD of $BaZrO_3$ mapping of 4 wt% $BaZrO_3$ (YB6) film (a) the image quality, (b) the $BaZrO_3$ phase in pink, (c) the YBCO phase in red and blue

6.6 Summary

According to the results discussed above there is a clear enhancement of J_c and F_p between BZO doped and pure YBCO films. A decrease of T_c was discovered for both BZO doped films compared to the pure YBCO film. The above results disclose that, in terms of J_c in magnetic field performance, BZO affects the flux pinning at different temperatures and fields. It has been shown that the 2 wt% BZO are more beneficial to the flux pinning force at high temperatures and low thickness. The results also show that the thicker films can maintain their J_c very well especially at higher fields up to 3.6 T.

Since for many applications the important parameter is the critical current in applied fields, it should be noted that with increasing 2 wt% BZO doped film thickness from 1.29 to 3.45 μm, I_c also continuously increases from 200 to 400 A at 77.3 K. The maximum F_p value in this study reaches 21 GN/m^3 at 2.8 T and 65 K. This enormous F_p value is achieved by the enhancement of J_c according to the effective pinning centres. From AC susceptibility measurements it is found that the frequency-dependent critical current density is also significantly increased in the YB6 1.2 μm thick film grown from the 4 wt% BZO doped target, and the above mentioned dependence is linear in a double-logarithmic plot, which is consistent with a logarithmic dependence of pinning potential on the current density.

On the other hand, the surface of the 4 wt% BZO doped film has bigger grains in comparison to the fine grains of the 2 wt% BZO doped films. This is another factor that can limit the J_c. It is interesting to examine the film's thickness dependent behaviour on the critical current density since both crystallinity degradation and structural roughness

have been considered to be factors that might cause the critical current density to decrease with increasing thickness [217].

Scaling of the flux pinning force based on the Dew-Hughes model has been established in this work. By using this method, the flux pinning mechanism in BZO doped films can be investigated more systematically and accurately. For example in high T_c superconductors, there may exist several different multi-elementary pinning mechanisms. A remarkable improvement of the pinning force, $F_{p,}$ is seen for both 2 wt% BZO and 4 wt% BZO films, presumably caused by multi-elementary pinning mechanism.

The Dew-Hughes pinning analysis shows that normal point and normal surface pinnings contribute for the thinnest 2 wt% BZO doped film. The normal point pinning becomes the dominant mechanism to enhance flux pinning in the 2 wt% BZO doped films and seems to mainly arise from the defects introduced due to BZO doping. These normal point defects are thought to develop from the non-superconducting state caused by $BaZrO_3$ doping to the YBCO superconducting layer. However three different pinning mechanisms (point $\Delta\kappa$, normal surface and normal point) were found for the 4 wt% BZO doped films.

From the EBSD mapping analysis, the distribution of 2 wt.% and 4 wt.% of $BaZrO_3$ are quite decent with 1.6 % and 3.6 %, respectively. It is evident that the $BaZrO_3$ nano particles are in a random distribution with good ratio.

Chapter 7

Conclusions and Future Work

7.1 Introduction

Thin films of the high temperature superconductor $YBa_2CuO_{7-\delta}$ offer potential applications in the fabrication of superconducting electronics and large current carrying power engineering wires and tapes. Since the superconducting properties of $YBa_2Cu_3O_{7-x}$ (Y123) films are very sensitive to the deposition conditions, the values of T_c are highly dependent on several important conditions, such as the laser energy (E), oxygen pressure (O_p), substrate temperature (T_s), distance between target and substrate (D_t), annealing oxygen pressure (O_{ap}) and cooling time (cooling rate) (C_t). Proper combination of these conditions could lead to high quality films. It is found that T_s of 780° C, E ~ 218 mJ/pulses,

D_t about 55 mm, O_{ap} 450 Torr and C_t 8°/min are the optimum condition in making good films with T_c of 91 K . The XRD results have revealed 100 % (*00l*) orientation. The highest J_c gives values of 2.8 $MAcm^{-2}$ in self-field and 0.8$MAcm^{-2}$ at 1 Tesla at this condition. In situ high temperature annealing carried out immediately after the deposition with optimum oxygen pressure and cooling rate is proven to be effective to obtain high T_c and J_c.

From the microstructure observations by SEM analysis at different annealing oxygen pressures, the presence of white spots with maximum diameter of approximately 0.5 μm is typical in all areas of these films. It is likely that these particles originate from the targets. However, the white spots become less frequent for the films with O_{ap} of 450 and 650 Torr. Films with high annealing oxygen pressure (optimised condition) exhibit droplets with a granular surface. Spherically shaped features and irregular pores with sizes of 150-350 nm can also be seen. All the AFM images of films exhibited a clear texture of growth islands.

The surface roughness of the YBCO films is mainly affected by the growth temperature and the oxygen pressure [176]. The smoothest root mean square (RMS) roughness of the film shows the minimum value of approximately 2.403 nm for the film grown at T_s of 780° C with average height of 17.28 nm. All the grains seem to be well connected. From the surface morphology by AFM at different deposition temperatures, the apparent trenches between growth islands are irregular with various dimensions for films with different deposition temperatures. The deepest trenches were found for the film deposited at 820° C.

In this work a method in introducing artificial pinning centres has been approached, which is proven to be successful in the nanotechnology of pinning centres: distributing a

secondary phase in the film by modifying the target composition. Three target compositions have been used: YBCO with 1% $Gd_2Ba_4CuWO_y$ (2411W) nano-phase inclusions and nano-crystalline YBCO doped with 2 and 4% wt $BaZrO_3$ (BZO). All of the obtained optimised conditions have been used to grow all the films relating to the effect of Gd2411 and BZO additions on the flux pinning that are summarised in the followings.

The $YBa_2Cu_3O_{7-x}$ / $Gd_2Ba_4CuWO_{12}$ films grown on STO single crystal substrates revealed a significant enhancement in the critical current density at temperatures exceeding 50 K compared to pure YBCO films. This impressive enhancement of J_c in high fields is due to the artificial pinning centres induced by the $Gd_2Ba_4CuWO_{12}$ nano-inclusions. However, as the film thickness increases above 1 μm, a significant reduction of J_c was observed in all Gd2411 films which become even lower than the J_c of 0.96 μm-thick pure YBCO film. From XRD analysis, there is no evidence to indicate the presence of Gd2411W since the amount of Gd2411W phase is very small, unlike the case in which XRD indicated the presence of Y2411Nb phase in a composite film with a much larger amount (15 mol%) of secondary phase [200].

The magnitude of the flux pinning force ($F_{p,}$ max) increases as the film thickness decreases because of the contribution of the strong-pinning interface layer. F_p, max = 1.77 GN/m^3 is more than two times higher for the thinnest film YG1 (0.78 μm) as compared with F_p, max = 0.51 GN/m^3 for the thickest film YG6 (2.65 μm). The peak in F_p shifted to higher magnetic fields as the thickness was increased. This is possibly due to different pinning mechanisms that dominate at different thicknesses in $YBa_2Cu_3O_{7-x}$/$Gd_2Ba_4CuWO_{12}$ films. The enhancement in the flux pinning force in the $YBa_2Cu_3O_{7-x}$/$Gd_2Ba_4CuWO_{12}$ films (compared with the pure YBCO film) can be explained as a result of the presence of $Gd_2Ba_4CuWO_{12}$ nano-inclusions in the intergrain regions. This in turn causes

the increase of intergrain contact surface [193] (decreasing the intergrain resistance) and increases the number of flux pinning centres due to the presence of $Gd_2Ba_4CuWO_{12}$ particles in the intergrain regions and results in an enhancement of J_c even in the presence of higher magnetic field.

The model of Dew-Hughes is a direct summation model of the elementary pinning forces and predicts many forms of pinning types. The Dew-Hughes model is used because there are various pinning mechanisms acting concurrently in YBCO film and it is important to find the dominating one. The position of the peak in the pinning force, F_p, dependence on the reduced field is at $b = 0.2$ for the thinner films (0.78 μm and 0.96 μm), meaning that normal surface pinning centre is dominant. This is also supported by the larger value of the scaling parameter A_1 as compared with A_2. The results of pinning force scaling in the Dew-Hughes model for the thicker films (1.29 μm to 2.65 μm) show that $\Delta\kappa$ point pinning is the dominant pinning mechanism. In this case, the source of $\Delta\kappa$ point pinning could be from the small-scale variations (n) of T_c. Several researchers found evidence for δT_c or $\Delta\kappa$ point pinning mechanism in Pr-doped YBCO and (K,Ba)BiO_3 single crystal film [197]. Several possible explanations for this behaviour have been proposed: a minority secondary superconducting phase with a slightly lower critical temperature appears to form during the PLD growth process due probably to the substitution of compatible atoms between YBCO and 2411W (Gd with Y, as suggested also from EDS analysis). This phase may provide some additional pinning centres of δT_c-type, in addition to those associated with the Gd2411W nano-inclusions.

For the $YBa_2Cu_3O_{7-x}$/BZO films, it is found that there is a clear enhancement of J_c and F_p between BZO doped and pure YBCO films. A decrease of T_c was discovered for both BZO doped films compared to the pure YBCO film. In terms of J_c in magnetic field

performance, BZO affects the flux pinning at different temperatures and fields. It is shown that the 2 wt% BZO are more beneficial to the flux pinning force at high temperatures and low thicknesses. The results also show that the thicker films can maintain their J_c very well especially at higher fields up to 3.6 T.

Since for many applications the important parameter is the critical current in applied fields, it should be noted that with increasing thickness of the 2 wt% BZO doped film from 1.29 to 3.45 μm, I_c also continuously increases from 200 A to 400 A at 77.3 K. The maximum F_p value in this study reaches 21 GN/m^3 at 2.8 T and 65 K. This enormous F_p value is achieved by the enhancement of J_c according to the effective pinning centres. From AC susceptibility measurements it is found that the frequency-dependent critical current density is also significantly increased in the YB6 1.2 μm thick film grown from the 4 wt% BZO doped target, and the above mentioned dependence is linear in a double-logarithmic plot, which is consistent with a logarithmic dependence of pinning potential on the current density.

A remarkable improvement of the pinning force, F_p, is seen for both 2 wt% and 4 wt% BZO films, presumably caused by multi-elementary pinning mechanism. The Dew-Hughes pinning analysis shows that normal point and normal surface pinning contribute for the thinnest 2 wt% BZO doped film. The normal point pinning becomes the dominant mechanism to enhance flux pinning in the 2 wt% BZO doped films and seems to mainly arise from the defects introduced due to BZO doping. These normal point defects are thought to develop from the non-superconducting state caused by $BaZrO_3$ doping to the YBCO superconducting layer. However three different pinning mechanisms (point $\Delta\kappa$, normal surface and normal point) were found for the 4 wt% BZO doped films.

7.2 Recommendations for future work

It is recommended to undertake further researches in the following areas based on observations regarding the theoretical and experimental results.

To ensure that the highly energised particles hit more closely and precisely perpendicular to the substrate position during the laser ablation, some modification on the substrate stage holder needs to be done. Modification of the stage holder with some mechanical adjustable positions will allow greater flexibility in positioning the substrate on the x and y axes during the deposition. It should save time and improve the deposition procedure in order to grow better quality epitaxial films.

This study has shown that a small amount of 1 mol % $Gd_2Ba_4CuWO_y$ (the '2411' phase) addition in $Y_1Ba_2Cu_3O_{7-\delta}$ films improves the J_c and flux pinning force values in films with several different thicknesses. $Y_1Ba_2Cu_3O_{7-\delta}$/ $Gd_2Ba_4CuWO_y$ has drawn great attention since they are known to possess good flux pinning centres. Further work should be focused on modifying the percentage addition of $Gd_2Ba_4CuWO_y$. By adding various percentages of $Gd_2Ba_4CuWO_y$ phase in YBCO, the correlation between superconducting properties and density and type of nano-addition can be deduced. Further TEM would be of interest to study the effect of thickness on the $Gd_2Ba_4CuWO_y$ phase in the YBCO film.

Further AC susceptibility measurements on the frequency-dependent critical current in fields parallel to the *c*-axis and on the pinning potential can be measured on other 2 wt% BZO-doped films at different thicknesses. It would be interesting to examine the film's thickness dependent behaviour on the effective pinning potential, U_0, to obtain a better understanding of this dependence.

Other important features, which determine the formation of nano-rod or nano-dot within 2 wt% BZO-doped films and 4 wt% BZO-doped films at different thicknesses, are worthy of study. Formation of nano rods or nano dots and its evolution in YBCO film films can be studied by TEM and EBSD. Further detailed work on cross sectional TEM analysis for 2 wt% BZO-doped films and 4 wt% BZO-doped films at different thicknesses would also be useful for microstructure analysis.

The orientation of the crystalline grains within $Y_1Ba_2Cu_3O_{7-\delta}$ films with nano-inclusions could affect their current-carrying capability. As a result, the microstructures of these films are of great interest to be further studied. Several researchers have observed that growth on a (001)-type surface of a reasonably lattice-matched substrate (such as SrTiO,) promotes an epitaxy at the interface in which the *c*-axis of $Y_1Ba_2Cu_3O_{7-\delta}$ is perpendicular to the substrate surface [218-220]. However, in the thicker films, 90° boundaries always occur, bringing about a transition to a region in which the *a* or *b* axes of the film are perpendicular to the substrate and the *c*-axis lies parallel to the surface. The understanding and control of orientation development in these films thicknesses would be worthy of investigation.

APPENDIX

Eq. (4.1) can be rewritten as $\ln J = \ln J_0 - b\ln\left(\frac{t}{t_0}\right)$, where t is the time, $t_0 = f_0^{-1}$ and J_0 is the critical current density in the absence of thermally-activated flux creep, or

$$J = J_0\left(\frac{t}{t_0}\right)^{-b}. \qquad (1)$$

In an inductive circuit, the voltage V is proportional to the time-derivative of the current[28], and, from eq. (1), is given by

$$V \propto \frac{dJ}{dt} = -bJ_0 t_0^{-1}\left(\frac{t}{t_0}\right)^{-(b+1)}. \qquad (2)$$

In the thermally-activated flux creep regime, the dissipation (voltage) is proportional to the probability of flux jumping over the pinning barrier:

$$V \propto e^{-\frac{U_{eff}}{k_B T}} \qquad (3)$$

From eqs. (2) and (3), replacing U_{eff} from eq. (5), one has:

$$-bJ_0 t_0^{-1}\left(\frac{t}{t_0}\right)^{-(b+1)} = C\exp\left[-\frac{U_0}{k_B T}\ln\left(\frac{J^*}{J}\right)\right] = C\exp\left\{\ln\left[\left(\frac{J^*}{J}\right)^{-\frac{U_0}{k_B T}}\right]\right\} = C\left(\frac{J^*}{J}\right)^{-\frac{U_0}{k_B T}} \qquad (4)$$

Introducing the current density J from eq. (1), the above equation becomes:

$$-bJ_0 t_0^{-1}\left(\frac{t}{t_0}\right)^{-(b+1)} = C\left(\frac{J^*}{J_0}\right)^{-\frac{U_0}{k_B T}}\left(\frac{t}{t_0}\right)^{-b\frac{U_0}{k_B T}} \qquad (5)$$

For eq. (5) to hold for any value of the variable time, it is necessary that the exponents of (t/t_0) in both sides are equal, hence $U_0/k_B T = 1+1/b$.

REFERENCES

1. A. Robert, A. Hawsey, K. David, and Christena, *Progress in Research, Development, and Pre-Commercial Deployment of Second Generation Hts Wires in the USA* Physica C-Superconductivity and Its Applications, 2006. **445-448**: p. 488-495.

2. M.M. Awang Kechik, R. Abd-Shukor, S.A. Halim, and A. Masrianis, *Transport Critical Current Density of ($Bi_{1.6}$ $Pb_{0.4}$) $Sr_2Ca_2Cu_3O_\delta$ Superconductor by Fe_3O_4 Addition.* J. Solid St. Sci. and Technol. Letters, 2006. **13**(1): p. 232-236.

3. D.M. Feldmann, *Grain Orientations and Grain Boundary Networks of $YBa_2Cu_3O_{7-\delta}$ Films Deposited by Metalorganic and Pulsed Laser Deposition on Biaxially Textured Ni-W Substrates.* Journal of Materials Research, 2006. **21**: p. 923-934

4. M. J. Van Bael, L. Van Look, K. M. Lange, G. Temst, V.V. Guntherodt, Moshchalkov, and Y. Bruynseraede., *Vortex Self-Organization in the Presence of Magnetic Pinning Arrays.* J. of Superconductivity: Incorporating Novel Magnetism, 2001. **14**(2).

5. R. P. Aloysius, P. Guruswamy, and U. Syamaprasad, *Highly Enhanced Critical Current Density in Pr-Added (Bi, Pb)-2212 Superconductor.* Superconductor Science and Technology, 2005. **18**: p. L23–L28.

6. Y.K.a.T.I. Yuh Shiohara, *Highlights in R&D for Coated Conductors in Japan* Physica C-Superconductivity and Its Applications, 2006. **445-448**: p. 496-500.

7. A. Goyal, Norton, D. P., Budai, J. D., Paranthaman, M.; Specht, E. D.,Kroeger, D. M.; Christen, D. K.; He, Q., Saffian, B.; List, F. A.; Lee, D. F., Martin, P. M., Klabunde, C. E., Hartfield, E., and Sikka, V. K., *High Critical Current Density Superconducting Tapes by Epitaxial Deposition of $YBa_2Cu_3O_x$ Thick Films on Biaxially Textured Metals.* Appl. Phys. Lett, 1996. **69**(12): p. 1795-1797.

8. A. Goyal, D. F. Leea, F. A. Lista, E. D. Spechta, R. Feenstraa, M. Paranthamana, X. Cuib, S. W. Luc, P. M. Martina, D. M. Kroegera, D. K. Christena, B. W. Kanga, D. P. Nortond, C. Parke, D. T. Verebelyib, J. R. Thompsona, R. K. Williamsa, T. Aytuga, and C. Cantonia, *Recent Progress in the Fabrication of High-J_c Tapes by Epitaxial Deposition of YBCO on Rabits.* Physica C-Superconductivity and Its Applications, 2001. **357-360**(Part 2): p. 11.

9. Y. Iijima, K. Kakimoto, and K. Takeda, *Long Length Ion-Beam-Assisted Deposition Template Films for Y-123 Coated Conductors.* Physica C-Superconductivity and Its Applications, 2001. **357-360**(Part 2,).

10. K. Hasegawaa, K. Fujinoa, H. Mukaia, M. Konishia, K. Hayashia, K. Satoa, S. Honjob, Y. Satob, H. Ishiib and Y. Iwatab *Biaxially Aligned YBCO Film Tapes*

Fabricated by All Pulsed Laser Deposition. Applied Superconductivity 1996. **4**(10-11).

11. D.G. Larbalestier, A.; Feldmann, D. M.; Polyanskii A., *High-Tc Superconducting Materials for Electric Power Applications.* Nature Materials, 2001. **414**(6861).

12. H.W.a. R.W.Ralston, *The New Superconducting Electronics*1993, Netherlands: Kluwer Academic Publishers.

13. A. Crisan, S. Fujiwara, J.C. Nie, A. Sundaresan, and H. Ihara, *Sputtered Nanodots: A Costless Method for Inducing Effective Pinning Centers in Superconducting Thin Films.* Applied Physics Letters, 2001. **79**(27): p. 4547-4549.

14. M.E. Gross, M. Hong, S.H. Liou, P.K. Gallagher, and J. Kwo, *Versatile New Metalorganic Process for Preparing Superconducting Thin-Films.* Applied Physics Letters, 1988. **52**(2): p. 160-162.

15. F.J. Owens and J. Charles P. Poole, *The New Superconductors*2002: Kluwer Academic Publishers. 216.

16. J.G. Bednorz and K.A. Muller, *Possible High Tc Superconductivity in the Ba-La-Cu-O System.* Z. Phys. B. Condens. Matter 1986. **64**.

17. M.K. Wu, J.R. Ashburn, C.J.Tong, P.H. Hor, R.L. Meng, L.Gao, Z.J.Huang, Y.Q. Wang, and C.W.Chu, *Superconductivity at 93k in a New Mixed-Phase Y-Ba-Cu-O Compund System at Ambient Pressure.* Physical Review Letters, 1987. **58**(9): p. 908-910.

18. H. Maeda, Tanaka, Y., Fukotomi, M & Asano, T. , *A New High T_c Oxide Superconductor without Rare Earth Elemant.* Jpn. J. Appl. Phys, 1988. **27**.

19. Z.Z. Sheng and A.M.Hermann, *Bulk Superconductor at 120k in Ti-Ca/Ba-Cu-O System.* Nature, 1988. **232**: p. 138-139.

20. A. Schilling, M. Cantoni, J.D. Guo, and H.R. Ott, *Superconductivity above 130 K in the Hg-Ba-Ca-Cu-O System.* Nature, 1993. **363**.

21. R. Innes, A. Christoper, and E.H. Rhoderick, *Introduction to Superconductivity*1978: Pergamon Press.

22. *BCS Theory of Superconductivity.* http://hyperphysics.phy-astr.gsu.edu/hbase/solids/bcs.html.

23. A.M. Campbell and J.E. Evetts, *Flux Vortices and Transport Current in Type-Ii Superconductors.* Adv. Phys., 1972. **21**: p. 194-428.

24. A. A. Gapud, D. Kumar, S. K. Viswanathan, C. Cantoni, M. Varela, J. Abiade, S. J. Pennycook, and D.K. Christen, *Enhancement of Flux Pinning in $YBa_2Cu_3O_{7-\delta}$ Thin*

Films Embedded with Epitaxially Grown Y_2O_3 Nanostructures Using a Multi-Layering Process Superconductor & Science Technology, 2005. **18**: p. 1502-1505.

25. V.Kovachev, *Application Problems of High Current Superconducting Materials.* Materials Science: Materials in Electronics, 2003. **14**(10-12).

26. D.J. Bishop, P.L. Gammel, and D.A. Huse, *Resistance in High-Temperature Superconductors.* Scientific American, 1993. **268**(2): p. 48-55.

27. R. Abd-Shukor, *Introduction to Superconductivity in Metals, Alloys and Cuprates* 2004: UPSI Publisher.

28. M. Tinkham, *Introduction to Superconductivity*. Second ed1996: McGraw Hill. 472.

29. H. Yamasaki, K. Ohki, H. Yamada, Y. Nakagawa, and Y. Mawatari, *Strong Flux Pinning in $YBa_2Cu_3O_{7-\delta}$ Thin Films Due to Nanometer-Sized Precipitates.* Superconductor Science & Technology, 2008. **21**(12): p. -.

30. M.H. Pu, Y. Feng, P.X. Zhang, L. Zhou, and J.X. Wang, *Investigating the Flux Pinning in High Temperature Superconductors More Accurately.* Physica C-Superconductivity and Its Applications, 2003. **386**: p. 47-51.

31. D.D. Hughes, *Flux Pinning Mechanism in Type II Superconductors*, in *Philosophical Magazine* 1974, Taylor & Francis: England.

32. C. Gerber, D. Anselmetti, J.G. Bednorz, J. Mannhart, and D.G. Schlom, *Screw Dislocations in High-Tc Films.* Nature, 1991. **350**(6316): p. 279-280.

33. M. Hawley, I.D. Raistrick, J.G. Beery, and R.J. Houlton, *Growth-Mechanism of Sputtered Films of $YBa_2Cu_3O_{7-\delta}$ Studied by Scanning Tunneling Microscopy.* Science, 1991. **251**(5001): p. 1587-1589.

34. J. Mannhart, D. Anselmetti, J.G. Bednorz, A. Catana, C. Gerber, K.A. Muller, and D.G. Schlom, *Correlation between J_c and Screw Dislocation Density in Sputtered $YBa_2Cu_3O_{7-\delta}$ Films.* Zeitschrift Fur Physik B-Condensed Matter, 1992. **86**(2): p. 177-181.

35. J.L. Macmanus-Driscoll, S.R. Foltyn, Q.X. Jia, H. Wang, A. Serquis, L. Civale, B. Maiorov, M.E. Hawley, M.P. Maley, and D.E. Peterson, *Strongly Enhanced Current Densities in Superconducting Coated Conductors of $YBa_2Cu_3O_{7-\delta}$ $+BaZrO_3$.* Nature Materials, 2004. **3**(7): p. 439-443.

36. K.S. Harshavardhan, M. Rajeswari, D.M. Hwang, C.Y. Chen, T. Sands, T. Venkatesan, J.E. Tkaczyk, K.W. Lay, and A. Safari, *Dominant Pinning Mechanisms in $YBa_2Cu_3O_{7-\delta}$ Films on Single and Polycrystalline Yttria Stabilized Zirconia Substrates.* Applied Physics Letters, 1992. **60**(15): p. 1902-1904.

37. T.L. Hylton and M.R. Beasley, *Flux-Pinning Mechanisms in Thin Films of $YBa_2Cu_3O_{7-\delta}$.* Physical Review B, 1990. **41**: p. 11669-11672.

38. T. Haage, J. Zegenhagen, J.Q. Li, H.U. Habermeier, M. Cardona, C. Jooss, R. Warthmann, A. Forkl, and H. Kronmuller, *Transport Properties and Flux Pinning by Self-Organization in $YBa_2Cu_3O_{7-\delta}$ Films on Vicinal Srtio3(001).* Physical Review B, 1997. **56**(13): p. 8404-8418.

39. C. Jooss, R. Warthmann, H. Kronmuller, T. Haage, H.U. Habermeier, and J. Zegenhagen, *Vortex Pinning Due to Strong Quasiparticle Scattering at Antiphase Boundaries in $YBa_2Cu_3O_{7-\delta}$.* Physical Review Letters, 1999. **82**(3): p. 632-635.

40. C. Jooss, R. Warthmann, and H. Kronmuller, *Pinning Mechanism of Vortices at Antiphase Boundaries in $YBa_2Cu_3O_{7-\delta}$.* Physical Review B, 2000. **61**(18): p. 12433-12446.

41. P.C. Mcintyre, M.J. Cima, J.A. Smith, R.B. Hallock, M.P. Siegal, and J.M. Phillips, *Effect of Growth-Conditions on the Properties and Morphology of Chemically Derived Epitaxial Thin-Films of $YBa_2Cu_3O_{7-\delta}$ on (001) $LaAlO_3$.* Journal of Applied Physics, 1992. **71**(4): p. 1868-1877.

42. K. Matsumoto and P. Mele, *Artificial Pinning Center Technology to Enhance Vortex Pinning in YBCO Coated Conductors.* Superconductor Science & Technology, 2010. **23**(1): p. -.

43. V.V. Moshchalkov, M. Baert, V.V. Metlushko, E. Rosseel, M.J. VanBael, K. Temst, R. Jonckheere, and Y. Bruynseraede, *Magnetization of Multiple-Quanta Vortex Lattices.* Physical Review B, 1996. **54**(10): p. 7385-7393.

44. A. Silhanek, L. Van Look, R. Jonckheere, B.Y. Zhu, S. Raedts, and V.V. Moshchalkov, *Enhanced Vortex Trapping by a Composite Antidot Lattice in a Superconducting Pb Film.* Physica C-Superconductivity and Its Applications, 2007. **460**: p. 1434-1435.

45. W. Gillijns, A.V. Silhanek, and V.V. Moshchalkov, *Superconducting Microrings as Magnetic Pinning Centers.* Applied Physics Letters, 2007. **91**(20): p. -.

46. A.V. Silhanek, W. Gillijns, M.V. Milosevic, A. Volodin, V.V. Moshchalkov, and F.M. Peeters, *Optimization of Superconducting Critical Parameters by Tuning the Size and Magnetization of Arrays of Magnetic Dots.* Physical Review B, 2007. **76**(10): p. -.

47. V.F. Solovyov, H.J. Wiesmann, L. Wu, Q. Li, L.D. Cooley, M. Suenaga, B. Maiorov, and L. Civale, *High Critical Currents by Isotropic Magnetic-Flux-Pinning Centres in a 3 Mu M-Thick $YBa_2Cu_3O_{7-\delta}$ Superconducting Coated Conductor.* Superconductor Science & Technology, 2007. **20**(4): p. L20-L23.

48. A. Crisan, P. Badica, S. Fujiwara, J.C. Nie, A. Sundaresan, Y. Tanaka, and H. Ihara, *Strong Reduction of Thermally Activated Flux Jump Rate in Superconducting*

Thin Films by Nanodot-Induced Pinning Centers. Applied Physics Letters, 2002. **80**(19): p. 3566-3568.

49. A. Crisan, P. Badica, S. Fujiwara, J.C. Nie, A. Sundaresan, A. Iyo, and Y. Tanaka, *Nanodots-Induced Pinning Centers in Thin Films: Effects on Critical Current Density, Activation Energy and Flux Jump Rate.* IEEE Transactions on Applied Superconductivity, 2003. **13**(2): p. 3726-3729.
50. P. Paturi, M. Peurla, K. Nilsson, and J. Raittila, *Crystalline Orientation and Twin Formation in YBCO Thin Films Laser Ablated from a Nanocrystalline Target.* Superconductor Science & Technology, 2004. **17**(3): p. 564-570.

51. T. Haugan, P.N. Barnes, R. Wheeler, F. Meisenkothen, and M. Sumption, *Addition of Nanoparticle Dispersions to Enhance Flux Pinning of the $YBa_2Cu_3O_{7-\delta}$ Superconductor.* Nature, 2004. **430**(7002): p. 867-870.

52. C. Cai, J. Hanisch, R. Huhne, V. Stehr, C. Mickel, T. Gemming, and B. Holzapfel, *Structural and Magnetotransport Properties of $YBa_2Cu_3O_{7-\delta}$ /Y_2O_3 Quasimultilayers.* Journal of Applied Physics, 2005. **98**(12)

.
53. H. Huhtinen, P. Paturi, and E. Lahderanta, *Enhancement of Critical Current by Post-Annealing of Thin YBCO Films Prepared by Laser Ablation from a Nanocrystalline Target.* Physics of Low-Dimensional Structures, 1999. **9-10**: p. 25-37.

54. P. Paturi, H. Huhtinen, K. Laajalehto, and R. Laiho, *Reason for High Critical Current in Thin YBCO Films Prepared by Laser Ablation from Nanostructured Target.* Superconductor Science & Technology, 2000. **13**(5): p. 622-628.

55. J. Raittila, M. Peurla, H. Huhtinen, P. Paturi, and R. Laiho, *High Pinning Potential in YBCO Thin Films Deposited from a Target Prepared from YBCO Nanopowder.* Physica C-Superconductivity and Its Applications, 2004. **408-10**: p. 647-648.

56. H. Huhtinen, M. Peurla, M.A. Shakhov, Y.P. Stepanov, P. Paturi, J. Raittila, R. Palai, and R. Laiho, *Superconducting Properties of Films Deposited from Micro-Nanocrystalline and Optimally BZO-Doped YBCO Targets.* IEEE Transactions on Applied Superconductivity, 2007. **17**(2): p. 3620-3623.

57. G.W. Crabtree and D.R. Nelson, *Vortex Physics in High-Temperature Superconductors.* Physics Today, 1997. **50**(4): p. 38-45.

58. G. Blatter, M.V. Feigel'man, V.B. Gershkenbein, A.I. Larkin, and V.M. Vinokur, *Vortices in High-Temperature Superconductors.* Rev. Mod. Phys., 1994. **66**: p. 1125-1388.

59. E.H. Brandt, *The Flux-Line-Lattice in Superconductors.* Reports on Progress in Physics, 1995. **58**(11): p. 1465-1594.

60. G. Blatter, *Vortex Matter.* Physica C, 1997. **282**: p. 19-26.

61. H. Safar, P.L. Gammel, D.A. Huse, D.J. Bishop, J.P. Rice, and D.M. Ginsberg, *Experimental-Evidence for a 1st-Order Vortex-Lattice-Melting Transition in Untwinned, Single-Crystal $YBa_2Cu_3O_{7-\delta}$.* Physical Review Letters, 1992. **69**(5): p. 824-827.

62. S. Watauchi, H. Ikuta, J. Shimoyama, and K. Kishio, *Observation of Resistivity Drops and the Vortex Phase Diagram in $Bi_2Sr_2CaCu_2O_y$.* Physica C, 1996. **259**(3-4): p. 373-378.

63. J.R. Schrieffer, *Handbook of High-Temperature Superconductivity: Theory and Experiment*, ed. J.S. Brooks2007, New York: Springer Science.

64. N. Khare, ed. *Handbook of High Temperature Superconductor Electronic*. 2003, Marcel Dekker: New York.

65. C.J. F.Weiss, *Second Generation of HTS Cables: Coated Conductors* European Superconductivity Summer School, Grenoble, 2009.

66. D.P. Norton, *Science and Technology of High-Temperature Superconducting Films.* Annual Review of Materials Science, 1998. **28**: p. 299-347.

67. F.C. Klaassen, G. Doornbos, J.M. Huijbregtse, R.C.F. van der Geest, B. Dam, and R. Griessen, *Vortex Pinning by Natural Linear Defects in Thin Films of $YBa_2Cu_3O_{7-\delta}$.* Physical Review B, 2001. **64**(18): p. 20.

68. S. Kohiki, S. Hatta, T. Kamada, A. Enokihara, T. Satoh, K. Setsune, K. Wasa, Y. Higashi, S. Fukushima, and Y. Gohshi, *X-Ray-Irradiation Enhanced Critical Current-Density and Strong Pinning Sites Created in $GdBa_2Cu_3O_{7-\delta}$ Thin-Films.* Applied Physics a-Materials Science & Processing, 1990. **50**(5): p. 509-514.

69. T.S. Wang, W. Peng, W.F. Hu, J.W. Xiong, Y.J. Tian, C. Lei, Y.F. Chen, L. Li, Y.Q. Zhou, Z. Zhao, and D.C. Li, *Formation and Orientation Control of Y_2O_3 Inclusions in Pulsed Laser Deposited $YBa_2Cu_3O_{7-\delta}$ a Films by Using a Melt-Textured Target.* Journal of Crystal Growth, 2003. **252**(4): p. 560-564.

70. J.C. Nie, H. Yamasaki, H. Yamada, Y. Nakagawa, K. Develos-Bagarinao, and Y. Mawatari, *Evidence for c-Axis Correlated Vortex Pinning in $YBa_2Cu_3O_{7-\delta}$ Films on Sapphire Buffered with an Atomically Flat CeO_2 Layer Having a High Density of Nanodots.* Superconductor Science & Technology, 2004. **17**(7): p. 845-852.

71. S.C. Wimbush, J.H. Durrell, R. Bali, R. Yu, H.Y. Wang, S.A. Harrington, and J.L. MacManus-Driscoll, *Practical Magnetic Pinning in YBCO.* IEEE Transactions on Applied Superconductivity, 2009. **19**(3): p. 3148-3151.

72. J.I. Martin, M. Velez, J. Nogues, and I.K. Schuller, *Flux Pinning in a Superconductor by an Array of Submicrometer Magnetic Dots.* Physical Review Letters, 1997. **79**(10): p. 1929-1932.

73. N.M. Strickland, N.J. Long, E.F. Talantsev, P. Hoefakkera, J.A. Xia, M.W. Rupich, W. Zhang, X. Li, T. Kodenkandath, and Y. Huang, *Nanoparticle Additions for Enhanced Flux Pinning in YBCO HTS Films.* Current Applied Physics, 2008. **8**(3-4): p. 372-375.

74. M.W. Rupich, D.T. Verebelyi, W. Zhang, T. Kodenkandath, and X.P. Li, *Metalorganic Deposition of YBCO Films for Second-Generation High-Temperature Superconductor Wires.* Mrs Bulletin, 2004. **29**(8): p. 572-578.

75. U. Schoop, M.W. Rupich, C. Thieme, D.T. Verebelyi, W. Zhang, X. Li, T. Kodenkandath, N. Nguyen, E. Siegal, L. Civale, T. Holesinger, B. Maiorov, A. Goyal, and M. Paranthaman, *Second Generation HTS Wire Based on Rabits Substrates and MOD YBCO.* Ieee Transactions on Applied Superconductivity, 2005. **15**(2): p. 2611-2616.

76. N. Long, N. Strickland, B. Chapman, N. Ross, J. Xia, X. Li, W. Zhang, T. Kodenkandath, Y. Huang, and M. Rupich, *Enhanced in-Field Critical Currents of YBCO Second-Generation (2G) Wire by Dy Additions.* Superconductor Science & Technology, 2005. **18**(12): p. S405-S408.

77. W. Zhang, Y. Huang, X. Li, T. Kodenkandath, M.W. Rupich, U. Schoop, D.T. Verebelyi, C.L.H. Thieme, E. Siegal, T.G. Holesinger, B. Maiorov, L. Civale, D.J. Miller, V.A. Maroni, J. Li, P.M. Martin, E.D. Specht, A. Goyal, and M.P. Paranthaman, *Control of Flux Pinning in MOD YBCO Coated Conductor.* IEEE Transactions on Applied Superconductivity, 2007. **17**(2): p. 3347-3350.

78. A. Goyal, S. Kang, K.J. Leonard, P.M. Martin, A.A. Gapud, M. Varela, M. Paranthaman, A.O. Ijaduola, E.D. Specht, J.R. Thompson, D.K. Christen, S.J. Pennycook, and F.A. List, *Irradiation-Free, Columnar Defects Comprised of Self-Assembled Nanodots and Nanorods Resulting in Strongly Enhanced Flux-Pinning in $YBa_2Cu_3O_{7-\delta}$ Films.* Superconductor Science & Technology, 2005. **18**(11): p. 1533-1538.

79. S. Horii, K. Yamada, H. Kai, A. Ichinose, M. Mukaida, R. Teranishi, R. Kita, K. Matsumoto, Y. Yoshida, J. Shimoyama, and K. Kishio, *Introduction of C-Axis-Correlated 1d Pinning Centers and Vortex Bose Glass in Ba-Nb-O-Doped $ErBa_2Cu_3O_y$ Films.* Superconductor Science & Technology, 2007. **20**(12): p. 1115-1119.

80. K. Yamada, A. Ichinose, S. Horii, H. Kai, R. Teranishi, M. Mukaida, R. Kita, S. Kato, Y. Yoshida, K. Matsumoto, and S. Toh, *Characterization of Nanorods in $BaNb_2O_6$-Doped Er123 Films Revealed by Cross-Sectional Transmission Electron Microscopy.* Physica C-Superconductivity and Its Applications, 2008. **468**(15-20): p. 1638-1642.

81. P. Mele, K. Matsumoto, A. Ichinose, M. Mukaida, Y. Yoshida, S. Horii, and R. Kita, *Systematic Study of the $BaSnO_3$ Insertion Effect on the Properties of*

$YBa_2Cu_3O_{7-\delta}$ Films Prepared by Pulsed Laser Ablation. Superconductor Science & Technology, 2008. **21**(12): p. -.

82. S.A. Harrington, J.H. Durrell, B. Maiorov, H. Wang, S.C. Wimbush, A. Kursumovic, J.H. Lee, and J.L. MacManus-Driscoll, *Self-Assembled, Rare Earth Tantalate Pyrochlore Nanoparticles for Superior Flux Pinning in $YBa_2Cu_3O_{7-\delta}$ Films.* Superconductor Science & Technology, 2009. **22**(2): p. -.

83. A. Crisan, P. Badica, S. Fujiwara, J.C. Nie, A. Sundaresan, A. Iyo, and Y. Tanaka, *Nanodots-Induced Pinning Centers in Thin Films: Effects on Critical Current Density, Activation Energy and Flux Jump Rate.* IEEE Transactions on Applied Superconductivity, 2003. **13**(2).

84. M. Ionescu, A.H. Li, Y. Zhao, H.K. Liu, and A. Crisan, *Enhancement of Critical Current Density in $YBa_2Cu_3O_{7-\delta}$ Thin Films Grown Using PLD on YSZ (001) Surface Modified with Ag Nano-Dots.* Journal of Physics D-Applied Physics, 2004. **37**(13): p. 1824-1828.

85. P. Mele, K. Matsumoto, T. Horide, O. Miura, A. Ichinose, M. Mukaida, Y. Yoshida, and S. Horii, *Tuning of the Critical Current in $YBa_2Cu_3O_{7-\delta}$ Thin Films by Controlling the Size and Density of Y_2O_3 Nanoislands on Annealed $SrTiO_3$ Substrates.* Superconductor Science & Technology, 2006. **19**(1): p. 44-50.

86. P. Mele, K. Matsumoto, T. Horide, A. Ichinose, M. Mukaida, Y. Yoshida, and S. Horii, *Insertion of Nanoparticulate Artificial Pinning Centres in $YBa_2Cu_3O_{7-\delta}$ Films by Laser Ablation of a Y_2O_3-Surface Modified Target.* Superconductor & Science Technology, 2007. **20**(7).

87. K. Matsumoto, T. Horide, A. Ichinose, S. Horii, Y. Yoshida, and M. Mukaida, *Critical Current Control in $YBa_2Cu_3O_{7-\delta}$ Films Using Artificial Pinning Centers.* Japanese Journal of Applied Physics Part 2-Letters & Express Letters, 2005. **44**(1-7): p. L246-L248.

88. T. Aytug, M. Paranthaman, A.A. Gapud, S. Kang, H.M. Christen, K.J. Leonard, P.M. Martin, J.R. Thompson, D.K. Christen, R. Meng, I. Rusakova, C.W. Chu, and T.H. Johansen, *Enhancement of Flux Pinning and Critical Currents in $YBa_2Cu_3O_{7-\delta}$ Films by Nanoscale Iridium Pretreatment of Substrate Surfaces.* Journal of Applied Physics, 2005. **98**(11).

89. J. Hanisch, C. Cai, R. Huhne, L. Schultz, and B. Holzapfel, *Formation of Nanosized $BaIrO_3$ Precipitates and Their Contribution to Flux Pinning in Ir-Doped $YBa_2Cu_3O_{7-\delta}$ Quasi-Multilayers.* Applied Physics Letters, 2005. **86**(12).

90. P.N.B. T. Haugan, I. Maartense, and C.B. Cobb, *Island Growth of Y_2BaCuO_5 Nanoparticles in (211<1.5 Nm/123<10 Nm)×N Composite Multilayer Structures to Enhance Flux Pinning of $YBa_2Cu_3O_{7-\delta}$ Films.* Material Reseacrh, 2003. **18**(11).

91. M. Tomita and M. Murakami, *High-Temperature Superconductor Bulk Magnets That Can Trap Magnetic Fields of over 17 Tesla at 29 K.* Nature, 2003. **421**(6922): p. 517-520.

92. G. Fuchs, P. Schatzle, G. Krabbes, S. Gruss, P. Verges, K.H. Muller, J. Fink, and L. Schultz, *Trapped Magnetic Fields Larger Than 14 T in Bulk $YBa_2Cu_3O_{7-\delta}$.* Applied Physics Letters, 2000. **76**(15): p. 2107-2109.

93. R.P. Sawh, Y. Ren, R. Weinstein, W. Hennig, and T. Nemoto, *Uranium Chemistry and Pinning Centers in High Temperature Superconductor.* Physica C-Superconductivity and Its Applications, 1998. **305**(3-4): p. 159-166.

94. S.R. Foltyn, Q.X. Jia, P.N. Arendt, L. Kinder, Y. Fan, and J.F. Smith, *Relationship between Film Thickness and the Critical Current of $YBa_2Cu_3O_{7-\delta}$ Coated Conductors.* Applied Physics Letters, 1999. **75**(23): p. 3692-3694.

95. J. H. Park, Y. S. Jeong, and S.Y. Lee, *Investigation on the Relation between the Thickness and the Orientation of Epitaxially Grown YBCO Thin Films by Laser Ablation.* Thin Solid Films, 1998. **318**: p. 4.

96. Y.V. Cherpak, V.O. Moskaliuk, A.V. Semenov, V.L. Svetchnikov, C.G. Tretiatchenko, and V.M. Pan, *Thickness Dependence Mechanisms of the Critical Current Density in High-T_c Cuprate Superconductor Films.* Superconductor Science & Technology, 2007. **20**(12): p. 1159-1164.

97. R.L.S. Emergo, J.Z. Wu, T. Aytug, and D.K. Christen, *Thickness Dependence of Superconducting Critical Current Density in Vicinal $YBa_2Cu_3O_{7-\delta}$ Thick Films.* Applied Physics Letters, 2004. **85**(4): p. 618-620.

98. M. Itoh, K. Sudoh, Y. Ichino, Y. Yoshida, and Y. Takai, *Influence of Surface Morphology on the Thickness Dependence of High-J_c Sm_1+XBa_2-XCu_3O_6 Films.* Physica C-Superconductivity and Its Applications, 2003. **392**: p. 1265-1269.

99. S.R. Foltyn, L. Civale, J.L. Macmanus-Driscoll, Q.X. Jia, B. Maiorov, H. Wang, and M. Maley, *Materials Science Challenges for High-Temperature Superconducting Wire.* Nature Materials, 2007. **6**(9): p. 631-642.

100. A.D. Berry, D.K. Gaskill, R.T. Holm, E.J. Cukauskas, R. Kaplan, and R.L. Henry, *Formation of High-Tc Superconducting Films by Organometallic Chemical Vapor-Deposition.* Applied Physics Letters, 1988. **52**(20): p. 1743-1745.

101. P.N. J. Zhao, *Metalorganic Chemical Vapor Deposition of YBCO Thin Films.* Materials Science Forum, 1993. **130-132**: p. 233-254.

102. T. Sugimoto, *Chemical Vapor Depostion of Oxide HTS Thin Films.* Materials Science Forum, 1993. **137-139**: p. 395-454.

103. R.V. Justinas Palisaitis, *Epitaxial Growth of Thin Films.* Physics of Advanced Materials Winter School 2008.

104. K. Frohlich, J. Souc, A. Rosova, D. Machajdik, I.E. Graboy, V.L. Svetchnikov, A. Figueras, and F. Weiss, *Superconducting $YBa_2Cu_3O_{7-\delta}$ Films Prepared by Aerosol Metal Organic Chemical Vapour Deposition on Al_2O_3 Substrate with CeO_2 Buffer Layer.* Superconductor Science & Technology, 1997. **10**(9): p. 657-662.

105. C.Y. Cho, D. Hwang, K.S. No, J.S. Chun, and S.H. Kim, *Effects of Deposition Temperature on the Microstructure of MOCVD $YBa_2Cu_3O_{7-\delta}$ Thin-Films.* Journal of Materials Science, 1993. **28**(11): p. 2915-2922.

106. V. Selvamanickam, A. Ivanova, D.B. Fenner, T. Thurston, M.S. Walker, A.E. Kaloyeros, and P. Haldar, *Fabrication of Biaxially-Textured Thick Film Y-Ba-Cu-O Superconductor by MOCVD on Cube-Textured Metal Substrates*, in *High-Temperature Superconductors: Synthesis, Processing, and Applications Ii*, U. Balachandran and P.J. McGinn, Editors. 1996, Minerals, Metals & Materials Soc: Warrendale. p. 165-174.

107. T. Aytug, M. Paranthaman, E.D. Specht, Y. Zhang, K. Kim, Y.L. Zuev, C. Cantoni, A. Goyal, D.K. Christen, V.A. Maroni, Y. Chen, and V. Selvamanickam, *Enhanced Flux Pinning in MOCVD-YBCO Films through Zr Additions: Systematic Feasibility Studies.* Superconductor Science & Technology, 2010. **23**(1).

108. Y.H. Kim, C.J. Kim, B.H. Jun, T.H. Sung, Y.H. Han, S.C. Han, H.J. Paik, J.S. Youn, and K. No, *Effect of Oxygen Partial Pressure on the Morphology and Properties of Ce Doped YBCO Films Fabricated by a MOCVD Process.* Physica C-Superconductivity and Its Applications, 2009. **469**(15-20): p. 1410-1413.

109. O. Stadel, R.Y. Muydinov, G. Brauer, M.O. Rikel, J. Ehrenberg, J. Bock, G. Kotzyba, R. Nast, W. Goldacker, S.V. Samoylenkov, and A.R. Kaul, *MOCVD and MOD of YBCO and Buffer Layers on Textured Metal Tapes.* IEEE Transactions on Applied Superconductivity, 2009. **19**(3): p. 3160-3163.

110. R.J. Mensah, G. Majkic, Y.M. Chen, V. Selvamanickam, P. Putman, and K. Salama, *Effect of Mn Addition on in-Field Behavior of Ibad/MOCVD Gd-YBCO Second Generation HTS Tapes.* IEEE Transactions on Applied Superconductivity, 2009. **19**(3): p. 3216-3220.

111. B.J. Kim, S.W. Lim, H.J. Kim, G.W. Hong, and H.G. Lee, *New MOD Solution for the Preparation of High $J_{(C)}$ Rebco Superconducting Films.* Physica C-Superconductivity and Its Applications, 2006. **445**: p. 582-586.

112. A. Sheth, H. Schmidt, and V. Lasrado, *Review and Evaluation of Methods for Application of Epitaxial Buffer and Superconductor Layers.* Applied Superconductivity, 1998. **6**(10-12): p. 855-873.

113. S. Sathyamurthy and K. Salama, *Application of Metal-Organic Decomposition Techniques for the Deposition of Buffer Layers and Y123 for Coated-Conductor*

Fabrication. Physica C-Superconductivity and Its Applications, 2000. **329**(1): p. 58-68.

114. M. Paranthaman, M.S. Bhuiyan, S. Sathyamurthy, H.Y. Zhai, A. Goyal, and K. Salama, *Epitaxial Growth of Solution-Based Rare-Earth Niobate, Re_3NbO_7, Films on Biaxially Textured Ni-W Substrates.* Journal of Materials Research, 2005. **20**(1): p. 6-9.

115. A. Gupta, R. Jagannathan, E.I. Cooper, E.A. Giess, J.I. Landman, and B.W. Hussey, *Superconducting Oxide-Films with High Transition-Temperature Prepared from Metal Trifluoroacetate Precursors.* Applied Physics Letters, 1988. **52**(24): p. 2077-2079.

116. Y. Iijima, N. Tanabe, O. Kohno, and Y. Ikeno, *Inplane Aligned $YBa_2Cu_3O_{7-\delta}$ Thin-Films Deposited on Polycrystalline Metallic Substrates.* Applied Physics Letters, 1992. **60**(6): p. 769-771.

117. M. Klee, W. Brand, and J.W.C. Devries, *Superconducting Films in the Y-Ba-Cu-O System Made by Thermal-Decomposition of Metal Carboxylates.* Journal of Crystal Growth, 1988. **91**(3): p. 346-351.

118. C. Dubs, K. Fischer, and P. Gornert, *Liquid-Phase Epitaxy of $YBa_2Cu_3O_{7-\delta}$ on $NdGaO_3$ and $LaGaO_3$ Substrates.* Journal of Crystal Growth, 1992. **123**(3-4): p. 611-614.

119. K. Fischer, N.M. Chebotaev, and S. Naumov, *Isothermal Crystal-Growth of $YBa_2Cu_3O_{7-\delta}$ in BaO-CuO-CuO0.5 Flux Melts at Reduced Oxygen Partial Pressures.* Journal of Crystal Growth, 1993. **132**(3-4): p. 444-450.

120. K. Nomura, S. Hoshi, Y. Nakamura, T. Izumi, and Y. Shiohara, *Initial Growth Mechanism of $YBa_2Cu_3O_{7-\delta}$ Crystal on MgO Substrate by Liquid-Phase Epitaxy.* Journal of Materials Research, 2001. **16**(10): p. 2947-2958.

121. J. Shanker, S.S. Kushwah, and P. Kumar, *Theory of Thermal Expansivity and Bulk Modulus for MgO and Other Minerals at High Temperatures.* Physica B, 1997. **233**(1): p. 78-83.

122. T. Izumi, K. Kakimoto, K. Nomura, and Y. Shiohara, *Preferential Growth Mechanism of YBCO Film on MgO Substrate in Initial Stage of LPE Growth.* Journal of Crystal Growth, 2000. **219**(3): p. 228-236.

123. K. Kakimoto, Y. Sugawara, T. Izumi, and Y. Shiohara, *Initial Growth Mechanism of YBCO Films in Liquid Phase Epitaxy Process.* Physica C-Superconductivity and Its Applications, 2000. **334**(3-4): p. 249-258.

124. L.H. Perng, T.S. Chin, K.C. Chen, and C.H. Lin, *Y-Ba-Cu-O Superconducting Films Grown on (100) Magnesia and Sapphire Substrates by a Melt Growth Method without Crucible.* Superconductor Science & Technology, 1990. **3**(5): p. 233-237.

125. H.J. Scheel, C. Klemenz, F.K. Reinhart, H.P. Lang, and H.J. Guntherodt, *Monosteps on Extremely Flat $YBa_2Cu_3O_{7-\delta}$ Surfaces Grown by Liquid-Phase Epitaxy.* Applied Physics Letters, 1994. **65**(7): p. 901-903.

126. J. Tsujino, N. Tatsumi, and Y. Shiohara, *Superconducting $YBa_2Cu_3O_{7-\delta}$ Films Prepared by Rf Thermal Plasma Evaporation.* Physica C, 1994. **235**: p. 583-584.

127. S. Yuhya, K. Kikuchi, Y. Shiohara, K. Terashima, and T. Yoshida, *Superconducting $YBa_2Cu_3O_{7-\delta}$ Films Prepared by Rf Plasma Flash Evaporation.* Journal of Materials Research, 1992. **7**(10): p. 2673-2679.

128. K. Seshan, *Handbook of Thin-Film Deposition Processes and Techniques*2002. 692.

129. J.R. Ahn, S.G. Lee, Y.S. Hwang, G.Y. Sung, and D.K. Kim, *Fabrication of MgB_2 Thin Film by Rf Magnetron Sputtering.* Physica C-Superconductivity and Its Applications, 2003. **388**: p. 127-128.

130. Z. Mori, K. Eitoku, T. Doi, S. Koba, and Y. Hakuraku, *MgB_2 Thin Film Fabrication by Rf Magnetron Sputtering.* Physica C-Superconductivity and Its Applications, 2003. **388**: p. 115-116.

131. C. Latief and M. Barmawi, *Deposition of YBCO Thin Film with Buffer Layer by Unbalanced Magnetron Sputtering*, in *Third International Conference on Thin Film Physics and Applications*, S.X. Zhou, Y.L. Wang, Y.X. Chen, and S.Z. Mao, Editors. 1998, Spie-Int Soc Optical Engineering: Bellingham. p. 196-199.

132. D. Dijkkamp, T. Venkatesan, X.D. Wu, S.A. Shaheen, N. Jisrawi, Y.H. Minlee, W.L. Mclean, and M. Croft, *Preparation of Y-Ba-Cu Oxide Superconductor Thin-Films Using Pulsed Laser Evaporation from High-T_c Bulk Material.* Applied Physics Letters, 1987. **51**(8): p. 619-621.

133. H.Weinstock and R.W.Ralston, *The New Superconducting Electronics*1993: Kluwer Academic Publishers.

134. R. Eason, *Pulsed Laser Deposition of Thin Films* 2007, Canada: Wiley.

135. R.K. Singh, O.W. Holland, and J. Narayan, *Theoretical-Model for Deposition of Superconducting Thin-Films Using Pulsed Laser Evaporation Technique.* Journal of Applied Physics, 1990. **68**(1): p. 233-247.

136. R.K. Singh, *Target Ablation Characteristics During Pulsed-Laser Deposition of Thin-Films.* Journal of Non-Crystalline Solids, 1994. **178**: p. 199-209.

137. D. Bhattacharya, R.K. Singh, and P.H. Holloway, *Laser-Target Interactions During Pulsed Laser Deposition of Superconducting Thin-Films.* Journal of Applied Physics, 1991. **70**(10): p. 5433-5439.

138. A. Cohen, P. Allenspacher, M.M. Brieger, I. Jeuck, and H. Opower, *Beam Target Interaction During Growth of $YBa_2Cu_3O_{7-\delta}$ by the Laser Ablation Technique.* Applied Physics Letters, 1991. **59**(17): p. 2186-2188.

139. S.R. Foltyn, R.C. Dye, K.C. Ott, E. Peterson, K.M. Hubbard, W. Hutchinson, R.E. Muenchausen, R.C. Estler, and X.D. Wu, *Target Modification in the Excimer Laser Deposition of $YBa_2Cu_3O_{7-\delta}$ Thin-Films.* Applied Physics Letters, 1991. **59**(5): p. 594-596.

140. D.L. Lin, X. Li, Z.D. Liu, and T.F. George, *Internal Explosion in Laser Ablation of Superconducting Targets.* Journal of Applied Physics, 1992. **72**(9): p. 4227-4231.

141. R.K. Singh, D. Bhattacharya, and J. Narayan, *Subsurface Heating Effects During Pulsed Laser Evaporation of Materials.* Applied Physics Letters, 1990. **57**(19): p. 2022-2024.

142. R.A. Neifeld, S. Gunapala, C. Liang, S.A. Shaheen, M. Croft, J. Price, D. Simons, and W.T. Hill, *Systematics of Thin-Films Formed by Excimer Laser Ablation - Results on $SmBa_2Cu_3O_7$.* Applied Physics Letters, 1988. **53**(8): p. 703-704.

143. J. Narayan, N. Biunno, R. Singh, O.W. Holland, and O. Auciello, *Formation of Thin Superconducting Films by the Laser Processing Method.* Applied Physics Letters, 1987. **51**(22): p. 1845-1847.

144. J.A. Venables, G.D.T. Spiller, and M. Hanbucken, *Nucleation and Growth of Thin-Films.* Reports on Progress in Physics, 1984. **47**(4): p. 399-459.

145. E. Bauer, *Phänomenologische Theorie Der Kristallabscheidung an Oberflächen.* . Zeitschrift für Kristallographie, 1958. **110**: p. 372-394.

146. M.I. Faley, S.B. Mi, A. Petraru, C.L. Jia, U. Poppe, and K. Urban, *Multilayer Buffer for High-Temperature Superconductor Devices on MgO.* Applied Physics Letters, 2006. **89**(8): p. -.

147. J. Du, S. Gnanarajan, and A. Bendavid, *Characterization of MgO Substrates for Growth of Epitaxial YBCO Thin Films.* Superconductor Science & Technology, 2005. **18**(8): p. 1035-1041.

148. K.T. Y. Yamada, H. Kobayashi, M. Konishi, T. Watanabe, A. Ibi, T. Muroga, and S. Miyata , T. Kato and T. Hirayama, Y. Shiohara *Epitaxial Nanostructure and Defects Effective for Pinning in $Y(Re)Ba_2Cu_3O_{7-x}$ Coated Conductors.* Applied Physics Letters, 2005. **87**.

149. J.M. Phillips, *Substrate Selection for High-Temperature Superconducting Thin Films.* Journal of Applied Physics, 1996. **79**(4): p. 1829-1848.

150. Y.W. Ma and L.Y. Xiao, *Second Generation YBCO Coated Conductors: A Review.* Chinese Science Bulletin, 2004. **49**(23): p. 2435-2439.

151. X.D. Wu, S.R. Foltyn, P.N. Arendt, W.R. Blumenthal, I.H. Campbell, J.D. Cotton, J.Y. Coulter, W.L. Hults, M.P. Maley, H.F. Safar, and J.L. Smith, *Properties of $YBa_2Cu_3O_{7-\delta}$ Thick-Films on Flexible Buffered Metallic Substrates.* Applied Physics Letters, 1995. **67**(16): p. 2397-2399.

152. Y. Iijima, M. Kimura, T. Saitoh, and K. Takeda, *Development of Y-123-Coated Conductors by Ibad Process.* Physica C-Superconductivity and Its Applications, 2000. **335**(1-4): p. 15-19.

153. Y. Iijima, N. Kaneko, S. Hanyu, Y. Sutoh, K. Kakirnoto, S. Ajimura, and T. Saitoh, *Development of Ibad/PLD Process for Long Length Y-123 Conductors in Fujikura.* Physica C-Superconductivity and Its Applications, 2006. **445**: p. 509-514.

154. S.H. Wee, A. Goyal, J. Li, Y.L. Zuev, S. Cook, and L. Heatherly, *The Incorporation of Nanoscale Columnar Defects Comprised of Self-Assembled $BaZrO_3$ Nanodots to Improve the Flux Pinning and Critical Current Density of $NdBa_2Cu_3O_{7-\delta}$ Films Grown on Rabits.* Superconductor Science & Technology, 2007. **20**(8): p. 789-793.

155. U. Alexander, F. Herbert, I. Alexander, D. Juergen, K. Juergen, O. Marijn, L. Martino, and N.Heinz-W., *Large Area YBCO-Coated Stainless Steel Tapes with High Critical Currents.* IEEE Transactions on Applied Superconductivity, 2003.

156. T.A. Campbell, T.J. Haugan, I. Maartense, J. Murphy, L. Brunke, and P.N. Barnes, *Flux Pinning Effects of Y_2O_3 Nanoparticulate Dispersions in Multilayered YBCO Thin Films.* Physica C-Superconductivity and Its Applications, 2005. **423**(1-2): p. 1-8.

157. J. Gutierrez, A. Llordes, J. Gazquez, M. Gibert, N. Roma, S. Ricart, A. Pomar, F. Sandiumenge, N. Mestres, T. Puig, and X. Obradors, *Strong Isotropic Flux Pinning in Solution-Derived $YBa_2Cu_3O_{7-\delta}$ Nanocomposite Superconductor Films.* Nature Materials, 2007. **6**(5): p. 367-373.

158. Y. Sato, K. Matsuo, Y. Takahashi, K. Muranaka, K. Fujino, S. Hahakura, K. Ohmatsu, and H. Takei, *Development of $YBa_2Cu_3O_{7-\delta}$ Tape by Using Inclined Substrate Method.* IEEE Transactions on Applied Superconductivity, 2001. **11**(1): p. 3365-3370.

159. K. Ohmatsu, K. Muranaka, S. Hahakura, T. Taneda, K. Fujino, H. Takei, Y. Sato, K. Matsuo, and Y. Takahashi, *Development of in-Plane Aligned YBCO Tapes Fabricated by Inclined Substrate Deposition.* Physica C-Superconductivity and Its Applications, 2001. **357**: p. 946-951.

160. S. Soltan, J. Albrecht, and H.U. Habermeier, *Spin-Polarized Quasiparticles Injection Effects in the Normal State of YBCO Thin Films.* Physica C-Superconductivity and Its Applications, 2007. **460**: p. 1088-1089.

161. N.H. Babu, E.S. Reddy, D.A. Cardwell, A.M. Campbell, C.D. Tarrant, and K.R. Schneider, *Artificial Flux Pinning Centers in Large, Single-Grain (Re)-Ba-Cu-O Superconductors.* Applied Physics Letters, 2003. **83**(23): p. 4806-4808.

162. J. Raittila, H. Huhtinen, P. Paturi, and Y.P. Stepanov, *Preparation of Superconducting $YBa_2Cu_3O_{7-\delta}$ Nanopowder by Deoxydation in Ar before Final Oxygenation.* Physica C-Superconductivity and Its Applications, 2002. **371**(2): p. 90-96.

163. B. Ma, M. Li, R.E. Koritala, B.L. Fisher, A.R. Markowitz, R.A. Erck, R. Baurceanu, S.E. Dorris, D.J. Miller, and U. Balachandran, *Pulsed Laser Deposition of YBCO Films on ISD MgO Buffered Metal Tapes.* Superconductor Science & Technology, 2003. **16**(4): p. 464-472.

164. N. Yao and Z.L. Wang, eds. *Handbook of Microscopy for Nanotechnology*. 2005, Kluwer Academic Publishers: Boston, USA.

165. *Jeol Jem-2100 Lab6 Transmission Electron Microscope*. http://www.cem.bham.ac.uk/jeol_2100.shtml 2010 [cited 2010 10.10.2010].

166. Z.R. Li, ed. *Industrial Applications of Electron Microscopy*. 2003, Marcel Dekker, Inc.: New York.

167. D.A. Cardwell and D.S. Ginley, eds. *Handbook of Superconducting Materials*. Vol. II:Characterization, Applications and Cryogenics. 2003, Insitute of Physics.

168. *Physical Property Measurement System (PPMS®)*. http://www.qdusa.com/products/ppms.html